

Negative Magnetophoresis of Submicron Species in Magnetic Nanofluids

by

Lino A. Gonzalez

B.S., Chemical Engineering - University of Florida, 1999

M.S., Chemical Engineering - Massachusetts Institute of Technology, 2002

M.S., Chemical Engineering Practice - Massachusetts Institute of Technology, 2002

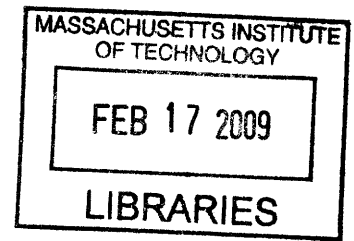
Submitted to the Department of Chemical Engineering in partial fulfillment of the requirements for the degree of

Doctor of Philosophy

at the

Massachusetts Institute of Technology

February 2009



© 2009 Massachusetts Institute of Technology. All rights reserved.

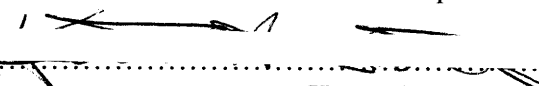
Signature of Author.....

.....
Department of Chemical Engineering
September 26, 2008

Certified by.....

T. Alan Hatton
Ralph Landau Professor of Chemical Engineering Practice
Thesis Supervisor

Certified by.....


Kenneth A. Smith
Gilliland Professor of Chemical Engineering
Thesis Supervisor

Accepted by.....

.....
William M. Deen
Carbon P. Dubbs Professor of Engineering
Chairman, Committee for Graduate Students

Negative Magnetophoresis of Submicron Species in Magnetic Nanofluids

by

Lino A. Gonzalez

Submitted to the Department of Chemical Engineering on September 26, 2008 in partial fulfillment of the requirements of the Degree of Doctor of Philosophy

ABSTRACT

In this work we studied the focusing and trapping of submicron, nonmagnetic species immersed in a magnetic nanofluid under applied magnetic fields. Focusing was achieved using two pairs of permanent magnets, which forced submicron fluorescently-tagged polystyrene beads to focus in the region between the two magnet pairs. Size-based trapping was achieved using a microchip that produced spatially increasing magnetic-field gradients that trapped flowing polystyrene beads at different locations, depending on their relative sizes.

In the focusing experiments, a mixture of magnetic nanoparticles and nonmagnetic, fluorescently tagged latex beads (435 nm and 910 nm in diameter) were loaded into a capillary tube and placed in-between the magnet pairs. The concentration profiles of the latex beads were measured using fluorescence imaging and simulated results were obtained using continuum modeling. Good quantitative agreement was found between experiments and theory for both latex-bead sizes at various experimental conditions.

Size-based trapping of latex beads was accomplished by balancing drag and magnetic buoyancy forces in such a way that smaller and larger nonmagnetic species were trapped at different locations. A microfabricated device with two external magnets was used to generate the trapping forces, and a syringe pump was used to flow the mixture of magnetic fluid and nonmagnetic particles through the device. Size-based trapping was achieved for a feed mixture of 435 nm and 865 nm latex beads, as measured using fluorescence imaging. Semi-quantitative agreement was found between experiments and Brownian-dynamics simulations. Our work shows that negative magnetophoresis in magnetic nanofluids can be used to size-selectively trap and focus submicron, nonmagnetic species.

Thesis Supervisor: T. Alan Hatton, Ralph Landau Professor of Chemical Engineering
Thesis Supervisor: Kenneth A. Smith, Gilliland Professor of Chemical Engineering

Acknowledgements

Through my rather extensive stay at MIT, I have benefitted from the help of numerous colleagues and professors as well as family and friends. The first two individuals I would like to thank are my thesis advisors, Professors T. Alan Hatton (also known as Trevor in a previous life) and Kenneth A. Smith. Their patience, suggestions, endless supply of ideas, and the amount of freedom they provided for me resulted in a great educational experience. I will never forget Ken Smith's endless laughter during all our meetings and Alan Hatton's witty sense of humor. I would like to also thank my committee members, Professors Pat Doyle and Markus Zahn, for all their helpful suggestions throughout this project.

I would like to thank many of the past and current members of the Hatton group for their help and support. Dr. Seif Fateen was the first person I worked with when I joined the group, and his work on negative magnetophoresis opened the door for this project. His help at the beginning stages of this work was invaluable. Dr. Tim Finegan taught me everything I know about optics and guided me through the design and setup of the optical setup used. I would like to thank Dr. Geoff Moeser for providing me with most of the magnetic nanofluid used in this work. For the work on magnetophoretic trapping, a million thanks go to my former lab mate and best of friends Edward Park. We worked as a team on the conceptual design of the micro-chip and performed all of the trapping experiments together. I really enjoyed hanging out working and with Ed during his stay at MIT.

Drs. Harpreet Sign, Huan Zhang, Smeet Deshmukh, Lev Bromberg, and Tatsushi Isojima were very helpful with the different experimental procedures used in this work. When I came into the lab, I had never done a single experiment outside of chemistry lab classes, so their help was invaluable. I would like to thank Ravikanth Annavarapu, Sanjoy Sircar, Saurabh Tejwani, and Fei Chen for very helpful discussions on physics optics. My appreciation goes to Liang Chen for providing me with the SEM images presented in this thesis. Finally, I would like to thank handyman Nate Aumock for helping me fix the various optical equipment that broke down at one point or another.

There were a few other colleagues outside of the Hatton group that were of great help. Two undergrads, Willie Sanchez and Bryan Haddon, wrote a large portion of the Labview and Matlab codes used for data acquisition and analysis. Vikram Sivakumar from Material Science trained me to use their VSM equipment and was very helpful with all my magnetization measurements. Ramin Haghgooie from the Doyle group was incredibly helpful with the Brownian dynamics simulations. A special thanks goes out to Andy Gallant from the MIT Central Machine Shop from fabricating just about every experimental fixture used in this work.

Last but not least, I would like to thank my parents Roberto y Milagros Gonzalez and my brother Luis Gonzalez for their endless support and unconditional love. My parents left everything they ever knew behind in Cuba to give my brother and me an opportunity to succeed in a free country. I dedicate this thesis to them.

Table of Contents

List of Figures	9
List of Tables.....	15
Nomenclature	16
List of Acronyms.....	20
Chapter 1. Introduction	21
1.1 Recent trends in size-based separations	21
1.1.1 Size-based separation techniques.....	22
1.1.2 Separations using external fields	23
1.2 Magnetic separation	24
1.2.1 Categories	25
1.2.2 Magnetophoresis	26
1.2.2.1 Positive magnetophoresis.....	26
1.2.2.2 Negative magnetophoresis	27
1.3 Magnetic nanofluids.....	28
1.3.1 Applications	30
1.3.2 Magnetophoretic focusing	31
1.3.3 Magnetophoretic trapping.....	33
1.4 Thesis objectives and outline	35
1.5 Bibliography	36
Chapter 2. Properties of Magnetic Nanofluids.....	45
2.1 Magnetic and hydrodynamic size distributions	45
2.2 Actual magnetic diameters.....	47
2.3 Nanofluid magnetization.....	50
2.3.1 Langevin expression for nanofluid magnetization.....	53
2.3.2 Magnetic curve reconstruction.....	55
2.4 Average magnetic and hydrodynamic sizes.....	61
2.5 Bibliography	63

Chapter 3. Magnetophoresis in Magnetic Nanofluids.....	65
3.1 Maxwell’s equations for MQS systems	65
3.1.1 Field generated by permanent magnets.....	66
3.1.2 Numerical solutions for linear and nonlinear materials.....	70
3.2 Continuum equations for magnetic nanofluids	71
3.2.1 Force on immersed species	72
3.2.1.1 Arbitrariness of magnetic pressures, stresses, and body forces	76
3.3 Thermodynamics of magnetic nanofluids.....	79
3.3.1 Equilibrium thermodynamics.....	80
3.3.2 Rate of entropy generation.....	83
3.4 Diffusion in magnetic nanofluids.....	85
3.4.1 Binary diffusion of nonmagnetic species.....	85
3.4.2 Generalized multicomponent diffusion.....	89
3.4.2.1 Multicomponent diffusion summary.....	93
3.4.3 Application to binary system	94
3.4.3.1 Comparison with other approaches.....	95
3.4.3.1.1 Forced diffusion using Stokes migration velocity	95
3.4.3.1.2 Forced diffusion using magnetic fluid force density	97
3.4.3.1.3 Forced diffusion using force density on nonmagnetic particles	97
3.4.4 Binary diffusion of magnetic species.....	98
3.5 Summary	99
3.6 Bibliography	100
Chapter 4. Magnetophoretic Focusing.....	103
4.1 Focusing experiments	103
4.1.1 Materials	103
4.1.2 Experimental Setup.....	106
4.1.3 Magnetic and force fields.....	108
4.1.4 Sample preparation	110
4.1.5 Fluorescence imaging	111
4.1.6 Data acquisition	112

4.2 Data processing.....	114
4.2.1 Fluorescence calibration	116
4.2.2 Magnetic nanofluid absorption	119
4.3 Experiments	121
4.3.1 Focusing of 910 nm latex beads.....	122
4.3.2. Magnetic nanofluid defocusing.....	123
4.3.3 Effect of magnetic fluid and field strength	125
4.3.4 Effect of latex bead concentration	126
4.3.5 Effect of particle size	128
4.4 Continuum model.....	128
4.4.1 Governing equations and parameters.....	129
4.4.2 Ideal pseudo-binary system.....	131
4.4.3 Excess chemical potentials	133
4.4.3.1 Statistical mechanics.....	134
4.4.3.2 Volume exclusion	135
4.4.3.3 Electrostatic repulsion.....	138
4.4.3.4 Depletion forces	141
4.4.3.5 Magnetic dipole-dipole interactions	143
4.4.3.6 Excess chemical potential summary	146
4.4.4 Nonideal pseudo-binary diffusion.....	147
4.5 Comparison with experimental data	148
4.5.1 Analytical approximations	148
4.5.1.1 Dynamics at short time scales.....	148
4.5.1.2 Focusing at steady state	150
4.5.2 Magnetic nanofluid defocusing.....	151
4.5.3 Nonmagnetic species focusing.....	155
4.5.3.1 Effect of magnetic fluid and field strength	159
4.5.3.2 Effect of initial latex bead concentration	162
4.5.3.3 Effect of latex bead size	163
4.5.4 Focusing under different magnet configuration.....	164

4.5.5 Sensitivity studies	166
4.5.5.1 Magnetic field resolution	166
4.5.5.2 M-H curves	168
4.5.6 Experimental artifacts	170
4.5.6.1 Latex bead settling	170
4.5.6.2 Fluorescence enhancement from non-fluorescent beads	171
4.5.6.2 Species aggregation	173
4.6 Conclusions.....	174
4.7 Bibliography	174
Chapter 5. Magnetophoretic Trapping.....	177
5.1 Micro-chip trapping experiments.....	178
5.1.1 Materials	178
5.1.2 Experimental Setup.....	179
5.1.3 Magnetic and force fields.....	180
5.1.4 Sample preparation	182
5.1.5 Fluorescence imaging	183
5.1.6 Data acquisition	184
5.2 Data processing.....	185
5.3 Micro-chip experiments	187
5.4 Continuum and Brownian modeling.....	188
5.4.1 Governing continuum equations	189
5.4.2 Brownian dynamics	193
5.4.2.1 Particle-particle interactions	194
5.4.3 Magnetic force-density fitting.....	194
5.5 Model-predicted results	196
5.5.1 Magnetic nanoparticles	196
5.5.2 Latex beads	198
5.5.2.1 Effect of magnetic-field resolution	200
5.5.3 Micro-chip simulation summary.....	201

5.6 Plug-flow device	202
5.6.1 Magnetic and force fields.....	204
5.6.2 Sample preparation	205
5.6.3 Data acquisition	206
5.6.4 Data processing.....	206
5.6.5 Experiments	207
5.6.5.1 Focusing.....	207
5.6.5.2 Size-based trapping.....	208
5.6.6 Discussion.....	209
5.7 Summary and conclusions	210
5.8 Bibliography	210
Chapter 6. Concluding Discussion.....	212
6.1 Principal contributions.....	212
6.2 Limitations	213
6.2.1 Multicomponent diffusion	213
6.2.2 Focusing model.....	213
6.2.3 Trapping devices.....	214
6.3 Recommendations for future work	214
6.4 Bibliography	214

List of Figures

Figure 1-1: Schematic of a magnetic nanoparticle suspension. The arrows represent the direction of the permanent magnetic moment of each nanoparticle.	29
Figure 1-2: Schematic of mineral-separation process using magnetic buoyancy.	31
Figure 1-3: Focusing experiments performed by Fateen: (a) focusing setup; (b) measured magnetic-field intensity; (c) concentration profiles obtained for 840 nm latex beads, measured using fluorescence imaging.	32
Figure 1-4: Schematic for size-based trapping of nonmagnetic particles immersed in a magnetic nanofluid.	35
Figure 2-1: (a) TEM image of the magnetite cores and (b) size distribution fitted by a log-normal distribution with a median of 7.5 nm and a standard deviation of 0.32. ..	46
Figure 2-2: Number-average and volume-average hydrodynamic diameters of the polymer-coated magnetic nanoparticles.	47
Figure 2-3: Possible structures of the polymer-stabilized magnetic nanoparticles; (a) one polymer chain coats one magnetite nanoparticle, (b) multiple chains attach to one magnetite nanoparticle, (c) multiple magnetite nanoparticles are coated by a single polymer chain, and (d) a cluster of magnetite nanoparticles are covered by one or more polymer chains.	48
Figure 2-4: Dead region due to the attached polymer-coating.	49
Figure 2-5: Magnetization as a function of applied magnetic field; a) no applied field, b) small applied field, and c) large applied field.	51
Figure 2-6: Magnetization curve for a 2.1 wt% magnetic nanofluid.	53
Figure 2-7: M-H data fit using a log-normal function for the magnetic-size distribution.	56
Figure 2-8: Comparison between (a) magnetite particle-size distribution and (b) effective magnetic-size distribution.	59
Figure 2-9: M-H data fit using a magnetic size distribution consisting of three superimposed log-normal probability curves; (a) fit across a wide range of magnetic-field strengths and (b) in the region of small magnetic field strengths.	60

Figure 2-10: M - H curves for the three log-normal distributions used (dashed curves) and their linear superposition (solid curve). The curves are normalized to have the same M_{sat} value. 61

Figure 3-1: Hysteresis curve for a typical permanent magnet. 67

Figure 3-2: Operating curve for N48 neodymium magnets. The blue curve with data points is the manufacturer data, while the pink line corresponds to a straight-line fit..... 68

Figure 3-3: Permanent magnet with a uniformly distributed magnetic moment ($\mu_r \approx 1$) pointing in the z -direction. 68

Figure 4-1: Fluorescence spectra of “pink” and “purple” latex beads 104

Figure 4-2: SEM images of small and large fluorescently tagged latex-beads..... 105

Figure 4-3: Schematic of the setup used for focusing experiments. The origin is at the radial center of the capillary tube..... 107

Figure 4-4: Schematic of the aluminum fixture used to keep the magnets in position and allow for fluorescence imaging from overhead. 108

Figure 4-5: Magnetic field and force-density profiles for the configuration depicted in Figure 4-3..... 109

Figure 4-6: Force densities in the y and z directions..... 110

Figure 4-7: Schematic illustrating the principle behind Laser-Induced Fluorescence Imaging. 111

Figure 4-8: Data acquisition setup. The top image is a schematic for the actual setup shown in the bottom image..... 113

Figure 4-9: Background image (left) and reference image (right) obtained for a typical focusing experiment..... 114

Figure 4-10: Normalized fluorescence-intensity profile at a given time t (left) and its cross-section average (right). 115

Figure 4-11: Calibration curves for fluorescent beads; a) 435 nm beads, b) 910 nm beads, and c) 81 nm beads. 116

Figure 4-12: Calibration curve for the 910 nm beads, extended to include higher concentrations. 117

Figure 4-13: Normalized fluorescence intensity at a given latex-bead concentration as a function of magnetic fluid concentration.....	120
Figure 4-14: Fluorescence intensity profiles for 910 nm fluorescent beads immersed in a 0.08 vol% (0.41 wt%) magnetic nanofluid.....	122
Figure 4-15: Schematic for the increase in fluorescence due to “defocusing” of magnetic nanoparticles.....	123
Figure 4-16: Increase in fluorescence near $x = 0$ due to magnetic fluid “defocusing.”..	124
Figure 4-17: Focusing of 910 nm fluorescent, nonmagnetic beads in a magnetic nanofluid; (a) 0.1 vol % magnetite concentration and (b) 0.2 vol % magnetite concentration. The magnet spacing was 7 mm.....	125
Figure 4-18: Focusing of 910 nm fluorescent, nonmagnetic beads in a magnetic nanofluid at a stronger magnetic field; (a) 0.05 vol % magnetite concentration and (b) 0.1 vol % magnetite concentration. The magnet spacing was 6 mm.....	126
Figure 4-19: Focusing of 910 nm fluorescent, nonmagnetic beads in a magnetic nanofluid with different initial bead concentrations; (a) 0.02 vol %, (b) 0.1 vol %, and (c) 0.5 vol %.....	127
Figure 4-20: Focusing comparison of (a) 910 nm beads and (b) 435 nm beads in a 0.1 vol % magnetic nanofluid.....	128
Figure 4-21: Comparison between experimental and model-predicted fluorescence-intensity profiles due to magnetic fluid defocusing. The simulation results treat the magnetic nanoparticles as monodisperse.....	152
Figure 4-22: Comparison between experimental and model-predicted fluorescence-intensity profiles due to magnetic-fluid defocusing. The simulation results treat the magnetic nanoparticles as a mixture of three different-sized species.....	154
Figure 4-23: Comparison between experimental fluorescence-intensity profiles and the profiles predicted by the 1-component (plus solvent) magnetic-fluid model.....	156
Figure 4-24: Comparison between experimental fluorescence-intensity profiles and the profiles predicted by the 3-component (plus solvent) magnetic-fluid model.....	157
Figure 4-25: Comparison between fluorescence-intensity and latex-bead concentration profiles, as predicted by our model.....	158

Figure 4-26: Contour plot of the model-predicted concentration profile for the 910 nm beads at $t = 80$ min. The z -direction is along the thickness of the capillary.	159
Figure 4-27: Comparison between experimental and model-predicted fluorescence-intensity profiles for a lower magnetic fluid concentration (0.05 vol % magnetite)..	160
Figure 4-28: Comparison between experimental and model-predicted fluorescence-intensity profiles for a spacing of 7 mm between the magnet and the capillary at different magnetic fluid strengths; (a) 0.1, (b) 0.08, and (c) 0.2 vol % initial magnetite concentrations.	161
Figure 4-29: Comparison between experimental and model-predicted fluorescence-intensity profiles for 7 mm spacing between the magnet and the capillary at different initial latex-bead concentrations; (a) 0.02, (b) 0.1, and (c) 0.5 vol%... ..	162
Figure 4-30: Comparison between experimental and model-predicted fluorescence-intensity profiles for 435 nm fluorescent beads.	163
Figure 4-31: Schematic of the experimental setup with a different magnet configuration.	164
Figure 4-32: Experimental fluorescence-intensity profiles for the flipped magnet configuration; (a) 910 nm beads and (b) 435 nm beads.	165
Figure 4-33: Model-predicted fluorescence-intensity profiles for the flipped magnet configuration; a) 910 nm beads and b) 435 nm beads.	165
Figure 4-34: Comparison between analytic and numerical magnetic-field intensity profiles for the original magnet configuration depicted in Figure 4-3.	167
Figure 4-35: Comparison between fluorescence intensity results using numerical and analytic magnetic-field intensity profiles.	168
Figure 4-36: Fit to experimental $M-H$ data using eq. (4.92).	169
Figure 4-37: Comparison between fluorescence intensity results using numerical and analytic magnetic-field intensity profiles.	170
Figure 4-38: Increase in fluorescence due to the focusing of non-fluorescent beads.	172
Figure 4-39: Increase in fluorescence due to an increase of non-fluorescent bead concentration.	172

Figure 5-1: Schematic of the technique used to size-selectively trap nonmagnetic particles immersed in a magnetic nanofluid.....	177
Figure 5-2: Schematic of the experimental setup used for the micro-chip trapping experiments.....	179
Figure 5-3: Schematic (left) and photograph (right) of the micro-chip used for the trapping experiments.....	180
Figure 5-4: Magnetic field intensity (left) and force density in the z direction for a 0.1 vol % magnetic nanofluid (right) averaged across the flow-channel cross-section..	180
Figure 5-5: Magnetic field intensity over a cross-section of the flow channel.....	181
Figure 5-6: Force densities in the x and y directions for a 0.1 vol % magnetic nanofluid averaged over the cross-section of the flow channel.	182
Figure 5-7: Schematic of LIFI for multiple species.....	183
Figure 5-8: Schematic of the data-acquisition setup for multiple species.	184
Figure 5-9: Normalized fluorescence spectra of pink and purple beads.....	185
Figure 5-10: Experimental results for size-based trapping of latex beads.....	187
Figure 5-11: Velocity profile in a rectangular channel.....	190
Figure 5-12: Test of the validity of continuum models for the flow-chip experiments as a function of the distance down the channel (z).	192
Figure 5-13: Empirical fits to the cross-sectional averaged magnetic force densities....	195
Figure 5-14: Normalized, cross-section averaged concentration of magnetic nanoparticles.	197
Figure 5-15: Normalized concentration of magnetic nanoparticles at the cross-section corresponding to $z = 14.5$ mm.	198
Figure 5-16: Comparison between experimental and model-predicted results for the size-based trapping of latex beads.....	199
Figure 5-17: Effect of neglecting variations in the force densities over the channel cross-section.	201
Figure 5-18: Schematic of “plug flow” device.....	202
Figure 5-19: Magnetic fixture and tube holder used for the plug-flow experiments.....	203

Figure 5-20: Magnetic field and force-density distributions for a 0.3 vol % magnetic nanofluid. 204

Figure 5-21: Fluorescence-intensity profiles for 435 nm (left) and 910 nm (right) fluorescent beads immersed in a 0.1 vol % magnetic nanofluid. The fluid velocity was zero in these experiments..... 207

Figure 5-22: Fluorescence-intensity profiles for 435 nm (left) and 910 nm (right) fluorescent beads immersed in a 0.3 vol % magnetic nanofluid, with the capillary tube traveling at 5 $\mu\text{m/s}$ 208

List of Tables

Table 1.1: Methods used for size-based separation of macroscopic and submicron species.....	22
Table 2.1: Parameters used for the log-normal distributions used to generate the plots in Figure 2-8.....	58
Table 4.1: Zeta potentials for the colloidal species used in the focusing experiments...	106
Table 4.2: Typical sample volumes and concentrations	110
Table 4.3: Values for the universal constants used in this chapter	135
Table 4.4: Values for the parameters used to calculate excluded-volume effects	137
Table 4.5: Values for the parameters used to calculate electrostatic effects	140
Table 4.6: Electrostatic interaction coefficients (dimensionless)	141
Table 4.7: Depletion interaction coefficients.....	142
Table 4.8: Magnetic interaction coefficients	144
Table 5.1: Common sample volumes and concentrations used in the flow-chip experiments	183
Table 5.2: Common sample volumes and concentrations used in the plug-flow experiments	205

Nomenclature

The following are the most commonly used constants and variables in this thesis. The constants and variables with no units included are unit-less. Unless noted otherwise, a quantity with no subscript refers to the mixture and a quantity with a subscript refers to the component in the subscript. For example, ρ denotes the density of the mixture and ρ_i denotes the density of component i . The convention used is italics for scalars, one underline for vectors, and two underlines for tensors.

Electromagnetic Constants and Variables

Symbol	Description	SI Unit
\underline{H}	Magnetic field	A/m
\underline{B}	Magnetic induction	T
\underline{M}	Magnetization	A/m
\widehat{m}	Magnetic moment	H · A/m ²
$G(\widehat{m})$	Magnetic moment distribution	m ² /(H · A)
\underline{H}_0	Applied magnetic field	A/m
\underline{h}	Induced magnetic field	A/m
$\underline{M}_{\text{sat}}$	Saturation magnetization	A/m
\underline{M}_p	Permanent magnet magnetization	A/m
\underline{M}_d	Bulk material magnetization	A/m
μ_0	Permeability of space	H/m or N/m ²
μ	Magnetic permeability	N/A ²
μ_r	Reduced permeability	-
χ	Magnetic susceptibility	-
ρ_e	Free-charge density	C/m ³
\underline{E}	Electric field	N/C or V/m
\underline{D}	Electric displacement	C/m ²
\underline{J}_e	Free electric current flux	A/m ²
ϵ_0	Permittivity of space	F/m
ϵ	Electric permittivity	F/m
ϵ_r	Dielectric constant	-
κ^{-1}	Debye length	m
e	Elementary charge	C
ψ	Zeta potential	V
I_t	Total magnetic moment	A · m ²
α	Langevin parameter	-

Mechanical Constants and Variables

Symbol	Description	SI Unit
t	Time	s
\underline{r}	Position vector	m
d	Diameter	m
a	Radius	m
\bar{d}	Mean diameter	m
\underline{v}	Mass-average velocity	m/s
\underline{v}^*	Molar-average velocity	m/s
\bar{v}	Mean velocity	m/s
\underline{v}_r	Velocity relative to the fluid continuum	m/s
m	Mass	kg
V	Volume	m ³
\underline{F}	Force	N
\underline{f}	Force density	N/m ³
$\underline{\tau}$	Torque	N · m
p	Pressure	N/m ²
$\underline{\underline{T}}$	Stress tensor	N/m ²
$\underline{\underline{I}}$	Idemfactor	-
ρ	Density	kg/m ³
η	Viscosity	kg/(m · s)
\underline{g}_i	Body force per unit mass	m ² /s
\underline{g}	Gravitational acceleration	m ² /s
θ	Angle	radians
S_p	Surface area	m ²

Transport Constant and Variables

Symbol	Description	SI Unit
C	Concentration	mol/m^3
v	Molar volume	m^3/mol
ϕ_i	Volume fraction	-
w_i	Weight fraction	-
x_i	Mole fraction of species i	-
T	Temperature	K
n_i	Number of species	-
k	Boltzmann's constant	J/K
R	Gas constant	$\text{J}/(\text{mol} \cdot \text{K})$
N_A	Avogadro's number	mol^{-1}
\underline{q}	Heat flux	W/m^2
W_i	Molecular weight	kg/mol
\underline{J}_i^*	Molar flux relative to molar-average velocity	$\text{mol}/(\text{m}^2 \cdot \text{s})$
\underline{J}_i	Molar flux relative to mass-average velocity	$\text{mol}/(\text{m}^2 \cdot \text{s})$
\underline{j}_i	Molar flux relative to molar-average velocity	$\text{mol}/(\text{m}^2 \cdot \text{s})$
D_{ij}	Multicomponent diffusion coefficient	m^2/s
\mathcal{D}_{ij}	Binary diffusion coefficient	m^2/s
α_{ij}	Onsager coefficient	$\text{kg} \cdot \text{m}^3/\text{t}$
\underline{d}_i	Generalized driving force	m^{-1}

Thermodynamic Variables

Symbol	Description	SI Unit
U	Internal energy density	J/kg
S	Entropy density	J/(kg · K)
W_m	Magnetic work density	J/kg
E_m	Magnetic energy	J
p_0	Pressure at zero magnetic field	N/m ²
\bar{V}_i	Partial molar volume	m ³ /mol
ξ_i	Chemical potential	J/kg
ξ_i^{id}	Ideal chemical potential	J/kg
ξ_i^{ex}	Excess chemical potential	J/kg
ξ_0	Solvent chemical potential	J/kg
ϑ_i	Specific magnetic moment	A · m ² /kg
$\bar{\vartheta}_i$	Partial mass magnetic moment	A · m ² /kg
γ_i	Activity coefficient	-
b_{ij}	Virial coefficient	m ³ /mol
W_{ij}	Potential of mean force	J
u_{ij}	Force potential	J
θ_S	Rate of entropy generation	W/(m ³ · K)
\underline{j}_S	Entropy flux	W/(m ² · K)

Miscellaneous

σ	Standard deviation	-
z_i	Ion charge valance	-
ℓ	Microscopic length scale	m
L	Macroscopic length scale	m
λ	wavelength	m
$\tilde{\alpha}$	Electrostatic interaction coefficient	-
$\tilde{\beta}$	Depletion interaction coefficient	-
$\tilde{\lambda}$	Magnetic dipole interaction coefficient	-
I	Fluorescence intensity	-
θ_m	Dimensionless magnetic concentration	-
θ_p	Dimensionless latex bead concentration	-

List of Acronyms

This is a list of most of the acronyms used in this thesis.

Acronym	Description
CCD	Charge Coupled Device
DI	De-Ionized
DLVO	Derjaguin, Landau, Verwey and Overbeek
DLS	Dynamic Light Scattering
FL	Fluorescent Particles
HGMS	High Gradient Magnetic Separation
ID	Inside Dimension
LIFI	Laser Induced Fluorescence Imaging
MQS	Magneto Quasi Static
MRI	Magnetic Resonance Imaging
OD	Outside Dimension
PAA	Poly-(Acrylic Acid)
PEO	Poly-(Ethylene Oxide)
PS	Polystyrene
PSD	Particle Size Distribution
SANS	Small Angle Neutron Scattering
SDS	Sodium dodecyl sulfate (surfactant)
SEC	Size-Exclusion Chromatography
SEM	Scanning Electron Microscopy
SG	Specific Gravity
TEM	Transmission Electron Microscopy
VSM	Vibrating Sample Magnetometry

Chapter 1

1. Introduction

The goal of this thesis is to investigate the magnetophoretic focusing and trapping of submicron, nonmagnetic species immersed in magnetic nanofluids in the presence of nonuniform magnetic fields. Focusing is achieved using two pairs of permanent magnets, which force fluorescently tagged polystyrene beads to focus in-between the two magnet pairs where the magnetic-field intensity has a local minimum. Size-based trapping is achieved using a microchip that produces spatially increasing magnetic-field gradients that trap flowing polystyrene beads at different locations, depending on their relative sizes. A potential application of this work is size-based separation and focusing of species such as DNA, viruses, cell fragments, inclusion bodies, and other biological species in the submicron range. Since our techniques do not involve any binding of the magnetic nanoparticles, they are equally applicable to the separation of synthetic species as well. This chapter gives an overview of recent trends in separations, some background in magnetic nanofluids, and different ways in which these fluids can be used in separations.

1.1 Recent trends in size-based separations

Separation is one of the most important and active fields of research in chemical engineering. With advances in technology, the focus has shifted in recent years from macro-scale to micro-scale separations, especially in biological applications [1-4]. It is very important to be able to separate cells, proteins, DNA, and viruses based on both their physical and chemical/biological properties. Separation and purification can be a significant portion of the total cost in pharmaceutical processes.

In the synthesis of submicron particles, cost-effective synthetic procedures tend to yield particles with nonuniform size distributions. As it is difficult to form ordered structures without uniform size distributions, many applications require a narrow particle

size distribution (PSD) in order to obtain the desired optical [5-7] and mechanical [8-10] properties. Size-based sorting of a polydisperse mixture can be an economical alternative to the more sophisticated synthetic procedures necessary to yield a narrow PSD.

1.1.1 Size-based separation techniques

Methods to trap and manipulate micron- and submicron-sized particles are applicable to many fields, particularly in the life sciences and medicine [1-4]. Depending on the particle size-range of interest, there are several separation methods that have been used traditionally to separate particles based on size, specific gravity, and chemical properties. Some of the methods are summarized in Table 1.1, where the size 1 μm was chosen arbitrarily to separate small from large particles.

Table 1.1: Methods used for size-based separation of macroscopic and submicron species.

> 1 μm	< 1 μm
Filtration	Size exclusion chromatography
Cycloning	Ultracentrifugation
Sedimentation	Ultrafiltration
Sieving	Entropic trapping
Centrifugation	Vector chromatography
Flotation	Two phase aqueous partitioning

Although most of the methods given in Table 1.1 can be used for size-based separation, they each have their shortcomings and researchers are always looking for alternative methods. Ultrafiltration [11-14] is effective in separating relatively “small” species from “large” species, but is not useful for size fractionation. Clogging [13] is also an issue with ultrafiltration and other processes such as entropic trapping [15-17] that rely on physical barriers. Size exclusion chromatography (SEC) [18-22] suffers from

sorption of the stationary phase. Ultracentrifugation [23-27] requires large density differences between the species and the carrier fluid, and generally suffers from low resolution.

1.1.2 Separations using external fields

In order to avoid problems such as clogging and sorption, several methods utilizing external fields have been developed. Particle traps based on electric [28-30], light intensity (optical) [31, 32], and magnetic fields [33, 34] have been investigated and developed. Perhaps the most popular separation method using external fields is electrophoresis [35-38], which is the migration of species due to applied electric fields. When immersed in a carrier fluid such as water, most colloidal-sized species will have a net surface charge that can be used to move them towards cathodes or anodes, depending on their charge. A balance between this electric force and the viscous drag on the species as it migrates through the carrier fluid can potentially be used to separate species of similar properties based on size.

One of the main problems with electrophoresis is the interaction of the counterions with the migrating species. Because of the surface charge of the species, there will be local electric fields that will draw counterions near its surface, forming a so-called electrical double layer [39]. This double layer will shield some of the applied field effects and can significantly affect the net electric force on the species. In the case of DNA, both the electrophoretic and the resulting drag force are proportional to the thickness of the electrical double layer (also known as Debye length), making it impossible to perform size-based separations of DNA chains using free-solution electrophoresis [40]. Another concern with electrophoresis is the electrolysis of water, which produces bubbles that interfere with the separation process.

Dielectrophoresis [41,42] also uses applied electric fields to induce migration of species, but it relies on differences in electric permittivities (or dielectric constants). The process uses nonuniform electric fields, as migration is induced by electric field gradients. The electric fields are generally oscillated in time, preventing electrolysis and the formation of bubbles. Dielectrophoretic traps have been investigated to separate

specific cells [43-46] and viruses [47] from other species in heterogeneous mixtures, as well as to perform single-cell observation and sorting [48]. One of the drawbacks with dielectrophoresis is selectivity, especially in aqueous systems, since most species have dielectric constants different from unity. It is difficult to use this procedure to separate species exclusively based on size. Because of the alternating fields, there is also some heat generation, which may make dielectrophoresis unsuitable for some biological applications.

Magnetophoresis [49-51] is analogous to dielectrophoresis, with magnetic field gradients serving as the driving force. The applied fields can be static, so there are no problems with heat generation. Magnetophoresis and magnetic separations are the subject of this work, and are discussed in more detail in the following sections.

1.2 Magnetic separation

Magnetic separation has traditionally been used for large-scale processes such as water treatment [52-55] and mineral separation [56-59]. The first reported use of magnetic separations was by the mining industry in the mid-1800s. Minerals containing significant amounts of iron were separated from ores using electromagnetic drum separators [60]. High gradient magnetic separation (HGMS) was developed in the mid 1900s, allowing for the trapping and capture of smaller, less magnetic species [61-64]. This technique enabled magnetic separation to address challenges in the chemical [65,66], biological [67], and environmental industries [68].

Recently, magnetic separation and trapping have become important clinical techniques for isolating cells and molecules from crude biological mixtures [69,70], such as the isolation of stem cells from peripheral blood [71,72], separation of blood cells [67,73], blood detoxification [74], and immobilization of DNA for sequencing [75]. Also, like its optical counterpart, magnetic traps have proven valuable for single-particle trapping to study the mechanical properties of biological species, such as living cells [76] and DNA molecules [77-79]. These techniques are likely to expand in scope and significance as new trapping and separation techniques (i.e., based on micro-patterned magnetic elements [80,81] and circuits [82,83]) are developed.

1.2.1 Categories

The different categories of magnetic separations are discussed in detail by Fateen [84]. They are listed as follows:

Magnetocollection: A magnetic force attracts a magnetically susceptible species towards a collection area.

Magnetoflocculation: Magnetic particles are aggregated by the action of the magnetic field. This leads to easier separation through settling or filtration. Non-magnetic species can also be separated through entrainment in the magnetic aggregates.

Magnetosedimentation: Magnets are placed at the bottom of the vessel to accelerate the sedimentation of the magnetic particles.

Magnetoflotation: The density of the magnetic particle suspension is varied by the application of a magnetic field. Nonmagnetic particles with different densities can be separated by flotation in the magnetic fluid.

Magnetotransport: A magnetic field can be used to transport a bed of magnetically susceptible particles.

Magnetic Carrier Technology: Magnetic carrier particles are attached to the desired species through specific interactions. Magnetocollection is then used for separation.

Magnetic Tagging Technology: Magnetic tags are generally used for the separation of colloidal and biological species larger than those associated with magnetic carrier technology but smaller than those associated with conventional separation operations. Tags can take the form of ions or fine magnetic particles that coat or cluster around non-magnetic species to allow them to be manipulated using an external magnetic field.

All of the above techniques involve magnetophoresis, which is discussed in the next section. More details on the different magnetic separation categories can be found in Moffat et al.[85].

1.2.2 Magnetophoresis

The term magnetophoresis refers to the migration of species in the presence of magnetic field gradients. The force responsible for the migration is the magnetic force \underline{F}_m , which acts on a particle p that is immersed in a fluid f according to [86]

$$\underline{F}_m = \mu_0 V_p (\chi_p - \chi_f) H \underline{\nabla} H . \quad (1.1)$$

Here μ_0 is the permeability of free space, V_p is the volume of the particle, χ_p is the volume magnetic susceptibility of the particle, χ_f is the volume magnetic susceptibility of the fluid surrounding the particle, and H is the magnetic field magnitude. When the difference between susceptibilities is positive, the particle will be drawn to regions of high field (positive magnetophoresis), and when the difference is negative, the particle will be driven away from high fields (negative magnetophoresis).

In this work we employ the convention used by Deen [87], where scalar variables are italicized, vector quantities underlined, second-order tensors underlined twice, etc. Among other things, eq. (1.1) assumes that there are no electric currents in the fluid. A full derivation of eq. (1.1) is performed in Chapter 3.

1.2.2.1 Positive magnetophoresis in life sciences

Magnetophoresis has emerged as an important analytical technique over the last 25 years [88]. Some of the earliest use of magnetophoresis was for the separation of red blood cells, which are one of the few biological species with high magnetic susceptibilities [67]. A review of magnetophoretic uses in life sciences is given by Safarik and Safarikova [69].

Apart from a few exceptions, the majority of magnetic trapping techniques used in life science and medicine make use of magnetic carrier particles. In general, magnetic carrier particles are micrometer-sized or smaller, and their surfaces are functionalized with ligands that bind to the particles of interest. Once a magnetic carrier particle is attached (tagged) to a particle of interest, the bound complex is then captured by means of positive magnetophoresis. Magnetic tagging is required to impart a sufficiently high susceptibility to the particles of interest relative to the medium in which they are dispersed. Without tagging, the difference in susceptibility would typically be too small to generate the force necessary for capture.

1.2.2.2 Negative magnetophoresis in life sciences

An alternative way to achieve trapping while avoiding the use of magnetic carriers is to create a sufficient susceptibility difference by increasing the susceptibility of the dispersion medium relative to the un-tagged particles of interest. Such a condition would drive the particles into field minima by negative magnetophoresis [84]. Negative magnetophoresis is advantageous in that it does not require magnetic tagging, which eliminates a preparation step, and it enables the trapping of particles away from the magnetic field source. A number of studies have investigated this approach, and they have successfully trapped micron-scale particles using paramagnetic salt solutions as their dispersion media [34, 89-92].

Although paramagnetic salt solutions have proven capable as dispersion media for negative magnetophoresis, their use is limited in specific respects. First, salt solutions carry the risk of charge screening, which could lead to agglomeration and settling of particles of interest. Second, salt solutions may not provide adequate biocompatibility when used in life science and medical applications. Furthermore, in the context of cell trapping, the salt concentration is limited to avoid damaging or killing the cells due to osmotic pressure differences. This in turn limits the strength of the magnetic force, thereby reducing the ability to trap cells or similar species of interest.

A magnetic nanofluid, or ferrofluid, could act as an effective alternative to a paramagnetic salt solution for negative magnetophoresis. Magnetic nanofluids are

colloidal suspensions of magnetic nanoparticles dispersed in carrier liquid [93]. Ferrofluids are superparamagnetic, having magnetic susceptibilities much larger than any paramagnetic salt solution. Because they can be prepared as a water-based suspension, ferrofluids are fundamentally biocompatible. Magnetic fluids have a lower number density of magnetic species than paramagnetic salts, which significantly reduces osmotic effects. Moreover, the suspended species carry less charge than equivalent amounts of paramagnetic salts, which reduces charge screening effects. Magnetic nanofluids are discussed in more detail in the next section.

Recently, ferrofluids have been used as the dispersion medium in which to study negative magnetophoresis of submicrometer particles [84,86,88]. The particles were nonmagnetic polystyrene beads, and the resulting force caused them to migrate to a region of zero field. This observation suggests submicrometer particles immersed in a ferrofluid could experience gradient forces that are strong enough to confine them in well-defined magnetic traps.

1.3 Magnetic nanofluids

The principal type of magnetic nanofluid (ferrofluid) used in practice is a colloidal suspension of magnetic, single-domain nanoparticles in a liquid carrier, stabilized against agglomeration by a molecular layer of dispersant. Thermal agitation keeps the particles suspended because of Brownian motion, and the coatings prevent the particles from sticking to each other. Most colloidal ferrofluids are synthesized, for they are not commonly found in nature (certain bacteria produce colloidal magnetite, but not in sufficient amounts for commercial use). The two most common methods for preparing a magnetic colloid are size reduction (grinding) and precipitation [94].

The most common magnetic material used to make ferrofluids is magnetite ($\text{FeO-Fe}_2\text{O}_3$). The average magnetite particle diameter is 5-10 nm. The total diameter of the nanoparticles is 7-15 nm if a surfactant layer is used to stabilize the magnetite nanoparticles, or 15-30 nm if a polymer layer is used instead. Some of the most common carrier fluids include diesters, hydrocarbons, esters, fluorocarbons, and water. The most common carrier for biological applications is water, as it is the most compatible with

biological materials and the resulting ferrofluid would not be hazardous if trace amounts are left behind in separation processes.

In this research, we use a magnetic nanofluid prepared by precipitation using the techniques developed by Moeser et al. [66]. The fluid consists of an aqueous suspension of magnetite nanoparticles with a monolayer coating of polyethylene oxide-polyacrylic acid (PEO-PAA) copolymer. Due to their hydrophilicity, the PEO chains extend outward into the water, providing steric stabilization. The resulting suspension consists of single-domain magnetite nanoparticles (7 nm in diameter with a 9 nm thick copolymer layer on average) immersed in water.

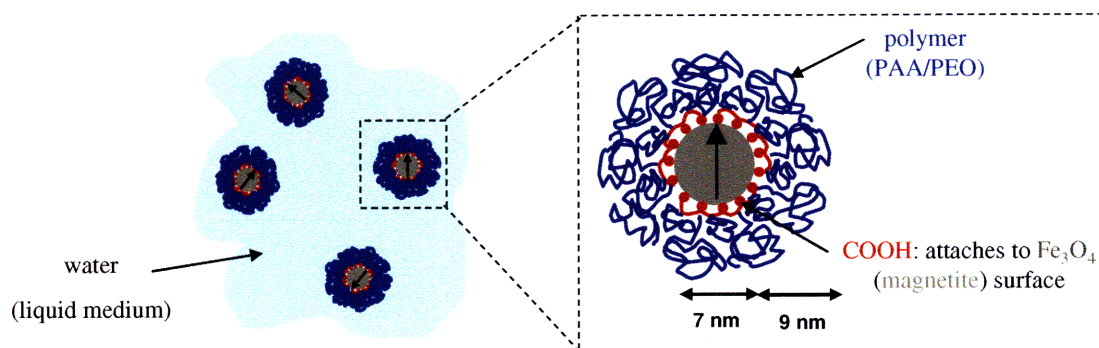


Figure 1-1: Schematic of a magnetic nanoparticle suspension. The arrows represent the direction of the permanent magnetic moment of each nanoparticle.

A schematic of the magnetic nanofluid used is shown in Figure 1-1. Each magnetite nanoparticle contains a single magnetic domain, and thus has a permanent magnetic moment. However, because of Brownian motion, the directions of the magnetic moments are randomly distributed in the absence of an applied magnetic field. The fluid has no net magnetic moment in the absence of an applied field.

1.3.1 Applications

Magnetic nanofluids were developed in the mid-1960s, motivated initially by the objective of converting heat to work with no mechanical parts [94]. Since then, their use has expanded to a large variety of applications, including zero-leakage rotary shaft seals [95] and heat transfer in audio loudspeakers [96]. They have been used in biological applications such as targeted drug delivery [97], tracers of blood flow [98], as MRI contrast agents [99], and numerous other applications. Berkovsky et al. [100] lists other commercial applications that employ magnetic nanofluids.

In life-science applications, magnetic nanofluids have mostly been used to bind to the species of interest, which can then be removed using HGMS. The polymer coatings used to stabilize the magnetic nanoparticles have been functionalized to bind proteins [101] or attach to target cells [102]. These processes all require additional steps to remove the magnetic nanoparticles for the species of interest. Avoiding the binding of the nanoparticles to the species of interest motivated the work presented in this thesis.

Of more relevance to our work is the use of magnetic buoyancy effects to separate nonmagnetic materials based on specific gravity [103-106]. This concept is illustrated schematically in Figure 1-2, where the ρ_i denote the densities of the immersed solids, ρ_f the density of the magnetic fluid, and \underline{g} the standard gravity 9.81 m/s^2 . The magnetic fluid is placed in a triangular gap formed by permanent magnets, generating a magnetic field whose intensity and gradient increases in the direction of gravity (i.e., down). Since the immersed materials are less magnetic than the ferrofluid, they experience a net force in the direction of decreasing magnetic field (against the direction of gravity), resulting in negative magnetophoresis. Both the magnetic buoyancy force pushing the species away from the magnets and the net gravitational force \underline{E}_b pulling them in the direction of the magnets scale with the nonmagnetic species volume, so the species will reach different equilibrium heights based on their specific gravities (regardless of their size). More dense materials require a stronger magnetic buoyancy force, so they will equilibrate at heights closer to the magnets. Less dense species will have equilibrium heights further away from the magnets. Processes for continuous separation of nonmagnetic materials have been devised on this basis [103-105].

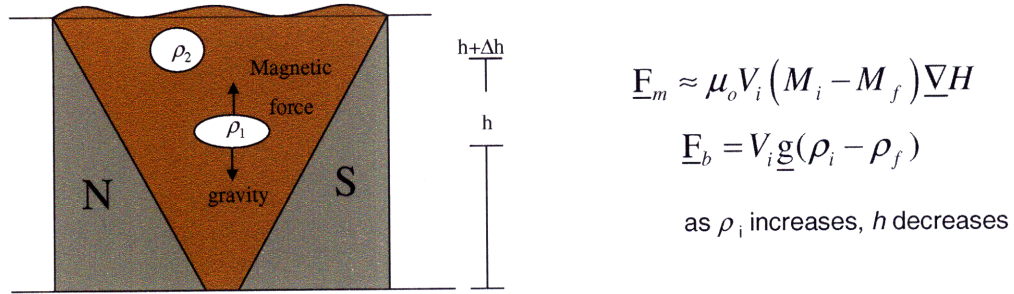


Figure 1-2: Schematic of mineral-separation process using magnetic buoyancy.

The above process is only applicable for large materials, where gravity effects dominate over the diffusive Brownian effects. For species in the submicron regime, gravitational settling is slow and diffusion greatly reduces the resolution of the separation process. Separation techniques using magnetic buoyancy effects in ferrofluids did not make way into the submicron regime until Edward Park [88], in conjunction with the author of this thesis, developed a device that could size-selectively trap submicron, nonmagnetic species based on a balance between magnetic and viscous drag forces. The concept behind this process is discussed in Section 1.3.3, and the results from this work are discussed and modeled in Chapter 5.

1.3.2 Magnetophoretic focusing

As diffusion can be appreciable in the submicron regime, being able to concentrate or focus the species of interest is critical for separation processes involving submicron species. The first magnetophoretic focusing experiments involving submicron, nonmagnetic species immersed in magnetic nanofluids were reported by Fateen [84]. In his experiments, Fateen loaded 840 nm fluorescent polystyrene beads immersed in a water-based ferrofluid into round capillary tubes. Using two permanent disk magnets, he was able to focus the nonmagnetic latex beads in a region where the magnetic-field intensity was a minimum. The setup used by Fateen is depicted in Figure 1-3(a), with the measured magnetic field profile given in Figure 1-3(b) and the measured concentration profiles of the 840 nm beads shown in Figure 1-3(c).

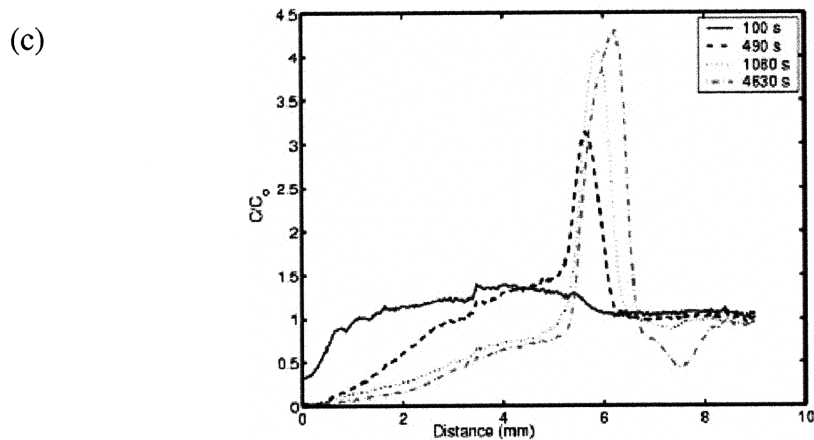
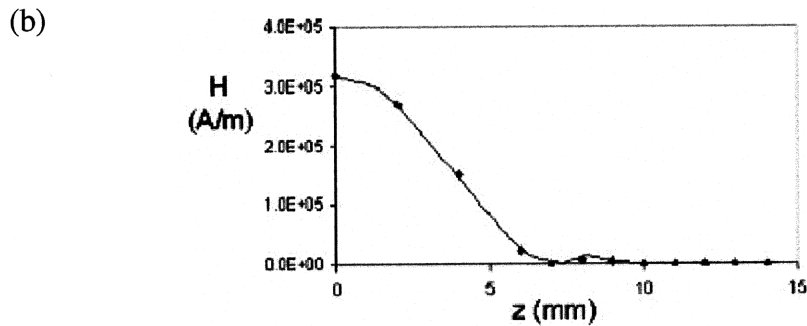
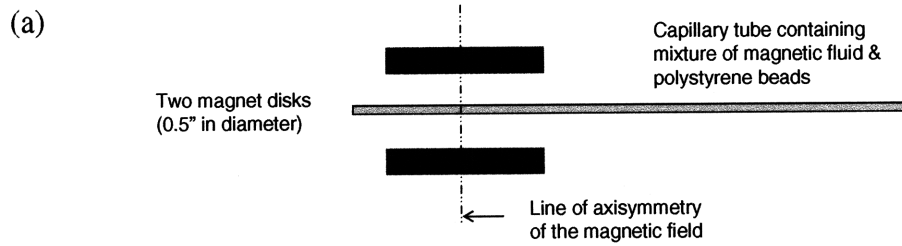


Figure 1-3: Focusing experiments performed by Fateen: (a) focusing setup; (b) measured magnetic-field intensity; (c) concentration profiles obtained for 840 nm latex beads, measured using fluorescence imaging.

Fateen performed some modeling work on his system and obtained good qualitative agreement with his experiments. His model was highly simplified, using a constant magnetic susceptibility for the magnetic fluid and an approximate magnetic-field

profile. It also contained some artifacts such as an inaccurate expression for volume exclusion interactions and double counting of the force of magnetic origin acting on the polystyrene beads. His experimental scheme may have introduced some photobleaching of the latex beads and could not account for the loss of fluorescence signal due to settling of the latex beads (the latex beads are denser than the magnetic fluid used in his experiments). One of the main tasks of this current work is to build upon his experiments and models to obtain better quantitative agreement between theory and experiments. A more rigorous theoretical analysis of negative magnetophoresis is given in Chapter 3 of this work. Chapter 4 is entirely devoted to magnetophoretic focusing and comparisons between experimental results and theoretical predictions.

1.3.3 Magnetophoretic trapping

The ultimate goal of this work is to show how negative magnetophoresis can be used for size-based trapping of submicron, nonmagnetic species. The approach taken to reach this goal is a balance between magnetophoretic and drag forces. When a nonmagnetic particle is suspended in a flowing magnetic nanofluid, it experiences a drag force given by [87]

$$\underline{F}_d = 6\pi\eta a(\underline{v}_f - \underline{v}_p), \quad (1.2)$$

where η is the viscosity of the fluid, a is the hydrodynamic radius of the nonmagnetic particle, and \underline{v}_f and \underline{v}_p denote the velocity of the fluid and the particle, respectively. A particle is considered to be trapped when its velocity $\underline{v}_p = \underline{0}$. In the absence of other forces, the particle will move with the fluid at a velocity $\underline{v}_p = \underline{v}_f$.

When a nonuniform magnetic field is applied, the force of magnetic origin acting on the nonmagnetic particle is given by

$$\underline{F}_m = -\mu_0 V_p M_f \underline{\nabla} H, \quad (1.3)$$

where M_f is the magnetization of the fluid, $M_f = \chi_f H$. Eq. (1.3) is equivalent to eq. (1.1) when the particle is nonmagnetic ($\chi_p = 0$). As inertial effects are negligible for the

particle sizes of interest, we can combine eqs. (1.2) and (1.3) to obtain the force required to trap the nonmagnetic particle against flow,

$$\underline{F}_s \equiv -\underline{F}_m = \mu_0 V_p M_f \underline{\nabla} H . \quad (1.4)$$

Combining eqs. (1.2) and (1.4) and then setting $\underline{v}_p = \underline{0}$, we can obtain the force density required to trap the nonmagnetic particle against flow, given by

$$\underline{f}_s \equiv \frac{\underline{F}_s}{V_p} = \frac{6\pi\eta a \underline{v}_f}{V_p} . \quad (1.5)$$

For a spherical particle, we have

$$\underline{f}_s = \frac{9\eta \underline{v}_f}{2a^2} \sim \frac{1}{a^2} . \quad (1.6)$$

From eq. (1.6), we see that the force density required to stop (or trap) a nonmagnetic particle suspended in a ferrofluid is proportional to the inverse of its hydrodynamic surface area. This means that larger force densities are required to trap smaller particles and smaller force densities are required to trap larger particles.

A schematic of the approach taken to separate nonmagnetic particles based on size is depicted in Figure 1-3. A mixture of relatively small and large particles is suspended in a ferrofluid and convected in the + z direction of a flow channel. A magnetic field is generated in such a way that its gradient is small in the entrance region and increases in magnitude further downstream. These gradients generate a trapping force density that increases in magnitude as the particles flow down the channel. As per eq. (1.6), smaller force densities are sufficient to trap larger particles, so these are expected to be trapped against flow near the entrance of the channel. The smaller red particles require higher stopping force densities, so they are expected to be trapped further downstream.

The proposed method has the benefit of concentrating the different-sized particles as they are trapped and separated in space. This is an advantage over techniques such as field-flow fractionation (FFF), where the species are diluted as they are being separated. The design and fabrication of the devices used to generate these trapping forces are discussed by Park [88]. Experimental and modeling results obtained using such devices are discussed in Chapter 5.

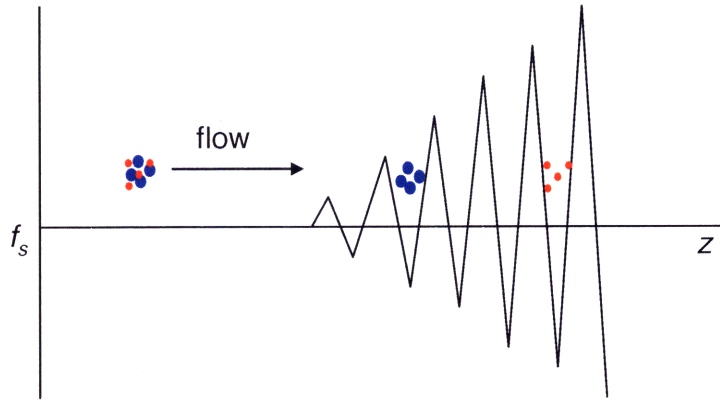


Figure 1-4: Schematic for size-based trapping of nonmagnetic particles immersed in a magnetic nanofluid.

1.4 Thesis objectives and outline

The objective of this thesis is to study the focusing and size-based trapping of submicron, nonmagnetic species immersed in magnetic nanofluids in the presence of nonuniform magnetic fields. Potential applications of this research include the size-based trapping and separation of biological species such as viruses, inclusion bodies, and DNA, as well as size-based sorting of polydisperse synthetic mixtures.

The aim of Chapter 2 is to discuss the physical and magnetic properties of the ferrofluids used in this work. Chapter 3 discusses the continuum theory of magnetic nanofluids and how it relates to multicomponent diffusion in magnetic systems. With the theory now in place, Chapter 4 deals with focusing of nonmagnetic species in magnetic nanofluids. Chapter 5 then describes how negative magnetophoresis can be used for size-based trapping of nonmagnetic species. Finally, Chapter 6 finishes with conclusions from this work and recommendations for future work.

1.5 Bibliography

1. Fiedler, S., et al., Dielectrophoretic sorting of particles and cells in a microsystem. *Analytical Chemistry*, 70(9): 1909-1915, 1998.
2. Huang, Y., et al. Electric manipulation of bioparticles and macromolecules on microfabricated electrodes. *Analytical Chemistry*, 73(7): 1549-1559, 2001.
3. Blankenstein, G. *Microfabricated flow system for magnetic cell and particle separation*, in *Scientific and Clinical Applications of Magnetic Carriers*. Plenum Press, New York, 1997.
4. Berger, M., et al. Design of a microfabricated magnetic cell separator. *Electrophoresis*, 22: 3883-3892, 2001.
5. Rengarajan, D. et al. Effect of disorder on the optical properties of colloidal crystals. *Physical Review E*. 71(1): 016615.1-016115.11, 2005.
6. Allard, M. and Sargent, E.H. Impact of polydispersity on light propagation in colloidal photonic crystals. *Applied Physics Letters*, 85(24): 5887-5889, 2004.
7. Allard, M. and Sargent, E.H. Characterization of internal order of colloidal crystals by optical diffraction. *Optical and Quantum Electronics*, 34(1-3): 27-36, 2005.
8. Aksel, C. and Riley, F.L. Effect of the particle size distribution of spinel on the mechanical properties and thermal shock performance of MgO–spinel composites. *Journal of the European Ceramic Society*, 23(16): 3079-3087, 2003.
9. Ichazo, M.N. et al. Effects of particle size and size distribution on the mechanical properties of EPDM/silica vulcanizates. *Advanced Materials Research*, 47-50: 113-116, 2008.
10. Hwang, S. and Kim, H. Dependence of particle size distribution upon brittleness in glass. *Journal of the European Ceramic Society*, 28(1): 193-197, 2008.
11. Fu, L.F. and Dempsey, B.A. Modeling the effect of particle size and charge on the structure of the filter cake in ultrafiltration. *Journal of Membrane Science*, 149(2): 221-240, 1998.
12. Peng, H., Tremblay, A.Y., and Veinot, D.E. The use of backflushed coalescing microfiltration as a pretreatment for the ultrafiltration of bilge water. *Desalination*, 181(1-3): 109-120, 2005.

13. Waite, T.D., et al. Colloidal fouling of ultrafiltration membranes: Impact of aggregate structure and size. *Journal of Colloid and Interface Science*, 212(2): 264-274, 1999.
14. Welsch, K., et al. Calculation of limiting fluxes in the ultrafiltration of colloids and fine particulates. *Journal of Membrane Science*, 99(3): 229-239, 1995.
15. Liu, L., Li, P. S., and Asher, S.A. Entropic trapping of macromolecules by mesoscopic periodic voids in a polymer hydrogel. *Nature*, 397(6715): 141-144, 1999.
16. Nixon, G.I. and Slater, G.W. Entropic trapping and electrophoretic drift of a polyelectrolyte down a channel with a periodically oscillating width. *Physical Review E*, 53(5): 4969-4980, 1996.
17. Xu, F. and Baba, Y. Polymer solutions and entropic-based systems for double-stranded DNA capillary electrophoresis and microchip electrophoresis. *Electrophoresis*, 25(14): 2332-2345, 2004.
18. Aspanut, Z., et al. Light-scattering and turbidimetric detection of silica colloids in size-exclusion chromatography. *Analytical and Bioanalytical Chemistry*, 391(1): 353-359, 2008.
19. Krueger, K.M., et al. Characterization of nanocrystalline CdSe by size exclusion chromatography. *Analytical Chemistry*, 77(11): 3511-3515, 2005.
20. Otto, D.P., Vosloo, H.C. M., and de Villiers, M.M. Application of size exclusion chromatography in the development and characterization of nanoparticulate drug delivery systems. *Journal of Liquid Chromatography & Related Technologies*, 30(17): 2489-2514, 2007.
21. Wei, G.T., Liu, F.K., and Wang, C.R.C. Shape separation of nanometer cold particles by size-exclusion chromatography. *Analytical Chemistry*, 71(11): 2085-2091, 1999.
22. Zheng, Y.M. and Yu, H.Q. Determination of the pore size distribution and porosity of aerobic granules using size-exclusion chromatography. *Water Research*, 41(1): 39-46, 2007.
23. Brown, P.H., Balbo, A., and Schuck, P. Using prior knowledge in the determination of macromolecular size-distributions by analytical ultracentrifugation. *Biomacromolecules*, 8(6): 2011-2024, 2007.
24. Brown, P.H. and Schuck, P. Macromolecular size-and-shape distributions by sedimentation velocity analytical ultracentrifugation. *Biophysical Journal*, 90(12): 4651-4661, 2006.

25. Schuck, P. et al. Size-distribution analysis of proteins by analytical ultracentrifugation: Strategies and application to model systems. *Biophysical Journal*, 82(2): 1096-1111, 2002.
26. Segura, M.D.M., Garnier, A., and Kamen, A. Purification and characterization of retrovirus vector particles by rate zonal ultracentrifugation. *Journal of Virological Methods*, 133(1): 82-91, 2006.
27. Svedberg, E.B., et al. FePt nanoparticle hydrodynamic size and densities from the polyol process as determined by analytical ultracentrifugation. *Nanotechnology*, 16(6): 953-956, 2005.
28. Arnold, W.M. and Franich, N.R. Cell isolation and growth in electric-field defined micro-wells. *Current Applied Physics*, 6(3): 371-374, 2006.
29. Rosenthal, A. and Voldman, J. Dielectrophoretic traps for single-particle patterning. *Biophysical Journal*, 88(3): 2193-2205, 2005.
30. Voldman, J., et al. Holding forces of single-particle dielectrophoretic traps. *Biophysical Journal*, 80(1): 531-541, 2001.
31. Ferrari, E., et al. Biological samples micro-manipulation by means of optical tweezers. *Microelectronic Engineering*, 78-79: 575-581, 2005.
32. Friese, M.E.J., et al. Optical alignment and spinning of laser-trapped microscopic particles. *Nature*, 394(6691): 348-350, 1998.
33. Mirowski, E., et al. Manipulation and sorting of magnetic particles by a magnetic force microscope on a microfluidic magnetic trap platform. *Applied Physics Letters*, 86(24), 2005.
34. Winkleman, A., et al. A magnetic trap for living cells suspended in a paramagnetic buffer. *Applied Physics Letters*, 85(12): 2411-2413, 2004.
35. Reuss, F.F. Notice sur un nouvel effet de l'électricité galvanique. *Mem. Soc. Imperiale Naturalistes de Moscow*, 2: 327, 1809.
36. Hunter, R.J. *Foundations of Colloid Science*. Oxford University Press, New York, 1989.
37. Dolnik, V., Liu, S., and Jovanovich, S. Capillary electrophoresis on microchip. *Electrophoresis*, 21: 41-54, 2000.
38. Chen, X., et al. A prototype two-dimensional capillary electrophoresis system fabricated in poly(dimethylsiloxane). *Analytical Chemistry*, 74: 1772-1778, 2002.

39. Hiemenz, P.C. and Rajagopalan, R. *Principles of Colloid and Surface Chemistry*. Marcel Dekker, New York, 1997.
40. Mitnik, L., et al. Segregation in DNA solutions induced by electric-fields. *Science*, 267(5195): 219-222, 1995.
41. Flores-Rodriguez, N. and Markx, G.H. Improved levitation and trapping of particles by negative dielectrophoresis by the addition of amphoteric molecules. *Journal of Physics D-Applied Physics*, 37(3): 353-361, 2004.
42. Hawkins, B.G., et al. Continuous-flow particle separation by 3D insulative dielectrophoresis using coherently shaped, dc-biased, ac electric fields. *Analytical Chemistry*, 79: 7291-7300, 2007.
43. Markx, G.H., Talary, M.S. and Pethig, R. Separation of viable and nonviable yeast using dielectrophoresis. *Journal of Biotechnology*, 32: 29-37, 1994.
44. Wang, X.B., et al. Selective dielectrophoretic confinement of bioparticles in potential-energy wells. *Journal of Physics D.: Applied Physics*, 26: 1278-1285, 1993.
45. Gascoyne, P.R.C., et al. Dielectrophoretic separation of cancer cells from blood. *IEEE Transactions on Industry Applications*, 33: 670-678, 1997.
46. Becker, F.F., et al. Separation of human breast-cancer cells from blood by differential dielectric affinity. *Proceedings of the National Academy of Sciences of the USA*, 92: 860-864, 1995.
47. Morgan, H., Hughes, M. P., and Green, N.G. Separation of submicron bioparticles by dielectrophoresis. *Biophysical Journal*, 77: 516-525, 1999.
48. Voldman, J., et al. A microfabrication-based dynamic array cytometer. *Analytical Chemistry*, 74: 3984-3990, 2002.
49. Che, J.J. and Wan, Q.H. Bioseparation and bioanalysis based on magnetophoresis. *Progress in Chemistry*, 18(2-3): 344-348, 2006.
50. Iwasaka, M., Miyakoshi, J., and Ueno, S. Magnetophoresis of diamagnetic cells and microorganisms in a culture medium. *IEEE Transactions on Magnetics*, 37(4): 2644-2646, 2001.
51. Winotomorbach, S., Tchikov, V., and Mullerruchholtz, W. Magnetophoresis .1. Detection of magnetically labeled cells. *Journal of Clinical Laboratory Analysis*, 8(6): 400-406, 1994.

52. Delatour, C. Magnetic separation in water-pollution control. *IEEE Transactions on Magnetism*, 9(3):314-316, 1973.
53. DeLatour, C. *Magnetic fields in aqueous systems*. Ph.D. thesis, Massachusetts Institute of Technology, 1974.
54. Vyatkin, V.E., et al. Purification of aqueous systems from tributylphosphate by magnetic separation and ozonation. *Soviet Radiochemistry*, 32(1):74-78, 1990.
55. Vanvelsen, A.F.M., et al. High-gradient magnetic separation technique for wastewater treatment. *Water Science and Technology*, 24(10):195-203, 1991.
56. Smolkin, R.D., et al. New process for placer gold recovery by means of magnetic separation. *IEEE Transactions on Magnetism*, 28(1):671-674, 1992.
57. Fofana, M. and Klima, M.S. Use of a magnetic fluid based process for coal separations. *Minerals Metallurgical Processes*, 14(1):35-40, 1997.
58. Walker, M.S. and Devernoe, A.L. Mineral separations using rotating magnetic fluids. *International Journal of Mineral Processing*, 31(3-4):195-216, 1991.
59. Wasmuth, H.D. and Unkelbach, K.H. Recent developments in magnetic separation of feebly magnetic minerals. *Minerals Engineering*, 4(7-11):825-837, 1991.
60. Svoboda, J. *Magnetic Methods for the Treatment of Minerals*. Elsevier Science, New York, 1987.
61. Gerber, R. and Birss, R. *High Gradient Magnetic Separation*. Magnetic Materials and Their Applications Series. John Wiley & Sons Ltd., Chichester, 1983.
62. Oberteuffer, J.A. High gradient magnetic separation. *IEEE Transaction of Magnetism*, MAG-9(3):303-306, 1973.
63. Luborsky, F.E. and Drummond, B.J. High gradient magnetic separation - theory versus experiment. *IEEE Transactions on Magnetism*, 11(6):1696-1700, 1975.
64. Kolm, H., Oberteuffer, J., and Kelland, D. High-gradient magnetic separation. *Scientific America*, 223(5): 46-54, 1975.
65. Chiba, A., et al. Removal of arsenic from geothermal water by high gradient magnetic separation. *IEEE Transactions on Applied Superconductivity*, 12(1): 952-954, 2002.

66. Moeser, G.D., et al. Water-based magnetic fluids as extractants for synthetic organic compounds. *Industrial & Engineering Chemistry Research*, 41(19): 4739-4749, 2002.
67. Melville, D., Paul, F., and Roath, S. High gradient magnetic separation of red cells from whole blood. *IEEE Transactions on Magnetics*, 11(6): 1701-1704, 1975.
68. Ngomsik, A.F., et al. Magnetic nano- and microparticles for metal removal and environmental applications: a review. *Comptes Rendus Chimie*, 8(6-7): 963-970, 2005.
69. Safarik, I. and Safarikova, M. Overview of magnetic separations used in biochemical and biotechnological applications. In Hafeli, U., et al. *Scientific and Clinical Applications of Magnetic Carriers*, pages 323-340. Plenum Press, New York, 1997.
70. Safarik, I. and Safarikova, M. Use of magnetic techniques for the isolation of cells. *Journal of Chromatography B*, 722: 33-53, 1999.
71. Handgretinger, R., et al. Transplantation of highly purified peripheral allogeneic CD34+ cells obtained from haploidentical or mismatched family donors. *Bone Marrow Transplantation*, 21: 987-993, 1998.
72. Kato, K. and Radbruch, A. Isolation and characterization of CD34+ hematopoietic stem-cells from human peripheral-blood by high gradient magnetic cell sorting. *Cytometry*, 14: 384-392, 1993.
73. Watarai, H. and Namba, M. Capillary magnetophoresis of human blood cells and their magnetophoretic trapping in a flow system. *Journal of Chromatography A*, 961(1): 3-8, 2002.
74. Chen, H., et al. Theoretical analysis of a magnetic separator device for ex-vivo blood detoxification. *Separation Science and Technology*, 43(5): 996-1020, 2008.
75. Hultman, T., et al. Direct solid-phase sequencing of genomic and plasmid DNA using magnetic beads as solid support. *Nucleic Acids Research*, 17: 4937-4946, 1989.
76. Bausch, A.R., Moller, W., and Sackmann, E. Measurement of local viscoelasticity and forces in living cells by magnetic tweezers. *Biophysical Journal*, 76, 573-579, 1999.
77. Gosse, C. and Croquette, V. Magnetic tweezers: Micromanipulation and force measurement at the molecular level. *Biophysical Journal*, 82 : 3314-3329, 2002.

78. Smith, S.B., Finzi, L., and Bustamante, C. Direct mechanical measurements of the elasticity of single DNA-molecules by using magnetic beads. *Science*, 258: 1122-1126, 1992.
79. Strick, T.R., et al. The elasticity of a single supercoiled DNA molecule. *Science*, 271: 1835-1837, 1996.
80. Mirowski, E., et al. Integrated microfluidic isolation platform for magnetic particle manipulation in biological systems. *Applied Physics Letters*, 84: 1786-1788, 2004.
81. Inglis, D.W., et al. Continuous microfluidic immunomagnetic cell separation. *Applied Physics Letters*, 85: 5093-5095, 2004.
82. Lee, H., Purdon, A.M., and Westervelt, R.M. Micromanipulation of biological systems with microelectromagnets. *IEEE Transactions on Magnetics*, 40: 2991-2993, 2004.
83. Deng, T., et al. Manipulation of magnetic microbeads in suspension using micromagnetic systems fabricated with soft lithography. *Applied Physics Letters*, 78: 1775-1777, 2001.
84. Fateen, S. *Magnetophoretic Focusing of Submicron Particles Dispersed in a Polymer-Based Magnetic Fluid*. Ph.D. thesis, Massachusetts Institute of Technology, 2002.
85. Moffat, R., et al. Selective separations in environmental and industrial-processes using magnetic carrier technology. *Minerals Engineering*, 7(8):1039-1056, 1994.
86. Gonzalez, L.A., et al. Magnetophoresis of Nonmagnetic, Submicrometer Particles in Magnetic Fluids. *MEBCS Proceedings of the Forth SMA Symposium*, Singapore, 2004.
87. Deen, W.M. *Analysis of Transport Phenomena*. Oxford University Press, New York, 1998.
88. Park, E.S. *Microfabricated Focusing Systems for the Separation of Submicrometer Particles*. M.S. thesis, Massachusetts Institute of Technology, 2004.
89. Kimura, T., Yamato, M., and Nara, A. Particle trapping and undulation of a liquid surface using a microscopically modulated magnetic field. *Langmuir*, 20: 572-574, 2004.
90. Kimura, T., et al. Micropatterning of cells using modulated magnetic fields. *Langmuir*, 21: 830-832, 2005.

91. Watarai, H. and Namba, M. Magnetophoretic behavior of single polystyrene particles in aqueous manganese (II) chloride. *Analytical Sciences*, 17: 1233-1236, 2001.
92. Watarai, H. and Namba, M. Capillary magnetophoresis of human blood cells and their magnetophoretic trapping in a flow system. *Journal of Chromatography A*, 961: 3-8, 2002.
93. Blums, E., Cebers, A., and Maiorov, M.M. *Magnetic Fluids*; Walter de Gruyter & Co., Berlin, 1996.
94. Rosensweig, R.E. *Ferrohydrodynamics*. Cambridge University Press, New York, 1985.
95. Bailey, R.L. Lesser known applications of ferrofluids. *Journal of Magnetism and Magnetic Materials*, 39(1-2): 178-182, 1983.
96. Hathaway, D.B. Use of ferrofluid in moving-coil loudspeakers. *dB-Sound Engineering Magazine*, 13(2): 42-44, 1979.
97. Akimoto, M. and Morimoto, Y. The development of a magnetic emulsion as drug carrier. *Journal of Pharmacobio-Dynamics*, 5(1): S15-S15, 1982.
98. Newbower, R.S. A new technique for circulatory measurements employing magnetic fluid tracers. *Proceedings from 1972 Biomedical Symposium*, San Diego, 1972.
99. Kim, E.H., et al. Synthesis of ferrofluid with magnetic nanoparticles by sonochemical method for MRI contrast agent. *Journal of Magnetism and Magnetic Materials*, 289: 328-330, 2005.
100. Berkovsky, B.M., Medvedev, V.F., and Krakov, M.S. *Magnetic Fluids: Engineering Applications*. Oxford University Press, New York, 1993.
101. Bucak, S., et al. Protein separations using colloidal magnetic nanoparticles. *Biotechnology Progress*, 19(2): 477-484, 2003.
102. Sestier, C., et al. Surface modification of superparamagnetic nanoparticles (ferrofluid) studied with particle electrophoresis: Application to the specific targeting of cells. *Electrophoresis*, 19(7): 1220-1226, 1998.
103. Rosensweig, R.E. *Material separation using ferromagnetic liquid techniques*. U.S. patent 3,700,595, 1969.
104. Shimoiizaka, J., et al. Sink-float separators using permanent magnets and water based magnetic fluid. *IEEE Trans. Magnetics*, 16(2): 368-371, 1980.

105. Khalafalla, S.E. and Reimers, G.W. Separating non-ferrous fluid metals in incinerator residue using magnetic fluids. *Separation Sci.*, 8: 161-78, 1973.
106. Reimers, G.W., et al. Cell design to separate non-ferrous-metals in incinerator residue with magnetic fluids. *Materials Science and Engineering*, 15(2-3):129-135, 1974.

Chapter 2

2. Properties of Magnetic Nanofluids

This work used water-based magnetic nanofluids, synthesized according to Moeser [1]. The fluid consisted of a suspension of magnetite (Fe_3O_4) nanoparticles with a monolayer coating of polyethylene oxide-polyacrylic acid (PEO-PAA) copolymer. This copolymer was synthesized by attaching amino-terminated PEO side chains to a PAA backbone via an amidation reaction. Only 16% of the carboxyl groups in the PAA backbone were used to form the side chains; the remaining carboxyl groups were used to attach the copolymer chains to the nanoparticles.

The magnetite nanoparticles were produced by co-precipitation of iron (II) and iron (III) salts in an aqueous solution of PEO-PAA copolymer chains. Shortly after particle nucleation, free carboxyl groups on the PAA backbone attached to the magnetite particle surfaces, inhibiting further growth and forming magnetic nanoparticles with a permanent PEO-PAA copolymer shell. Due to their hydrophilicity, the PEO chains extend outward into the water, providing steric stabilization. After being synthesized, the magnetic nanofluid was washed to remove salts and excess polymer and passed through a High-Gradient Magnetic Separation (HGMS) column to remove large magnetic particles and aggregates.

2.1 Magnetic and hydrodynamic size distributions

A Transmission Electron Microscopy (TEM) image of the magnetite nanoparticles is shown in Figure 2-1(a). The measurements were performed using a JEOL 2010 (200 kV) instrument and published by Moeser [2]. The polymer layer coating the nanoparticles is almost invisible to TEM, so the images in Figure 2-1 are only of the magnetite cores of the nanoparticles. As seen in the figure, the nanoparticles have a core diameter of about 7.5 nm. The size distribution can be approximated by a log-normal probability curve, as shown in Figure 2-1(b). In general, water-based ferrofluids

tend to be very polydisperse in size unless they are synthesized in organic mediums before being re-suspended in water [3].

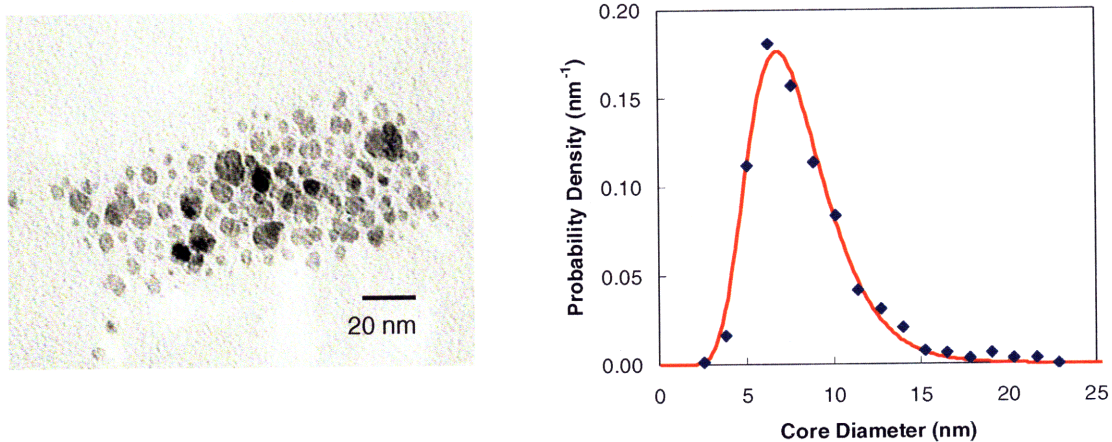


Figure 2-1: (a) TEM image of the magnetite cores and (b) size distribution fitted by a log-normal distribution with a median of 7.5 nm and a standard deviation of 0.32.

The hydrodynamic diameter of the magnetic nanoparticles was measured by Dynamic Light Scattering (DLS) using a Brookhaven BI-200SM light scattering system at a measurement angle of 90°. This technique uses information from the Brownian motion of the nanoparticles (magnetite + polymer shell) to give the diameters of equivalent hard spheres. A typical distribution of the total (i.e., hydrodynamic) diameter of the nanoparticles can be found in Figure 2-2, where the inner curve corresponds to the number-average size distribution and the outer curve corresponds to the volume-average size distribution. The latter distribution gives higher weight to the larger nanoparticles and nanoparticle aggregates, thus resulting in a more-noticeable second peak at around 80 nm.

Depending on the conditions used during HGMS, the average hydrodynamic diameter of the magnetic nanoparticles can vary from about 15 to 30 nm. Regardless of the mean value, the number- and volume-average particle sizes were always found to have the same qualitative shapes as in Figure 2-2. HGMS can reduce the number of nanoparticle aggregates, but can never eliminate them completely.

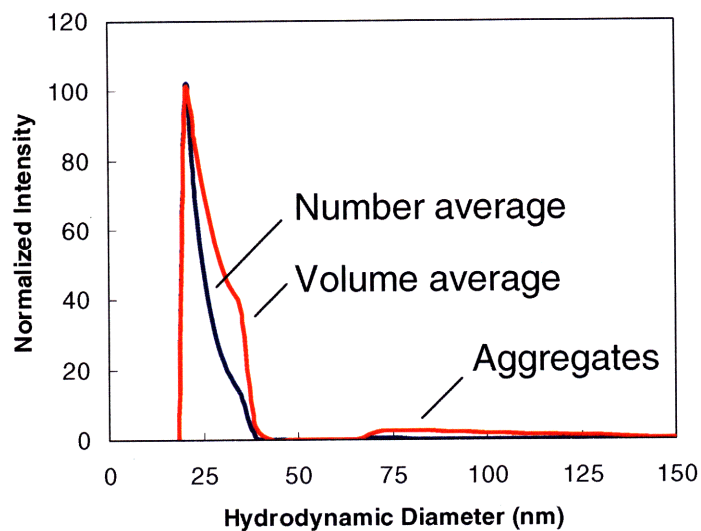


Figure 2-2: Number-average and volume-average hydrodynamic diameters of the polymer-coated magnetic nanoparticles.

2.2 Actual magnetic diameters

The schematic shown earlier in Figure 1-1 is valid only for the ideal case where each copolymer chain attaches to only one magnetite nanoparticle. In reality, the current synthetic scheme offers little control over the number of polymer chains attaching to one nanoparticle or the number of nanoparticles being attached to one chain. Figure 2-3 shows some of the other configurations that are possible, such as (b) multiple polymer units attaching to one magnetite nanoparticle, (c) multiple nanoparticles being attached to the same polymer chain, and (d) clusters of nanoparticles being coated by one or more chains. There are of course numerous other configurations attainable based on combinations of (a)-(d).

The TEM image found in Figure 2-1 cannot differentiate between the different scenarios presented in Figure 2-3. Since the polymer shells are invisible to TEM, the magnetite nanoparticles will appear the same in a TEM image whether they are individual nanoparticles, multiple nanoparticles coated by a single chain, or clusters of nanoparticles.

Although some of the configurations depicted in Figure 2-3 may contain more than one magnetite nanoparticle, each of the configurations was treated as a single magnetic nanoparticle in this work, as these magnetite units cannot move independently from each other. For example, the diagram shown in Figure 2-3(c) consists of two magnetite nanoparticles, but is regarded as one magnetic nanoparticle in this work.

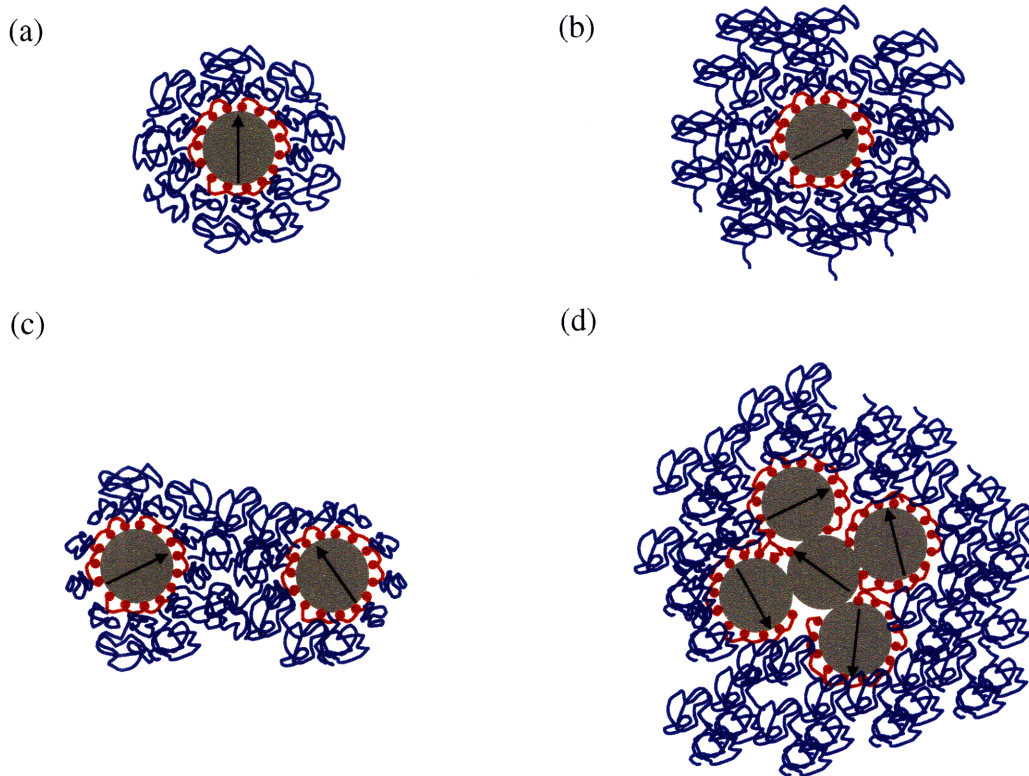


Figure 2-3: Possible structures of the polymer-stabilized magnetic nanoparticles; (a) one polymer chain coats one magnetite nanoparticle, (b) multiple chains attach to one magnetite nanoparticle, (c) multiple magnetite nanoparticles are coated by a single polymer chain, and (d) a cluster of magnetite nanoparticles are covered by one or more polymer chains.

Another factor that needs to be considered in estimating the magnetic size of the nanoparticles is the “dead shell” caused by the attached polymer [4-6]. When the chelate

bonds between the carboxyl groups of the copolymer and magnetite surface are formed, the crystal structure of the nanoparticle surface is disrupted, leading to a loss of magnetic activity near the surface. This is illustrated in Figure 2-4 for the case of a single copolymer chain completely coating one magnetite nanoparticle. For the case of complete surface coverage, the thickness of dead shell is given by the lattice constant for the cubic crystal structure of magnetite, which is 0.83 nm [7].

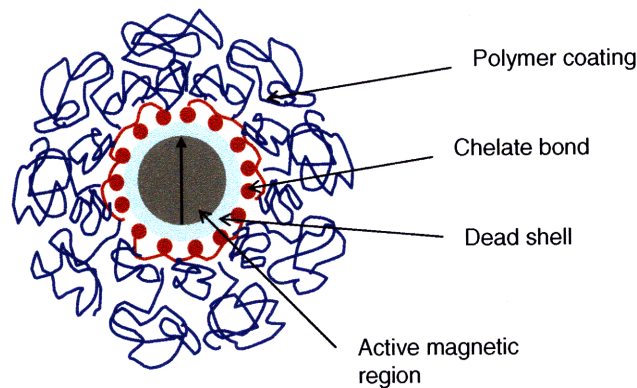


Figure 2-4: Dead region due to the attached polymer-coating.

In order to predict the magnetic properties of a ferrofluid accurately, it is essential to have a good estimate of the effective magnetic size distribution. Determining this size distribution is not a trivial problem, however [8,9]. If each magnetite nanoparticle were completely coated by one or more polymer chains, then the thickness of the dead shell would be 0.83 nm for each magnetic nanoparticle. Assuming also that each polymer chain is only attached to one magnetite nanoparticle, the particle-size distribution (PSD) obtained from TEM images would readily give the size distribution of the effective magnetic region by simply subtracting 1.66 from each diameter. In reality this is not the case, as some of the configurations in Figure 2-3 do not result in complete surface coverage by the polymer chains. To further complicate the analysis, there is also some oxidation of the magnetite nanoparticles that can decrease their magnetic moment over time [9].

Other methods such as Small-Angle Neutron Scattering (SANS) can also be used to estimate the core size of the magnetic nanoparticles [8]. However, just like TEM, SANS does not provide much information on the size distribution of the effective magnetic region. Perhaps the best way to estimate this size distribution is to use a technique called magnetic curve reconstruction [9], which uses the so-called Langevin function [10] and experimental magnetization data in order to ‘reconstruct’ the magnetic moment distribution. In this work, we make use of this technique to estimate the magnetic moment (and therefore size) distribution of our magnetic nanoparticles. TEM data are used as reference to make sure that the magnetic-size distribution obtained is physically reasonable.

2.3 Nanofluid magnetization

As previously noted, each magnetite nanoparticle has a single magnetic domain, and thus a permanent magnetic moment. Because of thermal motion, in the absence of an applied magnetic field the magnetic moments \underline{m} and their induced fields \underline{h} will on average cancel each other out. If no external field is applied, the magnetic nanofluid will have no net magnetic moment, as depicted in Figure 2-5(a). The arrows in this figure represent the direction of the local magnetic moments.

When an external field \underline{H}_0 is applied to the sample, a magnetic torque given by

$$\tau = \hat{m}H_0 \sin \theta \quad (2.1)$$

will try to align the magnetic moment of each nanoparticle with the applied field. In the above expression, \hat{m} and H_0 denote the magnitude of the nanoparticle moment and the applied field, respectively, and θ is the angle between them. This torque has to compete with thermal kT effects (where T is the absolute temperature and k is Boltzmann’s constant) trying to randomize the direction of the magnetic moments, meaning that not all of the nanoparticles become aligned with the applied field. However, there will be some net alignment in the direction of the applied field, and the nanofluid will acquire a net magnetic moment, as depicted in Figure 2-5(b).

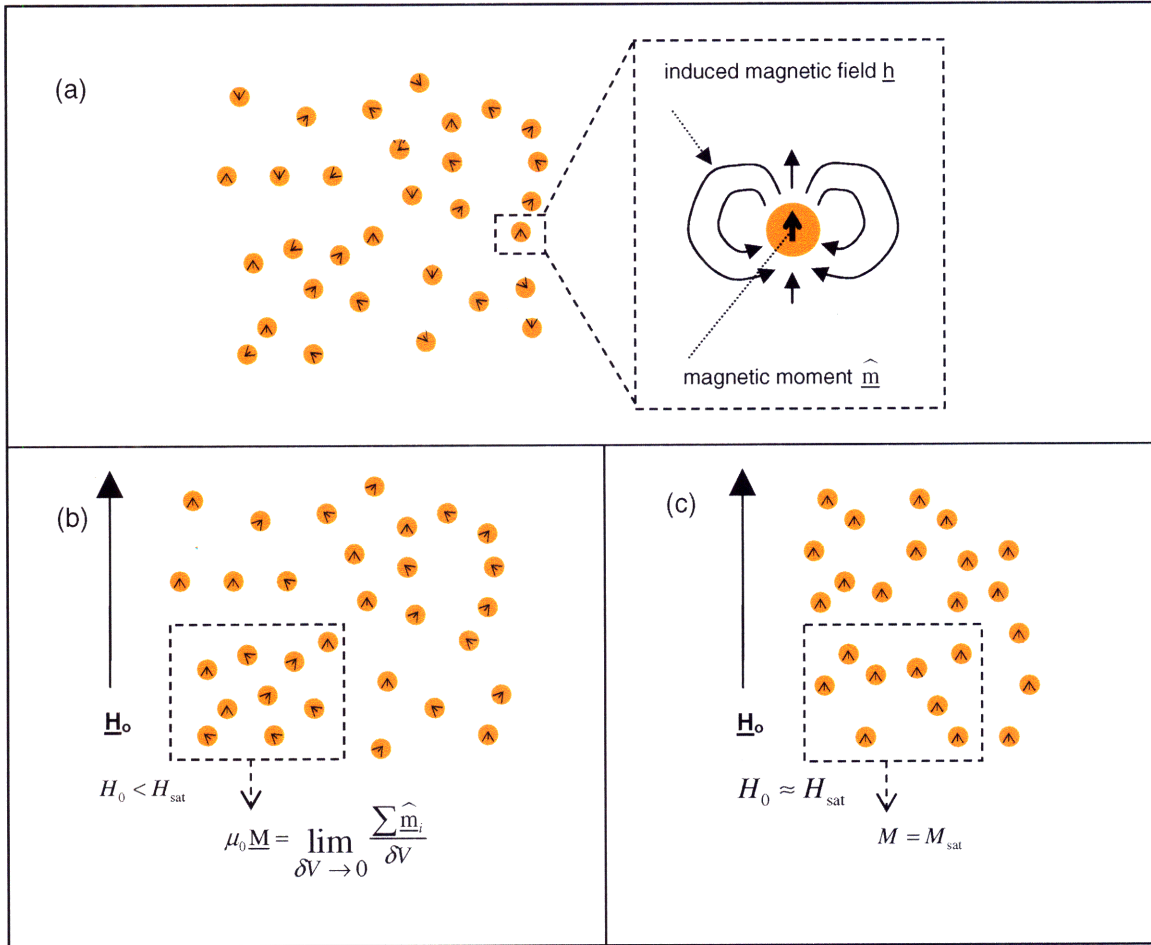


Figure 2-5: Magnetization as a function of applied magnetic field; a) no applied field, b) small applied field, and c) large applied field.

A macroscopic quantity M called the fluid magnetization can be defined from ensemble averages of microscopic magnetic moments \hat{m} by (see Figure 2-5(b))

$$\mu_0 \underline{M} = \lim_{\delta V \rightarrow 0} \frac{\sum \hat{m}_i}{\delta V}. \quad (2.2)$$

The constant $\mu_0 = 4\pi \cdot 10^{-7} \text{ H/m}$ (N/A^2) is called the permeability of free space, where H is the magnetic unit Henry, m is meters, N is the force unit Newtons, and A is the current unit Amperes. It is included in the definition (2.2) so that the fluid magnetization M and the magnetic field H have the same units (A/m, where m is meters). When \underline{M} and \underline{H} are collinear, as is the case in this work, they are related by

$$\underline{M} = \chi \underline{H} , \quad (2.3)$$

where χ is the magnetic susceptibility of the fluid. In the above expression, the total magnetic field H is related to the applied field H_0 by

$$\underline{H} = \underline{H}_0 + \sum \underline{h}_i , \quad (2.4)$$

where h_i are the local fields induced by the permanent magnetic moments of the nanoparticles. At low applied fields, where the condition $\hat{m}H/kT \ll 1$ holds, χ is a constant.

As the applied field grows larger, the magnetization will no longer be a linear function of the magnetic field. The magnetic nanoparticles become more aligned with the applied field, and adding extra field strength does not result in a linear increase in magnetization. Eventually, the nanoparticles become completely aligned with the applied field, and any increase in H does not result in further increases in M . At this point, the fluid is said to be magnetically saturated, or $M = M_{\text{sat}}$ for $\hat{m}H/kT \gg 1$. Such a scenario is depicted in Figure 2-5(c).

A typical magnetization versus applied-field curve is given in Figure 2-6. The data in the figure were acquired using Vibrating Sample Magnetometry (VSM) for the ferrofluid used in this work. The device used for the measurements was a VSM 880 from ADE Magnetics, and the magnetic fluid concentration used was 2.1% by weight of magnetite. In accordance with the mechanism illustrated in Figure 2-5, the magnetization of the fluid is zero in the absence of an applied field, grows linearly with the applied field at low field strengths, and saturates to an asymptotic value M_{sat} at large field strengths.

As seen in the figure, the magnetic fluid exhibits superparamagnetic behavior [7], meaning that it exhibits paramagnetic behavior but with large saturation values, similar to those of ferromagnetic materials. At equivalent concentrations, paramagnetic salts would have magnetic susceptibilities that are about an order of magnitude lower. Another characteristic of superparamagnetism (and of paramagnetism in general) is that the magnitude of the fluid magnetization is the same when the direction of the field is reversed, as seen in Figure 2-6 for the ferrofluid used in this study.

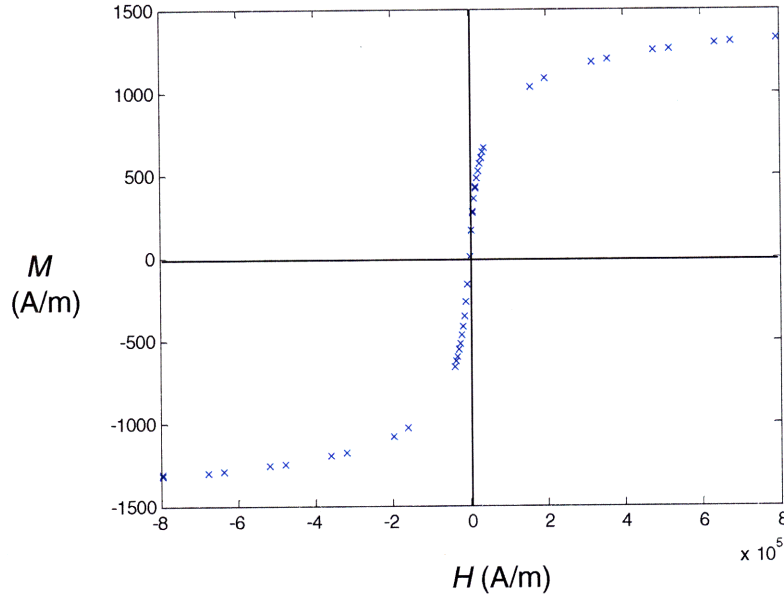


Figure 2-6: Magnetization curve for a 2.1 wt% magnetic nanofluid.

2.3.1 Langevin expression for nanofluid magnetization

The primary mechanism governing the relationship between the magnetization M of the fluid and the magnetic field H is a balance between magnetic torques trying to align the nanoparticles with the field and thermal effects randomizing the direction of the magnetic moments. For a monodisperse magnetic nanofluid, where all the magnetic moments are equal in magnitude, the relationship between M and H is given by the Langevin expression [11]

$$\frac{M}{\phi_m M_d} = \coth \alpha - \frac{1}{\alpha} \equiv L(\alpha), \quad (2.5)$$

$$\alpha \equiv \frac{\widehat{m}H}{kT} = \frac{\pi \mu_0 M_d H d^3}{6 kT}. \quad (2.6)$$

In the above expressions, ϕ_m is the volume fraction of magnetic material in the fluid, M_d is the magnetization of the magnetic region, and d is the effective magnetic diameter of the nanoparticles.

One of the assumptions of eq. (2.5) is that magnetic particle interactions are negligible compared to their interactions with the applied field. At room temperature, this assumption is valid for magnetite nanoparticles with effective magnetic diameters of less than 23 nm [8]. Another assumption, which is not valid for most water-based ferrofluids including the one used in this work, is magnetic moment monodispersity. However, since eq. (2.5) neglects particle-particle interactions, it is possible to superimpose the contributions from the different-sized magnetic moments. Eq. (2.5) can therefore be written in a generalized form as

$$\frac{M}{\phi_m M_d} = \int G(\hat{m}) \left(\coth \alpha - \frac{1}{\alpha} \right) d\hat{m}, \quad (2.7)$$

where $G(\hat{m})$ is the magnetic-moment probability distribution, having the property

$$\int_0^\infty G(\hat{m}) d\hat{m} = 1 \quad (2.8)$$

and having units of $1/\hat{m}$. In discrete form, eq. (2.7) can be written as

$$\frac{M}{\phi_m M_d} = \frac{\sum_i n_i \hat{m}_i \left(\coth \alpha_i - \frac{1}{\alpha_i} \right)}{\sum_i n_i \hat{m}_i}, \quad (2.9)$$

$$\alpha_i \equiv \frac{\hat{m}_i H}{kT} = \frac{\pi \mu_0 M_d H d_i^3}{6 kT}. \quad (2.10)$$

Here n_i are the number of magnetite nanoparticles having an effective magnetic diameter d_i and magnetic moment \hat{m}_i .

If the magnetic moment distribution is known *a priori*, eq. (2.7) can be used to generate the M - H curve of the ferrofluid. In most cases, however, the M - H curve can be obtained experimentally, while the magnetic moment distribution is generally unknown. As discussed in Section 2.2, TEM data give the distribution of the total size of the magnetite nanoparticles, but cannot distinguish between the magnetic and dead regions. In the following section, a technique called magnetic curve reconstruction is used to estimate the magnetic moment distribution of the ferrofluid of interest. A good estimate for this moment distribution is necessary for the analysis presented in Chapters 4 and 5.

2.3.2 Magnetic curve reconstruction

The magnetite cores of water-based magnetic nanofluids generally tend to have log-normal type distributions, such as the one found in Figure 2-1(b). This is more of an experimental observation, as there is no general mechanism of magnetic nanoparticle formation that would predict such distributions. In the past, researchers have estimated ferrofluid magnetic-moment distributions by finding the log-mean and variance of the log-normal distribution that best fits their $M-H$ data [12-14]. Other researchers have observed better fits when using the Γ -distribution, which is claimed to provide better accuracy when describing the large moment tails of the experimentally observed distributions [15].

The reality is that, for highly polydisperse ferrofluids, no single normal, log-normal, or Γ -distribution can fit the $M-H$ data with good accuracy at both low and high magnetic-field intensities. Figure 2-7 shows the best fit to the $M-H$ data given in Figure 2-6 using a single, physically realistic log-normal distribution (mean of 5.85 nm). As seen in the figure, the fitting curve shows the general trends found in the $M-H$ data, but does not match up with the data over the entire range of magnetic-field intensities. The fit has the largest error at low magnetic-field strengths, as seen in part (b) of the figure. Even small differences such as these between experimental and model-predicted results can lead to substantial errors in predicting the magnetophoretic focusing of nonmagnetic particles. This is discussed in more detail in Chapter 4.

Several methods have been proposed in the literature to obtain more accurate magnetic-moment distributions. These methods are designed to reconstruct the moment distribution without assuming a form for the distribution *a priori*. For fluids having a single, smooth peak in their magnetic moment distributions, one can obtain very accurate, physically-reasonable results using these techniques [8]. If the moment distribution is more complex, any experimental error in the $M-H$ data will lead to less accurate magnetic curve reconstruction [9].

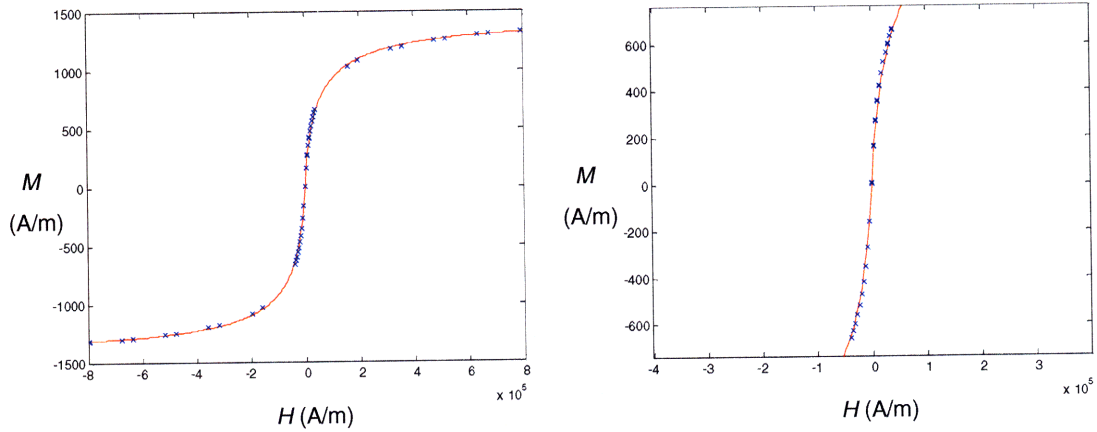


Figure 2-7: M-H data fit using a log-normal function for the magnetic-size distribution.

If eq. (2.7) is solved directly, small (but unavoidable) experimental errors in $M(H)$ will result in large, non-physical oscillations in $G(\hat{m})$ [9]. The so-called maximal entropy method (MaxEnt) [16] overcomes this difficulty, but it involves the complicated nonlinear minimization problems and requires an exact knowledge of the measurement errors. Berkov et al. [17] recently proposed a method that avoids nonlinear minimization and an exact knowledge of the measurement errors. The drawback to their method is that it tends to give much broader peaks for $G(\hat{m})$, especially for higher moments, unless the experimental data are accurate to within 0.1% [9]. Our VSM data are only accurate to about 1%, meaning that the predicted peaks in the magnetic-size distribution would be much broader than what they are in reality.

In the analysis presented in Chapters 4 and 5, we are interested in simulating the dynamics of a finite number of magnetic moments. Instead of attempting to reconstruct the entire distribution $G(\hat{m})$ and then decomposing it into a finite number of moments, we elected to find the minimum number of log-normal distributions which, when superimposed, would yield a magnetization curve that fits the experimental $M-H$ data over the entire range of magnetic-field intensities. That is, the unknown distribution $G(\hat{m})$ was approximated as

$$G(\hat{m}) \approx \sum_{i=1}^n x_i G_i(\hat{m}), \quad (2.11)$$

where $G_i(\hat{m})$ are inferred from log-normal fits to the magnetic-size distribution,

$$G_i(d) = \frac{1}{\sqrt{2\pi}\sigma_i d} \exp\left[\frac{-(\ln d - \ln d_i)^2}{2\sigma_i^2}\right]. \quad (2.12)$$

In the above expressions, x_i are the number fractions of the moments having that distribution, and n is the minimum number of log-normal distributions that can be superimposed to yield an accurate estimate for the M - H data. In eq. (2.12), $\ln(d_i)$ is the mean of $\ln(d)$, σ_i is the standard deviation, and the moment \hat{m} is related to the diameter d as given in eq. (2.6),

$$\hat{m} = \frac{\pi}{6} \mu_0 M_d d^3. \quad (2.13)$$

To assure that the resulting magnetic-size distribution was physically reasonable, the magnetite size distribution given in Figure 2-1 was used as a starting point and as reference in constructing the distribution given by eq. (2.11). The procedure used is as follows:

1. Start with one log-normal distribution, such as the one that gives the results shown in Figure 2-1.
2. Find the mean and standard deviation that best fits the M - H curve. Make sure the mean is between ~ 0.5 to 2 nm *smaller* than the TEM value to account for the “dead shell” volume and for magnetization loss by magnetite oxidation.
3. Add additional log-normal curves, as needed, with the peaks centered at locations consistent with the data in Figure 2-1 (i.e., at around 14 and 19 nm, where the biggest discrepancy between the experimental data and the fitted curve are found).

4. Find the means, standard deviations, and number fractions that best fit the experimental $M-H$ curve. Make sure the means are between ~ 0.5 to 2 nm *smaller* than the TEM values for the reasons listed in step 2.
5. Continue until a satisfactory fit is found to the $M-H$ data with the minimum number of log-normal distributions possible.

Table 2.1: Parameters used for the log-normal distributions used to generate the plots in Figure 2-8.

Species	1	2	3
x_i	0.951	0.043	0.006
d_i (nm)	5.1	11.5	18.5
σ_i	0.28	0.18	0.06
ϕ_i	0.61	0.26	0.13

Using the above procedure, we were able to obtain the magnetic size distribution shown in Figure 2-8, which consists of three superimposed log-normal distributions. The mean, standard deviation, and number fraction for each of the log-normal curves are given in Table 2.1. The resulting $M-H$ fit is shown in Figure 2-9, corresponding to an error of about 2% between the data points and fitted curve. Using less than three superimposed log-normal distributions would result in considerable under-prediction of the dynamics of magnetic nanoparticles, as discussed in more detail in Chapter 4.

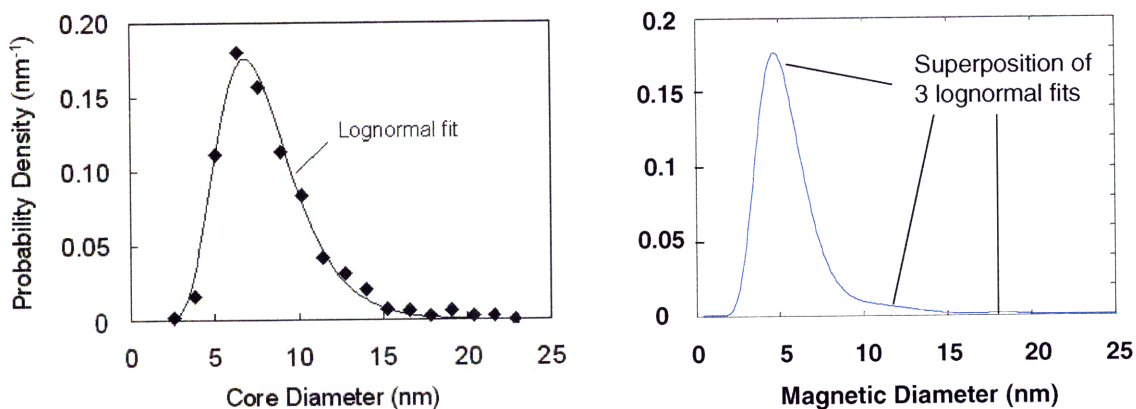


Figure 2-8: Comparison between (a) magnetite particle-size distribution and (b) effective magnetic-size distribution.

A comparison between the magnetic moment distribution used and the TEM data is shown in Figure 2-8. The constructed magnetic size distribution has the same general shape as the TEM distribution, but the size is shifted to the left. The peaks also have different thicknesses, which is consistent with different degrees of polymer coating on the magnetite nanoparticles. Another point to note is that the peak at 18.5 nm, although it appears insignificant, makes a big difference in the shape of the $M-H$ curve at small magnetic field strengths. This is because small number fractions actually correspond to significant volume fractions for larger magnetic sizes, as seen in Table 2.1. Larger magnetic moments lead to higher magnetization values at low fields, and neglecting them will lead to an appreciable underestimation of the magnetic susceptibility of the ferrofluid. This can be seen in Figure 2-10, where the $M-H$ curves corresponding to the three log-normal distributions superimposed in Figure 2-8 are plotted. The curves are normalized to have the same M_{sat} value.

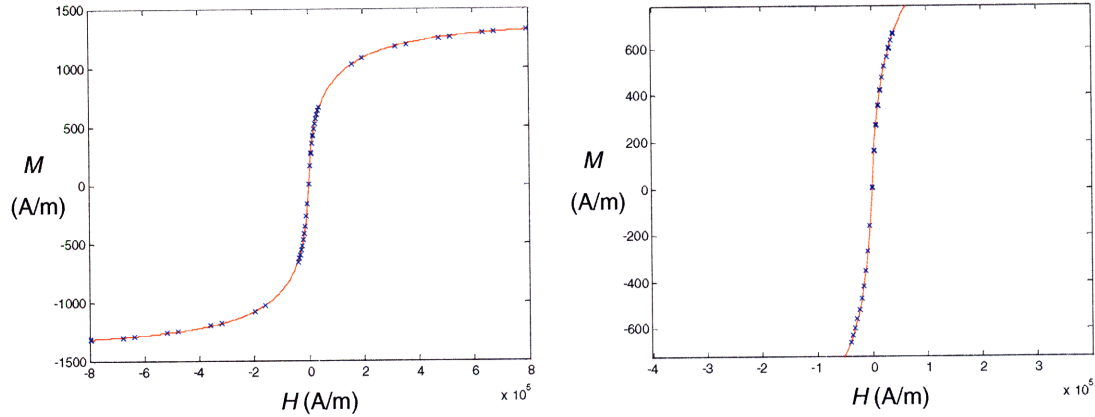


Figure 2-9: M-H data fit using a magnetic size distribution consisting of three superimposed log-normal probability curves; (a) fit across a wide range of magnetic-field strengths and (b) in the region of small magnetic field strengths.

The method outlined in steps 1-5 is not as robust and unbiased as some of the more recent moment reconstruction methods, such as the one proposed by Berkov [9]. It does, however, result in more physically-realistic magnetic moment distributions unless the M - H data are accurate to within 0.1%. Also, even if the magnetic moment curve were reconstructed by another method, it would have to be broken down into a finite number of moments to be of use for the analysis presented in Chapters 4 and 5 of this thesis. For this work, postulating the form of the magnetic moment distribution and adjusting it to match the experimental M - H data was found to be the better alternative.

It is worth noting that the solution presented in Figure 2-8 and Table 2.1 is not a unique solution. Because of the numerous fit parameters (2 number fractions, 3 means, and 3 standard deviations), it is possible to find other parameters that fit the data equally as well. However, since the means are constrained to a physically acceptable range, it was found that other slightly different log-normal distributions yielded very similar results. This is discussed in Chapter 4.

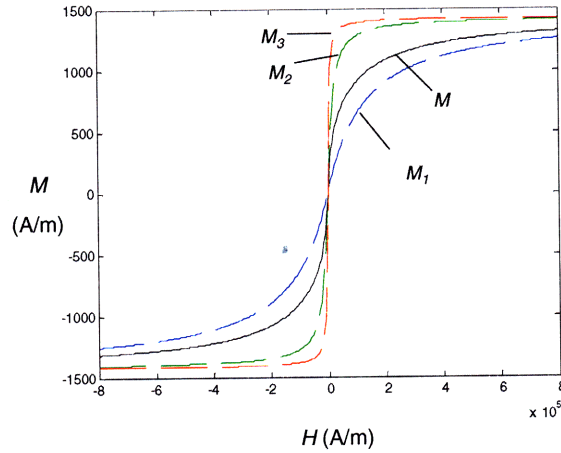


Figure 2-10: M - H curves for the three log-normal distributions used (dashed curves) and their linear superposition (solid curve). The curves are normalized to have the same M_{sat} value.

2.4 Average magnetic and hydrodynamic sizes

In order to predict the correct force of magnetic origin acting on submicron, nonmagnetic species, it is necessary to have accurate information on the concentration and M - H relationship of the magnetic nanofluid as a function of time and space. Since the ferrofluid is highly polydisperse in both magnetic and hydrodynamic diameters, it was necessary to model it as a mixture of different-sized nanoparticles. As discussed in the previous section, it was found that the minimum number of analytic moment distributions that can accurately describe the M - H relationship is three. Correspondingly, the simplest model that can accurately capture the evolution of the nanofluid concentration and magnetization profiles is one that uses three different-sized magnetic species.

Since the magnetic force on the magnetic nanoparticles is a volumetric force, the volume-averaged sizes of the distributions given in Table 2.1 were used to model the magnetic size of the nanoparticles. These effective magnetic sizes were calculated as

$$\overline{d_{m,i}} = \left(\overline{d_i^3} \right)^{1/3} = \left\{ \int d^3 \rho_i(d') \, d d' \right\}^{1/3}, \quad (2.14)$$

where d' is a dummy integration variable representing the diameter d . The magnetization corresponding to each effective diameter is given by

$$\frac{M_i}{\phi_m M_d} = \int G_i(\widehat{m}) \left(\coth \alpha - \frac{1}{\alpha} \right) d\widehat{m}. \quad (2.15)$$

When the fluid is in its initial state, the magnetization and volume-average diameter in our model should reduce to that of the bulk fluid. The volume-average diameter of our model ferrofluid is

$$\left(\overline{d^3} \right)^{1/3} = \left(\sum x_i \overline{d_i^3} \right)^{1/3} = \left(\int d^3 \{ \sum x_i G_i(d') \} d d' \right)^{1/3} = \left(\int d^3 G(d') d d' \right)^{1/3}, \quad (2.16)$$

which by definition is the volume-average diameter of the bulk ferrofluid. The magnetization of our model ferrofluid is

$$\begin{aligned} M &= \sum x_i M_i = \phi_m M_d \int \left\{ \sum x_i G_i(\widehat{m}) \right\} \left(\coth \alpha - \frac{1}{\alpha} \right) d\widehat{m} \\ &= \phi_m M_d \int G(\widehat{m}) \left(\coth \alpha - \frac{1}{\alpha} \right) d\widehat{m} \end{aligned}, \quad (2.17)$$

which by definition is the magnetization of the bulk ferrofluid. Thus, the magnetic properties our model fluid reduce to that of the bulk fluid in the absence of concentration gradients.

Figure 2-2 gives the hydrodynamic size distribution of one of the ferrofluids used in this work. What cannot be determined from the DLS, or any other method that we are aware of, is which hydrodynamic diameters correspond to which magnetite nanoparticle sizes. In general, the smaller hydrodynamic diameters observed in Figure 2-2 should correspond to the smaller magnetite nanoparticles observed in Figure 2-1, but that cannot be guaranteed due to the different scenarios for the magnetic nanoparticle structure depicted in Figure 2-3. In our model, we assume that, on average, magnetic nanoparticles having smaller magnetic cores will have smaller hydrodynamic diameters.

For the average hydrodynamic diameters $\overline{d_{H,i}}$ corresponding to the magnetic diameters $\overline{d_{m,i}}$, since the drag force on a diffusing nanoparticle scales with its diameter $d_{H,i}$, the only requirement that can be enforced is that

$$\overline{d_H} \equiv \int G_H(d') d d' = \sum x_i \overline{d_{H,i}}. \quad (2.18)$$

Here, $G_H(d)$ is the hydrodynamic diameter distribution given in Figure 2-2. Our model fluid requires three average hydrodynamic diameters, so two of these diameters ended up being fitting parameters. The fitting procedure used for the average hydrodynamic diameters is discussed in Chapter 4.

2.5 Bibliography

1. Moeser, G.D., et al. Water-based magnetic fluids as extractants for synthetic organic compounds. *Industrial & Engineering Chemistry Research*, 41(19): 4739-4749, 2002.
2. Moeser, G.D. *Colloidal Magnetic Fluids as Extractants for Chemical Processing Applications*. Ph.D. Thesis, Massachusetts Institute of Technology, 2003.
3. Lattuada, M. and Hatton, T.A. Functionalization of monodisperse magnetic nanoparticles. *Langmuir*, 23(4): 2158-2168.
4. Bean, C.P. and Livingston, J.D. Superparamagnetism. *Journal of Applied Physics*, 30(4): 120S-129S, 1959.
5. Kim, T. and Shima, M. Reduced magnetization in magnetic oxide nanoparticles. *Journal of Applied Physics*, 101(9), 2007.
6. Virden, A.E. and O'Grady, K. The temperature dependence of magnetization in ferrofluids. *Journal of Applied Physics*, 99(8), 2006.
7. Rosensweig, R.E. *Ferrohydrodynamics*. Cambridge University Press, New York, 1985.
8. Woodward, R.C., et al. A comparison of methods for the measurement of the particle-size distribution of magnetic nanoparticles. *Journal of Applied Crystallography*, 40: S495-S500, 2007.
9. Berkov, D.V., et al. New method for the determination of the particle magnetic moment distribution in a ferrofluid. *Journal of Physics D-Applied Physics*, 33(4): 331-337, 2000.
10. Kittel, C. *Introduction to Solid State Physics*. Wiley, New York, 1956.
11. Blums, E., Cebers, A., and Maiorov, M.M. *Magnetic Fluids*. Walter de Gruyter & Co., Berlin, 1996.

12. Upadhyay, R.V., Sutariya, G.M., and Mehta, R.V. Particle-size distribution of laboratory-synthesized magnetic fluid. *Journal of Magnetism and Magnetic Materials*, 123(3): 262-266, 1993
13. Popplewell, J. and Sakhnini, L.J. The dependence of the physical and magnetic-properties of magnetic fluids on particle-size. *Journal of Magnetism and Magnetic Materials*, 149: 72-78, 1995.
14. Shen, L.F., Laibinis, P.E., and Hatton, T.A. Bilayer surfactant stabilized magnetic fluids: Synthesis and interactions at interfaces. *Langmuir*, 15(2): 447-453, 1999.
15. Pshenichnikov, A.F, Mekhonoshin, V.V., and Lebedev, A.V. Magneto-granulometric analysis of concentrated ferrocolloids. *Journal of Magnetism and Magnetic Materials*, 161: 94-102, 1996.
16. Skilling, J. *Maximum Entropy and Bayesian Methods*. Kluwer, Boston, 1989.
17. Berkov, D.V., et al. New method for the reconstruction of the distribution of fine particle magnetic moments in a ferrofluid. *IEEE Transactions on Magnetics*, 35(5): 4064-4066, 1999.

Chapter 3

3. Magnetophoresis in Magnetic Nanofluids

This chapter is designed to develop the theory describing the magnetophoresis of submicron, nonmagnetic species immersed in magnetic nanofluids. In this analysis, we limit ourselves to Magneto Quasi Static (MQS) systems, where the changes in magnetic fields occur slowly enough that some of their coupling with electric fields can be neglected. The magnetic fields also change slowly enough that the fluid magnetization \underline{M} and the applied field \underline{H}_0 can be assumed to be collinear at all times [1]. We also limit our analysis to applied magnetic fields that vary spatially over length scales much larger than the size of the migrating species ($L \gg 1 \mu\text{m}$, where L is the characteristic length scales associated with the applied magnetic-field gradient). Finally, our fluids of interest conduct negligible electric currents under the conditions of interest, so any terms containing electric currents are neglected.

3.1 Maxwell's equations for MQS systems

For an MQS system, the set of governing equations is [2]

$$\underline{\nabla} \cdot \underline{B} = 0, \quad (3.1)$$

$$\underline{\nabla} \times \underline{H} = \underline{J}_e, \quad (3.2)$$

$$\underline{\nabla} \cdot \underline{J}_e = 0, \quad (3.3)$$

$$\underline{\nabla} \times \underline{E} = -\frac{\partial \underline{B}}{\partial t}, \quad (3.4)$$

$$\underline{\nabla} \cdot \underline{D} = \rho_e. \quad (3.5)$$

In these expressions, \underline{J}_e denotes the free electric-current flux, \underline{E} the electric field, \underline{D} the displacement field, ρ_e the free charge density, \underline{M} the fluid magnetization, and \underline{B} the magnetic induction field. The field \underline{B} is related to the magnetic field \underline{H} by the definition

$$\underline{B} \equiv \mu_0 (\underline{M} + \underline{H}) . \quad (3.6)$$

Since \underline{M} and \underline{H} are assumed to be collinear in our analysis, \underline{B} is collinear with both \underline{M} and \underline{H} . As noted earlier, this analysis is concerned with the case of negligible electric currents and magnetic fields that do not vary much with time, so eqs. (3.2) and (3.4) can be approximated as

$$\underline{\nabla} \times \underline{H} = \underline{0} , \quad (3.7)$$

$$\underline{\nabla} \times \underline{E} = \underline{0} . \quad (3.8)$$

3.1.1 Field generated by permanent magnets

In this work, the applied magnetic fields originate from permanent magnets. A “hard” or “permanent” magnet is a material that stays magnetized indefinitely in the absence of an applied field. Although these magnets always have a permanent magnetization, such magnetization is generally a function of the total magnetic field present. The typical relationship governing the field produced by a permanent magnet is [22]

$$\underline{B} = \mu_0 \mu_r (\underline{M}_p + \underline{H}) , \quad (3.9)$$

where \underline{M}_p is the constant part of the magnetization and μ_r is a function used to describe the difference between \underline{M}_p and the actual magnetization in the magnet \underline{M} . Referring to eq. (3.6), we see that the actual magnetization in the magnet is

$$\underline{M} = \mu_r \underline{M}_p + (\mu_r - 1) \underline{H} , \quad (3.10)$$

meaning that M is only constant (and equal to \underline{M}_p) when $\mu_r = 1$.

A typical B - H plot for a hard magnet is shown in Figure 3-1 [23]. Unless an externally applied field is large enough to switch the orientation of its permanent

magnetic moment, the magnet will operate in the “second quadrant,” or the quadrant in the figure where \underline{H} is negative and \underline{B} is positive (with respect to the orientation of \underline{M}_p). The magnetic field induced by the permanent moment is usually negative inside of the magnet, but positive outside of it.

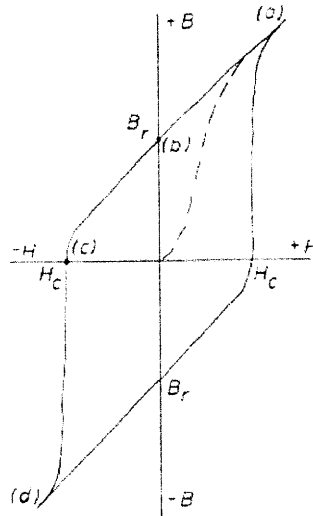


Figure 3-1: Hysteresis curve for a typical permanent magnet.

The permanent magnets used in this work are Neodymium magnets, $\text{Nd}_2\text{Fe}_{14}\text{B}$, from MMC Magnetics. The operating region for the N48 magnets used (i.e., the second quadrant) is shown in Figure 3-2. From the fitted line, the value of μ_r is 1.015, which means that the magnetization of the magnets can be approximated to be independent of \underline{H} with only a 1.5% error.

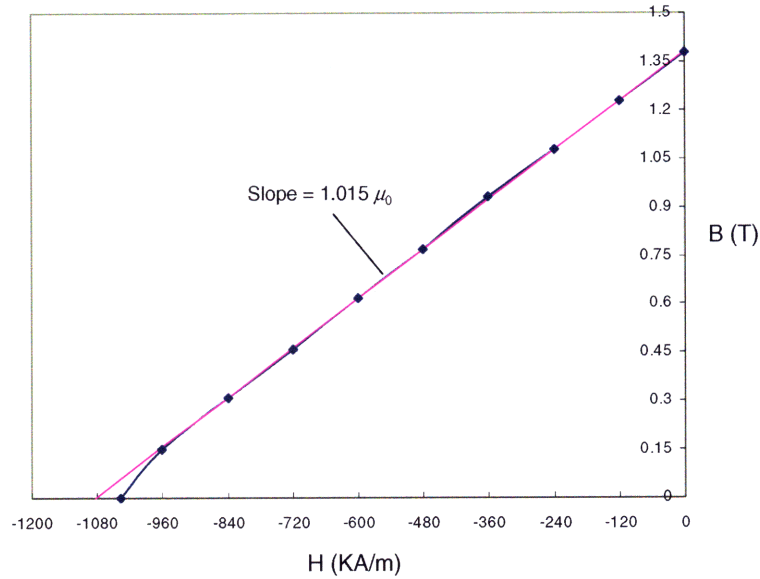


Figure 3-2: Operating curve for N48 neodymium magnets. The blue curve with data points is the manufacturer data, while the pink line corresponds to a straight-line fit.

In general, numerical techniques are used to solve for the magnetic fields generated by permanent magnets [3]. The problem with most of these solutions is that any numerical noise is amplified when the gradient of the field is computed. Since magnetophoresis is induced by magnetic field gradients, any numerical noise present in the magnetic field solution can have a significant impact on the predicted concentration profiles of the diffusing species, as discussed in more detail in Chapter 4.

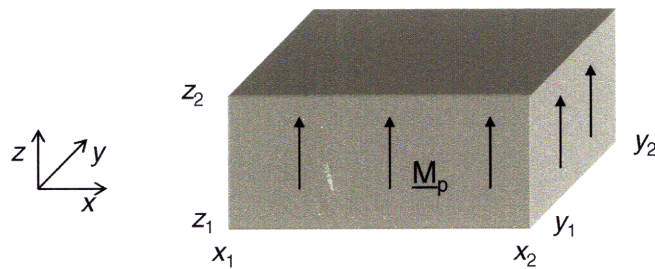


Figure 3-3: Permanent magnet with a uniformly distributed magnetic moment ($\mu_r \approx 1$) pointing in the z -direction.

For permanent magnets having a μ_r value close to unity, it is possible to obtain an analytical approximation for the magnetic field they generate in free space. If μ_r is taken to be unity, the permanent magnets essentially behave as constant magnetic moment sources in free space. If this magnetization is treated as an effective surface-current, eqs. (3.1) and (3.2) can be used to derive analytical expressions for \underline{H} and \underline{B} valid everywhere outside of the magnet. For the rectangular magnet depicted in Figure 3-3, with its magnetic moment oriented along the \underline{i}_z direction, the generated field and magnetic induction are [4, 22, 24]

$$B_x = \mu_0 H_x = \sum_{k=1}^2 \sum_{m=1}^2 K^{-(k+m)} \ln Q_x(x, y, z, k, m), \quad (3.11)$$

$$B_y = \mu_0 H_y = \sum_{k=1}^2 \sum_{m=1}^2 K^{-(k+m)} \ln Q_y(x, y, z, k, m), \quad (3.12)$$

$$B_z = \mu_0 H_z = \sum_{k=1}^2 \sum_{m=1}^2 \sum_{n=1}^2 K^{-(k+m+n)} \tan^{-1} Q_z(x, y, z, k, m, n). \quad (3.13)$$

In the above expressions,

$$K = \frac{\mu_0 M_p}{4\pi}, \quad (3.14)$$

$$Q_x(x, y, z, k, m) = \frac{y - y_1 + \left[(x - x_m)^2 + (y - y_1)^2 + (z - z_k)^2 \right]^{1/2}}{y - y_2 + \left[(x - x_m)^2 + (y - y_2)^2 + (z - z_k)^2 \right]^{1/2}}, \quad (3.15)$$

$$Q_y(x, y, z, k, m) = \frac{x - x_1 + \left[(x - x_1)^2 + (y - y_m)^2 + (z - z_k)^2 \right]^{1/2}}{x - x_2 + \left[(x - x_2)^2 + (y - y_m)^2 + (z - z_k)^2 \right]^{1/2}}, \quad (3.16)$$

$$Q_z(x, y, z, k, m, n) = \frac{(x - x_n)(y - y_m)}{(z - z_k) \left[(x - x_n)^2 + (y - y_m)^2 + (z - z_k)^2 \right]^{1/2}}. \quad (3.17)$$

The positions of x_1, x_2 , etc. are shown in Figure 3-3. For the magnets used in our work,

$$M_p = 1.1 \times 10^6 \frac{\text{A}}{\text{m}}.$$

Another property of eqs. (3.1) and (3.2) in the case where $\mu_r = 1$ is that they are linear, meaning that their solutions can be superimposed. This means that for a system of n magnets, the magnetic field at any point outside of the magnets is simply the sum of the magnetic fields generated by the individual magnets at that point, or

$$\underline{\mathbf{B}} = \mu_0 \underline{\mathbf{H}} = \sum_{i=1}^n \underline{\mathbf{B}}_i . \quad (3.18)$$

Here $\underline{\mathbf{B}}_i$ is the field generated by magnet i at a point x, y, z in the absence of the other magnets.

For the N48 neodymium magnets used in this study, the value of μ_r is actually 1.015, meaning that the fields predicted by eqs. (3.11) - (3.18) may be off by 1 or 2% in some regions. This slight loss in accuracy is compensated for by perfect resolution in the distribution of the magnetic field and its gradient, as the latter can now be obtained analytically. The gain in resolution is invaluable for the systems studied in this work, where resolution at the micron level is required.

3.1.2 Numerical solutions for linear and nonlinear materials

In the previous section, the magnetic field generated by a magnet with a constant, uniformly distributed magnetization was obtained analytically. For linear materials, where the magnetic susceptibility is constant, analytic solutions may be possible for simple geometries. For nonlinear materials, where the magnetic susceptibility is a function of the field H , or for more complex geometries, analytical solutions are not usually attainable. In these cases, eqs. (3.1) - (3.4) need to be solved numerically. For the devices described in Chapters 5 and 6 of this work, the magnetic field profiles were obtained numerically by using the finite-element program Maxwell 3D from Ansoft. More details on some of these numeric calculations are given by Park [5].

3.2 Continuum equations for magnetic nanofluids

A derivation of the momentum equation for a ferrofluid can be found in Rosensweig's *Ferrohydrodynamics* [6]. In the creeping flow limit, a mass and momentum balance for a magnetic fluid results in

$$\underline{0} = -\underline{\nabla}p + \eta\nabla^2 \underline{v} + \rho\underline{g} + \underline{f}_m. \quad (3.19)$$

Here p is the magnetic fluid pressure, η the viscosity (assumed constant), ρ the density, \underline{v} the fluid mass-average velocity, \underline{g} the gravity vector, and \underline{f}_m is the magnetic force density, given by

$$\underline{f}_m = \underline{\nabla} \cdot \underline{\underline{T}}_m, \quad (3.20)$$

where $\underline{\underline{T}}_m$ is the so-called Maxwell Stress Tensor,

$$\underline{\underline{T}}_m = \underline{\underline{B}}\underline{\underline{H}} - \frac{1}{2}\mu_0 H^2 \underline{\underline{I}}. \quad (3.21)$$

For the case where there are no electric currents ($\underline{\nabla} \times \underline{\underline{H}} \approx \underline{0}$) and the magnetization and magnetic field are in local equilibrium ($\underline{\underline{M}} \times \underline{\underline{H}} \approx \underline{0}$), eq. (3.20) reduces to

$$\underline{f}_m = \mu_0 M \underline{\nabla} H, \quad (3.22)$$

where M is the magnetization of the fluid. At equilibrium, the pressure appearing in eq. (3.19) is related to thermodynamic pressure p_0 in the absence of magnetic fields as

$$p = p_0(\rho, T, H=0) - \mu_0 \int_0^H \left[\rho^2 \frac{\partial}{\partial \rho} \left(\frac{M}{\rho} \right) \right]_{H,T} dH'. \quad (3.23)$$

The creeping flow equation for the ferrofluid of interest is therefore

$$\underline{\nabla}p = \eta\nabla^2 \underline{v} + \rho\underline{g} + \mu_0 M \underline{\nabla} H. \quad (3.24)$$

At nearly constant density *and* either nearly constant temperature T or temperatures far from the Curie temperature (such that $\left(\frac{\partial M}{\partial T} \right)_{\rho, H} \approx 0$), we can write eq. (3.24) as

$$\underline{\nabla} p = \eta \nabla^2 \underline{v} + \underline{\nabla} (\rho \underline{g} \cdot \underline{r} + \mu_0 \overline{M} H), \quad (3.25)$$

where

$$\overline{M} \equiv \frac{1}{H} \int_0^H M dH, \quad (3.26)$$

is the field-averaged magnetization of the fluid and \underline{r} is a position vector. We can define a buoyancy pressure, a magnetic pressure, and a viscous pressure, respectively, as

$$p_b \equiv \rho \underline{g} \cdot \underline{r}, \quad (3.27)$$

$$p_m \equiv \mu_0 \overline{M} H, \quad (3.28)$$

$$p_v \equiv p - p_b - p_m. \quad (3.29)$$

Using these definitions, eq. (3.25) can be written as

$$\underline{\nabla} p_v = \eta \nabla^2 \underline{v}. \quad (3.30)$$

Eq. (3.30) is identical to the classical creeping flow equation for a Newtonian fluid [7], with the exception that p_v takes the place of the dynamic pressure

$$\mathcal{P} \equiv p - \rho \underline{g} \cdot \underline{r}. \quad (3.31)$$

3.2.1 Force on immersed species

Rosensweig [6] provides a derivation for the force on a nonmagnetic species immersed in a magnetic fluid continuum using the Ferrohydrodynamic Bernoulli Equation. That result is valid for hydrostatic systems, but its validity in viscous flows is not obvious. As a first step in understanding the magnetophoresis of nonmagnetic particles in magnetic nanofluids, the force of magnetic origin is derived for the system of interest.

The total force on a particle immersed in a ferrofluid is given by

$$\underline{F} = - \oint_{S_p} p \underline{n} dS + \int_{V_p} \rho_p \underline{g} dV + \oint_{S_p} \underline{n} \cdot \underline{T}_v dS + \oint_{S_p} \underline{n} \cdot \underline{T}_m dS, \quad (3.32)$$

where ρ_p is the density of the particle, V_p is the particle volume, S_p its surface area, and $\underline{\underline{T}}_v$ the viscous stress. This expression is valid when the ferrofluid can be treated as a continuum with respect to the immersed particle. Expressing the magnetic stress tensor in the form

$$\underline{\underline{T}}_m = \underline{\underline{B}}\underline{\underline{H}} - \mu_0 \underline{\underline{I}} \int_0^H H' dH', \quad (3.33)$$

and using the definition $\underline{\underline{B}} = \mu_0 (\underline{\underline{M}} + \underline{\underline{H}})$ as well as eqs. (3.27) – (3.29), the force on a submerged particle becomes

$$\underline{\underline{F}} = -\oint_{S_p} p_v \underline{\underline{n}} dS + \oint_{S_p} \underline{\underline{n}} \cdot \underline{\underline{T}}_v dS + \int_{V_p} (\rho_p - \rho) \underline{\underline{g}} dV + \oint_{S_p} \underline{\underline{n}} \cdot \underline{\underline{T}}'_m dS, \quad (3.34)$$

where

$$\underline{\underline{T}}'_m = \underline{\underline{B}}\underline{\underline{H}} - \underline{\underline{I}} \int_0^H B' dH'. \quad (3.35)$$

The modified tensor given in eq. (3.35) was also obtained by Rosensweig [6] for a species suspended in a quiescent magnetic fluid.

For an MQS system, all the magnetic variables are invariant to Galilean transformations [2], meaning that the magnetic fields can be specified in a coordinate system where the particle and the magnetic field sources are stationary and the fluid is moving (such as what is done here) or in a coordinate system where the fluid and the magnetic sources are stationary and the particle is migrating (such as the case of interest to us). Thus, we can apply the results obtained for stationary magnetic fields with respect to the *particle* to the case where the magnetic fields are stationary with respect to the *fluid*. For a spherical particle, the first two terms in eq. (3.34), with the use of eq. (3.30), give the classic Stokes drag force [7]

$$\underline{\underline{F}}_d = -6\pi\eta a \underline{\underline{v}}_r, \quad (3.36)$$

where a is the radius of the particle and $\underline{\underline{v}}_r$ is the particle velocity with respect to the fluid. The third term gives the buoyancy force,

$$\underline{\underline{F}}_b = (\rho_p - \rho) V_p \underline{\underline{g}}. \quad (3.37)$$

The last term gives the force of magnetic origin

$$\underline{E}_m = \oint_{S_p} \underline{n} \cdot \underline{T}'_m dS. \quad (3.38)$$

For a nonmagnetic particle, the use of the appropriate magnetic boundary conditions on the particle surface results in

$$\underline{E}_m = -\oint_{S_p} \left(\frac{1}{2} \mu_0 (\underline{n} \cdot \underline{M})^2 + p_m \right) \underline{n} dS, \quad (3.39)$$

where all the variables are evaluated on the fluid side. For a dilute or highly saturated magnetic fluid, we generally have $\frac{M_n^2}{MH} \ll 1$, since the magnetic susceptibility is much less than unity. By neglecting the first term in the integral, we are effectively doing two things: (1) neglecting the "surface excess force" with respect to the "magnetic buoyancy" force and (2) neglecting the effect of the particle on the magnetic field distribution, since the magnetic fields are only affected by changes in magnetization (in the absence of electrical currents). This limit is equivalent to integrating the pressure profile over a surface that encloses an equivalent volume of magnetic fluid, as is typically done for calculating buoyancy forces [7]. This is convenient because the magnetic pressure would be continuous across the nonmagnetic particle surface and throughout its volume. Thus, we can invoke Gauss' theorem to convert the surface integral to a volume integral, giving us

$$\begin{aligned} \underline{E}_m &\approx -\oint_{S_p} p_m \underline{n} dS \\ &= -\int_{V_p} \underline{\nabla} p_m dV \\ &\approx -\mu_0 V_p M_f \underline{\nabla} H, \end{aligned} \quad (3.40)$$

which is valid for particle sizes much smaller than the length scale over which the field gradient varies. The subscript f is used on M_f to reiterate that the force on the nonmagnetic particle is proportional to the magnetization of the surrounding magnetic fluid. Eq. (3.40) is the same equation previously derived by Rosensweig [6] for a nonmagnetic species suspended in a quiescent magnetic fluid.

The above expression (3.40) is commonly used for the force on a nonmagnetic particle in a magnetizable fluid without taking into account the limitations introduced in its derivation. In this work, we will limit the use of this force expression to dilute magnetic fluids at nearly constant temperature (or temperatures far away from the Curie temperature) and density.

The last expression obtained is of significance for several reasons. First, it tells us that the force of magnetic origin scales with the volume of the nonmagnetic particles. Since the viscous drag scales with the hydrodynamic radius of these particles, their migration velocity will scale with their hydrodynamic surface area, meaning that larger nonmagnetic particles should migrate at faster velocities than smaller particles in a quiescent fluid under an applied magnetic field gradient. Conversely, a smaller magnetic force density is required to trap larger particles against flow in a non-quiescent fluid. This result is essential for size-based separations using negative magnetophoresis.

Another significant aspect of this force expression is that, for a dilute magnetic fluid containing a dilute dispersion of nonmagnetic particles, the force on these particles depends on a magnetic field that is not significantly affected by the presence of the particles. That is, the magnetic field appearing in eq. (3.40) can be taken to be the field in the absence of the particle. This is important in relating these microphysics results to the thermodynamic results presented in the next section, as the location of a particle is considered a point in a continuum in the latter. In the thermodynamic approach, the details involved in the distortion of magnetic fields in the vicinity of the particles must be incorporated in the form of excess chemical potentials. Fortunately, the derivation of eq. (3.40) tells us that the effects of local magnetic-field deviations from the applied field should be small for the conditions of interest.

Finally, another effect of having the force density not be significantly affected by the presence of the particles is that the hydrodynamic and species transport equations governing the migration of the nonmagnetic particles are decoupled from the magnetic field profile. We can solve for the magnetic field first, neglecting the effects of the dilute ferrofluid and the suspended nonmagnetic particles, and then model the migration of the nonmagnetic particles resulting from the applied magnetic fields.

A first-order correction to the force expression given by eq. (3.40), valid for more concentrated magnetic fluids (but dilute nonmagnetic species), is given by [25]

$$\underline{F}_m = -\mu_0 V_p \overline{M} \underline{\nabla} H, \quad (3.41)$$

where

$$\overline{M} = M_f \left(\frac{1 + \chi_f}{1 + \frac{2}{3} \chi_f} \right) \quad (3.42)$$

and $M_f = \chi_f H$. This expression assumes that

$$\frac{a |\underline{\nabla} H|}{H} \ll 1, \quad (3.43)$$

which is valid for our case of interest. Eq. (3.41) accounts for the “demagnetization” of the fluid by the particle, and reduces to eq. (3.40) for $\chi_f \ll 1$. For the conditions of interest to us (0.1 vol % magnetite concentration), the maximum value of χ_f is about 0.01, meaning that eq. (3.40) should be valid to within 0.5%.

3.2.1.1 Arbitrariness of magnetic pressures, stresses, and body forces

Before proceeding, it is important to show that the same results can be obtained using any of the various magnetic force densities available in the literature. Eq. (3.19) uses a force density equal to the divergence of the Maxwell Stress Tensor [8], given by eq.(3.21). However, there are numerous other stress tensors used in the literature, none of which can be shown to be more fundamental than the others [6]. In this section we show that all the differences resulting from the use of different stress tensors can be treated as effective pressures, and that all of the stress tensors available in the literature lead to the same force of magnetic origin on a particle submerged in a ferrofluid.

The analysis performed by Rosensweig [6] results in a total stress tensor, capturing both the viscous and magnetic effects, given by

$$\underline{\underline{\mathbf{T}}}_{\text{tot}} = \underline{\underline{\mathbf{T}}}_{\text{v}} - \left\{ p_0 - \mu_0 \int_0^H \left[\rho^2 \frac{\partial}{\partial \rho} \left(\frac{M}{\rho} \right) \right]_{H',T} dH' + \frac{1}{2} \mu_0 H^2 \right\} \underline{\underline{\mathbf{I}}} + \underline{\underline{\mathbf{B}}}\underline{\underline{\mathbf{H}}}. \quad (3.44)$$

This stress tensor is derived assuming that the magnetic forces are surface stresses and not body forces. Since it is not clear which terms should be treated as body forces and which should be treated as pressures or stresses, there are a lot of different interpretations available in the literature. The most commonly used form is the form presented in the previous section, in which we take

$$p = p_0 - \mu_0 \int_0^H \left[\rho^2 \frac{\partial}{\partial \rho} \left(\frac{M}{\rho} \right) \right]_{H',T} dH' \quad (3.45)$$

and

$$\underline{\underline{\mathbf{T}}}_{\text{m}} = \underline{\underline{\mathbf{B}}}\underline{\underline{\mathbf{H}}} - \frac{1}{2} \mu_0 H^2 \underline{\underline{\mathbf{I}}}, \quad (3.46)$$

which leads to the classical Navier-Stokes equations plus a Kelvin-type magnetic force density [8], such as the creeping flow eq. (3.24). However, we could have defined the fluid pressure as $p = p_0$ and

$$\underline{\underline{\mathbf{T}}}_{\text{m}} = \underline{\underline{\mathbf{B}}}\underline{\underline{\mathbf{H}}} + \mu_0 \left\{ \int_0^H \left[\rho^2 \frac{\partial}{\partial \rho} \left(\frac{M}{\rho} \right) \right]_{H',T} dH' - \frac{1}{2} H^2 \right\} \underline{\underline{\mathbf{I}}}, \quad (3.47)$$

which reduces to the famous Korteweg-Helmholtz magnetic force density for a linear magnetic fluid [2]. We could have also defined

$$\underline{\underline{\mathbf{T}}}_{\text{m}} = \underline{\underline{\mathbf{B}}}\underline{\underline{\mathbf{H}}} - \frac{1}{2} H \underline{\underline{\mathbf{B}}}\underline{\underline{\mathbf{I}}}, \quad (3.48)$$

which is another commonly used stress tensor [6]. This would be equivalent to defining the fluid pressure as

$$p = p_0 - \mu_0 \int_0^H \left[\rho \frac{\partial M}{\partial \rho} \right]_{H',T} dH' \quad (3.49)$$

in our original derivation.

None of these pressures or stresses is more fundamental than the others. Fortunately, all of the stress tensors presented here lead to the same total force of

magnetic origin on a submerged particle. This is because the only difference between all of the stress tensors is a scalar multiplying the idemfactor $\underline{\underline{I}}$, which can be treated as an effective pressure. Adding any quantity $b\underline{\underline{I}}$ to the stress tensor will result in an increase in the total pressure by an amount b . This change in pressure in turn cancels out the extra stress $b\underline{\underline{I}}$ when the total force on the particle is calculated using eq. (3.32). As a result, any stress tensor of the form

$$\underline{\underline{T}}_m = \underline{\underline{B}}H + b\underline{\underline{I}} \quad (3.50)$$

will give the correct force of magnetic origin on a submerged particle. This is demonstrated as follows.

Substituting eq. (3.50) into the creeping flow equation gives

$$\begin{aligned} \underline{\nabla}p &= \eta\underline{\nabla}^2\underline{\underline{v}} + \underline{\rho}\underline{\underline{g}} + \underline{\nabla} \cdot \underline{\underline{T}}_m \\ &= \eta\underline{\nabla}^2\underline{\underline{v}} + \underline{\rho}\underline{\underline{g}} + B\underline{\nabla}H + \underline{\nabla}b \\ &= \eta\underline{\nabla}^2\underline{\underline{v}} + \underline{\nabla} \left(\underline{\rho}\underline{\underline{g}} \cdot \underline{\underline{r}} + \mu_0 \overline{MH} + \mu_0 \frac{H^2}{2} + b \right). \end{aligned} \quad (3.51)$$

Again, the absence of free currents to go with constant temperature (or temperatures far away from the Curie temperature) and density are assumed in eq. (3.51). As before, we can define a set of pressures as

$$p_b \equiv \underline{\rho}\underline{\underline{g}} \cdot \underline{\underline{r}}, \quad (3.52)$$

$$p_m \equiv \mu_0 \overline{MH}, \quad (3.53)$$

$$p^* \equiv \mu_0 \frac{H^2}{2} + b, \quad (3.54)$$

$$p_v \equiv p - p_b - p_m - p^*. \quad (3.55)$$

We can thus write, just like in eq. (3.30)

$$\underline{\nabla}p_v = \eta\underline{\nabla}^2\underline{\underline{v}}. \quad (3.56)$$

A force balance around a submerged particle will give us the same force expression as before, namely

$$\underline{\underline{F}} = -\oint_{S_p} p \underline{\underline{n}} dS + \int_{V_p} \rho_p \underline{\underline{g}} dV + \oint_{S_p} \underline{\underline{n}} \cdot \underline{\underline{T}}_v dS + \oint_{S_p} \underline{\underline{n}} \cdot \underline{\underline{T}}_m dS, \quad (3.57)$$

except that now

$$\underline{\underline{T}}_m = \underline{\underline{B}}\underline{\underline{H}} + b\underline{\underline{I}}. \quad (3.58)$$

Substituting in for the pressure and the stress tensor gives

$$\underline{\underline{F}} = -\oint_{S_p} p_v \underline{\underline{n}} dS + \oint_{S_p} \underline{\underline{n}} \cdot \underline{\underline{T}}_v dS + \int_{V_p} (\rho_p - \rho) \underline{\underline{g}} dV + \oint_{S_p} \underline{\underline{n}} \cdot \underline{\underline{T}}'_m dS, \quad (3.59)$$

where

$$\underline{\underline{T}}'_m = \underline{\underline{B}}\underline{\underline{H}} - \underline{\underline{I}} \int_0^H B dH'. \quad (3.60)$$

This is, as anticipated, the same result obtained in the previous section (see eqs. (3.34) and (3.35)).

The above analysis proves that any of the widely used stress tensors or body-force densities will give the correct force of magnetic origin on a submerged particle for the conditions of interest to us. The pressure term appearing in the creeping flow equation acts as a degree of freedom that compensates for the differences in magnetic stress tensors used, as long as the stress tensor is of the form given in eq. (3.50). For a nonmagnetic particle immersed in a dilute ferrofluid continuum, the force of magnetic origin is

$$\underline{\underline{F}}_m \approx -\mu_0 V_p M \underline{\underline{\nabla}} H, \quad (3.61)$$

regardless of the magnetic stress tensor used to describe the ferrofluid.

3.3 Thermodynamics of magnetic nanofluids

The approach presented in the previous section treats each nonmagnetic particle individually, without taking into account particle-particle interactions and random fluctuations (Brownian motion). For very dilute solutions, it may be possible to introduce random fluctuations, electrostatic and volume exclusion forces, and perform dynamic simulations using a small number of these nonmagnetic particles. Since we are

more interested in volume fractions ranging from 0.1 to 1%, we find it more convenient to use a continuum, irreversible thermodynamic approach, which employs macroscopic concepts such as concentrations and excess chemical potentials. In this approach, the nonmagnetic particles are treated as a continuum of a nonmagnetic species. Magnetic forces, hydrodynamic drags, and random fluctuations are replaced with macroscopic concepts such as chemical potential gradients and diffusion coefficients. Electrostatic interactions between particles and the finite volume excluded by these particles are introduced as gradients in excess chemical potentials.

In this section, the thermodynamic framework used to derive expressions for diffusive fluxes is introduced. Starting from the Gibbs equation for magnetic systems, an expression is obtained for the rate of change of entropy of the system. The rate of entropy generation is related to the chemical potentials of the species, which in this case are functions of the magnetic field H . The derivation of binary and multicomponent diffusion fluxes, which are directly linked to the rate of entropy generation, is given in Section 3.4.

3.3.1 Equilibrium thermodynamics

A good overview of the thermodynamics of magnetic systems is given by Rosensweig in Astarita's book *Thermodynamics: an Advanced Textbook for Chemical Engineers* [9]. The analysis presented there is valid for fluids in which \underline{M} and \underline{H} are parallel, which is the case of interest to us. Other works have been published for the case in which \underline{M} and \underline{H} are not parallel due to rotating magnetic fields [1]. The work presented in this section (and in the rest of this thesis) is only concerned with fluids in which \underline{M} and \underline{H} are parallel.

The Gibbs equation for the magnetic system of interest is [9]

$$dU = TdS - p'd\left(\frac{1}{\rho}\right) + Hd\left(\frac{B}{\rho}\right) + \sum \xi_i dw_i . \quad (3.62)$$

Here U is the internal energy per unit mass, S is the system entropy per unit mass, ξ_i the chemical potentials on a per-mass basis, w_i the mass fractions of species i , and p' the

thermodynamic pressure. In this formulation we use the symbol ξ instead of the usual symbol μ for the chemical potential to avoid confusion with the magnetic permeability of a material,

$$\mu = \frac{B}{H} . \quad (3.63)$$

A different symbol is also used for the thermodynamic pressure p' appearing in eq. (3.62) to distinguish it from the magnetic fluid pressure p appearing in the momentum equation, given in eq. (3.23). The relationship between these two pressures is

$$p' = p + \frac{1}{2} \mu_0 H^2 . \quad (3.64)$$

The only difference between eq. (3.62) and the Gibbs equation in classical thermodynamics is the magnetic work term, given by [10]

$$dW_m = Hd \left(\frac{B}{\rho} \right) . \quad (3.65)$$

This work term comes from the work done on the system by external forces to establish the field [11]

$$E_m = \int_V \left[\int_0^B \underline{H} \cdot d\underline{B} \right] dV' . \quad (3.66)$$

The expression for the magnetic work density in eq. (3.65) is postulated, as eq. (3.66) only gives information on the total magnetic energy of the system and not its spatial distribution (the volume of integration is not arbitrary; the volume needs to include the entire system, and the magnetic field must vanish at the system boundaries). It is, however, the most widely accepted energy density distribution, and the one used throughout our analysis. The complete form of eq. (3.62) also includes electric field effects, but these are completely analogous to the magnetic effects and can be added at any point by inspection. Since there are no applied electric fields in our system of interest, only magnetic effects are included in our analysis.

Using the magnetic fluid pressure instead of the thermodynamic pressure, the Gibbs equation can be written as (after some rearrangement)

$$\rho T dS = \rho dU - \left(p - \frac{\mu_0 H^2}{2} - \mu_0 M H \right) \frac{d\rho}{\rho} - HdB - \sum \rho \xi_i dw_i , \quad (3.67)$$

and the generalized form of the Gibbs-Duhem equation is

$$SdT - \frac{1}{\rho} dp + \frac{\mu_0 M}{\rho} dH + \sum w_i d\xi_i = 0. \quad (3.68)$$

Differentiating eq. (3.67) with respect to time gives

$$\rho T \frac{dS}{dt} = \rho \frac{dU}{dt} - \left(p - \frac{\mu_0 H^2}{2} - \mu_0 MH \right) \frac{d\rho}{\rho dt} - H \frac{dB}{dt} - \sum \rho \xi_i \frac{dw_i}{dt}, \quad (3.69)$$

where $\frac{d}{dt}$ is the substantial derivative, or the time rate of change following a fluid element which moves with the mass-average velocity \underline{v} .

In order to relate diffusivities of species i to the rate of entropy generation, we first develop expressions for $\frac{d\rho}{dt}$, $\frac{dB}{dt}$, $\frac{dw_i}{dt}$, and $\frac{dU}{dt}$. The first term is obtained from the continuity equation,

$$\frac{d\rho}{\rho dt} = -\underline{\nabla} \cdot \underline{v} = -\underline{\underline{I}} : \underline{\nabla} \underline{v}. \quad (3.70)$$

For the case where $\frac{\partial B}{\partial t} \approx 0$, as is the case of interest to us, we have that [9]

$$H \frac{dB}{dt} = (\underline{BH} - BH\underline{\underline{I}}) : \underline{\nabla} \underline{v} - \underline{H} \cdot [\underline{\nabla} \times (\underline{v} \times \underline{B})]. \quad (3.71)$$

From a species balance in the absence of chemical reactions, we have that

$$\rho \frac{dw_i}{dt} = -\underline{\nabla} \cdot \underline{j}_i, \quad (3.72)$$

where \underline{j}_i is the mass flux of species i relative to the mass-average velocity \underline{v} .

To obtain the internal energy term needed in eq. (3.69), an overall energy balance, combined with a momentum balance to eliminate the mechanical energy terms, is performed. This results in

$$\rho \frac{dU}{dt} = \underline{\underline{T}}_{\text{tot}} : \underline{\nabla} \underline{v} - \underline{\nabla} \cdot \underline{q}' - \underline{H} \cdot [\underline{\nabla} \times (\underline{v} \times \underline{B})] + \sum \underline{j}_i \cdot \underline{g}_i, \quad (3.73)$$

where \underline{q}' is a combined heat flux (heat flux plus diffusive flux of internal energy), \underline{g}_i the body force per unit mass on species i , and $\underline{\underline{T}}_{\text{tot}}$ is the total stress tensor given in eq. (3.44), which in terms of the fluid pressure p is

$$\underline{\underline{T}}_{\text{tot}} = \underline{\underline{T}}_v - \left\{ p + \frac{1}{2} \mu_0 H^2 \right\} \underline{\underline{I}} + \underline{\underline{B}}\underline{\underline{H}}. \quad (3.74)$$

A similar result is obtained by Rosensweig [9], except that his analysis is for a single component without any external forces \underline{g}_i . Substitution of (3.70) - (3.74) into (3.69) finally yields the relationship for the rate of change of entropy

$$\rho T \frac{dS}{dt} = \Phi - \underline{\underline{\nabla}} \cdot \underline{q}' + \sum (\xi_i \underline{\underline{\nabla}} \cdot \underline{j}_i + \underline{g}_i \cdot \underline{j}_i), \quad (3.75)$$

where

$$\Phi = \underline{\underline{T}}_v : \underline{\underline{\nabla}}\underline{v} \quad (3.76)$$

is the viscous dissipation function.

3.3.2 Rate of entropy generation

In order to relate the species flux to the rate of entropy generation, eq. (3.75) needs to be rearranged to distinguish between entropy flux coming in and out of the system and rate of entropy generation within the system. In generalized form, a conservation of entropy statement is given by

$$\rho \frac{dS}{Dt} = \theta_s - \underline{\underline{\nabla}} \cdot \underline{j}_s, \quad (3.77)$$

where \underline{j}_s is the entropy flux and θ_s represents the rate of entropy generation. Expanding eq. (3.75) and comparing terms with eq. (3.77), we have that

$$\underline{j}_s = \frac{1}{T} (\underline{q} - \sum \underline{j}_i \xi_i), \quad (3.78)$$

and

$$\theta_s T = \underline{\underline{T}}_v : \underline{\underline{\nabla}}\underline{v} - \underline{j}_s \cdot \underline{\underline{\nabla}}T - \sum \underline{j}_i \cdot [\underline{\underline{\nabla}}\xi_i - \underline{g}_i]. \quad (3.79)$$

Eq. (3.78) accounts for the flux of entropy being exchanged between the system and its surroundings. The terms in this expression do not lead to any irreversible changes in entropy. The terms in eq. (3.79) are the ones that account for the amount of entropy being generated within the system, a quantity which is required to be positive.

It is worth noting that eq. (3.79) is the same equation given by Lightfoot [12] for the rate of entropy generation within the system. The only difference is that the chemical potentials now depend on the magnetic field. In particular, we have that [9]

$$\left(\frac{\partial \xi_i}{\partial H}\right)_{T,p,m_i} = -\mu_0 \bar{\vartheta}_i, \quad (3.80)$$

$$\bar{\vartheta}_i \equiv \left(\frac{\partial I_t}{\partial m_i}\right)_{T,p,H}, \quad (3.81)$$

$$I_t = MV, \quad (3.82)$$

where I_t is the total magnetic moment, $\bar{\vartheta}_i$ is the partial molar magnetic moment, and m_i are the masses of species i . Thus,

$$\xi_i(T, p, x_{j \neq i}, H) = \xi_i(T, p, x_{j \neq i}, 0) - \mu_0 \hat{\vartheta}_i H, \quad (3.83)$$

where x_j denote the mole fractions of species j and

$$\hat{\vartheta}_i = \frac{1}{H} \int_0^H \bar{\vartheta}_i dH'. \quad (3.84)$$

Our analysis shows that the rate of entropy generation for a magnetic fluid system has the same general form as for systems with no electromagnetic fields, but with the exception that the magnetic effects are introduced by the chemical potentials of the species i . Magnetic field gradients may therefore lead to forced diffusion of species in magnetic fluids, resulting in entropy generation.

For an ideal system, in which the species do not have magnetic interactions with each other, the partial-molar magnetic moment reduces to

$$\bar{\vartheta}_i = \vartheta_i = \frac{M_i}{\rho_i}, \quad (3.85)$$

where ϑ_i is the magnetic moment of pure species i , M_i is the magnetization of pure species i , and ρ_i is the mass density of species i .

3.4 Diffusion in magnetic nanofluids

In Section 3.3.2, we obtained relationships between the diffusive fluxes of species and the rate of entropy generation in the system. Since the chemical potentials of the species depend on magnetic fields, there will be entropy generation if the magnetic fields lead to diffusion of the species. In this section, we relate the diffusive fluxes of the species to their chemical potentials in such a way that the generation of entropy is guaranteed to be a positive quantity.

3.4.1 Binary diffusion of nonmagnetic species

In this work, we are interested in the diffusion of a nonmagnetic species ($i = 1$) in a magnetic fluid continuum ($i = 2$). For an ideal system at constant temperature and negligible viscous dissipation, with gravity being the only body force acting on the two species, eq. (3.79) reduces to

$$T\theta_s = -\underline{j}_1 \cdot (\underline{\nabla}\xi_1 - \underline{g}) - \underline{j}_2 \cdot (\underline{\nabla}\xi_2 - \underline{g}) . \quad (3.86)$$

By definition, the two fluxes are related by the expression

$$\underline{j}_1 + \underline{j}_2 = \underline{0} , \quad (3.87)$$

which results in

$$T\theta_s = -\underline{j}_1 \cdot \underline{\nabla}(\xi_1 - \xi_2) . \quad (3.88)$$

For the conditions of interest, we have that

$$\underline{\nabla}\xi_1 = \left(\frac{\partial \xi_1}{\partial x_1} \right)_{T,p,H} \underline{\nabla}x_1 + \left(\frac{\partial \xi_1}{\partial H} \right)_{T,p,x_1} \underline{\nabla}H + \left(\frac{\partial \xi_1}{\partial p} \right)_{T,H,x_1} \underline{\nabla}p , \quad (3.89)$$

$$\underline{\nabla}\xi_2 = \left(\frac{\partial \xi_2}{\partial x_1} \right)_{T,p,H} \underline{\nabla}x_1 + \left(\frac{\partial \xi_2}{\partial H} \right)_{T,p,x_1} \underline{\nabla}H + \left(\frac{\partial \xi_2}{\partial p} \right)_{T,H,x_1} \underline{\nabla}p. \quad (3.90)$$

The mole fractions x_i must add up to 1, so only one of them is independent. As in the previous section, the pressure appearing here is the same pressure used in the creeping flow eq.(3.19),

$$p = p_0 - \mu_0 \int_0^H \left[\rho^2 \frac{\partial}{\partial \rho} \left(\frac{M}{\rho} \right) \right]_{H',T} dH', \quad (3.91)$$

where $p_0(\rho, T)$ is the classic thermodynamic pressure in the absence of magnetic fields.

For an ideal system,

$$\left[\frac{\partial}{\partial x_1} (\xi_1 - \xi_2) \right]_{T,p,H} = RT \left(\frac{1}{W_1 x_1} - \frac{1}{W_2 x_2} \right), \quad (3.92)$$

$$\left[\frac{\partial}{\partial H} (\xi_1 - \xi_2) \right]_{T,p,x_1} = -\mu_0 (v_1^{\mathcal{I}} - v_2^{\mathcal{I}}), \quad (3.93)$$

$$\left[\frac{\partial}{\partial p} (\xi_1 - \xi_2) \right]_{T,x_1,H} = \frac{v_1}{W_1} - \frac{v_2}{W_2}, \quad (3.94)$$

where v_i and W_i denote the molar volumes and molecular weights, respectively. Species 1 is nonmagnetic, so $v_1^{\mathcal{I}} = 0$ and

$$v_2^{\mathcal{I}} = \frac{M_2}{\rho_2}. \quad (3.95)$$

We know that the rate of entropy production in our system cannot be negative.

The only way we can guarantee this is to set

$$\underline{j}_1 = -K \underline{\nabla} (\xi_1 - \xi_2), \quad (3.96)$$

where K is a positive number. We thus have

$$\underline{j}_1 = -\underline{j}_2 = -KRT \left(\frac{1}{W_1 x_1} - \frac{1}{W_2 x_2} \right) \underline{\nabla}x_1 - K \left(\frac{v_1}{W_1} - \frac{v_2}{W_2} \right) \underline{\nabla}p - K\mu_0 \frac{M_2}{\rho_2} \underline{\nabla}H. \quad (3.97)$$

The mole fractions are related to the mass fractions w_i through the relationship

$$x_1 = \frac{w_1}{W_1 \Delta}, \quad (3.98)$$

where

$$\Delta = \frac{w_1}{W_1} + \frac{w_2}{W_2} = \frac{C}{\rho}. \quad (3.99)$$

Here C is the overall molar concentration. Thus,

$$\underline{\nabla} w_1 = (\Delta^2 W_1 W_2) \underline{\nabla} x_1. \quad (3.100)$$

and

$$\left(\frac{1}{W_1 x_1} + \frac{1}{W_2 x_2} \right) = \frac{\Delta}{w_1 w_2}. \quad (3.101)$$

Substituting these results back into eq. (3.97), we get

$$\underline{j}_1 = -\underline{j}_2 = -\frac{KRT}{w_1 w_2 W_1 W_2 \Delta} \underline{\nabla} w_1 - K \left(\frac{v_1}{W_1} - \frac{v_2}{W_2} \right) \underline{\nabla} p - K \mu_o \frac{M_2}{\rho_2} \underline{\nabla} H. \quad (3.102)$$

We know that when $H = 0$ and there are no pressure gradients, our results should reduce to Fick's law

$$\underline{j}_1 = -\mathcal{D}_{12} \rho \underline{\nabla} w_1. \quad (3.103)$$

This tells us that

$$K = \frac{\mathcal{D}_{12} \rho w_1 w_2 W_1 W_2 \Delta}{RT}, \quad (3.104)$$

where \mathcal{D}_{12} is the binary diffusion coefficient. Substituting for K back into eq. (3.102)

gives

$$\begin{aligned} \underline{j}_1 = -\underline{j}_2 = & -\mathcal{D}_{12} \rho \underline{\nabla} w_1 - \frac{\mathcal{D}_{12} C w_1 w_2 W_1 W_2}{RT} \left(\frac{v_1}{W_1} - \frac{v_2}{W_2} \right) \underline{\nabla} p \\ & - \frac{\mathcal{D}_{12} C w_1 w_2 W_1 W_2}{RT} \left(\frac{w_1}{W_1} + \frac{w_2}{W_2} \right) \frac{\mu_o M_2}{\rho_2} \underline{\nabla} H \end{aligned}, \quad (3.105)$$

or

$$\underline{j}_1 = -\underline{j}_2 = -\mathcal{D}_{12} \rho \underline{\nabla} w_1 - \frac{\mathcal{D}_{12} C (\phi - w_1) W_1 W_2}{\rho RT} \underline{\nabla} p - \frac{\mathcal{D}_{12} C w_1 W_1 W_2}{\rho RT} \mu_o M \underline{\nabla} H. \quad (3.106)$$

Here ϕ_i is the volume fraction of species i .

The pressure gradient can be obtained from the momentum-balance equation. Limiting ourselves to systems in local mechanical equilibrium with negligible inertia, the pressure gradient reduces to

$$\nabla p \approx \rho \underline{\underline{g}} + \mu_o M \underline{\underline{\nabla H}} . \quad (3.107)$$

The mass flux relative to the mass-average velocity is therefore

$$\underline{\underline{j}}_1 = -\mathcal{D}_{12} \rho \underline{\underline{\nabla}} w_1 - \frac{\mathcal{D}_{12} C W_1 W_2}{\rho R T} [(\phi_1 - w_1) \rho \underline{\underline{g}} + \phi_1 \mu_o M \underline{\underline{\nabla H}}] . \quad (3.108)$$

The first term in the above expression is the classic Fick's law of diffusion. In the bracketed term, the gravitational term is the flux due to buoyancy effects and the last term is the flux due to magnetic field gradients. The molar flux relative to the mass average velocity is therefore

$$\underline{\underline{J}}_1 = \frac{\underline{\underline{j}}_1}{W_1} = -\frac{\mathcal{D}_{12} \rho}{W_1} \underline{\underline{\nabla}} w_1 - \frac{\mathcal{D}_{12} C W_2}{\rho R T} [(\phi_1 - w_1) \rho \underline{\underline{g}} + \phi_1 \mu_o M \underline{\underline{\nabla H}}] . \quad (3.109)$$

As a consistency check, let us examine the magnetic term of the above expression for different sized particles. We see that, for a fixed number of particles (or moles) of species 1, ϕ_1 scales with the volume of the particle and \mathcal{D}_{12} scales with the hydrodynamic radius, meaning that the forced diffusion of species 1 scales with its hydrodynamic surface area, as expected. The negative sign assures that magnetophoretic diffusion is in the direction of decreasing magnetic fields, again as expected.

A similar analysis to the one presented in this section was performed by Rosensweig [9] for a binary system. His analysis neglects pressure effects, and would thus lead to a flux having a weight fraction multiplying the magnetic force density instead of a volume fraction. This could lead to errors in calculating the forced diffusion of dense species such as silica particles, where the weight fraction would be twice as large as the volume fraction.

3.4.2 Generalized multicomponent diffusion

The same theory can now be generalized to a multicomponent system, which in turn should reduce to the results presented in the previous section for a binary system. It is assumed as a postulate of the thermodynamics of irreversible processes that, for situations not too far removed from equilibrium, the fluxes may be written in the form [13]

$$\underline{j}_i = \sum_j \alpha_{ij} \underline{X}_j, \quad (3.110)$$

which states that the fluxes are linear functions of generalized forces or affinities, designated by \underline{X}_j . The terms α_{ij} are phenomenological coefficients. The fundamental theorem of the thermodynamics of irreversible processes, due to Onsager, states that if a "proper choice" of the fluxes and affinities has been made, the phenomenological coefficients α_{ij} are symmetric [14]:

$$\alpha_{ij} = \alpha_{ji}. \quad (3.111)$$

These conditions are commonly referred to as the "reciprocal relations."

For an isothermal process with negligible viscous dissipation, eq. (3.79) gives the rate of entropy production as,

$$T\theta_s = -\sum_{i=1}^v (\underline{\Delta}_i \cdot \underline{j}_i), \quad (3.112)$$

where v is the number of species and

$$\begin{aligned} \underline{\Delta}_i &= \underline{\nabla}(\xi_i)_T - \underline{g}_i \\ &= \sum_{\substack{j=1 \\ j \neq i}}^v \left(\frac{\partial \xi_i}{\partial x_j} \right)_{T, P, x_{k \neq i, j}} \underline{\nabla} x_j + \frac{\bar{V}_i}{W_i} \underline{\nabla} p - \mu_0 \bar{v}_i \underline{\nabla} H - \underline{g}_i. \end{aligned} \quad (3.113)$$

Here \bar{V}_i is the partial molar volume of species i . The right-hand side of eq. (3.112) must be positive, but there is no requirement for each term in the summation to be negative, since the fluxes \underline{j}_i are not independent (their sum must add up to zero). One of the

components may be eliminated to obtain a linearly independent set. Eliminating the flux of the k th component we obtain

$$T\theta_s = -\sum_{i=1}^v \left(\{\underline{\Delta}_i - \underline{\Delta}_k\} \cdot \underline{j}_i \right). \quad (3.114)$$

The application of the linear law then gives

$$\underline{j}_i = -\sum_{j=1}^v \alpha_{ij} (\underline{\Delta}_j - \underline{\Delta}_k). \quad (3.115)$$

Since $\sum_{i=1}^v \underline{j}_i = \underline{0}$, we obtain

$$\underline{j}_k = \sum_{i=1}^v \sum_{j=1}^v \alpha_{ij} (\underline{\Delta}_j - \underline{\Delta}_k). \quad (3.116)$$

Setting $i = k$ in eq. (3.115), together with the symmetry condition on the α_{ij} , we get

$$\alpha_{kj} = -\sum_{\substack{j=1 \\ j \neq k}}^v \alpha_{ij} = \alpha_{jk}. \quad (3.117)$$

These relationships allow us to rewrite the diffusion flux as

$$\underline{j}_i = -\sum_{j=1}^v \alpha_{ij} \underline{\Delta}_j. \quad (3.118)$$

The α_{ij} are symmetric and satisfy the relationship

$$\sum_{i=1}^v \alpha_{ij} = \sum_{i=1}^v \alpha_{ji} = 0. \quad (3.119)$$

At this point, our derivation is essentially complete. The last step would be to determine the phenomenological coefficients α_{ji} , subject to the symmetry conditions and condition (3.119), and calculate the species fluxes from eq. (3.118). However, it is not convenient to express the fluxes in this manner, as the species fluxes cannot easily be related to the ordinary diffusive fluxes that are more readily available. It is more convenient to define a generalized driving force \underline{d}_i , defined as

$$CRT \underline{d}_i = C_i W_i \left(\underline{\Delta}_i - \frac{1}{\rho} \underline{\nabla} p + \sum_{j=1}^v w_j \underline{g}_j + \frac{\mu_o M}{\rho} \underline{\nabla} H \right), \quad (3.120)$$

where C_i is the molar concentration of species i . The quantity added to the term $\underline{\Lambda}_i$ is the hydrostatic form of the Navier-Stokes equation, on a per unit mass basis, generalized to include magnetic effects through the term $\frac{\mu_o M}{\rho} \underline{\nabla} H$ and all other body forces through the term $\sum_{j=1}^v w_j \underline{\mathbf{g}}_j$. Substituting in for $\underline{\Lambda}_i$ gives us

$$\begin{aligned}
 CRT \underline{\mathbf{d}}_i = & C_i W_i \sum_{\substack{j=1 \\ j \neq i}}^v \left(\frac{\partial \xi_i}{\partial x_j} \right)_{T,P,H,x_{k \neq i,j}} \underline{\nabla} x_j + (C_i \bar{V}_i - w_i) \underline{\nabla} p \\
 & - \mu_o C_i W_i \left(\bar{\vartheta}_i - \frac{M}{\rho} \right) \underline{\nabla} H - \rho_i \left(\underline{\mathbf{g}}_i - \sum_{k=1}^v w_k \underline{\mathbf{g}}_k \right), \quad (3.121)
 \end{aligned}$$

where ρ_i is the mass density of species i . Taking the sum of the driving forces for all the species, with the use of the Gibbs-Duhem eq. (3.68), we see that eq. (3.121) satisfies the condition

$$\sum_{j=1}^v \underline{\mathbf{d}}_j = \underline{\mathbf{0}}, \quad (3.122)$$

which motivates the definition of this driving force. The term $CRT \underline{\mathbf{d}}_i$ has the physical interpretation of being the total force per unit volume trying to move species i relative to the mass-average velocity. Substitution back into the flux equation, using the relations given in (3.120) and (3.122), gives us

$$\underline{\mathbf{j}}_i = -RT \sum_{j=1}^v \frac{\alpha_{ij}}{x_i W_i} \underline{\mathbf{d}}_j. \quad (3.123)$$

The above expression relates the diffusion of species i as a function of the driving forces $\underline{\mathbf{d}}_j$ and the phenomenological coefficients α_{ij} , which was our desired result.

However, experimental data is usually given in terms of the multicomponent diffusivities D_{ij} , so it is more convenient to express eq. (3.123) in terms of these diffusivities. There are numerous definitions for multicomponent diffusivities in the literature, as in colloidal systems it is not possible to relate the fluxes $\underline{\mathbf{j}}_i$ and the driving forces $\underline{\mathbf{d}}_j$ simply in terms

of the binary coefficients \mathcal{D}_{12} . One common definition used is the zero-diagonal-diffusivity definition [16], which relates the flux and the driving forces as [15]

$$\underline{j}_i = \frac{C^2}{\rho} \sum_{j=1}^v W_i W_j D_{ij} \underline{d}_j . \quad (3.124)$$

Comparing the last two expressions we obtain

$$D_{ij} = -\frac{\rho RT}{C^2 W_i W_j} \left(\frac{\alpha_{ij}}{x_j W_j} + \frac{1}{x_i W_i} \sum_{\substack{k=1 \\ k \neq i}}^v \alpha_{ik} \right) , \quad (3.125)$$

or

$$\alpha_{ij} = \frac{C x_j W_j W_i}{\rho^2 RT} \left(-\rho W_j D_{ij} + \sum_{\substack{k=1 \\ k \neq i}}^v C x_k W_k^2 D_{ik} \right) . \quad (3.126)$$

Inserting these results back into (3.123), we obtain

$$\underline{j}_i = \frac{C^2}{\rho} \sum_{j=1}^v W_i W_j D_{ij} \underline{d}_j . \quad (3.127)$$

The coefficients D_{ij} must be such that α_{ij} are symmetric and that condition (3.119) is satisfied. For convenience, it is preferable to translate the conditions on α_{ij} into direct conditions on D_{ij} . In eq. (3.125), setting $j = i$, we obtain

$$\begin{aligned} D_{ii} &= -\frac{\rho RT}{C^2 W_i W_j} \left(\frac{\alpha_{ii}}{x_i W_i} + \frac{1}{x_i W_i} \sum_{\substack{k=1 \\ k \neq i}}^v \alpha_{ik} \right) \\ &= -\frac{\rho RT}{C^2 W_i W_j x_i W_i} (\alpha_{ii} - \alpha_{ii}) \\ &= 0 . \end{aligned} \quad (3.128)$$

We can also set $j = k$ and $j = h$ in eq. (3.125) and conclude that

$$\sum_{i=1}^v (W_i W_k D_{ik} - W_i W_h D_{ih}) = -\frac{\rho RT}{C^2} \sum_{i=1}^v \frac{\alpha_{ik}}{x_k W_k} - \frac{\alpha_{ih}}{x_h W_h}$$

$$\begin{aligned}
&= -\frac{\rho RT}{C^2} \left(\frac{1}{x_k W_k} - \frac{1}{x_h W_h} \right) \sum_{i=1}^v (\alpha_{ik} - \alpha_{ih}) \\
&= -\frac{\rho RT}{C^2} \left(\frac{1}{x_k W_k} - \frac{1}{x_h W_h} \right) (0 - 0) \\
&= 0.
\end{aligned} \tag{3.129}$$

At this point, we have expressed all the conditions on α_{ij} as conditions on D_{ij} and our derivation is complete.

3.4.2.1 Multicomponent diffusion summary

Expressions for the diffusive flux in a magnetic system were obtained for a multicomponent system. The diffusive flux of component i is given by

$$\underline{j}_i = \frac{C^2}{\rho} \sum_{j=1}^v W_i W_j D_{ij} \underline{d}_j, \tag{3.130}$$

where

$$\begin{aligned}
CRT \underline{d}_i = C_i W_i \sum_{\substack{j=1 \\ j \neq i}}^v \left(\frac{\partial \xi_i}{\partial x_j} \right)_{T,P,H,x_k} \underline{\nabla} x_j + (C_i \bar{V}_i - w_i) \underline{\nabla} p \\
- \mu_o C_i W_i \left(\bar{\vartheta}_i - \frac{M}{\rho} \right) \underline{\nabla} H - \rho_i \left(\underline{g}_i - \sum_{k=1}^v w_k \underline{g}_k \right).
\end{aligned} \tag{3.131}$$

These are the same expressions obtained in the literature [16, 17], except for the new magnetic term $-\mu_o C_i W_i \left(\bar{\vartheta}_i - \frac{M}{\rho} \right) \underline{\nabla} H$. The diffusion coefficients are subject to the

conditions

$$D_{ii} = 0 \tag{3.132}$$

and

$$\sum_{i=1}^v (W_i W_k D_{ik} - W_i W_h D_{ih}) = 0. \tag{3.133}$$

3.4.3 Application to binary system

For the binary system described in Section 3.4.1, using eqs. (3.130) - (3.133) and taking species 1 to be the nonmagnetic beads and species 2 to be the magnetic fluid, we obtain

$$\begin{aligned}
 \underline{j}_1 &= \frac{C^2}{\rho} W_1 W_2 D_{12} \underline{d}_2 \\
 &= -\frac{C^2}{\rho} W_1 W_2 D_{12} \underline{d}_1 \\
 &\equiv -\frac{C^2}{\rho} W_1 W_2 \mathcal{D}_{12} \underline{d}_1 .
 \end{aligned} \tag{3.134}$$

where \mathcal{D}_{12} is the binary diffusion coefficient of species 1 in fluid 2. Neglecting inertial effects (low Reynolds number or unidirectional flow) and viscous dissipation relative to magnetic and gravitational forces, a momentum balance gives us

$$\underline{\nabla} p \approx \rho \underline{g} + \mu_o M \underline{\nabla} H . \tag{3.135}$$

For an ideal system, we therefore have

$$CRT \underline{d}_1 = CRT \underline{\nabla} x_1 + (\phi_1 - w_1) (\rho \underline{g} + \mu_o M \underline{\nabla} H) + \mu_o C_1 W_1 \frac{M}{\rho} \underline{\nabla} H . \tag{3.136}$$

Substituting back into eq. (3.134) gives

$$\begin{aligned}
 \underline{j}_1 &= -\frac{C^2}{\rho} W_1 W_2 \mathcal{D}_{12} \left(\underline{\nabla} x_1 + (\phi_1 - w_1) \frac{(\rho \underline{g} + \mu_o M \underline{\nabla} H)}{CRT} + \frac{\mu_o x_1 W_1 M \underline{\nabla} H}{\rho RT} \right) \\
 &= -\mathcal{D}_{12} \rho \underline{\nabla} w_1 - \frac{\mathcal{D}_{12} C W_1 W_2}{\rho RT} [(\phi_1 - w_1) \rho \underline{g} + \phi_1 \mu_o M \underline{\nabla} H] ,
 \end{aligned} \tag{3.137}$$

which is the same expression obtained earlier, eq. (3.108). This can easily be extended to include a number of nonidealities such as electrostatic repulsion, volume exclusion, and magnetic interactions by incorporating these as excess chemical potentials.

In the absence of magnetic and buoyancy effects, we see that eq. (3.137) reduces to Fick's law for binary diffusion, which is one of the main motivations behind definition (3.124).

3.4.3.1 Comparison with other approaches

The results obtained in the previous sections can also be derived using other methods, such as force balances and multicomponent diffusion of nonmagnetic systems. When using these methods, one needs to be careful when accounting for the force of magnetic origin on the nonmagnetic particles, as the force arises from magnetic pressure gradients within the fluid and not directly from the applied magnetic field. Also, the coupling between nonidealities and magnetic fields is not as straight-forward as in the approach introduced in this section, since magnetic effects are not captured in the chemical potentials of nonmagnetic systems. Nevertheless, in the ideal limit, one should be able to obtain the same expression for the diffusive flux of a nonmagnetic species in a magnetic fluid continuum (i.e., eq. (3.137)) if the magnetic forces are accounted for properly.

3.4.3.1.1 Forced diffusion using Stokes migration velocity

In this approach, we balance a "diffusion force" with the drag, gravitational, and force of magnetic origin acting on a nonmagnetic bead. A similar analysis can be found in a previous work by the author of this thesis [18]. The balance is written as

$$-W_i \underline{\nabla}_T \xi - 6\pi\eta a_1 (\underline{v}_1 - \underline{v}^*) + \rho_1 V_1 \underline{g} - \mu_o V_1 M \underline{\nabla} H = 0, \quad (3.138)$$

where \underline{v}^* is the molar-average velocity of the solution. Here the magnetic forces are treated as external forces, meaning that the chemical potential of species 1 does not depend on the magnetic field. For an ideal system, this reduces to

$$-\frac{kT}{x_1} \underline{\nabla}_{x_1} - V_1 \underline{\nabla} p - 6\pi\eta a_1 (\underline{v}_1 - \underline{v}^*) + \rho_1 V_1 \underline{g} - \mu_o V_1 M \underline{\nabla} H = 0, \quad (3.139)$$

where the pressure gradient now does not depend on the magnetic fields and is thus given by

$$\underline{\nabla} p \approx \rho \underline{g}. \quad (3.140)$$

The force-balance can therefore be rearranged to give

$$-\frac{kT}{x_1} \underline{\nabla} x_1 - \frac{\rho \underline{g} (\phi_1 - w_1)}{N_a C_1} - 6\pi\eta a_1 (\underline{v}_1 - \underline{v}^*) - \frac{\mu_o v_1 M \underline{\nabla} H}{N_a} = 0, \quad (3.141)$$

where N_a is Avogadro's number.

Solving for the quantity $(\underline{v}_1 - \underline{v}^*)$ gives us

$$\underline{v}_1 - \underline{v}^* = -\frac{kT}{6\pi\eta a_1} \left(\frac{\underline{\nabla} x_1}{x_1} + \frac{\rho \underline{g}}{RT C_1} + \frac{\mu_o v_1 M \underline{\nabla} H}{RT} \right). \quad (3.142)$$

Using the definition of the molar flux relative to the molar-average velocity

$$\underline{J}_1^* \equiv C_1 (\underline{v}_1 - \underline{v}^*) \quad (3.143)$$

and the Stokes-Einstein relationship for the diffusion coefficient

$$\mathcal{D}_{12} = \frac{kT}{6\pi\eta a_1}, \quad (3.144)$$

we obtain

$$\underline{J}_1^* = -C \mathcal{D}_{12} \left(\underline{\nabla} x_1 + \frac{\rho \underline{g} (\phi_1 - w_1)}{RT} + \frac{\mu_o \phi_1 M \underline{\nabla} H}{RT} \right). \quad (3.145)$$

Finally, using the binary mixture relationship

$$\underline{j}_1 = \frac{W_1 W_2 C}{\rho} \underline{J}_1^*, \quad (3.146)$$

we obtain

$$\underline{j}_1 = -\mathcal{D}_{12} \rho \underline{\nabla} w_1 - \frac{\mathcal{D}_{12} C W_1 W_2}{\rho RT} \left[(\phi_1 - w_1) \rho \underline{g} + \phi_1 \mu_o M \underline{\nabla} H \right], \quad (3.147)$$

which is the result obtained using the irreversible thermodynamic approach.

The above expression directly links the microphysics approach performed in Section 3.2 to the thermodynamic analysis performed in Section 3.3. One thing to notice is that by neglecting the magnetic field distortions in the microphysics description, we obtain the same macroscopic results for ideal systems. This supports our earlier claim that distortions in the magnetic fields at the microscale level must be introduced as excess chemical potentials at the macroscopic level.

3.4.3.1.2 Forced diffusion using magnetic fluid force density

The same result can be obtained by using a magnetic force density on the ferrofluid and using the well-known generalized multicomponent relations for nonmagnetic systems. Neglecting the term containing the gradient in H in eq. (3.131)

(which is the only new term introduced for magnetic systems), setting $\underline{g}_2 = \frac{\mu_0}{\rho_2} M_2 \underline{\nabla} H$,

and $\underline{\nabla} p = \rho \underline{g} + \mu_o M \underline{\nabla} H$ we obtain

$$\begin{aligned} CRT \underline{d}_1 &= CRT \underline{\nabla} x_1 + (\phi_1 - w_1) (\rho \underline{g} + \mu_o M \underline{\nabla} H) + \mu_o w_1 \rho w_2 \frac{M_2}{\rho_2} \underline{\nabla} H \\ &= CRT \underline{\nabla} x_1 + (\phi_1 - w_1) \rho \underline{g} + \mu_o \phi_1 M \underline{\nabla} H, \end{aligned} \quad (3.148)$$

which gives

$$\begin{aligned} \underline{j}_1 &= -\frac{C^2}{\rho} W_1 W_2 \mathcal{D}_{12} \left(\underline{\nabla} x_1 + \frac{(\phi_1 - w_1) \rho \underline{g}}{CRT} + \frac{\mu_o \phi_1 M \underline{\nabla} H}{CRT} \right) \\ &= -\mathcal{D}_{12} \rho \underline{\nabla} w_1 - \frac{\mathcal{D}_{12} C W_1 W_2}{\rho RT} [(\phi_1 - w_1) \rho \underline{g} + \phi_1 \mu_o M \underline{\nabla} H]. \end{aligned} \quad (3.149)$$

This is, as expected, the same expression obtained earlier. However, as before, it cannot be readily extended to include nonidealities in the chemical potential dependence on magnetic fields. It is also important to use the correct pressure corresponding to the force density \underline{g}_2 . Neglecting the magnetic pressure gradient would yield incorrect results if the nonmagnetic particles are not neutrally buoyant. It is also important not to double count and also introduce a force density \underline{g}_1 on the nonmagnetic particles, as was done by Fateen [19] when modeling this same binary system. The force on species 1 is an internal force resulting from a pressure gradient, not an external force.

3.4.3.1.3 Forced diffusion using force density on nonmagnetic particles

Although perhaps less intuitive, we can treat the magnetic fluid continuum as having zero magnetization and the nonmagnetic particles as having a negative

magnetization, equal in magnitude to the magnetization of the fluid. The actual magnetization of the mixture is given by

$$M = \phi_2 M_f, \quad (3.150)$$

where M_f is the magnetization of the ferrofluid continuum (water plus magnetic nanoparticles). Therefore, we can treat species 2 as having no magnetization and species 1 as having a magnetization

$$M_1 = -M_f = -\frac{M}{\phi_2}. \quad (3.151)$$

The resulting driving force in terms of this fictitious magnetization would be

$$\begin{aligned} CRT \underline{d}_1 &= CRT \underline{\nabla} x_1 + (\phi_1 - w_1) (\rho \underline{g} + \mu_o \phi_1 M_1 \underline{\nabla} H) - \mu_o w_1 \rho w_2 \frac{M_1}{\rho_1} \underline{\nabla} H \\ &= CRT \underline{\nabla} x_1 + (\phi_1 - w_1) \rho \underline{g} - \mu_o \phi_1 \phi_2 M_1 \underline{\nabla} H. \end{aligned} \quad (3.152)$$

Now substituting for M_1 by the actual magnetization M gives us

$$CRT \underline{d}_1 = CRT \underline{\nabla} x_1 + (\phi_1 - w_1) \rho \underline{g} + \mu_o \phi_1 M \underline{\nabla} H, \quad (3.153)$$

which gives

$$\begin{aligned} \underline{j}_1 &= -\frac{C^2}{\rho} W_1 W_2 \mathcal{D}_{12} \left(\underline{\nabla} x_1 + \frac{(\phi_1 - w_1) \rho \underline{g}}{CRT} + \frac{\mu_o \phi_1 M \underline{\nabla} H}{CRT} \right) \\ &= -\mathcal{D}_{12} \rho \underline{\nabla} w_1 - \frac{\mathcal{D}_{12} C W_1 W_2}{\rho RT} [(\phi_1 - w_1) \rho \underline{g} + \phi_1 \mu_o M \underline{\nabla} H]. \end{aligned} \quad (3.154)$$

Again, we obtain the expected result, which has the same limitations as the previous approach. This is probably the least intuitive approach and the one that can lead to the most errors because of the use of a fictitious negative magnetization.

3.4.4 Binary diffusion of magnetic species

Starting from eq. (3.134), the diffusion of magnetic species 1 in a nonmagnetic continuum 2 is given by

$$\underline{j}_1 = -\frac{C^2}{\rho} W_1 W_2 \mathcal{D}_{12} \underline{d}_1. \quad (3.155)$$

Neglecting inertial effects (low Reynolds number or unidirectional flow) and viscous dissipation relative to magnetic and gravitational forces, a momentum balance gives us

$$\underline{\nabla} p \approx \rho \underline{g} + \mu_o M \underline{\nabla} H. \quad (3.156)$$

For an ideal system, we therefore have

$$CRT \underline{d}_1 = CRT \underline{\nabla} x_1 + (\phi_1 - w_1) (\rho \underline{g} + \mu_o M \underline{\nabla} H) - \mu_o C_1 W_1 \left(\frac{M_1}{\rho_1} - \frac{M}{\rho} \right) \underline{\nabla} H. \quad (3.157)$$

Eq. (3.157) can be simplified to give

$$CRT \underline{d}_1 = CRT \underline{\nabla} x_1 + (\phi_1 - w_1) \rho \underline{g} - \mu_o \phi_1 (M_1 - M) \underline{\nabla} H. \quad (3.158)$$

Since $M = \phi_1 M_1$, the above expression can be written in terms of the magnetization of species 1 as

$$CRT \underline{d}_1 = CRT \underline{\nabla} x_1 + (\phi_1 - w_1) \rho \underline{g} - \mu_o \phi_1 (1 - \phi_1) M_1 \underline{\nabla} H. \quad (3.159)$$

Substituting back into eq. (3.155) gives

$$\underline{j}_1 = -\mathcal{D}_{12} \rho \underline{\nabla} w_1 + \frac{\mathcal{D}_{12} C W_1 W_2}{\rho R T} \left[(w_1 - \phi_1) \rho \underline{g} + \phi_1 (1 - \phi_1) \mu_o M_1 \underline{\nabla} H \right], \quad (3.160)$$

Eq. (3.160) is very similar in form to the flux of a nonmagnetic species in a magnetic fluid, but with the opposite sign on the forced-diffusion term.

3.5 Summary

In this chapter, we introduced the governing equations for the MQS system of interest. The analytical solution for the magnetic field generated by permanent magnets, obtained using this set of equations, was then presented.

To understand the origin of the magnetophoresis of nonmagnetic species immersed in magnetic fluids, the Navier-Stokes equations for magnetic fluids were used to derive the force of magnetic origin acting on these nonmagnetic species. The resulting force balance was used to derive an expression for the flux of nonmagnetic particles

immersed in magnetic nanofluids. Using a more generalized thermodynamic approach, the equations governing the diffusive flux of a multicomponent magnetic system were derived. These equations were applied to the simple case of binary diffusion to assure that they reduce to the expected results.

There have been various publications concerning multicomponent diffusion in different applications. A good summary is given by Bird [20]. To our knowledge, there has only been one previous attempt in the literature to derive multicomponent diffusion expressions, that of Blums et al. [21]. In their work, they derive expressions for the driving forces present in electromagnetic systems, although these are never expressed in the form of eq. (3.131) or related to the multicomponent fluxes in a form similar to eq. (3.130). Also, since the form of the Gibbs equation used in their work is only valid for constant-density systems, their expression for the magnetic driving force is incomplete. The total moment they use, mM , would only be a total moment if the magnetization were given on a per-mass basis, which it is not by definition. Their results are only valid for constant density systems, where

$$\bar{\vartheta}_i \equiv \left(\frac{\partial MV}{\partial m_i} \right)_{T,p,H} = V \left(\frac{\partial M}{\partial m_i} \right)_{T,p,H} = V \bar{M} . \quad (3.161)$$

In the above expression, \bar{M} is the specific magnetization used in their work.

3.6 Bibliography

1. Rosensweig, R.E. Continuum equations for magnetic and dielectric fluids with internal rotations. *Journal of Chemical Physics*, 121(3): 1228-1242, 2004.
2. Melcher, J.R. *Continuum Electromechanics*. MIT Press, Cambridge, 1981.
3. Schrefl, T., Finite elements in numerical micromagnetics Part I: granular hard magnets. *Journal of Magnetism and Magnetic Materials*, 207(1-3): 45-65, 1999.
4. Guo, X.F., Yang, Y., and Zheng, X.J. Analytic expression of magnetic field distribution of rectangular permanent magnets. *Applied Mathematics and Mechanics-English Edition*, 25(3): 297-306, 2004.

5. Park, E.S. *Microfabricated Focusing Systems for the Separation of Submicrometer Particles*. M.S. thesis, Massachusetts Institute of Technology, 2004.
6. Rosensweig, R.E. *Ferrohydrodynamics*. Cambridge University Press, New York, 1985.
7. Deen, W.M. *Analysis of Transport Phenomena*. Oxford University Press, New York, 1998.
8. Berkovsky, B.M., Medvedev, V.F., and Krakov, M.S. *Magnetic Fluids: Engineering Applications*. Oxford University Press, New York, 1993.
9. Rosensweig, R.E. Thermodynamics of electromagnetism. Chapter 13 in *Thermodynamics: an Advanced Textbook for Chemical Engineers*, by Astarita, G. Plenum Press, New York, 1989.
10. Tester, J.W. and Modell, M. *Thermodynamics and Its Applications*. Prentice Hall, New Jersey, 1997.
11. Stratton, J.A. *Electromagnetic Theory*. McGraw-Hill, New York, 1941.
12. Lightfoot, E.N. *Transport Phenomena and Living Systems*. John Wiley and Sons, New York, 1974.
13. Hirschfelder, J.O., Curtiss, C.F. and Bird, R.B. *Molecular Theory of Gases and Liquids*. John Wiley & Sons, New York, 1964.
14. De Groot, S.R. and Mazur, P. *Non-Equilibrium Thermodynamics*. Dover Publications, New York, 1984.
15. Curtiss, C.F. and Hirschfelder, J.O. Transport properties of multicomponent gas mixtures. *Journal of Chemical Physics*, 17: 550-555, 1949.
16. Curtiss, C.F. and Bird, R.B. Multicomponent Diffusion. *Ind. Eng. Chem. Res.*, 38: 2515-2522, 1999.
17. Bird, R.B., Stewart, N.E. and Lightfoot, E.N.. *Transport Phenomena*. John Wiley and Sons, New York, 1960.
18. Gonzalez, L.A., et al. Magnetophoresis of Nonmagnetic, Submicrometer Particles in Magnetic Fluids. *MEBCS Proceedings of the Fourth SMA Symposium*, Singapore, 2004.
19. Fateen, S. *Magnetophoretic Focusing of Submicron Particles Dispersed in a Polymer-Based Magnetic Fluid*. Ph.D. thesis, Massachusetts Institute of Technology, 2002.

20. Bird, R.B. Five decades of transport phenomena. *AIChE Journal*, 50(2): 273-287, 2004.
21. Blums, E., Mikhailov, Yu. A., and Ozols, R. *Heat and Mass Transfer in MHD Flows*. World Scientific Publ. Co., Singapore, 1987.
22. Furlani, E.P. *Permanent Magnet and Electromechanical Devices: Materials, Analysis, and Applications*. Academic Press, San Diego, 2001.
23. Obtained from G2 Consulting: www.consult-g2.com on Course – Chapter 1.
24. Heise, C. and Kock, M. Field Calculations for Permanent Magnets used for Glow Discharges. *Contrib. Plasma Phys.*, 35(6): 551-561, 1995.
25. Furlani, E.P. Analytical model of magnetic nanoparticle transport and capture in the microvasculature. *Physical Review E*, 75: 061919-1: 061919-10, 2006.

Chapter 4

4. Magnetophoretic Focusing

In order to understand how nonmagnetic species can be trapped and separated based on size in a magnetic fluid continuum, it is necessary to first understand how they focus and interact with the fluid in the absence of flow. In a quiescent fluid, we would expect the nonmagnetic species to migrate in the direction of decreasing magnetic-field intensity until they reach a region of zero magnetophoretic force. They will continue to concentrate, or focus, in such regions until diffusion and particle-particle interactions prevent further focusing. This behavior was studied experimentally using fluorescence imaging and numerically using continuum modeling. A previous attempt at understanding the focusing of nonmagnetic species in magnetic fluids can be found in Fateen [1], who was able to model his results qualitatively. In this work, the goal is to achieve good qualitative and quantitative agreement between theory and experiments for the focusing of nonmagnetic particles immersed in magnetic nanofluids.

4.1 Focusing experiments

The focusing of nonmagnetic, submicron particles in a magnetic nanofluid was studied experimentally by monitoring the concentration profiles of fluorescently tagged latex beads. Laser-induced fluorescence imaging (LIFI) was used to measure the temporal and spatial variations in their concentration profiles as they migrated within a capillary tube under nonuniform magnetic fields. Concentration profiles were obtained from the intensity of the fluorescence emitted by the latex beads. Among other things, we studied the effect of different magnetic-field profiles, magnetic fluid concentrations, and particle size on the resulting concentration profiles.

4.1.1 Materials

Fluorescent polystyrene beads (Spherotech, Inc, Libertyville, IL) were used as the nonmagnetic species in the focusing experiments. These beads were synthesized by the manufacturer using copolymerization of polystyrene and a fluorescent dye. The magnetic nanofluid used to induce focusing was the 16/0 ferrofluid synthesized according to Moeser [2]. Deionized water was used to dilute the concentration of the mixture to the desired values. NaCl (Mallinckrodt Baker, Inc, Phillipsburg, NJ) was used to control the Debye length in the mixture and minimize long-range electrostatic repulsion between the different species. Sucrose ($C_{12}H_{22}O_{11}$, Mallinckrodt Baker, Inc, Phillipsburg, NJ) was used to increase the specific gravity (SG) of the mixture to 1.05, matching that of the latex beads. This prevents gravitational settling of the latex beads, which was significant enough in the absence of sucrose to affect our fluorescence measurements.

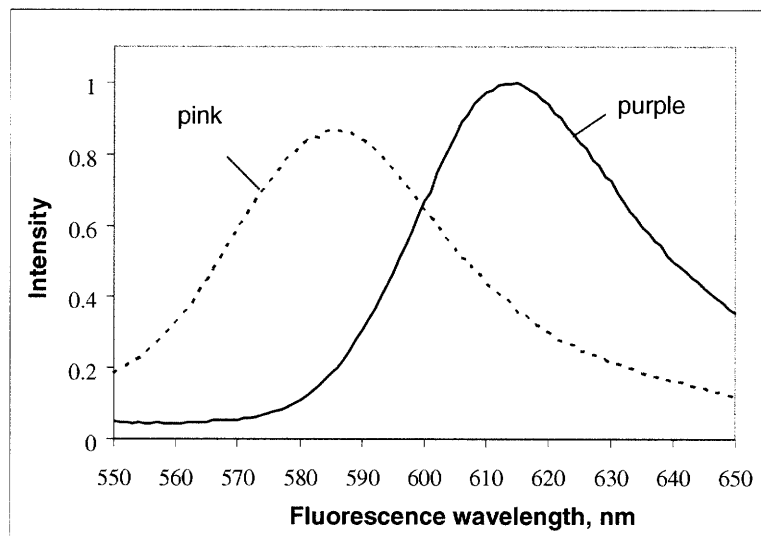


Figure 4-1: Fluorescence spectra of “pink” and “purple” latex beads

The fluorescence spectra for the latex beads were provided by the manufacturers and verified in-house using a spectro-fluoremeter (Photon Technology International, Lawrenceville, NJ). Figure 4-1 shows the normalized fluorescence spectra for the two types of fluorescent dyes (copolymerized with polystyrene) used in our experiments,

called “purple” and “pink” by the manufacturer. The fluorescence spectra shown correspond to an excitation wavelength of 514.5 nm, which is the wavelength used in our focusing experiments.

The smaller and larger particles used in this study were advertised to have diameters of 510 and 910 nm, respectively, by the manufacturer. Images obtained using Scanning Electron Microscopy (SEM), taken with a JEOL JSM-5910 SEM instrument, show that this value is accurate for the larger beads, but considerably off for the smaller beads. The images show average diameters of 437 and 900 nm for the small and large particles, respectively. Dynamic Light scattering (DLS) measurements were consistent with the numbers obtained from the SEM images, giving average values of 435 and 910 nm, respectively. SEM images for the two sizes of latex beads used are shown in Figure 4-2.

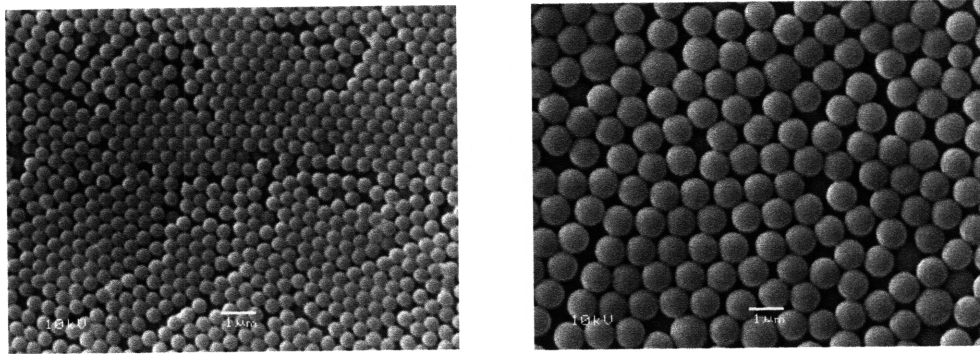


Figure 4-2: SEM images of small and large fluorescently tagged latex-beads.

When suspended in water, each polystyrene bead attains a negative surface charge due to sulfate groups scattered around its surface. These sulfate groups are present due to trace amounts of unreacted initiators left behind in the polymerization reaction used to make the latex beads. Due to the randomness of the resulting charge distribution, there can be regions on the bead surface that contain no charge, which at small Debye lengths could allow smaller particles to bind to that region even if the latter are negatively charged. Attachment of magnetic nanoparticles to the latex surfaces seemed to occur at

high salt concentrations based on the obtained concentration profiles. This was most likely due to this mechanism.

To overcome this binding, sodium dodecylsulfate (SDS) surfactants (Sigma-Aldrich, Saint Louis, MO) were added to our mixtures in order to add negative charge to the latex particle surfaces. The zeta potentials of the different colloidal species were then measured using a ZetaPALS device (Brookhaven Instruments Corp., Holtsville, NY). As expected, the potentials obtained were larger in magnitude than those reported by Fateen [1] and Moeser [3] due to the adsorption of SDS to the particle surfaces. The different zeta-potential values are listed in Table 4.1.

Table 4.1: Zeta potentials for the colloidal species used in the focusing experiments.

Species	Zeta Potential – no SDS	Zeta Potential with SDS	Previously Published Values
magnetic nanoparticles	-20 mV	-25 mV	-20 mV
435 nm latex beads	-40 mV	-60 mV	-42 mV
910 nm latex beads	-45 mV	-65 mV	NA

4.1.2 Experimental Setup

A schematic of the experimental setup used in this work is shown in Figure 4-3. At $t = 0$, a square capillary tube (Fiber Optic Center, New Bedford, MA) containing a mixture of magnetic fluid and nonmagnetic, fluorescent beads was placed between two opposing pairs of permanent magnets. Square capillaries were used instead of round ones due to their superior optical properties. The magnetic field was generated by Neodymium Iron Boron (NdFeB) magnets, obtained from MMC Magnetics and discussed in Chapter 2. Each magnet had a length of 20 mm, a height of 10 mm, a thickness of 6.35 mm, and was magnetized along its height. The magnet pairs were held

in place 10 mm apart along the length of the capillary and 6 to 7 mm away from the capillary tube. The 100 mm-long capillary tubes had an inner dimension of 0.4 mm and an outer dimension of 0.8 mm.

The nonmagnetic aluminum fixture used to hold the magnets in place is depicted in Figure 4-4. It was constructed at the MIT Central Machine shop and anodized with aluminum oxide to minimize laser reflections from its surface. In the configuration shown in Figure 4-3, the four magnets attract each other into position and their friction with the walls was enough to hold them in place (i.e., keep them from falling due to their own weight) during the experiments. Spacing between the magnets was varied by adding 1 mm aluminum spacers between the magnets and the fixture. The rectangular-shaped opening in the middle of the fixture allowed for fluorescence measurements in the region where the fluorescent particles focused.

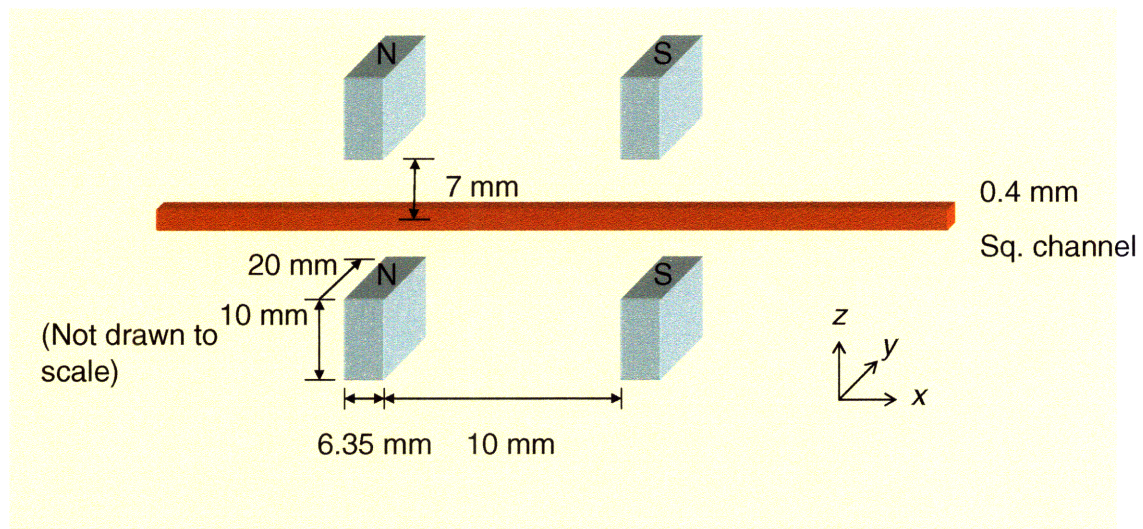


Figure 4-3: Schematic of the setup used for focusing experiments. The origin is at the radial center of the capillary tube.

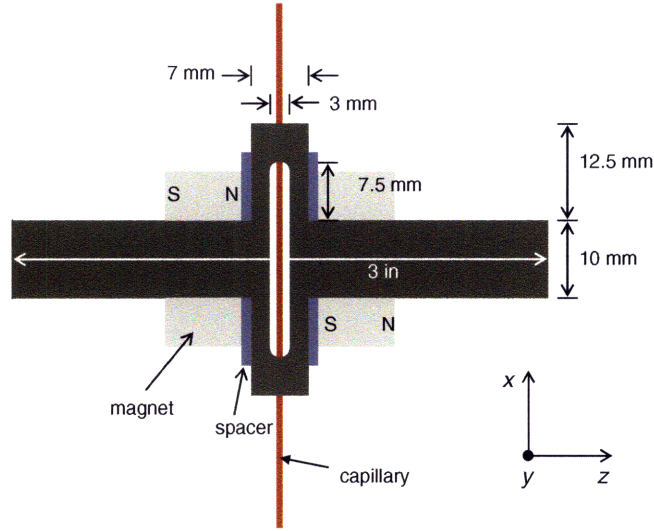


Figure 4-4: Schematic of the aluminum fixture used to keep the magnets in position and allow for fluorescence imaging from overhead.

4.1.3 Magnetic and force fields

The magnetic field profile generated by the permanent magnets was obtained analytically using the analysis presented in Section 2.1. Since a dilute magnetic nanofluid was used in this work, magnetic-field distortions due to the presence of the magnetic fluid were negligible. The magnetic field was used to calculate the magnetization profile of the fluid at $t = 0$ (in the absence of magnetic nanofluid concentration gradients) using the Langevin functions discussed in Chapter 2. The magnetic-field intensity profile and the x -component of the resulting force-density $\underline{f}_m = \mu_0 M_f \underline{\nabla} H$ at $t = 0$ are shown in Figure 4-5.

As seen in the figure, the force density on the nonmagnetic beads is negative between $x \approx -8$ mm and $x = 0$. The force on the nonmagnetic particles p is

$$\underline{F}_p = -\underline{f}_f V_p, \quad (4.1)$$

meaning that the latex beads are pushed in the $+x$ direction in this region. In the region between $x = 0$ and $x \approx 8$ mm, the beads are pushed in the $-x$ direction. As a result, the nonmagnetic beads will focus over time near the point $x = 0$.

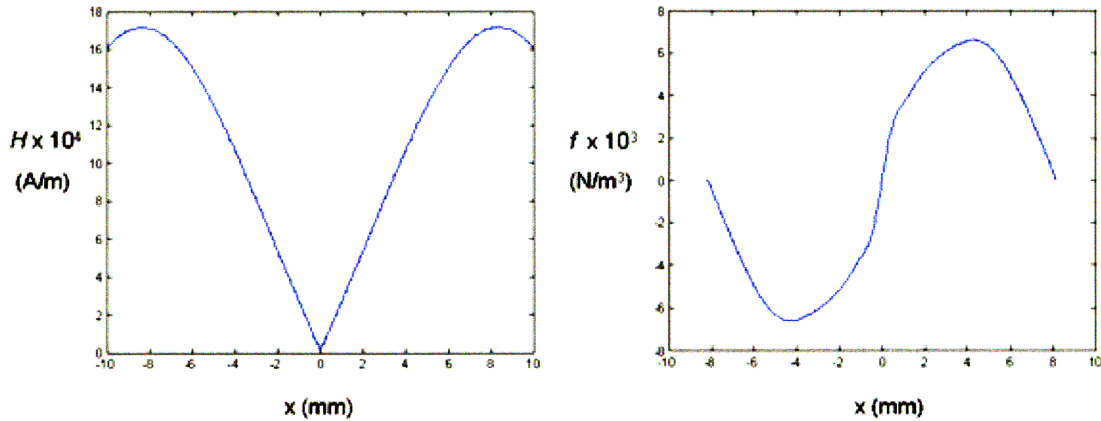


Figure 4-5: Magnetic field and force-density profiles for the configuration depicted in Figure 4-3.

Since the magnetic field profile is known analytically, we were also able to calculate the y and z force densities over the cross-section of the tube. The y and z forces are zero at $y = 0$ and $z = 0$, respectively, and would cancel out if averaged across the entire cross-section of the capillary tube, but do not cancel out if averaged over half of the tube cross-section. Figure 4-6 shows the cross-section averaged (half of the cross-section) y and z forces as a function of x . As seen in the figure, the y force is negligible with respect to the x force everywhere, but the z force is of the same order of magnitude as the x force near the focusing region. This leads to focusing in the z direction to go with the expected focusing in the x direction. Due to the small cross-section of the tube, obtaining high resolution on the y and z force densities shown in the figure would be difficult to do using numerically obtained magnetic field. The focusing simulation results presented later on in this chapter are two-dimensional simulations in the x - z plane, with the results averaged across the thickness of the capillary tube (i.e., across all z values).

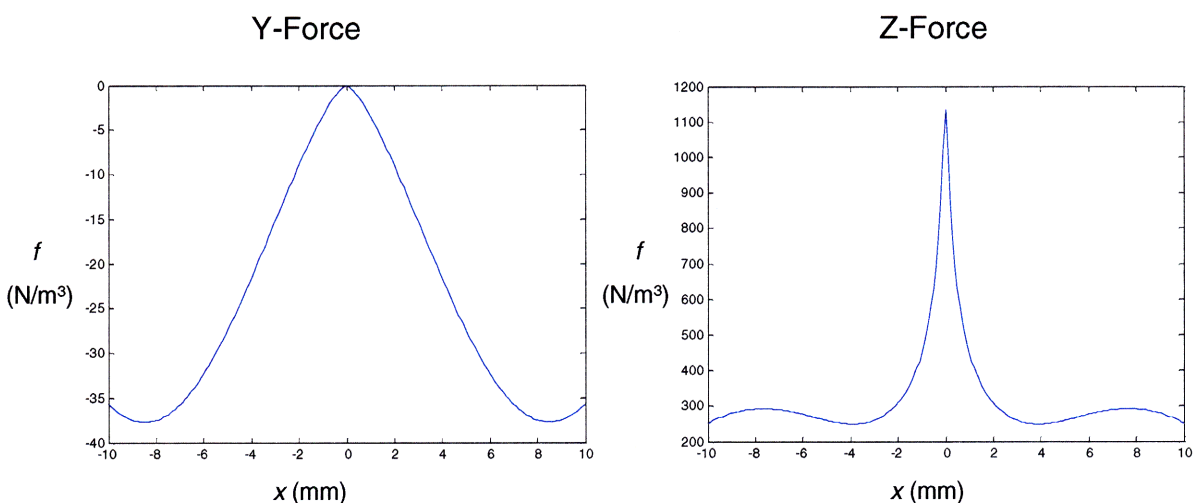


Figure 4-6: Force densities in the y and z directions.

4.1.4 Sample preparation

The samples were prepared in 2 mL plastic vials, with the typical sample volume being 200 μL . Some common amounts for each of the components used are listed in Table 4.2. The volume percents given for the magnetic fluid correspond to the volume percent of magnetite (i.e., without polymer shells) in the mixture. After preparation, about 15 μL of the mixture was loaded into a capillary tube using capillary action. The ends of the tubes were sealed with glue to prevent flow.

Table 4.2: Typical sample volumes and concentrations

Component	Amount (μL)	Concentration in Mixture
2.3 wt % magnetic fluid	45	0.1 vol % magnetite
1 wt % latex beads	20	0.1 vol % beads
1.28 SG ¹ sugar solution	31	15.5 vol % mixture
0.2 M salt solution	4.75	4.75 mM NaCL
3.5 mM SDS solution	14.25	0.25 mM SDS
DI water	85	-
total	200	-

¹ SG stands for specific gravity

4.1.5 Fluorescence imaging

The concentration profiles of the latex beads were monitored using LIFI, as illustrated schematically in Figure 4-7. Each of the fluorescent species used has a given excitation curve, which corresponds to the wavelengths at which fluorescence can be induced, and an emission curve, which corresponds to the wavelengths at which the species emits fluorescence. A Coherent I-90 Argon-Ion laser (Coherent, Inc, Santa Clara, CA) was used to excite the fluorescent latex particles at 514.5 nm, which lies somewhere near the peak of their excitation curve. An optical filter was then used to filter out the laser light and only pass wavelengths corresponding to latex bead fluorescence. The fluorescence-intensity distribution was then converted into concentration profiles using calibration techniques discussed later in Section 4.2.

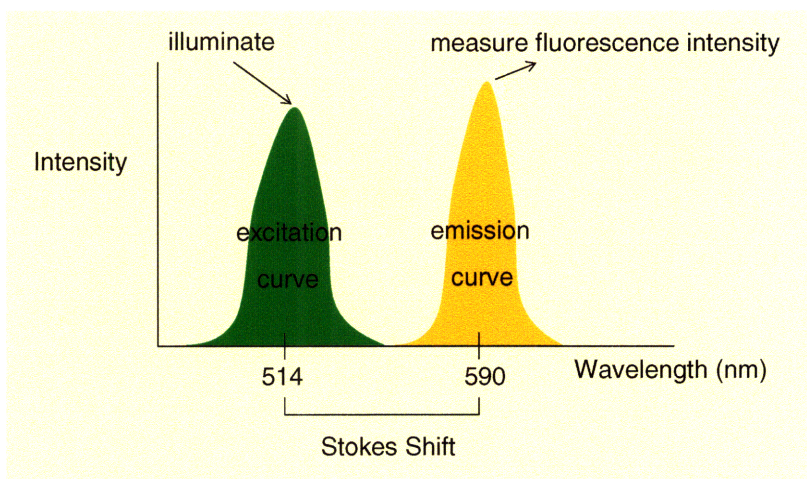


Figure 4-7: Schematic illustrating the principle behind Laser-Induced Fluorescence Imaging.

4.1.6 Data acquisition

The setup used to monitor the concentration profile of the fluorescent beads is depicted in Figure 4-8, with a photograph of the actual setup shown at the bottom of the figure. The 514.5 nm wavelength beam exiting the laser was converted into a “sheet” of light by expanding it in one direction using a cylindrical lens. This sheet of light was used to excite the sample contained in a 0.4 mm ID square capillary tube. The fluorescence-intensity profile was optically filtered out using a 10 nm bandpass optical filter (Newport Corporation – Oriel Products, Stratford, CT) and captured by a charge coupled device (CCD) digital camera (Orca ER C4742-95, Hamamatsu Corporation, Japan) outfitted with a macro-photography lens (Micro-Nikkor 105/2.8, Nikon Corporation, Japan). The fluorescence intensities captured by the camera were stored in a computer (Computer 2 in the diagram).

The laser used in this work is a continuous laser, which could photobleach the fluorescent particles unless the exposure times were kept at a minimum. A high-speed shutter (Uniblitz, Vincent Associates, Rochester, NY) controlled by a triggering computer (Computer 1 in the diagram) was used to allow laser light to shine on the sample only when a measurement was being taken. Computer 1 was programmed using LabVIEW to trigger the shutter and the CCD camera simultaneously, ensuring that the camera captured the fluorescence-intensity profile as the sample was being illuminated. This procedure kept photobleaching effects to a minimum in our experiments. Computer 2 was programmed using LabVIEW to record the images captured by the CCD camera.

In the photograph included in the figure, the 1” mirrors were used to guide the laser beam from the laser to the sample. The beam stopper captured the laser beam reflected off the shutter when the shutter was closed. The bottom 2” mirror was used to steer the expanded beam toward the sample, while the top 2” mirror reflected the fluorescence from the sample toward the CCD camera. The latter mirrors were on different working planes and did not interact with each other. CCD Camera 2, Computer 3, and the Beam Splitter were not used in the focusing experiments discussed in this chapter; their use is discussed in Chapter 5. The laser power used in the focusing experiments was about 500 mW, with typical exposures being 250 ms every 5 minutes.

The average experiment lasted 80 minutes after the sample was placed between the permanent-magnet pairs.

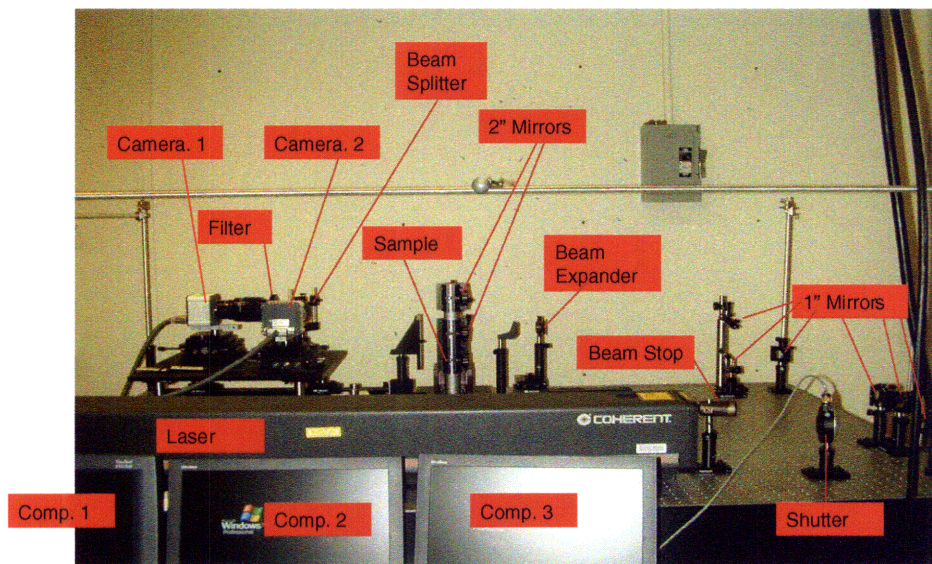
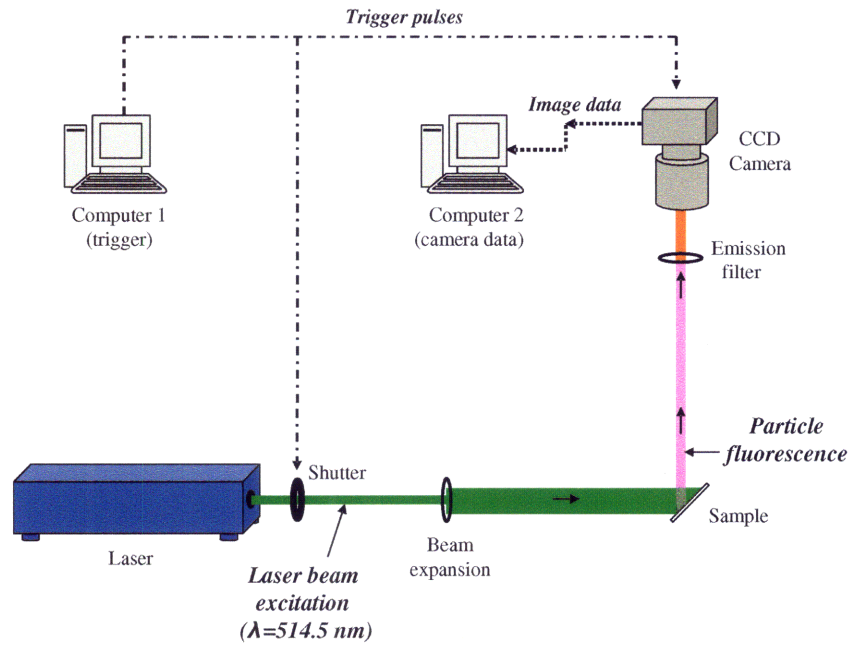


Figure 4-8: Data acquisition setup. The top image is a schematic for the actual setup shown in the bottom image.

4.2 Data processing

Before the start of each experiment, a background image was taken at the normal operating conditions (i.e., laser power, exposure time, etc.). The sample used for this image contained water and magnetic fluid, but did not contain the fluorescent latex beads. This image was later used to subtract background noise from the experimental data.

Once the actual sample was loaded and placed in the magnetic field, the initial image taken at $t = 0$ (minus the background) was used as the reference image for each experiment. Since there were no concentration gradients present at the beginning of each experiments, the initial image (minus the background) served as a measurement of the laser intensity profile. Typical background and reference images are given in Figure 4-9, where the axes correspond to actual pixels in the CCD camera and the colorbar is a legend for the light intensity captured by each pixel. The capillary layed horizontally in both images between pixels 15 and 27. In most cases, subtracting the background from an image was equivalent to subtracting 200 from the intensity of each pixel. The horizontal and vertical pixels are in the x and z axis, respectively, as defined in Figure 4-3.

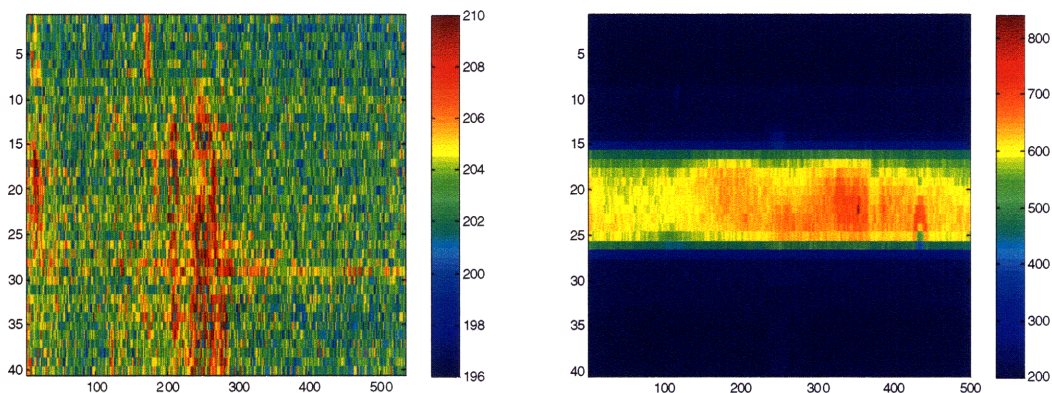


Figure 4-9: Background image (left) and reference image (right) obtained for a typical focusing experiment.

After subtracting off the background, each image was divided by the reference image in order to give normalized fluorescence-intensity profiles, which were independent of the laser intensity distribution. The division was done on a pixel-by-pixel basis and then averaged across the cross-section of the capillary tube. A two-dimensional, normalized fluorescence-intensity plot is given in Figure 4-10 for a typical focusing experiment. The figure also gives the corresponding cross-section averaged fluorescence-intensity profile, with the point $x = 0$ corresponding to the mid-point between the magnet pairs. All of the image-processing in this work was done using Matlab.

One thing to notice in these figures is that there are more data available from the left side of the focusing region than from the right. This is an artifact of the data-acquisition setup, where the laser light illuminates the sample at an angle and part of the sheet of light was blocked before it reached the sample. Since the data appeared to be symmetric about the point $x = 0$, the setup was left unmodified.

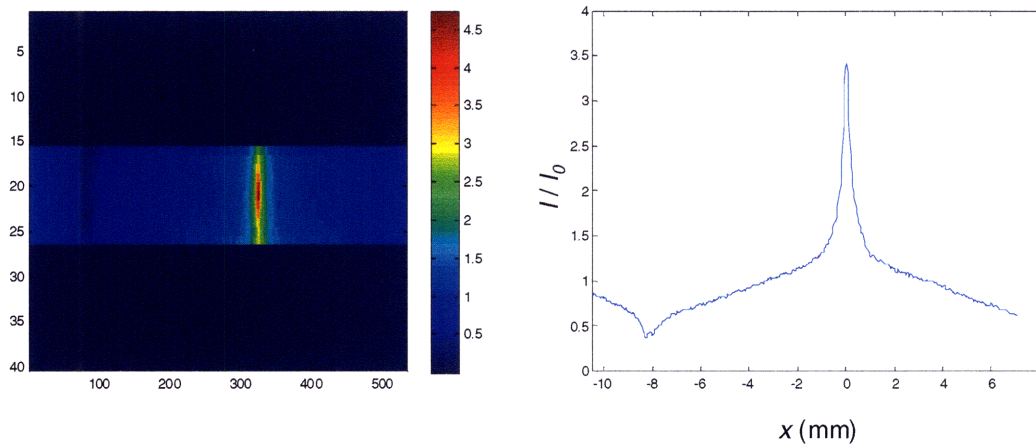


Figure 4-10: Normalized fluorescence-intensity profile at a given time t (left) and its cross-section average (right).

4.2.1 Fluorescence calibration

In order to convert from fluorescence intensities into concentration profiles for the latex beads, calibration curves between latex-bead concentration and fluorescence intensity were prepared. The total fluorescence was measured for samples at various concentrations of fluorescent beads for a fixed magnetic fluid concentration (0.1 vol % magnetite). The same type of capillaries used for the focusing experiments were used in these calibration experiments.

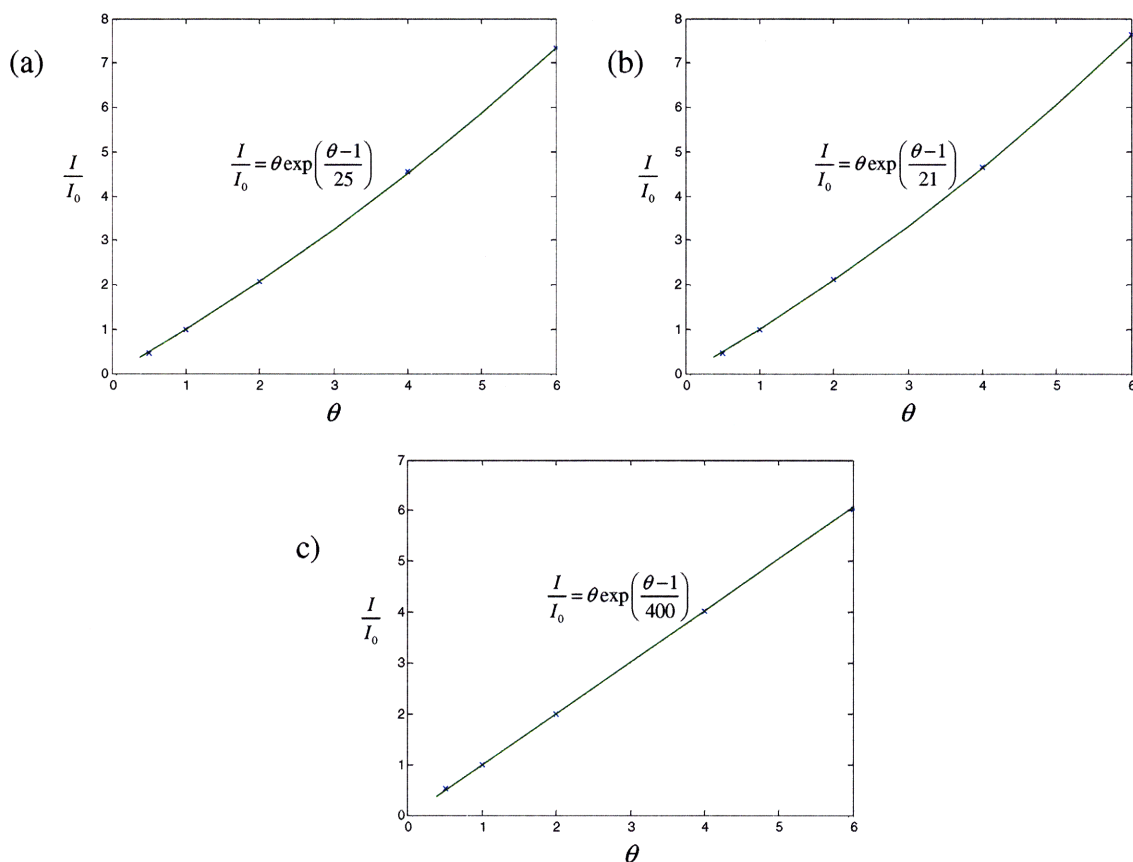


Figure 4-11: Calibration curves for fluorescent beads; a) 435 nm beads, b) 910 nm beads, and c) 81 nm beads.

Figure 4-11 shows calibration curves for fluorescence versus concentration for the different-sized fluorescent beads used in the focusing experiments. Parts (a) and (b) correspond to the smaller 435 nm beads and the larger 910 nm beads, respectively. Figure 4-11(c) shows the calibration curve for 81 nm fluorescent beads, which were used to estimate the concentration profile of the magnetic nanoparticles as a function of time. This procedure is discussed in more detail in Section 4.2.2. In all three plots, a 0.001 volume fraction of fluorescent beads was used as the reference concentration, such that $\theta_p = \phi_p / 0.001$ and $I_0 = I(\theta_p = 1)$. The functions listed in the plots are the empirical fits that result in the solid curves.

In most cases, one would expect a linear relationship between the bead concentration and total fluorescence at small volume fractions, which should then saturate at larger volume fractions. For a mixture of fluorescent beads in a magnetic nanofluid, we obtained the opposite effect, where instead of fluorescence saturation we observe fluorescence enhancement at larger volume fractions. As seen from the fits included with the plots, the fluorescence increases exponentially with increasing volume fractions, with the larger beads having higher exponential dependence. The mechanism behind this enhancement is believed to be multiple scattering [4], where one ray of laser light is able to excite multiple fluorescent beads after being deflected by the bead surfaces.

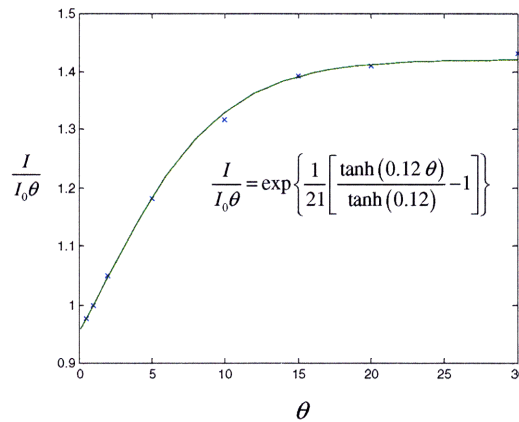


Figure 4-12: Calibration curve for the 910 nm beads, extended to include higher concentrations.

As discussed later in this chapter, the concentration of the 910 nm latex beads in our focusing experiments went above the range presented in Figure 4-11. Using more concentrated fluorescent-bead samples obtained from the manufacturer, the calibration curve for the 910 nm beads was extended up to volume fractions of 0.03, as shown in Figure 4-12. In this figure, the intensity is normalized by the bead concentration, such that a line of zero slope corresponds to a linear relationship between fluorescence and bead concentration. We see that for volume fractions somewhere between 0.015 and 0.03 the fluorescence enhancement becomes saturated, resulting in a linear relationship between fluorescence and 910 nm bead concentration.

In summary, for smaller fluorescent beads that do not undergo large changes in concentration, such as the 81 nm beads, we have that

$$\left(\frac{I}{I_0}\right)_{81 \text{ nm}} = \theta_p. \quad (4.2)$$

For the 435 nm beads, which undergo concentration changes where nonlinearity may be important, we have

$$\left(\frac{I}{I_0}\right)_{435 \text{ nm}} = \theta_p \exp\left(\frac{\theta_p - 1}{25}\right). \quad (4.3)$$

For the larger 910 nm beads, the concentrations varies by over an order of magnitude in some experiments, and the approximate calibration curve over the range of interest is

$$\left(\frac{I}{I_0}\right)_{910 \text{ nm}} = \theta_p \exp\left\{\frac{1}{21} \left[\frac{\tanh(0.12\theta_p)}{\tanh(0.12)} - 1 \right]\right\}, \quad (4.4)$$

which reduces to

$$\left(\frac{I}{I_0}\right)_{910 \text{ nm}} \approx \theta_p \exp\left(\frac{\theta_p - 1}{21}\right) \quad (4.5)$$

for the θ_p values shown in Figure 4-11c. In all cases,

$$\theta_p = \frac{\phi_p}{0.001}. \quad (4.6)$$

All of the calibration curves are purely empirical, but do provide adequate fits over the concentration ranges of interest. In general, at constant magnetic fluid concentrations, the fluorescence intensity is related to the to the nonmagnetic bead concentration as

$$\left(\frac{I}{I_0}\right)_p = \theta_p G(d_p, \theta_p), \quad (4.7)$$

where

$$G(d_p, \theta_p) = \left\{ \begin{array}{ll} 1, & d_p = 81 \text{ nm} \\ \exp\left(\frac{\theta_p - 1}{25}\right), & d_p = 435 \text{ nm} \\ \exp\left\{\frac{1}{21}\left[\frac{\tanh(0.12\theta_p)}{\tanh(0.12)} - 1\right]\right\}, & d_p = 910 \text{ nm} \end{array} \right\}. \quad (4.8)$$

An implicit assumption in the analysis presented here is that the concentration of both the magnetic and nonmagnetic species does not vary with y . The intensity of the excitation laser beam decreases as it penetrates the sample (in the y direction) due to scattering and absorbance by the sample, so any variations in concentration in the y direction would couple with the y -dependent laser-intensity profile. The focusing setup was designed in such a way that magnetic field gradients in the y direction were negligible, as verified in Figure 4-6, thus making this assumption valid.

4.2.2 Magnetic nanofluid absorption

The fluorescence signal given off by the sample is highly dependent on the concentration of the magnetic nanofluid in the mixture. The nanofluid is very opaque, blocking a large portion of the laser light and fluorescence emission. For the simulations presented later in this chapter, where magnetic fluid concentration gradients need to be taken into account, a calibration relationship between fluorescence and magnetic fluid concentration was necessary.

Figure 4-13 shows a plot of normalized fluorescence versus magnetic nanofluid concentration for four different concentrations of 910 nm fluorescent, nonmagnetic beads (volume percents of 0.05, 0.1, 0.25, and 0.5). The fluorescence intensities were normalized with respect to their fluorescence at a ferrofluid concentration of 0.1 vol %. The variable θ_m is a scaled magnetic fluid concentration, given by

$$\theta_m \equiv \frac{\phi_{\text{mag}}}{0.001}, \quad (4.9)$$

where ϕ_{mag} is the volume fraction of magnetite in the mixture. The fluorescence decreases exponentially with the ferrofluid concentration, which is consistent with a light extinction (absorption + scattering) mechanism. The fit is accurate for various fluorescent bead concentrations, meaning that at any bead concentration the expected relationship between fluorescence and magnetic fluid concentration is approximately given by

$$\frac{I}{I(\theta_m=1)} = \exp\left[-\left(\frac{\theta_m - 1}{1.35}\right)\right]. \quad (4.10)$$

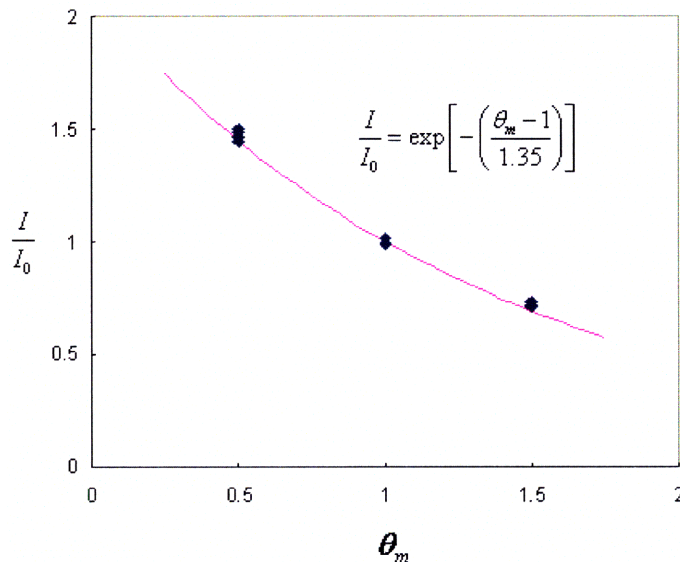


Figure 4-13: Normalized fluorescence intensity at a given latex-bead concentration as a function of magnetic fluid concentration.

In order to relate the fluorescence intensity in a given focusing experiment to the corresponding latex-bead concentration, both the nonlinearity effect presented in the previous section and the magnetic fluid light-extinction effect presented in this section must be considered. Using eqs. (4.7) and (4.10), the concentration of latex beads as a function of fluorescence and magnetic fluid concentration is given by

$$\theta_p G(d_p, \theta_p) = \frac{\left(\frac{I}{I_0}\right)_p}{\left(\frac{I}{I(\theta_m=1)}\right)} = \left(\frac{I}{I_0}\right)_p \exp\left(\frac{\theta_m - 1}{1.35}\right), \quad (4.11)$$

where θ_p and θ_m are defined by eqs. (4.6) and (4.9), respectively, and I_0 corresponds to the fluorescence signal when $\theta_p = 1$. If initial volume fractions different than $\phi_p = \phi_{\text{mag}} = 0.001$ are used in the focusing experiments, eq. (4.11) needs to be adjusted accordingly, as it is not linear in θ_m nor θ_p .

Eq. (4.11) does not allow for an explicit solution for the fluorescent-bead concentration as a function of the measured fluorescence intensity unless $G(\theta_p) = 1$. When comparing the experimental and model-predicted results, we found it more convenient to convert the concentrations obtained from the models into fluorescence-intensity profiles, given by

$$\left(\frac{I}{I_0}\right)_p = \theta_p G(d_p, \theta_p) \exp\left[-\left(\frac{\theta_m - 1}{1.35}\right)\right]. \quad (4.12)$$

4.3 Experiments

Each of the focusing experiments performed lasted 80 minutes. This was not enough time for the focusing process to reach a steady-state, but long enough to unveil most of the short-term dynamics before most of the assumptions made in our continuum models break down. In this section, we present the focusing results for 435 nm and 910 nm latex beads.

4.3.1 Focusing of 910 nm latex beads

Figure 4-14 shows the cross-section averaged fluorescence-intensity profile of 910 nm beads as a function of time. Two different experimental results are presented to show reproducibility. These results were obtained using a magnetic nanofluid concentration of 0.08 volume percent (volume of magnetite per total mixture volume), a fluorescent bead concentration of 0.1 volume percent, and a magnet-capillary spacing of 7 mm (see Figure 4-1). The beads focus about the point $x = 0$, which is consistent with the mechanism proposed in Section 4.1.3. The profiles given in the plots do not differentiate between fluorescence changes due to the focusing of the beads and those due to defocusing of the magnetic nanofluid. In order to translate these fluorescence profiles into concentration profiles, magnetic-fluid concentration gradients and fluorescence nonlinearities would have to be taken into account, as done in the analysis presented in Section 4.5.3.

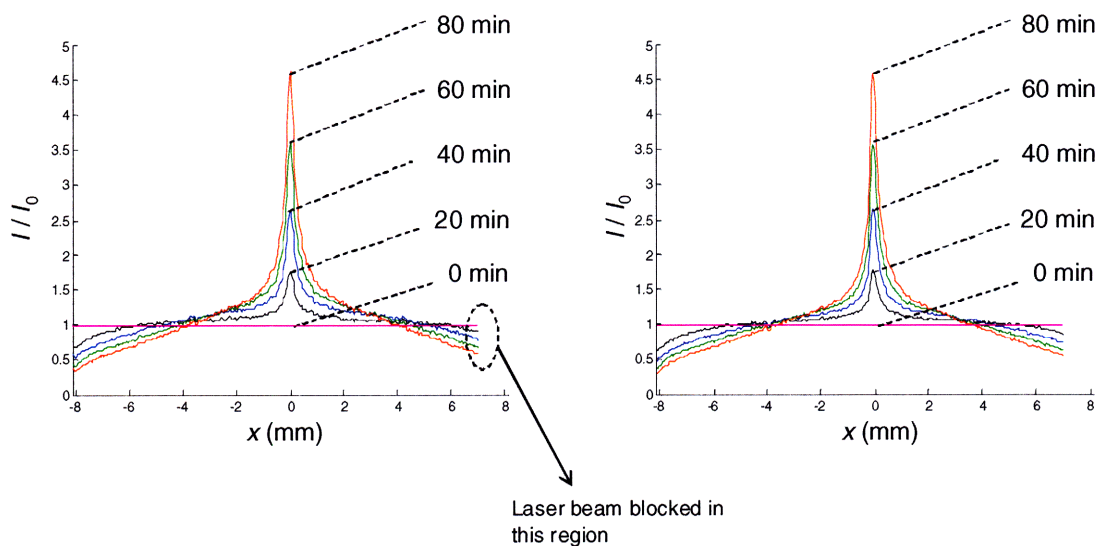


Figure 4-14: Fluorescence intensity profiles for 910 nm fluorescent beads immersed in a 0.08 vol% (0.41 wt%) magnetic nanofluid.

The plots only show the region where the latex beads are drawn towards the focusing point $x = 0$. In the regions to the left and right of the portion shown, the latex beads are pushed away from the focusing region, as seen previously in Figure 4-10. Again, the region missing on the right-hand-side of each image is due to the laser beam being blocked.

4.3.2. Magnetic nanofluid defocusing

The fluorescence intensity plots shown in Figure 4-14 could be directly converted into concentration profiles if the magnetic nanofluid concentration remained uniform during the experiments. In order to measure concentration variations in the ferrofluid, a similar experiment to the one shown in Figure 4-14 was repeated using 81 nm fluorescent beads in place of the 910 nm beads. These beads experience negligible magnetic forces, so any changes in fluorescence intensity are mostly due to changes in the magnetic fluid concentration.

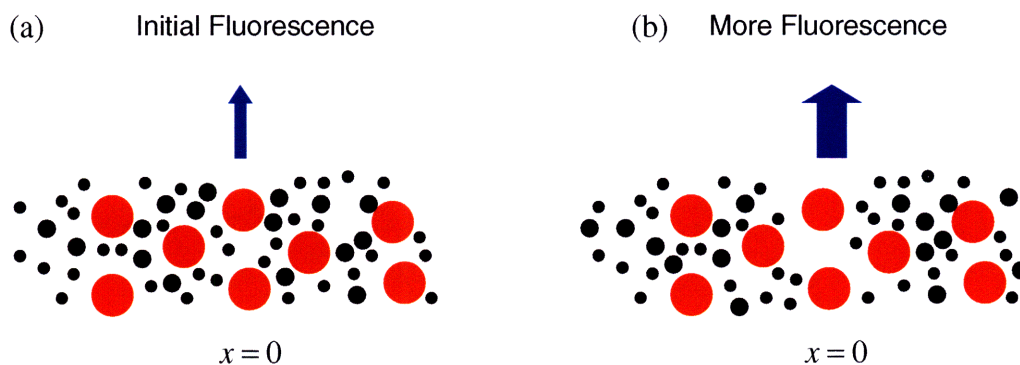


Figure 4-15: Schematic for the increase in fluorescence due to “defocusing” of magnetic nanoparticles.

The mechanism for fluorescence-intensity changes even when the concentration of the fluorescent species remains uniform is depicted in Figure 4-15. When the magnetic field profile shown in Figure 4-5 is applied to a sample containing magnetic nanoparticles and 81 nm nonmagnetic, fluorescent beads, it will lead to a concentration gradient in the magnetic nanoparticles (especially the larger magnetic nanoparticles), as depicted in Figure 4-15(b). Since the magnetic nanoparticles absorb light, there will be less absorption of laser and fluorescence light near $x = 0$, leading to a higher fluorescence signal in that region. Conversely, there will be less fluorescence signal at a given concentration of fluorescent beads in the regions where the magnetic nanoparticles concentrate.

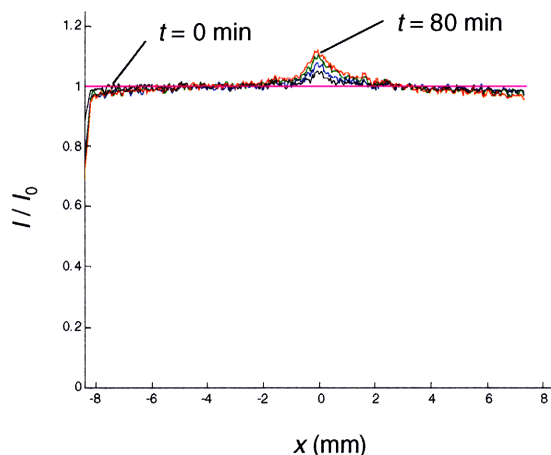


Figure 4-16: Increase in fluorescence near $x = 0$ due to magnetic fluid “defocusing.”

The fluorescence-intensity profile for the sample containing the 81 nm beads in a 0.1 vol % magnetic nanofluid is shown in Figure 4-16. Assuming negligible interactions between the beads and the magnetic nanoparticles, the curves in Figure 4-16 give the fraction of the fluorescence intensity that is due to magnetic fluid concentration gradients. Thus, dividing the results given in Figure 4-14 by those given in Figure 4-16 eliminates the fluorescence due to magnetic fluid concentration gradients.

4.3.3 Effect of magnetic fluid and field strength

The experiments given in Figure 4-14, which used a 0.08 vol % magnetic nanofluid concentration, were repeated for various nanofluid concentrations while keeping the initial 910 nm fluorescent bead concentration fixed at 0.1 vol %. Figure 4-17 shows the fluorescence intensity profiles (without accounting for magnetic fluid concentration gradients) for initial magnetic-fluid concentrations of 0.1 and 0.2 vol %. As expected, larger magnetic fluid concentrations lead to more focusing of the fluorescent beads near $x = 0$.

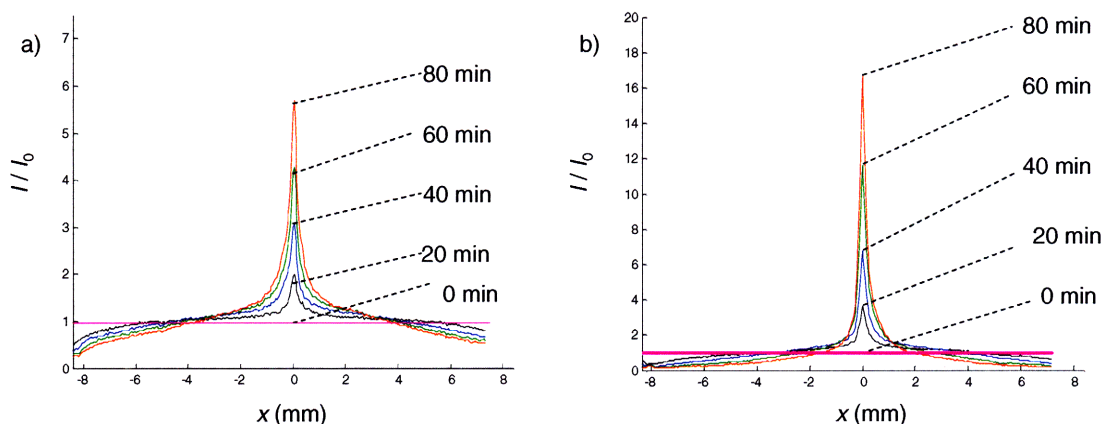


Figure 4-17: Focusing of 910 nm fluorescent, nonmagnetic beads in a magnetic nanofluid; (a) 0.1 vol % magnetite concentration and (b) 0.2 vol % magnetite concentration. The magnet spacing was 7 mm.

In Figure 4-17, the spacing between the magnets and the axis of the capillary tube was 7 mm, as depicted in Figure 4-3. Experiments were also performed using a spacing of 6 mm, as shown in Figure 4-18. The magnetic-fluid concentrations used in the plots are 0.1 and 0.05 vol %, respectively. Again, we see that focusing increases super-linearly with increasing magnetite concentrations. As expected, the higher field-gradients present

when the magnet spacing is decreased result in an increase in focusing. Figure 4-17(a) and Figure 4-18(a) use the same sample, but at different distances from the magnets.

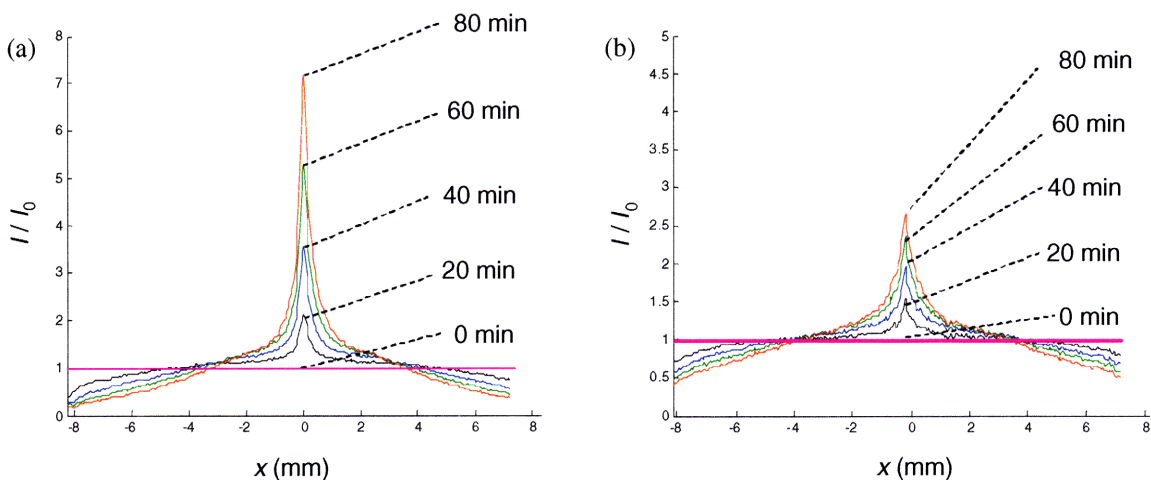


Figure 4-18: Focusing of 910 nm fluorescent, nonmagnetic beads in a magnetic nanofluid at a stronger magnetic field; (a) 0.05 vol % magnetite concentration and (b) 0.1 vol % magnetite concentration. The magnet spacing was 6 mm.

4.3.4 Effect of latex bead concentration

As discussed in Section 4.2.1, the relationship between latex bead concentration and fluorescence at constant magnetic nanofluid concentrations is nonlinear. As such, one would expect the normalized fluorescence-intensity profiles at a given magnetic-nanofluid concentration to depend on the initial concentration of the fluorescent beads. Such effect is presented in Figure 4-19, where three different nonmagnetic bead concentrations were used. The difference in behavior near $x = -8$ in part (a) of the figure is due to the low signal-to-noise ratio at such low bead concentrations.

One noticeable feature in these plots is that the normalized fluorescence-intensity peak is higher for an initial bead concentration of 0.1 vol % than for both higher and lower initial bead concentrations. This can be explained qualitatively using the

calibration plots shown in Figure 4-10 and Figure 4-11. At small fluorescent-bead concentrations, the relationship between fluorescence and concentration is approximately linear. At higher bead concentrations, the fluorescence increases exponentially with bead concentration, which explains the higher peak in Figure 4-19(b). At even higher bead concentrations, however, the fluorescence saturates and becomes a linear function of concentration again, giving the smaller peak observed in part (c) of the figure.

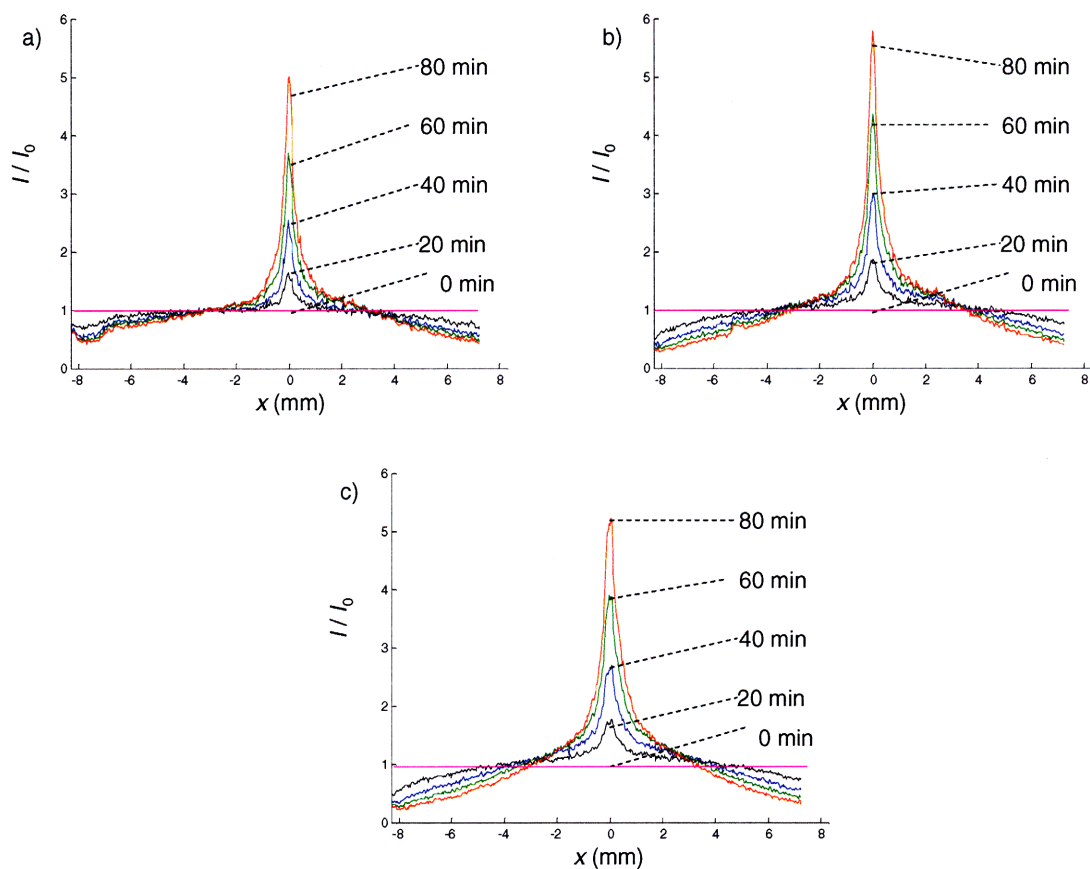


Figure 4-19: Focusing of 910 nm fluorescent, nonmagnetic beads in a magnetic nanofluid with different initial bead concentrations; (a) 0.02 vol %, (b) 0.1 vol %, and (c) 0.5 vol %.

4.3.5 Effect of particle size

Since the force of magnetic origin is proportional to the volume of the nonmagnetic beads, focusing should be highly dependent on the size of the latex beads. This is observed in Figure 4-20, where the focusing of 435 nm beads is compared to the focusing of the 910 nm beads under the same conditions. A 0.1 vol % magnetic fluid was used in both cases. The bead concentration used in both cases was 0.1 vol % and the spacing between the capillary and the magnets was 6 mm. As expected, the amount of focusing observed with the 910 nm beads was significantly higher than of the 435 nm beads.

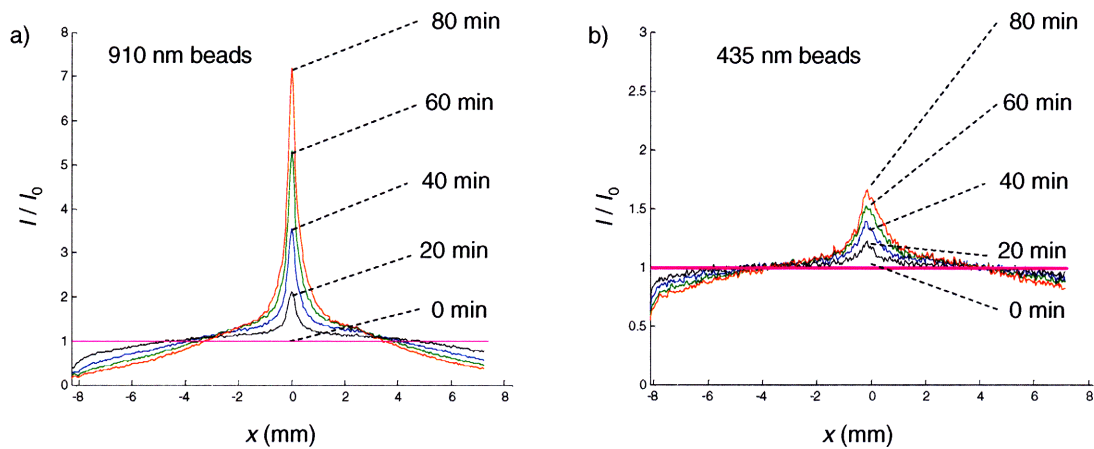


Figure 4-20: Focusing comparison of (a) 910 nm beads and (b) 435 nm beads in a 0.1 vol % magnetic nanofluid.

4.4 Continuum model

To understand the microphysics taking place in the experiments presented in Section 4.3, continuum simulations were performed using the flux expressions obtained in Chapter 3. When combined with the calibration curves presented in Section 4.2, the

simulations gave good quantitative agreement with the experimental data over a wide range of latex-bead sizes and concentrations, magnetic fluid strengths, and magnetic field profiles.

4.4.1 Governing equations and parameters

The governing equation for the concentration profile of the nonmagnetic beads is given by

$$\frac{\partial C_p}{\partial t} + \underline{\nabla} \cdot (C_p \underline{v}) = -\underline{\nabla} \cdot \underline{J}_p , \quad (4.13)$$

where \underline{J}_p is the molar flux of the polystyrene beads p relative to the mass-average velocity \underline{v} , C_p is the molar concentration of the beads, and t is time. A mole of latex beads is defined as 6.022×10^{23} beads. Since the latex beads are neutrally-buoyant (sucrose used to raise the specific gravity of the mixture to 1.05) and the concentration gradients in magnetic fluid are small, any density differences and the resulting convection induced by the diffusive process can be neglected. Eq. (4.13) therefore reduces to

$$\frac{\partial C_p}{\partial t} + \underline{\nabla} \cdot \underline{J}_p = 0 . \quad (4.14)$$

For the magnetic nanoparticles m , the conservation equation is identical in form,

$$\frac{\partial C_m}{\partial t} + \underline{\nabla} \cdot \underline{J}_m = 0 . \quad (4.15)$$

To simplify the analysis for the time being, we treat the different-sized magnetic nanoparticles as one species. As discussed in Chapter 2, we will eventually treat the magnetic nanofluid as a mixture of three different-sized magnetic species suspended in water.

The flux of species i in a solvent s in a pseudo-binary binary system is given by [5]

$$\underline{j}_i = -\frac{C^2}{\rho} W_i W_s \mathcal{D}_{is} \underline{d}_i , \quad (4.16)$$

where s stands for solvent. The above expression and the definition of each term are given in Chapter 3. For the system studied in this work, we are interested in two pseudo-binary diffusive processes occurring at different length scales. At the magnetic nanoparticle level, the pseudo-binary process is the forced diffusion of the nanoparticles in a water (plus sugar, salts, etc.) continuum. For this pseudo-binary assumption to hold, the interaction between the nanoparticles and the larger latex beads should be negligible. At the polystyrene bead level, the pseudo-binary process is the diffusion of the beads in a magnetic nanofluid continuum. For this assumption to hold, the suspension of magnetic nanoparticles in water must act as a continuum, meaning that the interaction between the beads and individual solvent “molecules” (whether water, ions, magnetic nanoparticles, etc.) are not considered. Only interactions between the beads and the solvent as a whole are considered.

From eq. (3.160), adjusting for the difference between the mass and molar fluxes, we have

$$\underline{J}_m = -\frac{\mathcal{D}_{mw}\rho}{W_m}\underline{\nabla}w_m + \frac{\mathcal{D}_{mw}CW_w}{\rho RT}\left[(w_m - \phi_m)\rho\underline{g} + \phi_m(1 - \phi_m)\mu_o M_m \underline{\nabla}H\right], \quad (4.17)$$

where the subscripts m and w denote magnetic nanoparticles and water, respectively. Due to the strong magnetic moment of the nanoparticles, the gravitational buoyancy term can be neglected with respect to the magnetic term. The flux thus reduces to

$$\underline{J}_m = -\frac{\mathcal{D}_{mw}\rho}{W_m}\underline{\nabla}w_m + \frac{\mathcal{D}_{mw}CW_w}{\rho RT}\left[\phi_m(1 - \phi_m)\mu_o M_m \underline{\nabla}H\right]. \quad (4.18)$$

For the latex beads p , we have from eq. (3.137) that

$$\underline{J}_p = -\frac{\mathcal{D}_{pf}\rho}{W_p}\underline{\nabla}w_p - \frac{\mathcal{D}_{pf}CW_f}{\rho RT}\left[(\phi_p - w_p)\rho\underline{g} + \phi_p\mu_o M \underline{\nabla}H\right], \quad (4.19)$$

where the subscript f denotes the magnetic nanofluid continuum. Since the beads are approximately neutrally-buoyant, the above relationship reduces to

$$\underline{J}_p = -\frac{\mathcal{D}_{pf}\rho}{W_p}\underline{\nabla}w_p - \frac{\mathcal{D}_{pf}CW_f}{\rho RT}\left[\phi_p\mu_o M \underline{\nabla}H\right]. \quad (4.20)$$

Eqs. (4.18) and (4.20) describe the molar fluxes relative to the mass-average velocity for the magnetic nanoparticles and the latex beads, respectively, in the absence

of any nonidealities. In Section 3.5.2, the main nonidealities that can affect the form of eqs. (4.18) and (4.20) are considered.

4.4.2 Ideal pseudo-binary system

Since the conservation equations are given in terms of molar concentrations, it is more convenient to express the fluxes in terms of concentrations as opposed to weight or mole fractions. The first simplification made is that the bulk density is assumed to be approximately constant, as was done in the species conservation equation. Combined with the equality

$$\frac{w_i \rho}{W_i} = C_i, \quad (4.21)$$

we have that the diffusive part of the flux can be approximated as

$$-\frac{\mathcal{D}_{ij} \rho}{W_i} \underline{\nabla} w_i \approx -\mathcal{D}_{ij} \underline{\nabla} C_i, \quad (4.22)$$

as is generally the case in liquid mixtures.

For the case of magnetic nanoparticle diffusion, the total concentration of the mixture can be expressed as

$$C = \sum \frac{\phi_i}{V_i} \approx \frac{1 - \phi_m}{v_w}, \quad (4.23)$$

since the molar volumes of the latex beads and the magnetic nanoparticles are much larger than that of water and $\phi_p \ll \phi_m$ (see Table 4.4). We therefore have that

$$\frac{C W_w}{\rho} \approx (1 - \phi_m) \frac{\rho_w}{\rho} \approx (1 - \phi_m), \quad (4.24)$$

since the density of the water continuum is less than 1% smaller than that of the mixture.

Substitution of eqs. (4.22) and (4.24) into (4.18) gives

$$\underline{J}_m = -\mathcal{D}_{mw} \underline{\nabla} C_m + \frac{\mathcal{D}_{mw} v_m (1 - v_m C_m)^2}{RT} [C_m \mu_o M_m \underline{\nabla} H]. \quad (4.25)$$

In the above expression we made use of the relationship $\phi_i = C_i v_i$ for mixtures with no excess volume of mixing. The term in parenthesis is negligible for the magnetophoresis of dilute magnetic species, but neglecting it for the volume fractions used in this work would lead to errors of about 15% in the forced-diffusion flux.

For the latex beads diffusing in a magnetic nanofluid continuum, we have that

$$\frac{CW_f}{\rho} \approx \frac{\rho_f}{\rho} \approx 1. \quad (4.26)$$

since the bead volume fraction is much less than unity. The molar flux therefore becomes

$$\underline{J}_p = -\mathcal{D}_{pf} \underline{\nabla} C_p - \frac{\mathcal{D}_{pf} v_p}{RT} [C_p \mu_o M \underline{\nabla} H]. \quad (4.27)$$

The magnetization of the mixture is related to that of the magnetic nanoparticles as

$$M = v_m C_m M_m, \quad (4.28)$$

so there is some coupling between the diffusion of the latex beads and the local concentration of the magnetic nanoparticles.

Since the magnetic nanoparticles are diffusing through water, their diffusion coefficient as given by the Stokes-Einstein relationship is

$$\mathcal{D}_{mw} = \frac{kT}{6\pi\eta_w a_m}. \quad (4.29)$$

For the latex beads, the diffusion coefficient is given by

$$\mathcal{D}_{pf} = \frac{kT}{6\pi\eta_f a_p}, \quad (4.30)$$

where

$$\eta_f = \eta_w \left(1 + \frac{5}{2} \phi_m\right) = \eta_w \left(1 + \frac{5}{2} v_m C_m\right). \quad (4.31)$$

The expressions presented here are valid for the case where the excess chemical potentials of the diffusing species are negligible. The accuracy of this assumption is examined in the next section.

4.4.3 Excess chemical potentials

Excess properties or variables are used in thermodynamics to describe deviations from ideal behavior in a system. The definition of an excess property is the difference between the actual and the ideal value for that property,

$$Q_i^{ex} = Q_i - Q_i^{id} . \quad (4.32)$$

For example, for an ideal mixture of two components, the total volume is the sum of the two individual component volumes. In a thermodynamic sense, any deviation from this expected volume is considered an excess volume of mixing.

For the case of diffusing species, the thermodynamic driving forces are chemical potential gradients, meaning that nonidealities enter the analysis in the form of excess chemical potentials. These excess chemical potentials are usually given in terms of activity coefficients, defined by the relationship

$$\xi_i^{ex} = RT \ln(\gamma_i) , \quad (4.33)$$

where γ_i is the activity coefficient of species i in the mixture. From eq. (4.32), the excess chemical potential of species i in a mixture is defined as

$$\xi_i^{ex} = \xi_i - \xi_i^{id} , \quad (4.34)$$

where the ideal chemical potential is given by

$$\xi_i^{id} = \xi_i^0(T, p, H) + RT \ln x_i . \quad (4.35)$$

Here $\xi_i^0(T, p, H)$ is the pure component chemical potential of species i .

Up this point, all of the derivations presented for the diffusive fluxes assume that the mixture behaves ideally. Since diffusion is driven by external forces and chemical potential gradients, nonidealities can be neglected if

$$\left| \frac{\nabla \xi_i^{ex}}{\nabla \xi_i^{id}} \right| \ll 1 . \quad (4.36)$$

4.4.3.1 Statistical mechanics

According to the statistical-mechanical solution theory of McMillan and Mayer, the activity coefficient of species i may be written as [6]

$$\ln \gamma_i = \sum_j b_{ij} C_j + \sum_{j,k} b_{ijk} C_j C_k + \dots, \quad (4.37)$$

where the interaction (or virial) coefficients b_{ij} , b_{ijk} , ... are calculated using the potential of mean force between 2 species, 3 species, and higher moments. For an orientation-independent potential, the two-body interaction coefficient is given by [7]

$$b_{ij} = 4\pi N_A \int_0^\infty [1 - g(r_{ij})] r_{ij}^2 dr_{ij}, \quad (4.38)$$

where r_{ij} is the distance between particles i and j in a solvent s , N_A is Avogadro's number, and $g(r_{ij})$ is the radial distribution function, which describes the probability of a particle j being a distance r_{ij} away from particle i . For dilute two-body interactions [8],

$$g(r_{ij}) = \exp\left(-\frac{W_{ij}(r_{ij})}{kT}\right), \quad (4.39)$$

where $W_{ij}(r_{ij})$ is the potential of mean force between species i and j in a solvent s .

The potential of mean force for n colloids is related to the force potential between the colloids and the infinite solvent molecules m by [9]

$$\exp\left(-\frac{W(r^n)}{kT}\right) = \sum_{m=0}^{\infty} \frac{z_0^m}{m!} \int \exp\left(-\frac{u(r^n, r^m)}{kT}\right) dr^m, \quad (4.40)$$

where

$$z_0 = \frac{\xi_0^s}{kT}. \quad (4.41)$$

In the above expressions, u is the force potential between the colloids without any solvent effects (such as interactions with ions in the solvent) and ξ_0^s is the chemical potential of the solvent. When the solvent does not contribute to the interaction between two colloids, u and W are equal.

For some simple force-potential distributions such as volume exclusion, where the potential is infinite when the colloids overlap each other and zero otherwise, the higher moments in eq. (4.37) can be obtained without too much difficulty for equally-sized particles. For more complex interactions, such as magnetic moment and electrostatic interactions, we are usually limited to using two-body interactions to approximate the activity coefficients. In our analysis, only two-body interactions are considered in obtaining expressions for the excess chemical potentials, meaning that only the first term of the summation in eq. (4.37) is used.

Table 4.3: Values for the universal constants used in this chapter

Constant	Description	Value	Units
μ_0	magnetic permeability of free space	$4\pi \times 10^{-7}$	$\text{H/m} \left(\text{N/A}^2 \right)$
ϵ_0	electric permittivity of free space	8.854×10^{-12}	$\text{F/m} \left(\frac{\text{C}^2}{\text{N} \cdot \text{m}^2} \right)$
e	elementary charge	1.062×10^{-19}	C
k	Boltzmann constant	1.381×10^{-23}	J/K

4.4.3.2 Volume exclusion

If the only nonideality in the mixture is the excluded-volume effect of the colloids, the potential is described by [10]

$$\begin{aligned}
 u_{ij} = W_{ij} &= \infty & r_{ij} &\leq a_i + a_j, \\
 &= 0 & r_{ij} &> a_i + a_j.
 \end{aligned} \tag{4.42}$$

This gives

$$\begin{aligned}
g(r_{ij}) &= 0 & r_{ij} \leq a_i + a_j, \\
&= 1 & r_{ij} > a_i + a_j,
\end{aligned}
\tag{4.43}$$

which results in

$$b_{ij} = \frac{4}{3} \pi (a_i + a_j)^3 N_A . \tag{4.44}$$

For a single colloidal species in a fluid with no excess volume of mixing, this reduces to the classic two-body result

$$\ln \gamma_i = b_{ii} C_i = 8\phi_i . \tag{4.45}$$

For a mixture, the excess chemical potential of species i due to exclude-volume effects is

$$\ln \gamma_i = \sum_j \phi_j \left(1 + \frac{a_i}{a_j} \right)^3 . \tag{4.46}$$

Higher moments for excluded volume effects are summarized by Minton [9] for particles of the same size.

For the magnetic nanoparticles, we have that

$$\underline{\nabla} \xi_m^{ex} = RT \underline{\nabla} \ln(\gamma_m) = 8 \underline{\nabla} \phi_m + \left(1 + \frac{a_m}{a_p} \right)^3 \underline{\nabla} \phi_p . \tag{4.47}$$

Unless the gradients in latex bead concentrations are two orders of magnitude larger than the gradients in magnetic nanoparticle concentrations, the second term in eq. (4.47) can be neglected. From eq. (4.36), the effects of volume exclusion for the magnetic nanoparticles can be neglected if

$$\frac{8x_m \underline{\nabla} \phi_m}{\underline{\nabla} x_m} \ll 1 . \tag{4.48}$$

For $O(1)$ changes in nanoparticle concentration, this inequality is *not* satisfied, so volume-exclusion effects cannot be neglected for the diffusion of magnetic nanoparticles.

For the diffusion of latex beads in a ferrofluid continuum, we have that

$$\underline{\nabla} \xi_p^{ex} = RT \underline{\nabla} \ln(\gamma_p) = 8 \underline{\nabla} \phi_p , \tag{4.49}$$

meaning that volume-exclusion effects can be neglected if

$$\frac{8x_p \nabla \phi_p}{\nabla x_p} \ll 1 . \quad (4.50)$$

For the initial conditions used in most experiments, volume-exclusion effects become important if focusing increases the concentration of the latex beads by an order-of-magnitude, which is the case in some of the experiments for the larger 910 nm beads. Volume-exclusion effects are not important for the smaller 435 nm particles over the time scales considered in this work.

Table 4.4: Values for the parameters used to calculate excluded-volume effects

Parameter	Description	Value	Units
T	Temperature	298	K
d_{mag}	volume-average diameter of magnetite cores	7.5	nm
d_m	volume-average diameter of magnetic nanoparticles	31.5	nm
ρ_{mag}	density of magnetite cores	5.17	g/cm ³
ρ_m	density of magnetite nanoparticles	1.1	g/cm ³
ϕ_{mag}	volume fraction of magnetite cores	0.001	-
ϕ_m	volume fraction of magnetic nanoparticles	0.074	-
ϕ_{910}	volume fraction of “large” 910 nm latex beads	0.001	-
ϕ_{435}	volume fraction of “small” 535 nm latex beads	0.001	-

One important approximation made here is that the volume fraction and equivalent hard-sphere diameter of the magnetic nanoparticles are calculated using their volume-averaged hydrodynamic diameter. In general, calculating accurate values for excluded-volume interactions between two magnetic nanoparticles, and between a

magnetic nanoparticle and a polystyrene bead, can be very difficult. This is due to the complex interactions between flexible, highly polydisperse polymer shells attached to solid cores with both each other as well as with latex-bead surfaces. Treating the magnetic nanoparticles as hard spheres of equivalent hydrodynamic volumes only provides an approximation for excluded-volume effects.

4.4.3.3 Electrostatic repulsion

When colloidal species are suspended in water, they generally acquire a net surface charge, which depends on the chemical nature of their surface. A colloidal mixture will only be kinetically stable if the charge on all the colloids has the same sign (all the colloids are positively charged or all are negatively charged). In this work, all of the polystyrene beads and magnetic nanoparticles are negatively charged and the mixtures are stable in a kinetic sense. Electrostatic effects are not sufficient to make a system thermodynamically stable, as they cannot fully counteract van der Waals forces at very short particle separations, but they do slow down aggregation significantly during the time scales of interest to us. The magnetic nanoparticles themselves are even more stable than the latex beads due to steric effects from the polymer shells attached to their surface.

Electrostatic repulsion takes place in regions where the volume-exclusion potential is zero (outside the particle surfaces), meaning that the two potentials are independent and the net potential of mean force is simply the sum of the two. To calculate the electrostatic potential of mean force, one would generally have to consider the repulsion between the species as well as their interaction with the nearby ions. Several authors have performed molecular dynamics and Monte Carlo simulations, which are necessary for more complex systems in which things like the size of the ions and solvation effects are important [11]. In our case, we limit our analysis to the simple case where the interactions can be approximated by a DLVO-type model (Derjaguin, Landau, Verwey, and Overbeek theory [12]), which uses a mean-field approach that treats the ions as point charges occupying no volume. For such case, the electrostatic potential of mean force is given by [12]

$$W_{ij}(r_{ij}) = 4\pi\epsilon_0\epsilon_r \bar{\Psi}_i \bar{\Psi}_j \frac{a_i a_j}{r_{ij}} \exp\left[-\kappa(r_{ij} - a_i - a_j)\right], \quad (4.51)$$

where r_{ij} is the center-to-center distance between the colloids, ϵ_0 is the electric permittivity of free space, ϵ_r the dielectric constant of the solvent, $\bar{\Psi}_i$ a function used to describe the electric potential at the particle surface, and $1/\kappa$ the Debye length, given by

$$\kappa^{-1} = \left(\frac{\epsilon_0 \epsilon_r kT}{1000 e^2 \sum_i z_i^2 C_{i,\infty}} \right)^{1/2}. \quad (4.52)$$

In the last expression, e is the charge of an electron, z_i is the valance of ionic species i , and $C_{i,\infty}$ is its molar concentration far away from the colloid surface. For the 1:1 salt used in this work (NaCl), the effective potential $\bar{\Psi}_i$ is given by [12]

$$\bar{\Psi}_i = \frac{\frac{8kT}{e} \tanh\left(\frac{\Psi_i e}{4kT}\right)}{1 + \left\{ 1 - \left[(2\kappa a_i + 1) / (\kappa a_i + 1)^2 \right] \tanh^2\left(\frac{\Psi_i e}{4kT}\right) \right\}^{1/2}}, \quad (4.53)$$

where Ψ_i is the theta potential of the species and e is the charge of an electron. The effective potential $\bar{\Psi}_i$ is approximately equal to the Zeta potential of species i for potentials less than 25 mV (millivolts) in magnitude. For Zeta potential magnitudes of about -60 mV, which are typical for the polystyrene beads used in our study, the effective potential $\bar{\Psi}_i$ is about 10% lower in magnitude than the Zeta potential. Eqs. (4.51) and (4.53) neglect the thickness of the Stern layer, which should be much less than 1 nm.

If electrostatic and volume-exclusion effects are taken as the main sources of excess chemical potential, the overall potential of mean force is given by

$$\begin{aligned} W_{ij}(r_{ij}) &= \infty, & r_{ij} &\leq a_i + a_j, \\ &= 4\pi\epsilon_0\epsilon_r \bar{\Psi}_i \bar{\Psi}_j \frac{a_i a_j}{r_{ij}} \exp\left[-\kappa(r_{ij} - a_i - a_j)\right], & r_{ij} &> a_i + a_j. \end{aligned} \quad (4.54)$$

Because of the complex form of eq. (4.54), the resulting expressions for the activity coefficients must be evaluated numerically. In order to compare the magnitude of electrostatic effects relative to volume-exclusion effects, it is convenient to model the

electrostatic repulsion as an effective excluded shell of thickness $\tilde{\alpha}_{ij}\kappa^{-1}$, where the $\tilde{\alpha}_{ij}$ ($=\tilde{\alpha}_{ji}$) values for the different interactions are calculated from numerical integration of eq. (4.38), (4.39), and (4.54). This results in an effective excluded radius for each colloid equal to $a_i + \tilde{\alpha}_{ij}\kappa^{-1}$, which leads to

$$\ln \gamma_i \approx \sum_j \phi_j \left(1 + \frac{a_i + \tilde{\alpha}_{ij}\kappa^{-1}}{a_j} \right)^3. \quad (4.55)$$

Values for $\tilde{\alpha}_{ij}$, which are given in Table 4.6, are of $O(1)$ for interactions involving polystyrene beads, but much less than unity for magnetic nanoparticle interactions. The reason for the latter is because the surface charge of the magnetic nanoparticles was assumed to be near the magnetic core, such that most of the electric double layer is within the region occupied by the polymer shell. This may under-predict electrostatic effects, but it does provide a better estimate than assigning the surface potential to be at the hydrodynamic radius of the magnetic nanoparticles.

Table 4.5: Values for the parameters used to calculate electrostatic effects

Parameter	Description	Value	Units
ϵ_r	dielectric constant of water	78.4	-
ψ_m	zeta potential of magnetic nanoparticles	-25	mV
ψ_{435}	zeta potential of 435 nm latex beads	-60	mV
ψ_{910}	zeta potential of 910 nm latex beads	-65	mV
$C_{i,\infty}$	bulk concentration of electrolyte (NaCl)	4.75	mM
$ z_i $	valance of NaCl ions	1	-
κ^{-1}	Debye length	4.4	nm

For two polystyrene beads of similar size, the increase in excess potential is proportional to $\left(\frac{\tilde{\alpha}_{pp}\kappa^{-1}}{a_p}\right)$, which is much smaller than unity in our system.

Electrostatic repulsion between two polystyrene beads is therefore negligible with respect to their physically excluded volume. For the interaction of magnetic nanoparticles with polystyrene beads, electrostatic interactions are of the same order as volume exclusion, both of which are negligible. Finally, since $\tilde{\alpha}_{mm} \ll 1$, electrostatic repulsion between the magnetic nanoparticles is also negligible with respect to volume exclusion effects.

Table 4.6: Electrostatic interaction coefficients (dimensionless)

Species <i>i</i>	Species <i>j</i>	$\tilde{\alpha}_{ij}$
magnetic nanoparticle	magnetic nanoparticle	0.0032
magnetic nanoparticle	435 nm polystyrene	0.60
magnetic nanoparticle	910 nm polystyrene	0.64
435 nm polystyrene	435 nm polystyrene	7.0
435 nm polystyrene	910 nm polystyrene	7.4
910 nm polystyrene	910 nm polystyrene	7.9

4.4.3.4 Depletion forces

An effect which can be important in some cases is the depletion force between the larger polystyrene beads due to the presence of the small magnetic nanoparticles surrounding them [13,14]. When two polystyrene beads come in close contact with each other, they exclude the magnetic nanoparticles from the region between them, which leads to osmotic-type forces trying to bring the latex beads even closer together. For the

case of small volume fractions and negligible electrostatic effects, the resulting depletion potential is given by [15]

$$W(\ell) = -\frac{3}{16}kT\phi_m \frac{a_1 + a_2}{a_m} \left(2 - \frac{\ell}{a_m}\right)^2, \quad \ell \leq 2a_m, \quad (4.56)$$

$$= 0, \quad \ell > 2a_m.$$

In the above expression, ℓ is the distance between the latex beads, ϕ_m the volume fraction of magnetic nanoparticles in the bulk, a_m the radius of the magnetic nanoparticles, and a_1 and a_2 denote the radii of the two polystyrene beads approaching each other.

Table 4.7: Depletion interaction coefficients

Species i	Species j	$\tilde{\beta}_{ii}$
435 nm polystyrene	435 nm polystyrene	0.18
435 nm polystyrene	910 nm polystyrene	0.25
910 nm polystyrene	910 nm polystyrene	0.38

The value of the activity coefficients resulting from eq. (4.56) are obtained numerically as before, and can be expressed in the form

$$b_{dep} = -\tilde{\beta}_{12} \frac{4}{3} \pi (a_1 + a_2)^3 N_A, \quad (4.57)$$

where $\tilde{\beta}_{12}$ are $O(1)$ quantities, given in Table 4.7. Depletion forces are attractive, thus resulting in negative virial contributions. Comparing eqs. (4.57) and (4.44), we see that

$$\left| \frac{b_{dep}}{b_{exc}} \right| = \tilde{\beta}_{12} \sim 1, \quad (4.58)$$

meaning that depletion effects between latex beads are of the same order-of-magnitude as their excluded-volume effects. Thus, in regions where the latex bead concentration

becomes larger than about 1% by volume, both volume exclusion and depletion effects need to be taken into account.

4.4.3.5 Magnetic dipole-dipole interactions

Each magnetic nanoparticle carries a permanent magnetic moment, which results in dipole-dipole interactions described by the potential [27]

$$u(r_{ij}) = \frac{1}{4\pi\mu_0} \left(\frac{\hat{\mathbf{m}}_i \cdot \hat{\mathbf{m}}_j}{r_{ij}^3} - 3 \frac{(\hat{\mathbf{m}}_i \cdot \mathbf{r}_{ij})(\hat{\mathbf{m}}_j \cdot \mathbf{r}_{ij})}{r_{ij}^5} \right). \quad (4.59)$$

Since the nanoparticles are sterically stabilized by a polymer layer, the radius of closest contact is larger than the magnetic diameter, which results in significantly less magnetic interaction between the nanoparticles used in this work as compared to uncoated nanoparticles. The ratio of the largest magnetic potential to the solvent kT energy is obtained by setting $r_{ij} = 2a_m$, or the closest distance possible between the nanoparticles.

This gives

$$\frac{u_{\max}}{kT} = -\frac{\hat{m}^2}{16\pi\mu_0 kT a_m^3}, \quad (4.60)$$

which motivates the definition of a magnetic coupling parameter

$$\tilde{\lambda} = \frac{\hat{m}^2}{16\pi\mu_0 kT a_m^3}. \quad (4.61)$$

For the magnetic nanoparticles used in this work, the parameter value in Table 4.8 tell us that $\tilde{\lambda}_{ij} \ll 1$.

In the absence of applied fields, where the magnetic moments are randomly distributed, the contribution of magnetic dipole-dipole interactions to the excess potential is [16]

$$\ln \gamma_m \approx -\frac{128}{3} \phi_m \tilde{\lambda}_{nm}^2, \quad (4.62)$$

which from the magnitude of $\tilde{\lambda}_{mm}$ and eq. (4.45) we know is negligible with respect to excluded volume effects (less than 0.1%).

When a magnetic field is applied, the analysis becomes more complicated due to the bias created in the direction of the field. For a magnetically saturated fluid, the magnetic nanoparticles will attract each other in the direction of the field and repel each other in the directions perpendicular to the field, which leads to cylindrical rather than spherical symmetry in their interactions. This in turn leads to anisotropic excess potentials, which are not consistent with the rest of the analysis presented in this work. Fortunately, since $\tilde{\lambda}_{mm} \ll 1$ for the nanoparticles of interest, these asymmetries can be neglected to leading order and the activity coefficient is approximately described by eq. (4.62).

Table 4.8: Magnetic interaction coefficients

Species i	Species j	$\tilde{\lambda}_{ij}$
magnetic nanoparticle	magnetic nanoparticle	0.0097
435 nm polystyrene	435 nm polystyrene	0.12
435 nm polystyrene	910 nm polystyrene	0.3
910 nm polystyrene	910 nm polystyrene	1.1

The magnetic nanoparticles are not the only species that interact “magnetically” in the mixture. Due to the large size-difference between the polystyrene beads and the magnetic nanoparticles, the latex beads act as magnetic holes [17] in a ferrofluid continuum, causing the magnetic field lines to bend around them. The latex beads end up behaving as negative magnetic moments of magnitude equal to that of an equivalent volume of ferrofluid. Just like the magnetic nanoparticles, the latex beads attract each other in the direction of the applied field and repel each other in the directions perpendicular to the field. Since these “negative moments” are induced by the average

magnetic moment of the fluid at that position, they always point in the opposite direction of the field even when the fluid is not saturated.

The parameter $\tilde{\lambda}$ can be defined for the nonmagnetic colloids using the above-mentioned negative magnetic moments, resulting in

$$\tilde{\lambda}_{ij} = \frac{8\pi\mu_0 M_f^2 a_i^3 a_j^3}{9kT (a_i + a_j)^3}. \quad (4.63)$$

In the above expression, $M_f = 330$ A/m is the saturation magnetization of the fluid at a magnetite volume fraction of 0.001. This value is 74% of the true magnetite magnetization at a volume 0.001 due to the dead shell volume discussed in Chapter 2. For the smaller 435 nm nonmagnetic beads used in this work, the maximum value of $\tilde{\lambda}$ is 0.12, corresponding to a saturated ferrofluid (for nonmagnetic particles $\tilde{\lambda} = 0$ when $H = 0$). Eq. (4.62) tells us that the magnitude of the “magnetic” interaction between these beads is about 8% of the value for volume exclusion. Since the excluded volume between the smaller polystyrene beads is negligible, the magnetic interaction between the 435 nm beads can also be neglected.

For the larger 915 nm beads, the interaction parameter corresponding to a saturated ferrofluid is $\tilde{\lambda} = 1.1$, meaning that the assumptions made in deriving eq. (4.62) are no longer valid. To obtain some bounds on the activity coefficient for these larger beads, the asymptotic limit of the activity coefficient for $\tilde{\lambda} \gg 1$ is given by [18]

$$\ln \gamma_p \approx -\frac{8}{3} \phi_p \frac{\exp(\tilde{\lambda}_{pp})}{\tilde{\lambda}_{pp}^2}. \quad (4.64)$$

Assuming that the magnitude of the activity coefficient always increases with $\tilde{\lambda}$, asymptotic matching of eqs. (4.62) and (4.64) for $\tilde{\lambda} = 1.1$ results in $\ln \gamma_p \sim -50\phi_p$, which is within an order of magnitude of the volume-exclusion effects ($\ln \gamma_p = 8\phi_p$).

Because of the asymmetries involved, magnetic-type interactions between the latex beads were not taken into account in our models. However, since the beads focus in regions where the magnetic field is a minimum, the magnetic interaction parameter should be much smaller than the maximum value in the regions where ϕ_p becomes large.

As such, neglecting these magnetic-type interactions between the latex beads is not expected to introduce much error into our analysis.

Note that if we were dealing with larger nonmagnetic particles or more concentrated ferrofluids, as is the case in the work done by Skjeltorp [19, 20] on “magnetic holes,” the activity coefficient as given by eq. (4.64) would increase exponentially. At such conditions, the magnetic beads form chains in the direction of the applied field, and their forced-diffusion under applied magnetic field gradients would be much more difficult to describe.

4.4.3.6 Excess chemical potential summary

In this section we considered the main sources of nonidealities in our system of interest. The interactions considered were excluded volume, electrostatic repulsion, depletion effects, and magnetic dipole interactions. By comparing the magnitude of each of the interaction terms, we concluded that the only important interaction for the diffusion of magnetic nanoparticles is their excluded volume. For the 435 nm latex beads, all of the nonidealities appear to be negligible. Finally, for the larger 910 nm beads, volume exclusion, depletion, and induced magnetic-dipole interactions can all be important in regions where the volume fractions of the beads reach values of 0.01 or above. Magnetic-dipole interactions are anisotropic and are not accounted for in our analysis. Since the beads focus on regions where the magnetic field is a minimum, the error introduced by neglecting these interactions is not expected to be appreciable.

For the magnetic nanoparticles, we therefore have that

$$\ln \gamma_m \approx 8\phi_m, \quad (4.65)$$

while for the latex beads, we have

$$\ln \gamma_p \approx 8 \left[1 - \tilde{\beta}(a_p, a_m, \phi_m) \right] \phi_p. \quad (4.66)$$

The value of the depletion parameter $\tilde{\beta}$ is given in Table 4.7 for the magnetic nanoparticle volume fraction listed in Table 4.4.

One thing to note is that Van der Waals interactions are not considered in this analysis. In general, these forces decay very rapidly away from particle surfaces (potentials decay as r^{-6}) and will not have an effect unless the particles are able to somehow overcome the large steric and electrostatic potentials as they are approaching each other. If the species do come close enough together to within distances where Van der Waals forces dominate, they will aggregate irreversibly and we would need to treat this as a chemical reaction between two species, forming a larger species. For the conditions of interest, the electrostatic and steric “barriers” are large enough that aggregation can be neglected within the time scale of our experiments.

4.4.4 Nonideal pseudo-binary diffusion

The molar fluxes derived in Section 4.4.2, given by eqs. (4.25) and (4.27), do not account for the nondidealities introduced in Section 4.4.3. Incorporating the results summarized in the previous section, after some algebra we obtain

$$\underline{J}_m = -\mathcal{D}_{mw} [1 + 8v_m C_m] \underline{\nabla} C_m + \frac{\mathcal{D}_{mw} v_m (1 - v_m C_m)^2}{RT} [C_m \mu_o M_m \underline{\nabla} H]. \quad (4.67)$$

The extra term in the brackets accounts for the volume exclusion between magnetic nanoparticles. Similarly, the flux of the latex beads becomes

$$\underline{J}_p = -\mathcal{D}_{pf} [1 + 8(1 - \tilde{\beta}) v_p C_p] \underline{\nabla} C_p - \frac{\mathcal{D}_{pf} v_p}{RT} [C_p \mu_o M \underline{\nabla} H], \quad (4.68)$$

where the extra term in brackets accounts for volume exclusion and depletion effects. This term is negligible for the smaller 435 nm beads at the concentrations used in this work, but can be appreciable for the larger concentration peaks obtained with the 910 nm beads.

The conservation equations and diffusion coefficients are the same as the ones obtained in Section 4.4.1, namely

$$\frac{\partial C_m}{\partial t} + \underline{\nabla} \cdot \underline{J}_m = 0 \quad (4.69)$$

and

$$\frac{\partial C_p}{\partial t} + \underline{\nabla} \cdot \underline{J}_p = 0 . \quad (4.70)$$

The diffusion coefficients also remain the same, given by

$$\mathcal{D}_{mw} = \frac{kT}{6\pi\eta_w a_m} \quad (4.71)$$

and

$$\mathcal{D}_{pf} = \frac{kT}{6\pi\eta_w \left(1 + \frac{5}{2} v_m C_m\right) a_p} . \quad (4.72)$$

Whereas the conservation equation of the magnetic nanoparticles is decoupled, the conservation equation for the latex beads is coupled to the concentration of the nanoparticles through the diffusion coefficient, the magnetization of the mixture, and the parameter $\tilde{\beta}$.

4.5 Comparison with experimental data

4.5.1 Analytical approximations

To obtain some physical insight into the focusing dynamics of nonmagnetic species immersed in magnetic fluids, several simplifications were made in order to obtain analytical results valid at either very short or very long times. The results give estimates of the behavior at short times, at steady state, and the time necessary to reach steady state.

4.5.1.1 Dynamics at short time scales

At very short times, before diffusion effects come into play and changes in the magnetic fluid profile become important, the one-dimensional governing equation for the latex beads can be approximated as

$$\frac{\partial C_p}{\partial t} = \varphi \frac{\partial (f_p C_p)}{\partial x}, \quad (4.73)$$

where

$$f_p = \mu_o M \nabla H \quad (4.74)$$

is the magnetic force density and the constant (at short times) φ is given by

$$\varphi = \frac{D_{pf} \bar{V}_p}{RT}. \quad (4.75)$$

Since f_p is not a function of time at the time scales of interest, eq. (4.73) can be written as

$$\frac{\partial (f_p C_p)}{\partial t} - \varphi f_p \frac{\partial (f_p C_p)}{\partial x} = 0, \quad (4.76)$$

so that $f_p C_p$ is a constant along the characteristics of eq. (4.76), which are given by

$$\frac{dx_c}{dt} = -\varphi f_p. \quad (4.77)$$

If the force density is linearized about $x = 0$, such that

$$f_p = f_0 x, \quad (4.78)$$

the characteristic equation has the solution

$$\frac{x_c}{x_{c,0}} = \exp(-\varphi f_0 t). \quad (4.79)$$

Since $f_p C_p$ is a constant along the characteristics, we have that

$$f_0 x_c C_p = f_0 x_{c,0} C_{p,0}, \quad (4.80)$$

which gives

$$\frac{C_p}{C_{p,0}} = \exp(\varphi f_0 t). \quad (4.81)$$

Eq. (4.81) tells us that near the region where eq. (4.78) is valid, the concentration of latex beads grows exponentially in time. From eq. (4.79), the characteristics all decay exponentially to $x_c = 0$ to allow for this exponential growth.

From the experimental results presented earlier in this chapter, we see more of a linear increase in the concentration profile of the latex beads. The main reason for this is that the linearized form of the force density is valid only over a very small region and over-predicts the force density everywhere else. However, eqs. (4.79) and (4.81) do provide a qualitative description of the focusing process, where material is coming from both directions and focusing at $x = 0$.

4.5.1.2 Focusing at steady state

At very long times, the concentration of beads in the peaks becomes large enough that Brownian diffusion becomes negligible with respect to volume exclusion and other nonidealities. At steady state, assuming that the term resulting from the excess chemical potential is still valid, the net flux is zero and we have

$$\underline{0} = -\mathcal{D}_{pf} \left[8(1-\tilde{\beta})v_p C_p \right] \underline{\nabla} C_p - \frac{\mathcal{D}_{pf} v_p}{RT} \left[C_p \mu_o M \underline{\nabla} H \right], \quad (4.82)$$

or

$$\underline{\nabla} C_p = -\frac{\mu_o M \underline{\nabla} H}{8RT(1-\tilde{\beta})}. \quad (4.83)$$

Using the previous linearization of the magnetic force density, the concentration profile in the x -direction is given by

$$\frac{dC_p}{dx} = -\frac{f_0}{8RT(1-\tilde{\beta})} x. \quad (4.84)$$

Solving this equation subject to the constraints of mass conservation between the magnet pairs (say $-L$ to L) and non-negative concentration values, we obtain

$$C_p = \frac{C_{p,0}L}{\ell} - \frac{f_0}{48RT(1-\tilde{\beta})} (3x^2 - \ell^2), \quad -\ell < 0 < \ell, \quad (4.85)$$

where

$$\ell = 2 \left(\frac{3RT(1-\tilde{\beta})C_{p,0}L}{f_0} \right)^{1/3}, \quad (4.86)$$

and the concentration is 0 elsewhere between $-L$ and L .

The concentration curve predicted by eq. (4.85) is qualitatively consistent with the concentration profiles obtained in our experiments, where the concentration evolves from the initial uniform profile into a parabolic profile. For the initial bead concentration ($\phi_p = 0.001$) and experimental conditions used in this work, eqs. (4.85) and (4.86) predict

steady-state peaks of thickness $\ell \sim 10 \mu\text{m}$ and normalized concentrations of $\frac{C_p}{C_{p,0}} \sim 1000$,

which essentially means that the beads will continue to accumulate until they reach their maximum packing volume fraction. Based on the focusing rates observed in our experiments, our systems would require about one week to reach steady state.

4.5.2 Magnetic nanofluid defocusing

As depicted in Figure 4-15 and demonstrated in Figure 4-16, the magnetic nanoparticles tend to defocus from the region near $x = 0$, leading to an increase in fluorescence in that region in addition to a smaller magnetic buoyancy force on the nonmagnetic beads. To calculate the concentration profile of the magnetic particles, eq. (4.69) was solved using Comsol Multiphysics, treating the nanoparticles as having an effective magnetic diameter of 6.6 nm and a hydrodynamic diameter of 21.5 nm. The results of the two-dimensional (x - z plane) simulation were then combined with eq. (4.12) to convert the concentration profiles into fluorescence-intensity profiles. The resulting cross-section averaged fluorescence-intensity profiles are shown in Figure 4-21.

As seen in the simulation results, treating the magnetic nanoparticles using only their volume-average magnetic size leads to significant under-prediction of the amount of defocusing near $x = 0$. To account for the polydispersity in magnetic nanoparticle size and get a better estimate for their concentration as a function of time, the magnetic fluid was modeled as a 3-component mixture in a water continuum, as discussed in Chapter 2.

The magnetic diameters and relative mole and volume fractions for each of the components are given in Table 2.1. The $M-H$ relationships for the three magnetic species given in Figure 2-10 were used to calculate their magnetic force densities. The three corresponding hydrodynamic diameters were used as fitting parameters, with the requirement that eq. (2.7) is satisfied for a number-average hydrodynamic diameter of 21.5 nm (obtained from DLS data).

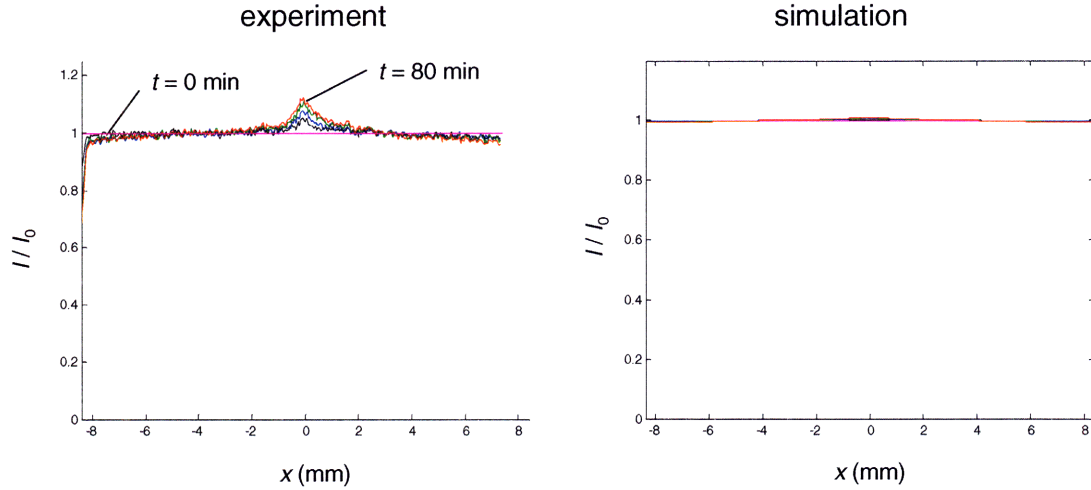


Figure 4-21: Comparison between experimental and model-predicted fluorescence-intensity profiles due to magnetic fluid defocusing. The simulation results treat the magnetic nanoparticles as monodisperse.

For simplicity, the diffusion of each of the three magnetic species was modeled using a pseudo-binary approach. For the model to be valid, the cross-interaction between each of the three species should be negligible, so that each species only “sees” the solvent and itself. The approximate set of equations for the magnetic species is

$$\frac{\partial C_i}{\partial t} + \underline{\nabla} \cdot \underline{J}_i = 0, \quad (4.87)$$

with

$$\underline{J}_i = -\mathcal{D}_{iw} \underline{\nabla} C_i [1 + 8v_i C_i] + \frac{\mathcal{D}_{iw} v_i (1 - v_i C_i)^2}{RT} [C_i \mu_o M_i \underline{\nabla} H]. \quad (4.88)$$

In the above expressions, v_i is the molar volume of magnetic species i and C_i is its molar concentration, given by

$$C_i = x_{m,i} C_p,$$

where $x_{m,i}$ are the fraction of the magnetic particles having size i . At $t = 0$, the values for the $x_{m,i}$ are given in Table 2.1. The total magnetic nanoparticle concentration at any time t is given by

$$C_m = \sum_{i=1}^3 C_i. \quad (4.89)$$

Relating the concentration of magnetic nanoparticles to the change in fluorescence (at constant fluorescent bead concentration) is not as straight-forward as before, since the amount of light attenuation depends on the concentration as well as the size-distribution of the magnetic nanoparticles. The calibration shown in Figure 4-16 assumes that the particle-size distribution is uniform throughout the sample, which of course is not the case in at $t > 0$. For particles much larger than the wavelength of light in the sample, the total amount of light extinction (absorption plus scattered light) is roughly proportional to the projected area of the particles. For colloidal particles much smaller than the wavelength of light, light-extinction effects are more complex. In the limit of small particle diameters with respect to the wavelength of light, the extinction is given by [21]

$$E(\lambda, a) = \frac{24\pi C_m a^3 \epsilon_w^{3/2} L}{\lambda \cdot \ln(10)} \left[\frac{\epsilon_i(\lambda, a)}{(\epsilon_r(\lambda, a) + 2\epsilon_w)^2 + \epsilon_i^2(\lambda, a)} \right], \quad (4.90)$$

where λ is the wavelength of light (from laser light and fluorescence), L is the depth at which the extinction is measured, ϵ_w is the dielectric constant of the medium (water), and ϵ_r and ϵ_i are the real and imaginary dielectric constants of the magnetite nanoparticles with radius a . Since most of the light extinction is due to the magnetic cores, the extinction was assumed to be a function of the magnetic core size, not the overall (hydrodynamic) size of the nanoparticles.

In the limit where the dielectric constants vary negligibly with particle size at a given wavelength, eq. (4.90) predicts that light extinction varies with the volume of the

magnetite nanoparticles. Experimentally, the variations in the dielectric constants result in a dependence of a^m , where m is somewhere between 2 and 4 for particles in the size-range of interest to us [22-25]. For simplicity, light extinction was assumed to be proportional to the volume fraction of magnetic material, or $m \approx 3$. Using the definition of θ_m given in eq. (4.9), for a 0.1 vol % magnetic fluid we therefore have

$$\theta_m = \frac{\sum_{i=1}^3 C_i v_{\text{mag},i}}{0.001}, \quad (4.91)$$

where $v_{\text{mag},i}$ is the magnetic molar volume of species i . This is different from the molar volume used in eq. (4.88), which is based on the total volume of species i (i.e., calculated using its hydrodynamic diameter as opposed to its magnetic diameter)

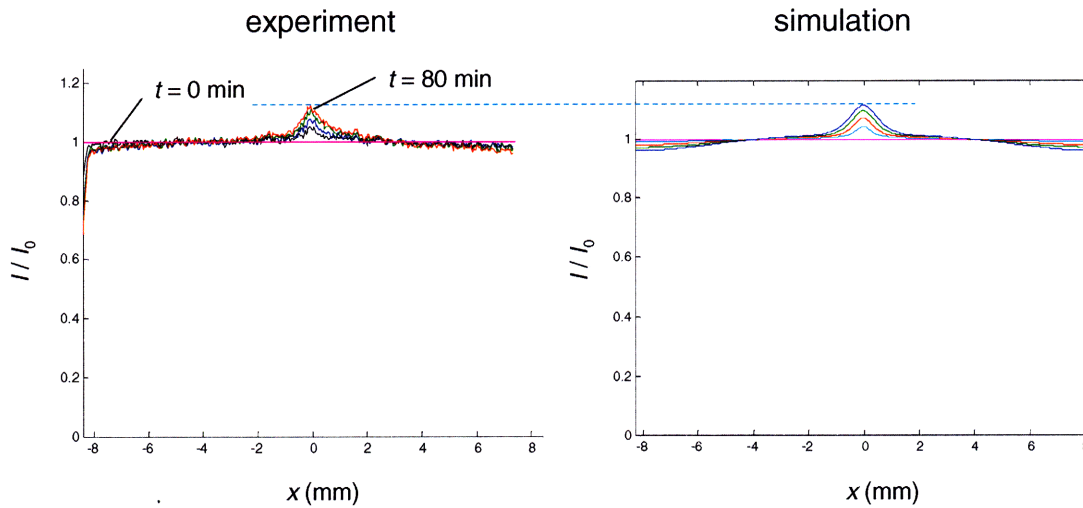


Figure 4-22: Comparison between experimental and model-predicted fluorescence-intensity profiles due to magnetic-fluid defocusing. The simulation results treat the magnetic nanoparticles as a mixture of three different-sized species.

Figure 4-22 shows a comparison between the experimental and the predicted three-component fluorescence-intensity profiles, obtained using the results from eqs. (4.87) and (4.91) in eq. (4.12). The three hydrodynamic diameters used were 21 nm, 30

nm, and 40 nm for the small, medium, and large magnetic nanoparticles, respectively. These three hydrodynamic diameters satisfy eq. (2.7) for a number-average hydrodynamic diameter of 21.5 nm and match the experimental data very well, as can be seen from the dashed line included in the figure. The only part of the profile that cannot be predicted is the sharp drop-off in fluorescence intensity where the magnetic field is a maximum. This is most likely due to errors arising from the approximation used to calculate the magnetic field analytically. Other potential sources of error are that the model only captures three moments of the particle-size distribution, neglects interaction between the different-sized species, and neglects magnetic dipole-dipole interactions, which may be significant for large magnetic nanoparticles at high magnetic-field strengths.

4.5.3 Nonmagnetic species focusing

After having obtained a solution for the magnetic nanoparticle concentration, eq. (4.70) was solved numerically to obtain concentration profiles for the nonmagnetic beads. The first results presented are for a mixture of 910 nm beads in a magnetic nanofluid, at volume fractions of 0.001 for both the beads and magnetite, with 6 mm spacing between the capillary tube and the magnets. The corresponding experimental fluorescence-intensity results were previously shown in Figure 4-18(a). If the magnetic nanoparticles are treated using only one equivalent magnetic diameter, the fluorescence-intensity results presented in Figure 4-23 are obtained.

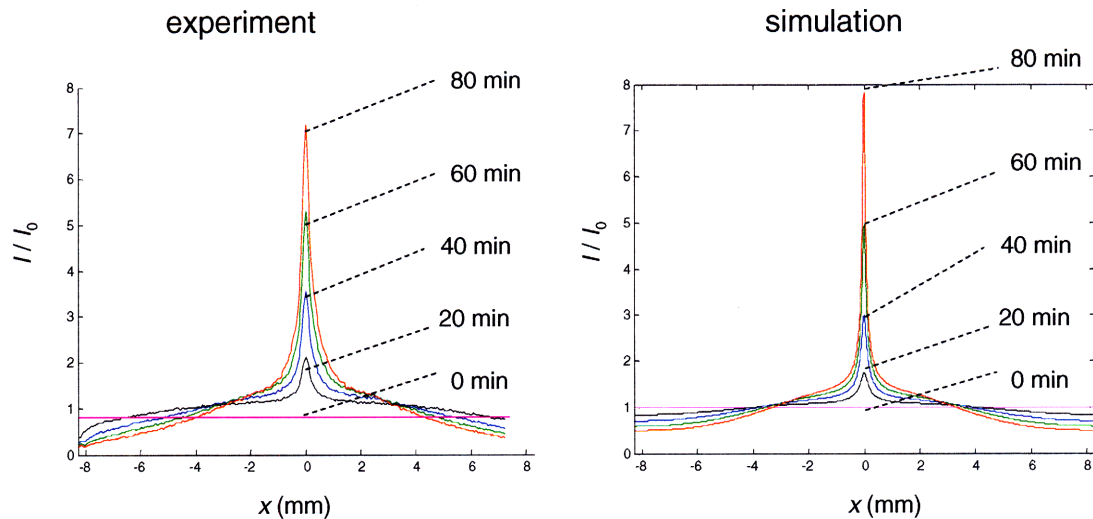


Figure 4-23: Comparison between experimental fluorescence-intensity profiles and the profiles predicted by the 1-component (plus solvent) magnetic-fluid model.

As seen in the figure, the fluorescence intensity in the focusing region is under-predicted at short times and over-predicted at longer times. The reason for the under-prediction at short times is the lack of predicted defocusing of the magnetic nanoparticles near $x = 0$. In the actual experiments, the defocusing of the magnetic nanoparticles in this region led to higher fluorescence intensities for a given latex-bead concentration. At longer times, since the magnetic nanoparticle concentration and average nanoparticle diameter are both over-predicted near the focusing region in this simple model, the force of magnetic origin on the latex bead is higher than it should be. This led to an over-prediction of the amount of latex-bead focusing.

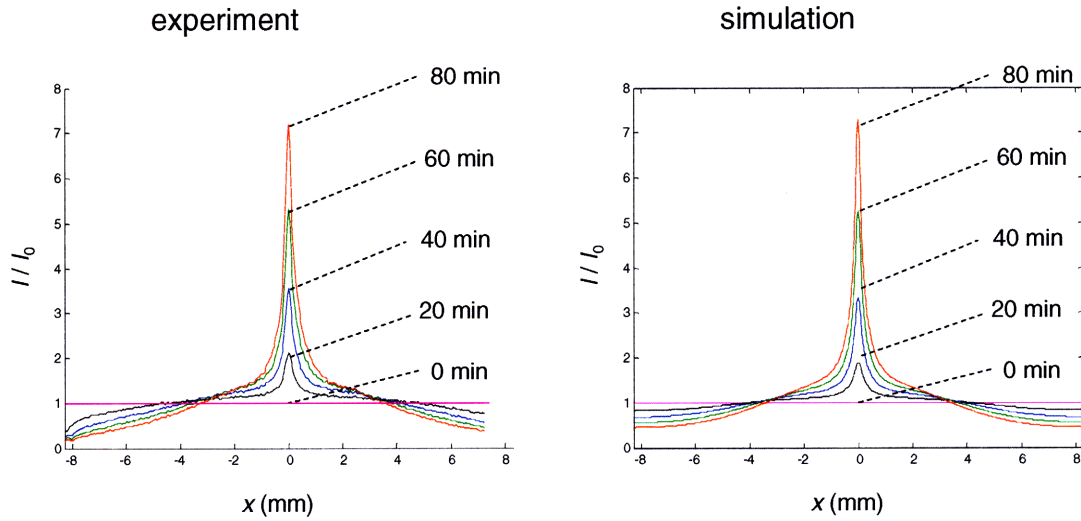


Figure 4-24: Comparison between experimental fluorescence-intensity profiles and the profiles predicted by the 3-component (plus solvent) magnetic-fluid model.

Figure 4-24 shows the results for the same experimental conditions, but using the three-magnetic-size model discussed in the previous section. Since this model does a better job of capturing the amount of magnetic nanoparticle defocusing, it gives better estimates for the fluorescence intensity at short times. At longer times, since it accounts for the lower magnetic fluid concentration and smaller magnetic nanoparticles sizes near the focusing region, the model does not over-predict the amount of latex-bead focusing. Again, as was the case for the magnetic nanoparticle profile, the simulations are off in the regions where the magnetic field strength is a maximum. The difference may be due to approximations made in obtaining the magnetic field profile, magnetic-dipole interaction between the larger magnetic nanoparticles, or the failure to include higher magnetic moments in our simulations.

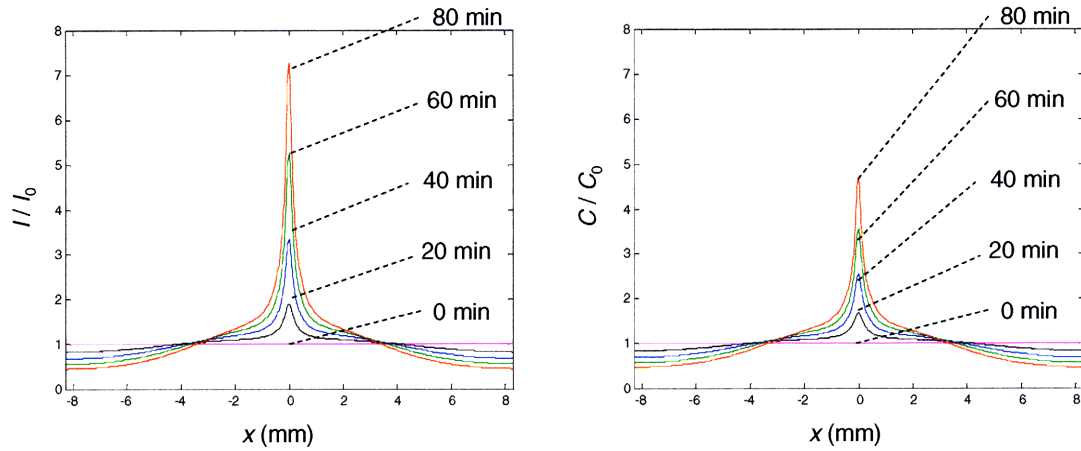


Figure 4-25: Comparison between fluorescence-intensity and latex-bead concentration profiles, as predicted by our model.

A comparison between the simulated fluorescence-intensity and concentration profiles is shown in Figure 4-25. We see that for $t = 80$ min, the fluorescence intensity is about 35% higher than the actual concentration. From Figure 4-22, we know that about 15% of the difference is due to the magnetic fluid concentration decreasing in that region. The other 20% difference comes from the nonlinearity of the fluorescence-intensity vs concentration relationship, as given by eq. (4.4). This nonlinearity is somewhat amplified by the two-dimensional nature of the concentration profile, as shown in Figure 4-26. This figure provides a contour plot of the bead concentration at $t = 80$ min. Due to the force in the z direction pushing the nonmagnetic beads towards the center region of the capillary tube, the maximum concentration at $x = 0$ is about 5 times larger than the cross-section average given in Figure 4-25.

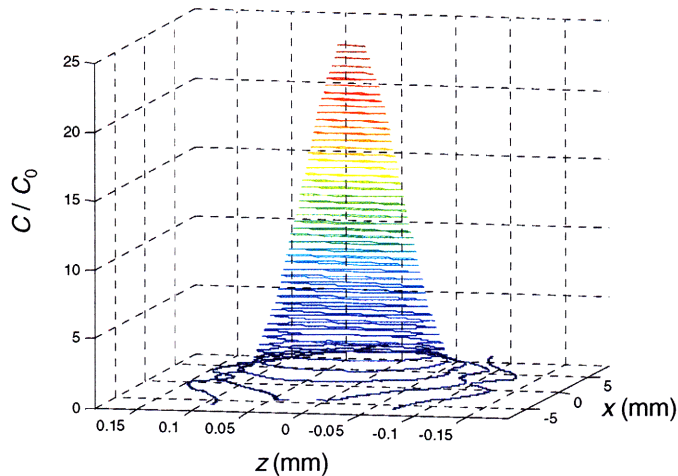


Figure 4-26: Contour plot of the model-predicted concentration profile for the 910 nm beads at $t = 80$ min. The z -direction is along the thickness of the capillary.

4.5.3.1 Effect of magnetic fluid and field strength

Our model was tested against the other experimental conditions presented earlier in this chapter. The first of these comparisons was for the effect of magnetic fluid strength at the same 6 mm spacing used in Figure 4-24. For a 0.05 vol % magnetic nanofluid, using the same conditions as before (0.1 vol % of 910 nm beads, 6 mm spacing, etc.), we obtained the results shown in Figure 4-27. The experimental data are the same as the data shown in Figure 4-18(b). Using no adjustable parameters, the model-predicted results again match the experimental data quantitatively except for the region of high magnetic field strengths.

Figure 4-28(a) shows a comparison between the experimental data and the model-predicted results using a 0.1 vol % magnetic fluid, but a wider spacing between the magnets (7 mm). Part (b) compares the results using the same 7 mm spacing, but at a slightly lower magnetic fluid concentration (0.08 vol %, as previously shown in Figure 4-14). Finally, part (c) of the figure compares the experimental and model-predicted results for a more concentrated fluid (0.2 vol %, as shown in Figure 4-17(b)). In each case, the

model is able to correctly predict the effects of changes in magnetic-fluid and magnetic-field strength, except for the region where the magnetic field strength is the highest.

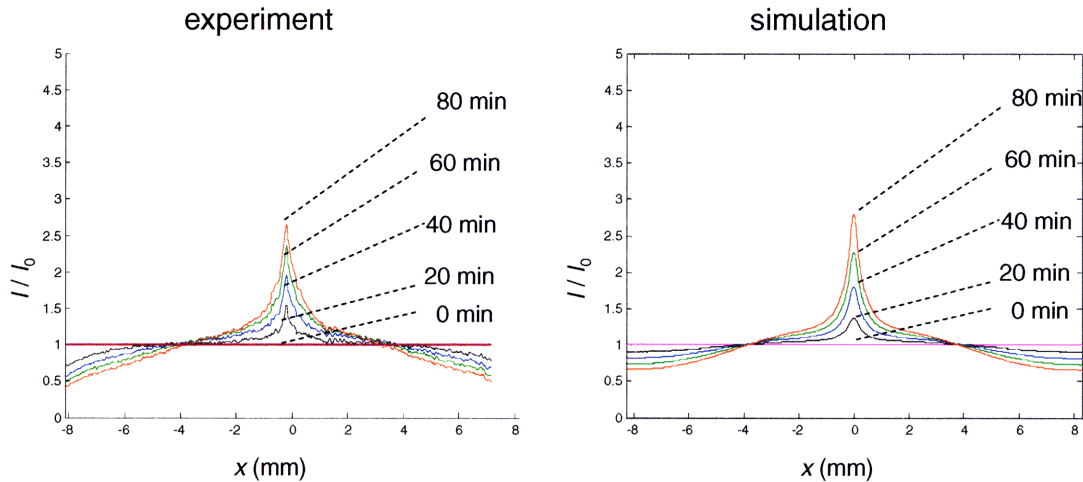


Figure 4-27: Comparison between experimental and model-predicted fluorescence-intensity profiles for a lower magnetic fluid concentration (0.05 vol % magnetite).

The accuracy of the results in Figure 4-28(c) are rather surprising, since many of the assumptions made in the model are no longer valid at such high magnetic fluid and latex-bead concentrations. The interaction between the latex beads and the magnetic nanoparticles, which is neglected in the model, is not negligible at such high latex bead concentrations. Magnetic dipole-dipole interactions between the beads are more important at higher magnetic-fluid concentrations, which may explain the difference in the peak thickness between the experimental and model-predicted results. These effects, however, do not appear to have a significant effect on the focusing peak heights over the 80 minute time-span considered.

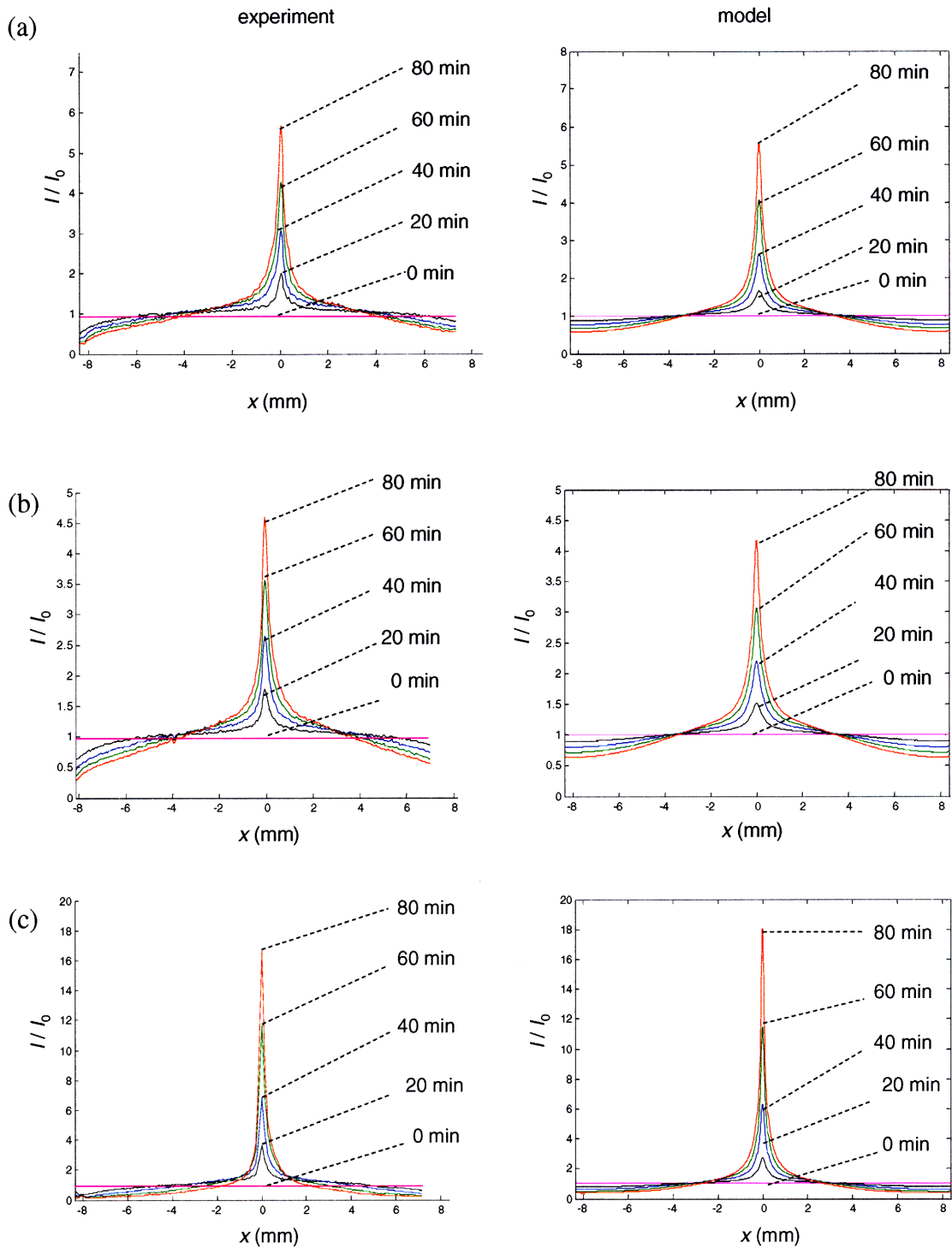


Figure 4-28: Comparison between experimental and model-predicted fluorescence-intensity profiles for a spacing of 7 mm between the magnet and the capillary at different magnetic fluid strengths; (a) 0.1, (b) 0.08, and (c) 0.2 vol % initial magnetite concentrations.

4.5.3.2 Effect of initial latex bead concentration

As previously discussed, the latex-bead fluorescence intensity is not a linear function of the bead concentration, meaning that the normalized fluorescence-intensity profiles should depend on the reference (initial) concentration. This was shown experimentally in Figure 4-19, where three different intensity profiles were obtained using three different initial concentrations for the beads, even though each plot was normalized by the initial fluorescence profile at that concentration.

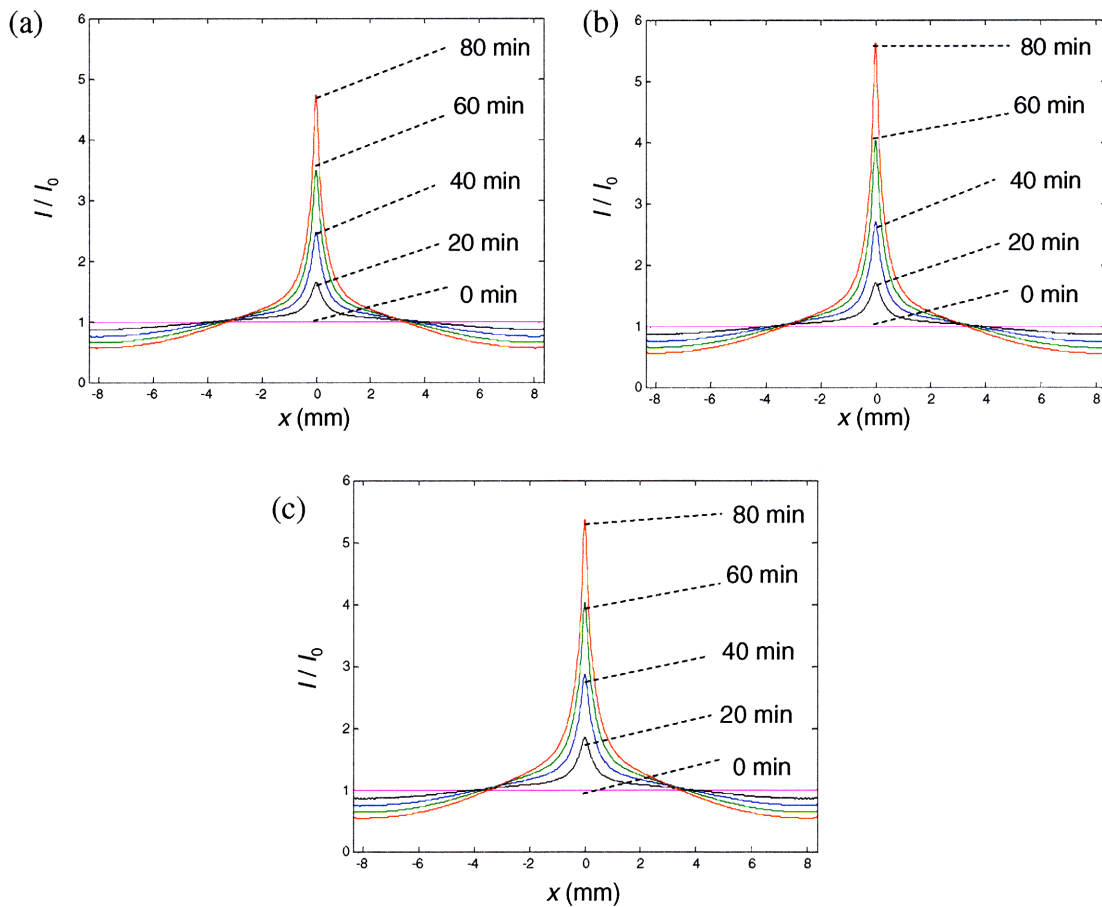


Figure 4-29: Comparison between experimental and model-predicted fluorescence-intensity profiles for 7 mm spacing between the magnet and the capillary at different initial latex-bead concentrations; (a) 0.02, (b) 0.1, and (c) 0.5 vol%.

Figure 4-29 shows the simulation results obtained using the same three initial concentrations presented in Figure 4-19. The model again captures the correct trends observed experimentally, where the highest focusing peak was obtained using an initial latex-bead volume-fraction of 0.001. At higher latex bead concentrations, a combination of fluorescence saturation and excluded-volume effects results in smaller fluorescence-intensity peaks.

4.5.3.3 Effect of latex bead size

In Figure 4-20, we showed the experimental effect of decreasing the latex bead size from 910 to 435 nm. Figure 4-30 shows a comparison between the experimental and model-predicted results for the smaller 435 nm beads at a magnetic fluid concentration of 0.1 vol %, a fluorescent bead concentration of 0.1 vol%, and 6 mm spacing between the magnets and the capillary. Our model is able to quantitatively account for the effect of latex-bead size on their focusing dynamics.

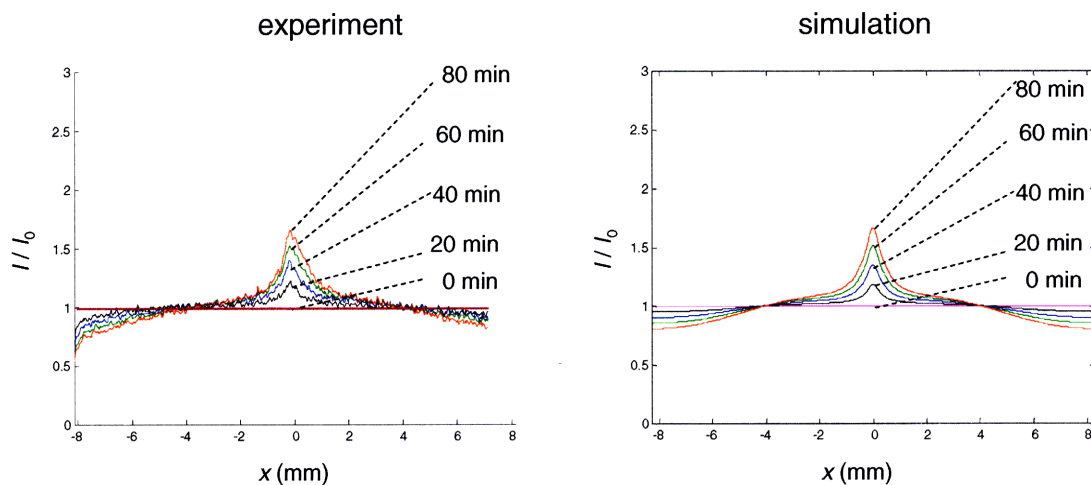


Figure 4-30: Comparison between experimental and model-predicted fluorescence-intensity profiles for 435 nm fluorescent beads.

4.5.4 Focusing under different magnet configuration

As seen in Figure 4-26, our simulation results show that the latex beads were focused in both the x and z directions. This was expected, since the focusing force was found to be of the same order of magnitude in both directions near the focusing region. Unfortunately, due to the lack of resolution at the large working distance used in these experiments (distance between the camera and the sample), we were not able to experimentally verify the amount of focusing in the z -direction predicted in Figure 4-26. The results obtained from the model do, however, suggest that if the capillary tube were lying along the z -axis (see Figure 4-3), the focusing peaks should be of the same order-of-magnitude as the ones obtained with the original configuration, albeit at different locations. This idea was tested using the magnet configuration shown in Figure 4-31, where the magnets are oriented with their magnetic moments along the axis of the capillary tube (now the z -axis).

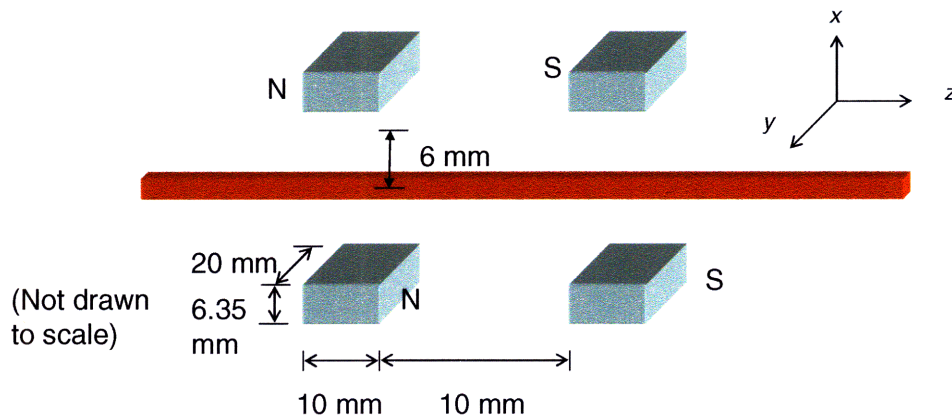


Figure 4-31: Schematic of the experimental setup with a different magnet configuration.

The experimental fluorescence-intensity profiles obtained using this setup are presented in Figure 4-32. Volume fractions of 0.001 of both magnetite and fluorescent beads were used for both of the results shown. The results on the left plot were obtained using 910 nm beads and the results on the right were obtained using 435 nm beads.

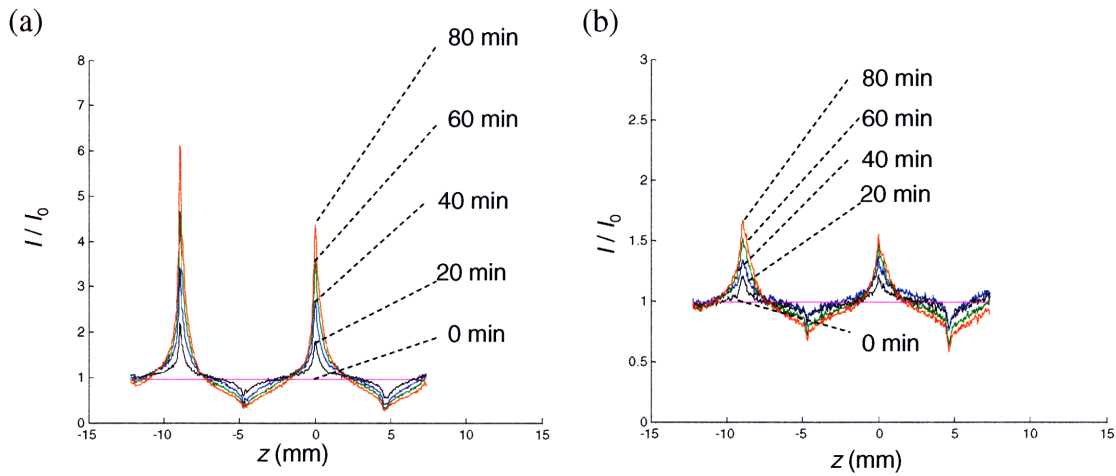


Figure 4-32: Experimental fluorescence-intensity profiles for the flipped magnet configuration; (a) 910 nm beads and (b) 435 nm beads.

Using the approach presented in Chapter 2, the magnetic field and force-density profiles were obtained for this “flipped” magnet configuration. The concentration and equivalent fluorescence-intensity profiles were numerically computed as before, and are given in Figure 4-33. With no adjustable parameters, the model was able to accurately predict the results except in the region where the magnetic field had its highest intensity. The experimental data do not have the third peak at the right because this region was not illuminated with the laser beam. Due to symmetry, we would expect the peaks at the far left and far right to be mirror images of each other, as predicted by the model.

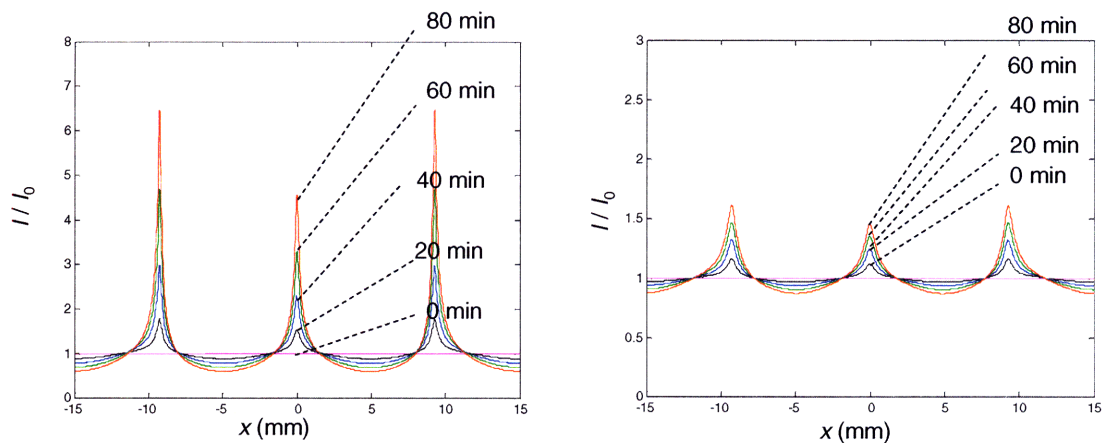


Figure 4-33: Model-predicted fluorescence-intensity profiles for the flipped magnet configuration; a) 910 nm beads and b) 435 nm beads.

4.5.5 Sensitivity studies

As discussed in Chapter 2, the shape of the M - H curve for the magnetic nanofluid is highly sensitive to the size distribution of the magnetic cores. As a consequence, the focusing force density is also sensitive to this size distribution, and simply changing the fluid batch used can yield very different results. The focusing force density is also highly sensitive to the magnetic field profile, as any small changes in the field can lead to appreciable changes in its gradient. In this section, we study the sensitivity of our model-predicted results to changes in M and H .

4.5.5.1 Magnetic field resolution

Figure 4-34 shows a comparison between the analytical solution used so far for the magnetic-field profile and a numerical solution obtained using the Maxwell 3D software. The field-intensity profiles are for the original magnet configuration shown in Figure 4-3, averaged across the capillary tube cross-section, for 7 mm spacing between the magnets and the capillary. In terms of the magnetic field itself, the difference is negligible over most of the range except for the regions closest to the magnets, where the numerical result may actually be more accurate, since it uses the correct value of μ_r (see eq. (3.9)).

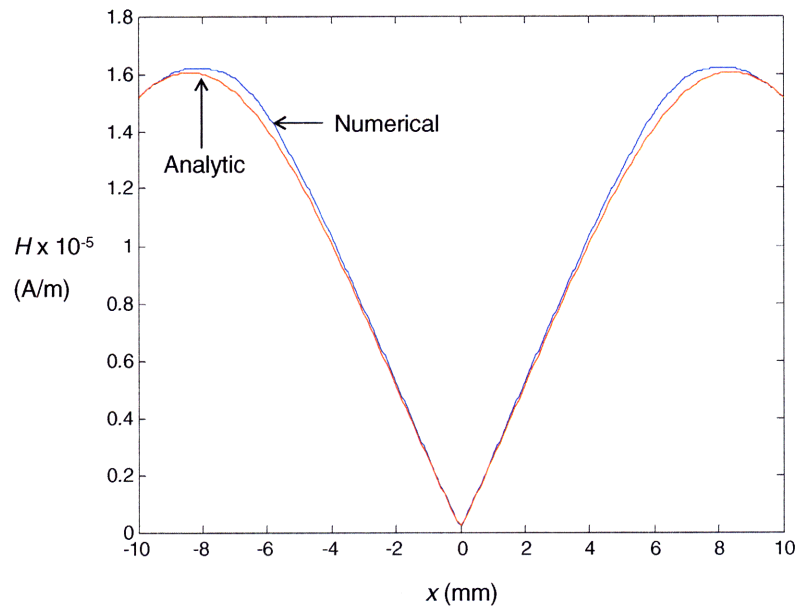


Figure 4-34: Comparison between analytic and numerical magnetic-field intensity profiles for the original magnet configuration depicted in Figure 4-3.

A comparison between the results obtained using the numerical and analytic magnetic fields is shown in Figure 4-35. These results are for a 0.0005 volume fraction of magnetite and a 0.001 volume fraction of 910 nm latex beads, with spacing of 7 mm between the magnets and the capillary tube. Even after a substantial amount of smoothing of both the magnetic field and its gradient, the numerical results still yield fluorescence-intensity profiles which show the effects of noise in the magnetic field profile. With further smoothing, we run the risk of over-smoothing the regions containing large magnetic-field gradients and under-predicting the amount of focusing. One interesting thing to notice about the experimental results is that small changes in the predicted magnetic field arising from numerical noise are enough to give the sharp “dip” in fluorescence intensity found in the experimental data at the regions where the magnetic field is a maximum.

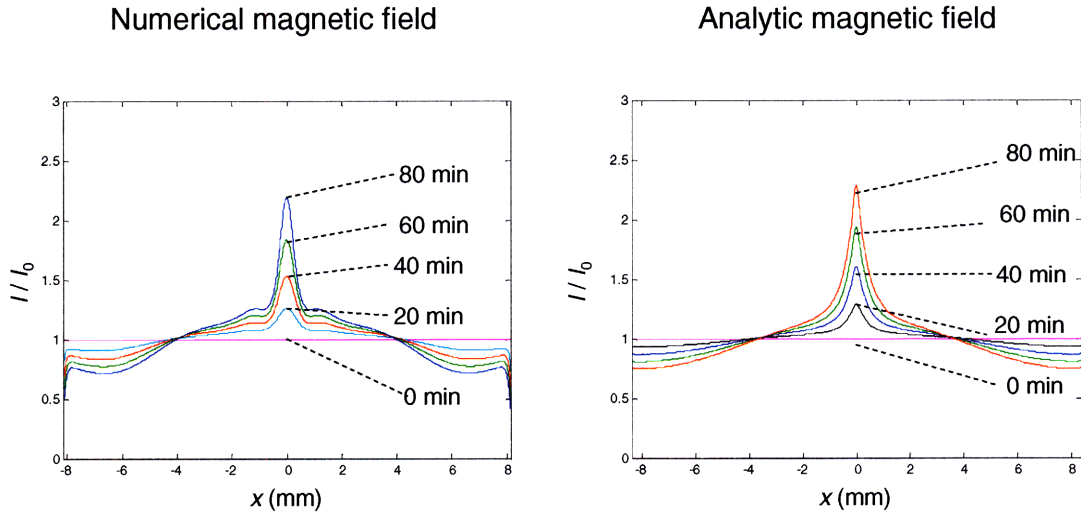


Figure 4-35: Comparison between fluorescence intensity results using numerical and analytic magnetic-field intensity profiles.

4.5.5.2 M-H curves

A simpler way to describe the M - H relationship of a magnetic nanofluid is to use the empirical relationship

$$M = \frac{M_{\text{sat}}}{H_t + H} H, \quad (4.92)$$

where M_{sat} is the saturation magnetization of the fluid and H_t is the value of H at which $M = M_{\text{sat}}/2$. This simple relationship captures the linear behavior of the M - H relationship at low fields and the saturation effect at large fields. This relationship has been used previously to study the magnetophoretic focusing of nonmagnetic species in magnetic nanofluids [25].

Figure 4-36 shows a plot of the experimental M - H data for a 1 wt % magnetic fluid (~0.2 vol %) fitted by eq. (4.92). As seen in the plot, the empirical model predicts magnetization values accurately at high fields, but under-predicts them at low field strengths. Since the focusing of nonmagnetic species occurs in regions where the field is a minimum, such under-prediction will have a significant effect on the resulting concentration profiles. Also, since the magnetization does not have the correct

dependency on the magnetic particle-size distribution, it also fails to account for the changes in magnetization as the magnetic fluid defocuses from the region where the nonmagnetic particles focus.

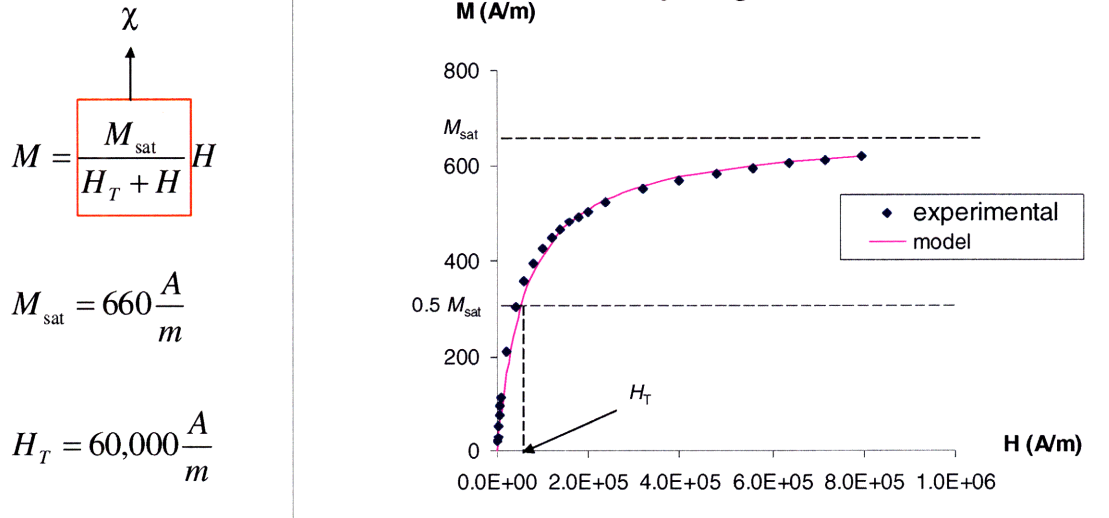


Figure 4-36: Fit to experimental M - H data using eq. (4.92).

Figure 4-37 provides a comparison between the results obtained using eq. (4.92) and a Langevin expression for the fluid magnetization. Since eq. (4.92) does not account for different-sized magnetic nanoparticles, the predictions using this empirical relationship were compared to the one-component (plus water) model described in Section 4.5.2. The parameters used in both simulations were 0.1 vol % of both magnetite and 910 nm fluorescent beads and a spacing of 6 mm between the magnets and the capillary tube. The results using a Langevin model were presented previously in Figure 4-23.

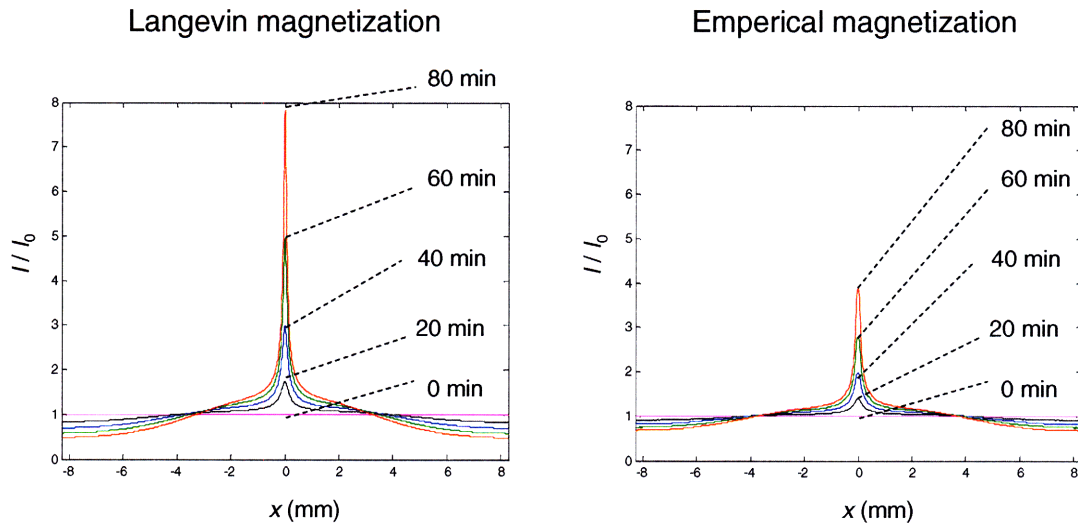


Figure 4-37: Comparison between fluorescence intensity results using numerical and analytic magnetic-field intensity profiles.

4.5.6 Experimental artifacts

There were several experimental artifacts encountered that were initially interpreted incorrectly. The main artifacts are discussed in this section, as these will probably present themselves during future experimental work in this area.

4.5.6.1 Latex bead settling

The fluorescent beads obtained from the manufacturer have a specific gravity of 1.05. In the absence of concentration gradients, the density of the magnetic nanofluid continuum is about 1.004, which means that the latex beads will settle over time. This slow settling was initially believed to be negligible, but when coupled with the small penetration depth of laser light into the sample (the intensity of the laser beam drops to 37% of its original value at about 1/4 of the way into the channel, or 100 μm), the effect of settling on fluorescence intensity can be appreciable.

For the 910 nm beads, a force balance between their weight, the gravitational buoyancy force from the fluid, and viscous drag results in a settling velocity of

0.12 $\mu\text{m}/\text{min}$, which equates to a settling distance of 9.6 μm over the 80 min duration of the focusing experiments. At this distance, the fluorescence intensity from a latex bead originally near the top surface of the capillary tube is 83% of its original value. This loss of fluorescence intensity is consistent with the values observed experimentally, where there would be 15-25 loss in fluorescence over a time period of 80 minutes.

Initially, this loss in fluorescence was attributed to photobleaching, which is the permanent loss of fluorescence catalyzed by high-intensity light. Fluorescence studies in the absence of magnetic nanoparticles eventually dismissed this hypothesis. The loss of fluorescence from the mixture of latex beads suspended in a magnetic nanofluid was eliminated by increasing the density of the magnetic nanofluid to match that of the latex beads using sucrose.

4.5.6.2 Fluorescence enhancement from non-fluorescent beads

In Figure 4-16, we approximated the increase in fluorescence due to magnetic nanofluid defocusing by measuring the increase in fluorescence from a mixture of magnetic fluid and 81 nm fluorescent, nonmagnetic beads. This would have been the same increase in fluorescence during a focusing experiment if the magnetic nanoparticles did not interact with the focusing species. In an attempt to measure possible interactions between the focusing latex beads and the magnetic nanoparticles, the experiment presented in Figure 4-16 was repeated, but with the addition of 910 nm nonmagnetic, non-fluorescent beads at a concentration of 0.1 vol%. The idea was that these non-fluorescent beads would affect the fluorescence-intensity profile only if there were any interactions (such as volume exclusion) between the beads and the magnetic nanoparticles.

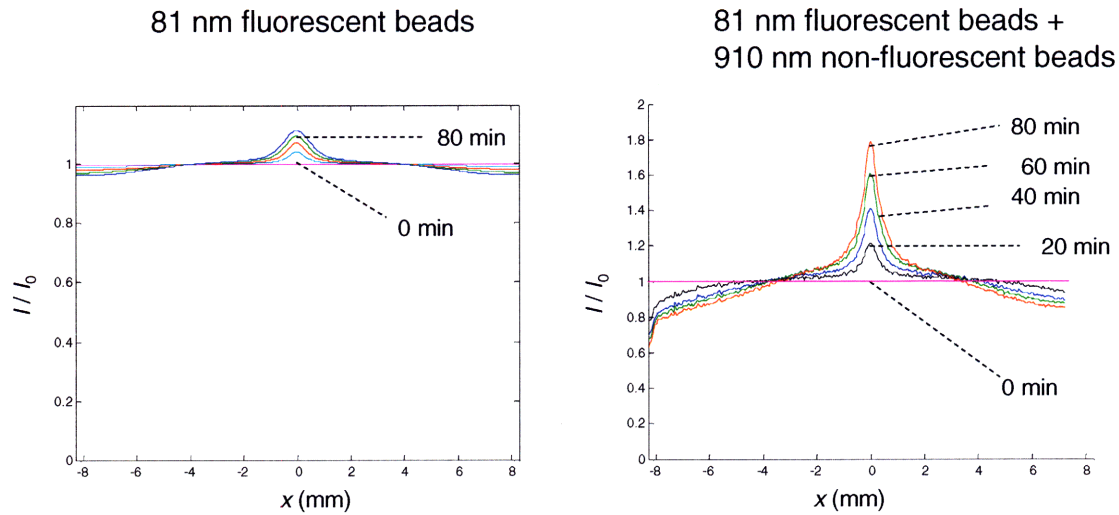


Figure 4-38: Increase in fluorescence due to the focusing of non-fluorescent beads.

Figure 4-38 shows a normalized fluorescence-intensity plot for a focusing experiment using a mixture of 81 nm fluorescent beads and 910 nm non-fluorescent beads. This profile is compared to the one obtained in the absence of the 910 non-fluorescent beads, as shown previously in Figure 4-16. As seen in Figure 4-38, there is an increase in fluorescence intensity near $x = 0$ when the non-fluorescent beads are added, which was initially attributed to exclusion of the magnetic nanoparticles by the focusing 910 nm beads.

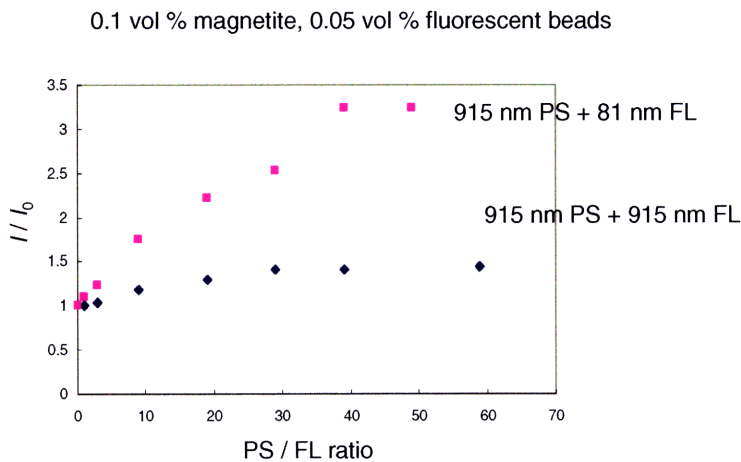


Figure 4-39: Increase in fluorescence due to an increase of non-fluorescent bead concentration.

In reality, this fluorescence enhancement was due to multiple scattering arising from the presence of the 910 nm beads. Figure 4-39 shows a plot of fluorescence intensity as a function of non-fluorescent bead concentration at a constant concentration of fluorescent beads. As seen in the image, increasing the concentration of latex beads increases the fluorescence intensity even if the number of fluorescent beads is kept constant. The effect is especially pronounced when the size ratio of non-fluorescent to fluorescent beads is large, as observed for the mixture of 81 nm and 910 nm beads. The increase in fluorescence observed in Figure 4-38 is not due to displacement of the magnetic nanoparticles, but to the increase in latex bead concentration in the focusing region. A similar phenomena was observed in the calibration curves presented in Figure 4-11 and Figure 4-12, where increasing the concentration of fluorescent beads resulted in a super-linear increase in fluorescence. In fact, the profile observed in Figure 4-12 greatly resembles the lower curve in Figure 4-39.

4.5.6.2 Species aggregation

The results presented in this chapter are for the case of negligible aggregation between the latex beads and between the beads and the magnetic nanoparticles. In general, the latex beads had to be used within three months of receipt from Spherotech or there would be some noticeable aggregation present. Focusing experiments performed using older samples would have concentration peaks much higher than the ones presented in this work due to the larger average-particle size.

Another type of aggregation encountered was the aggregation between the latex beads and the magnetic nanoparticles. Over time, the magnetic nanoparticles would stick to the latex beads and give them a positive magnetic moment. The use of SDS significantly reduced this rate of aggregation, but aggregation was still an issue for older samples. For the experimental results presented in this chapter, the samples were used within 24 hours of preparation to minimize this effect.

4.6 Conclusions

In this chapter, we investigated the different parameters affecting the focusing of submicron, nonmagnetic particles immersed in magnetic nanofluids. Focusing was monitored experimentally using fluorescence imaging. The results were modeled using continuum species-conservation equations with the forced diffusion driving forces presented in the previous chapter. Excess chemical potentials were introduced to account for nonidealities such as volume exclusion, electrostatic repulsion, depletion effects, and magnetic dipole interactions. Only volume exclusion and depletion effects were incorporated in the model.

Our model, which contains no adjustable parameters, was able to predict the experimentally-obtained concentration profiles of nonmagnetic particles both qualitatively and quantitatively over a wide range of experimental conditions. As expected, focusing was found to increase with magnetic fluid and magnetic field strength as well as nonmagnetic particle size. The model was highly sensitive to the accuracy and smoothness of the magnetic field data as well as with the magnetization dependence on the magnetic field strength.

Our studies unveiled that as the nonmagnetic particles are focusing in the region of minimum field strength, the larger magnetic nanoparticles are defocusing from that region, leading to a decrease in magnetophoretic focusing-force over time. Our model would not be able to capture the correct focusing dynamics if the polydispersity of the magnetic nanofluid were neglected. In order to obtain accurate results, three moments of the magnetic size distribution were used in our model.

4.7 Bibliography

1. Fateen, S. Magnetophoretic *Focusing of Submicron Particles Dispersed in a Polymer-Based Magnetic Fluid*. Ph.D. thesis, Massachusetts Institute of Technology, 2002.

2. Moeser, G.D., et al. Water-based magnetic fluids as extractants for synthetic organic compounds. *Industrial & Engineering Chemistry Research*, 41(19): 4739-4749, 2002.
3. Moeser, G.D. *Colloidal Magnetic Fluids as Extractants for Chemical Processing Applications*. Ph.D. thesis, Massachusetts Institute of Technology, 2003.
4. Lee, I.Y.S., and Suzuki, H. Energy transfer and amplified spontaneous emission in temperature-controlled random scattering media. *J. Phys. Chem. B*, 112:4561-4570, 2008.
5. Deen, W.M. *Analysis of Transport Phenomena*. Oxford University Press, New York, 1998.
6. McMillan, W.G. and Mayer, J.E. The statistical thermodynamics of multicomponent systems. *Journal of Chemical Physics*, 13(7): 276-305, 1945.
7. Hirschfelder, J.O., Curtiss, C.F. and Bird, R.B. *Molecular Theory of Gases and Liquids*. John Wiley & Sons, New York, 1964.
8. McQuarrie, D.A. *Statistical Mechanics*. Harper Collins Publishers, New York, 1976.
9. Lekkerkerker, H.N.W., et al. *Observation, prediction and simulation of phase transitions in complex fluids*. Kluwer Academic Publishers, Boston, 1995.
10. Minton, A.P. Molecular crowding: Analysis of effects of high concentrations of inert cosolutes on biochemical equilibria and rates in terms of volume exclusion. *Energetics of Biological Macromolecules, part B*. 295: 127-149, 1998.
11. Striolo, A., et al. Forces between aqueous nonuniformly charged colloids from molecular simulation. *Journal of Chemical Physics*, 116(17): 7733-7743, 2002.
12. Ohshima, H. and Furusawa, K. *Electrical Phenomena at Interfaces*. Marcel Dekker, New York, 1998.
13. Walz, J.Y. and Sharma, A. Effect of long-range interactions on the depletion force between colloidal particles. *J. Colloid Interface Sci.*, 168(2): 485-496, 1994.
14. Oversteegen, S.M. and Lekkerkerker, H.N.W. On the accuracy of the Derjaguin approximation for depletion potentials. *Physica A*, 341: 23 – 39, 2004.
15. Mao, Y., Cates, M.E., and Lekkerkerker, H.N.W. Depletion force in colloidal systems. *Physica A*, 222(1-4): 10-24, 1995.

16. Donselaar, L.N. and Philipse, A.P. Interactions between silica colloids with magnetite cores: diffusion, sedimentation and light scattering. *Journal of Colloid and Interface Science*, 212: 14–23, 1999.
17. Skjeltorp, A T. One-dimensional and two-dimensional crystallization of magnetic holes. *Physical Review Letters*, 51(25): 2306-2309, 1983.
18. Pincus, P. Static conformations and dynamics of colloidal suspensions of ferromagnetic grains. From *Thermomechanics of Magnetic Fluids*, by Berkovsky B. Hemisphere Publishing Corp., Washington, pp. 87-96, 1978.
19. Helgessen, G., Svasand, E., and Skjeltorp, A.T. Nanoparticle induced self-assembly. *Journal of Physics-Condensed Matter*, 20(20), 2008.
20. Clausen, S., Helgesen, G., Skjeltorp, A.T. Anomalous diffusion in a simple magnetic hole system. *Physica A*, 238(1-4): 198-210, 1997.
21. Haes, A., et al. Using solution-phase nanoparticles, surface-confined nanoparticle arrays and single nanoparticles as biological sensing platforms. *Journal of Fluorescence*, 14(4): 355-367, 2004.
22. Liu, X., et al. Extinction coefficient of gold nanoparticles with different sizes and different capping ligands. *Colloids and Surfaces B: Biointerfaces*, 58: 3-7, 2007.
23. Cademartiri, L., et al. Size-dependent extinction coefficients of PbS Quantum Dots. *J. Am. Chem. Soc*, 128: 10337-10346, 2006.
24. Muskens, O.L., et al. Single metal nanoparticle absorption spectroscopy and optical characterization. *Applied Physics Letters*, 88(063109): 1-3, 2006.
25. Evanoff, D.D. and Chumanov, G. Size-controlled synthesis of nanoparticles. 2. Measurement of extinction, scattering, and absorption cross sections. *J. Phys. Chem. B*, 108: 13957-13962, 2004.
26. Gonzalez, L.A., et al. Magnetophoresis of Nonmagnetic, Submicrometer Particles in Magnetic Fluids. *MEBCS Proceedings of the Fourth SMA Symposium*, Singapore, 2004.
27. Rosensweig, R.E. *Ferrohydrodynamics*. Cambridge University Press, New York, 1985.

Chapter 5

5. Magnetophoretic Trapping

In the previous chapter, the dynamics of nonmagnetic species immersed in magnetic nanofluids under applied magnetic fields were studied for systems with negligible flow. In this chapter, we study the coupling between negative magnetophoresis and flow-induced drag as applied to the size-based trapping of nonmagnetic species.

The concept behind the size-based trapping technique used in this work was introduced conceptually in Chapter 1 and is illustrated again in Figure 5-1. A mixture of relatively small (red) and large (blue) particles is suspended in a ferrofluid and convected in the $+z$ direction of a flow channel. A magnetic field is generated in such a way that its gradient is small in the entrance region and increases in magnitude further downstream. These gradients generate a trapping force density that increases in magnitude as the particles flow down the channel. As per eq. (1.5), smaller force densities are sufficient to trap larger particles, so these are expected to be trapped against flow near the entrance of the channel. The smaller red particles require higher stopping force densities, so they should be trapped further downstream.

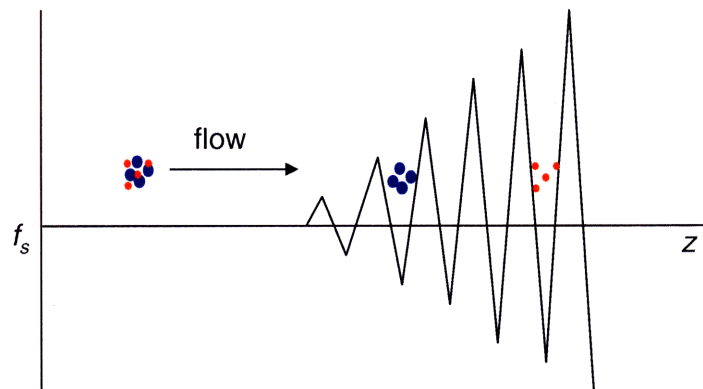


Figure 5-1: Schematic of the technique used to size-selectively trap nonmagnetic particles immersed in a magnetic nanofluid.

There are two reasons for the oscillating nature of the trapping force density depicted in Figure 5-1. The first is that high magnetic field gradients are needed to achieve the required stopping (or trapping) force densities, and the most effective way to achieve this is to have local peaks in the magnetic field profile. This automatically results in an oscillating trapping force density. The second reason is that we are interesting in focusing and concentrating the nonmagnetic particles as they are trapped.

Size-based trapping using this procedure was achieved using a micro-fabricated device (chip). The design and fabrication of such chips and the experimental results obtained using the chips in the presence of an external magnetic field have been published elsewhere [1]. This chapter is concerned with the modeling of these experimental results as well as with the design and implementation of macroscopic devices designed to improve on the shortcomings of the micro-chip.

5.1 Micro-chip trapping experiments

The trapping of nonmagnetic, submicron particles immersed in a magnetic nanofluid was studied experimentally by monitoring the concentration profiles of fluorescently-tagged latex beads. As in the focusing experiments, LIFI was used to measure the temporal and spatial variations in their concentration profiles as they flowed in a micro-chip in the presence of an externally applied magnetic field. Concentration profiles were approximated from the fluorescence intensity emitted by the latex beads. The experimental results have been published elsewhere [1] and are briefly summarized in this chapter.

5.1.1 Materials

The fluorescent beads used for trapping were also obtained from Spherotech. In the work published by Park [1], the small and large fluorescent polystyrene beads were described as having diameters of 510 nm and 840 nm, respectively. SEM images and Dynamic Light Scattering (DLS) data have since revealed that the diameters were

actually 435 nm and 865 nm, respectively. With the exception of the SDS surfactant and NaCl, the materials used to prepare the samples were the same as the ones discussed in Section 4.1.1.

5.1.2 Experimental Setup

A schematic of the experimental setup used is shown in Figure 5-2. A syringe pump (Model M365, Sage Instruments-Thermo Electron, Waltham, MA) was used to pump a mixture of magnetic nanofluid and fluorescent, nonmagnetic beads into a flow channel inside the chip using a 25 μ L precision syringe. Unlike the focusing experiments, the feed mixture contained both the small and the large nonmagnetic beads simultaneously. Two permanent magnets were used to generate a magnetic field which was modified into the desired profile by magnetic cores in the chip. A schematic and a photograph of the micro-chip are included in Figure 5-3.

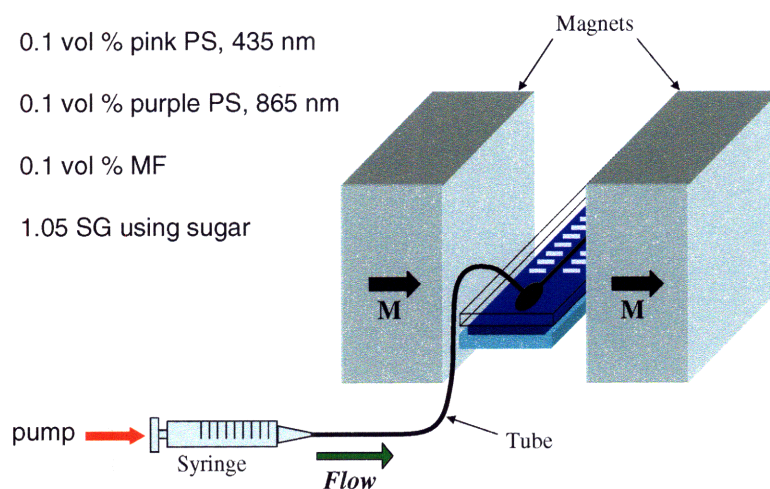


Figure 5-2: Schematic of the experimental setup used for the micro-chip trapping experiments.

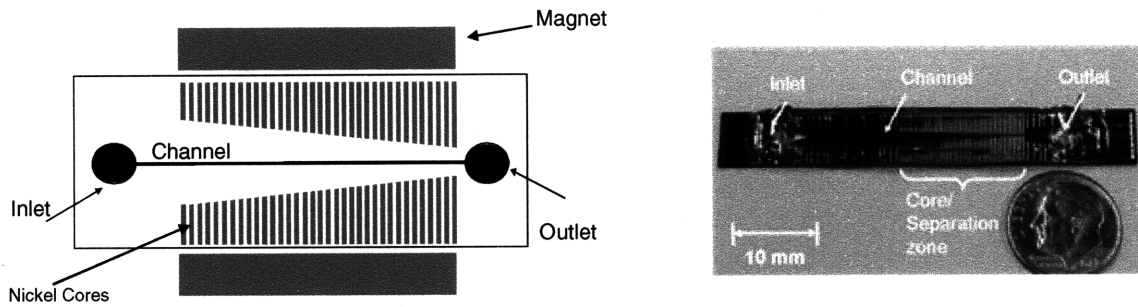


Figure 5-3: Schematic (left) and photograph (right) of the micro-chip used for the trapping experiments.

5.1.3 Magnetic and force fields

The magnetic field within the channel region was computed numerically using the software Maxwell 3D. The field intensity and resulting force density in the flow direction for a 0.1 vol % magnetic nanofluid, averaged across the flow-channel cross-section, are shown in Figure 5-4. The force density resembles the schematic profile depicted in Figure 5-1. More details on the design and computation of the magnetic and force-density profiles are given by Park [1].

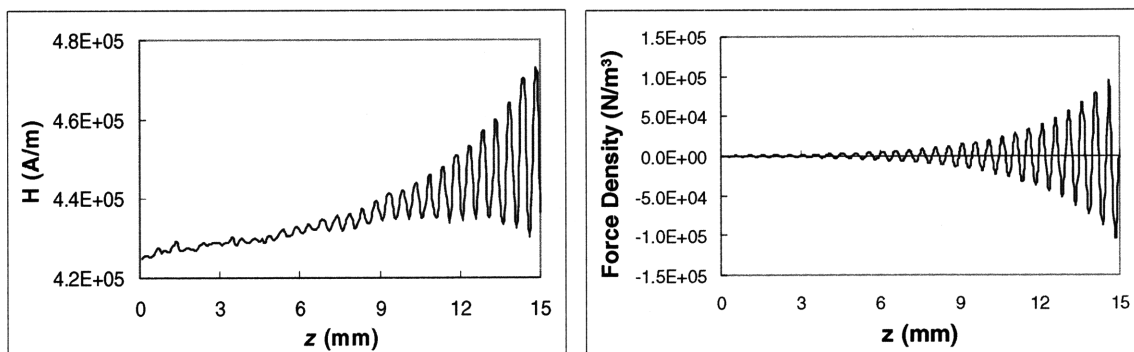


Figure 5-4: Magnetic field intensity (left) and force density in the z direction for a 0.1 vol % magnetic nanofluid (right) averaged across the flow-channel cross-section.

Since the height of the cores is approximately the same as the channel height, end effects (i.e., fringing fields) were appreciable and the magnetic field varied considerably in all three spatial directions. Figure 5-5 shows an intensity plot of the magnetic field in a cross section of the channel between two magnetic cores. In this figure, the flow field is in the z direction, the magnetic cores oppose each other in the x direction, and the y direction is the viewing direction, where the laser beam penetrates the sample and fluorescence intensity is measured. As seen in the figure, the magnetic field strength is highest near the cores and weakest at the top and bottom of the channel. As a result, there are force densities pushing the particles in the x direction towards the center of the channel and in the y direction towards the top and bottom of the channel. Cross-section averages of these force densities (in the square region between $x = y = 0$ and $x = y = 50 \mu\text{m}$) are given in Figure 5-6. As seen in this figure, the transverse (perpendicular to the flow direction) magnetic force-densities are of the same order-of-magnitude as the force density in the direction of flow. In the latter figure, the curves in blue were obtained using the magnetic field data generated using Maxwell 3D and the red curves are empirical fits, discussed later on in this chapter.

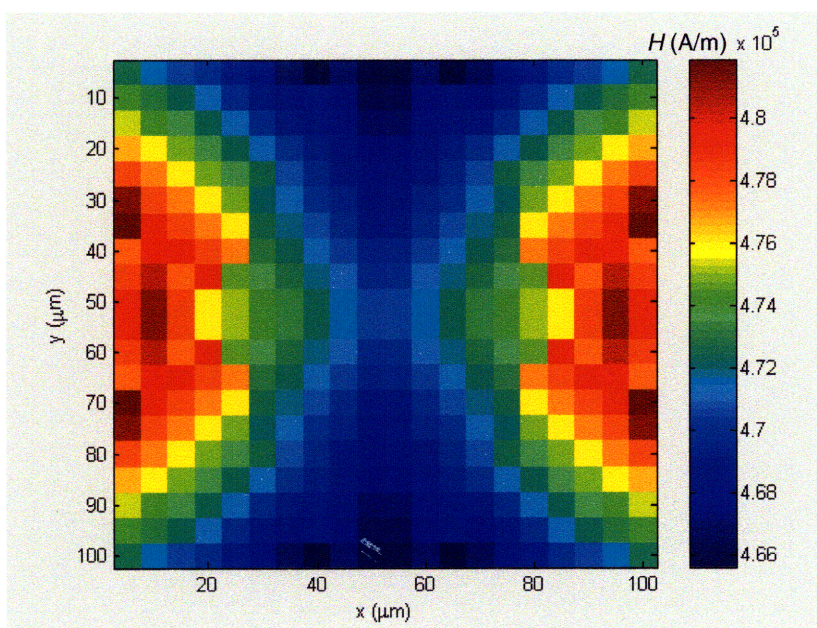


Figure 5-5: Magnetic field intensity over a cross-section of the flow channel.

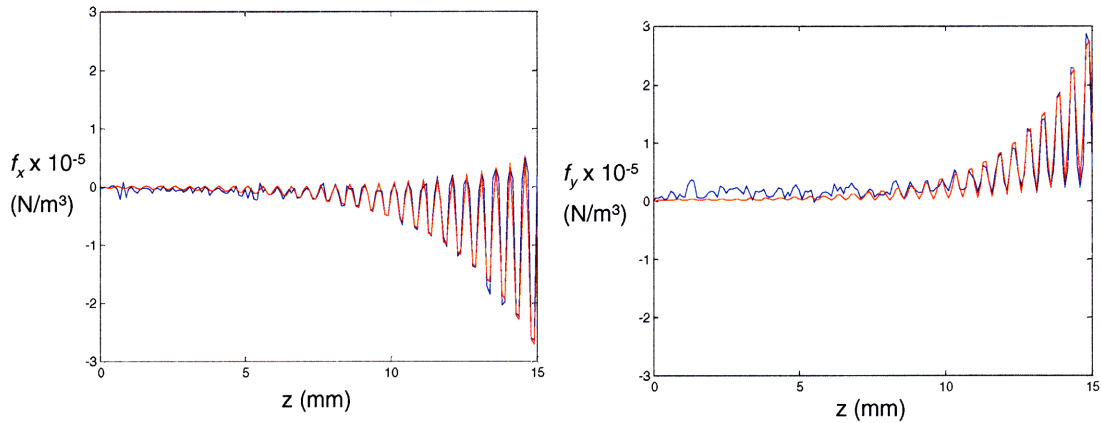


Figure 5-6: Force densities in the x and y directions for a 0.1 vol % magnetic nanofluid averaged over the cross-section of the flow channel.

The local force densities within the channel are not uniform over the entire cross-section of the channel. The x -force density varies approximately linearly with x , with the force density being zero at the center of the channel and $f_x(0, y) = -f_x(L_x, y)$, where L_x is the width of the channel. Similarly, the y -force density varies approximately linearly with y , with the force density being zero at the center of the channel and $f_y(x, 0) = -f_y(x, L_y)$, where L_y is the height of the channel. The dependence of f_x on y and the dependence of f_y on x are more complex. In general, the magnitude of f_y is smaller near the center of the channel than near the side walls, and the magnitude of f_x is higher near the center of the channel than near the top and bottom walls.

5.1.4 Sample preparation

The samples were prepared in 2 mL plastic vials, with the typical sample volume being 200 μ L. Some common amounts for each of the components are listed in Table 5.1. The quantities are very similar to the ones presented in Table 4.2, but without salt and SDS. For the flow experiments, we were not as concerned with controlling the extent of electrostatic interactions, so no efforts were made to control the Debye length via the addition of salt.

Table 5.1: Common sample volumes and concentrations used in the flow-chip experiments

Component	Amount (μL)	Concentration in Mixture
2.3 wt % magnetic fluid	45	0.1 vol %
1 wt % 435 nm latex beads	20	0.1 vol %
1 wt % 865 nm latex beads	20	0.1 vol %
1.28 SG sugar solution	31	15.5 vol %
DI water	84	-
total	200	-

5.1.5 Fluorescence imaging

The concentration of the different-sized latex beads were monitored using LIFI. For multiple species, the concept used is illustrated in Figure 5-7, where one wavelength of light was used to excite two species with overlapping excitation curves. Different optical filters were used to differentiate between the fluorescence being emitted by each species.

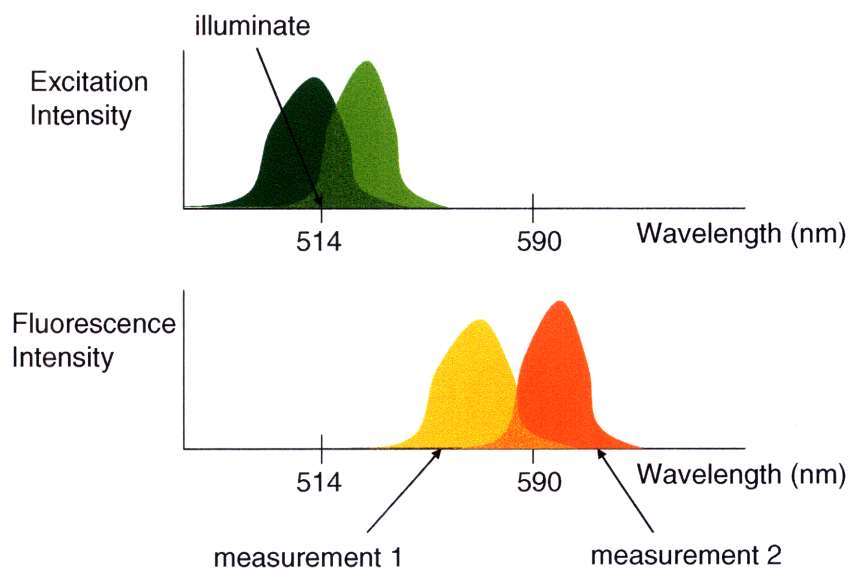


Figure 5-7: Schematic of LIFI for multiple species.

5.1.6 Data acquisition

The setup used to monitor the concentration profile of the fluorescent beads was similar to the one depicted earlier in Figure 4-8, but with the incorporation of the extra components shown in the photograph at the bottom of the figure. A schematic of this setup is given in Figure 5-8. A beam-splitter was used to split the fluorescence signal and send half of it to CCD Camera 2. Emission filter 1 was designed to pass the fluorescence signal from one of the species and Emission filter 2 to pass the fluorescence from the other species. More details about this setup are given by Park [1].

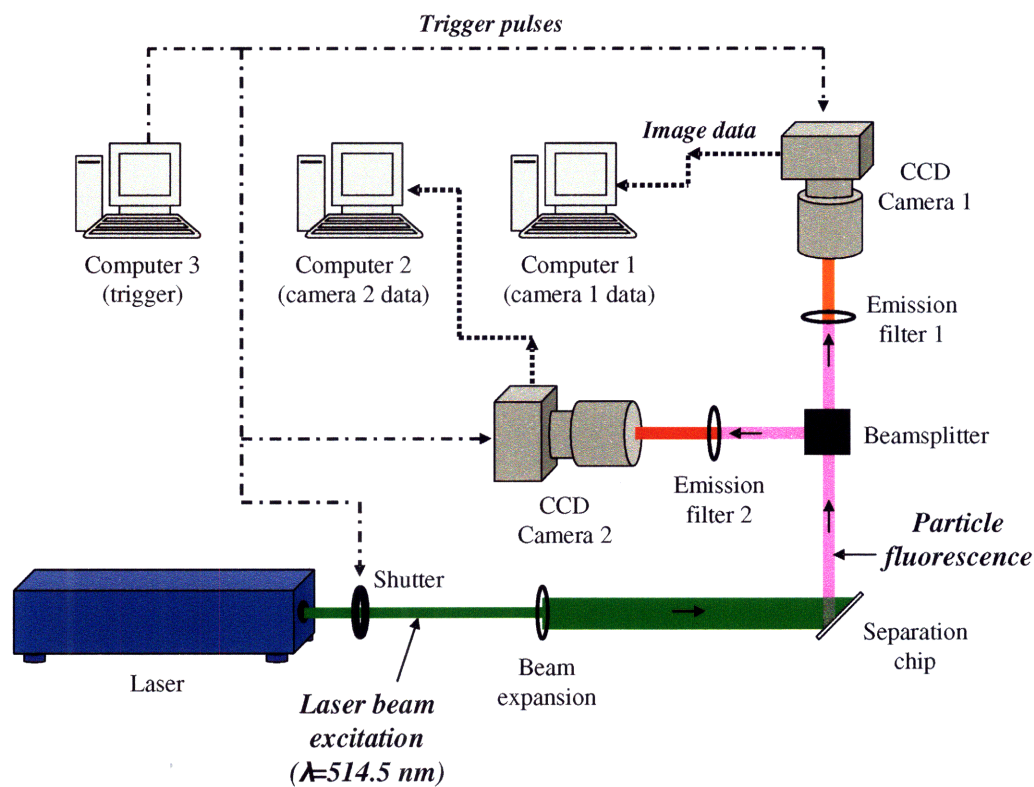


Figure 5-8: Schematic of the data-acquisition setup for multiple species.

5.2 Data processing

Before the start of each experiment, a background image was taken at the normal operating conditions (i.e., laser power, exposure time, etc.) with a 0.1 vol % ferrofluid in the channel. As before, this image was used to subtract out background noise. After emptying the channel, the full mixture containing the 435 nm and 865 nm beads was injected into the channel and a reference image was recorded.

Ideally, the fluorescence signal from each species could be isolated by each optical filter, resulting in no coupling between the signals of the two different-sized beads. Unfortunately, to obtain similar fluorescence intensities from both species at the same excitation wavelength (514.5 nm), the emission curves of the two dyes used (“purple” and “pink”) had some overlap. Figure 5-9 shows the normalized fluorescence spectra of the two species used, 435 nm “pink” particles and 865 nm “purple” particles. As seen within the shaded regions corresponding to the bandwidths of the optical filters used, there was some overlap between the two fluorescent signals, and the signals captured by each camera contained data from both species.

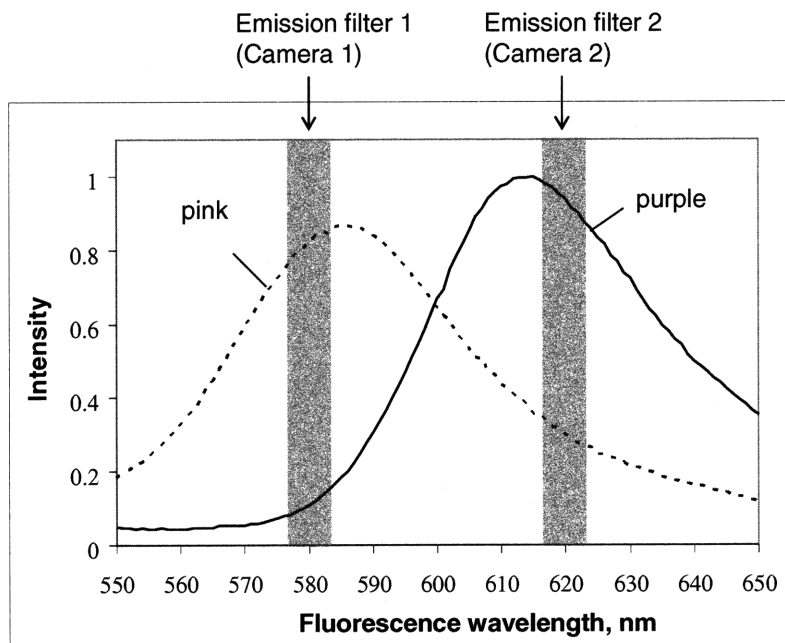


Figure 5-9: Normalized fluorescence spectra of pink and purple beads.

After performing some calibration experiments, the signal recorded by each CCD camera was related to the fluorescence of each species by the approximate relationships

$$S_1 = 0.89I_{\text{pink}} + 0.11I_{\text{purple}} , \quad (5.1)$$

$$S_2 = 0.25I_{\text{pink}} + 0.75I_{\text{purple}} . \quad (5.2)$$

In the above equations, S_1 and S_2 are the fluorescence signals (minus background) recorded by CCD cameras 1 and 2 and I_{purple} and I_{pink} are the fluorescence intensities emitted by the corresponding species. Solving for these fluorescence intensities gives

$$I_{\text{pink}} = 1.17S_1 - 0.17S_2 , \quad (5.3)$$

$$I_{\text{purple}} = 1.39S_2 - 0.39S_1 . \quad (5.4)$$

In Chapter 4, some empirical relationships were developed to account for the nonlinearity of the fluorescence-concentration relationship and for fluorescence changes due to magnetic-fluid concentration gradients. These relationships were useful because there was only one scattering species (latex beads) and because the force density pushing the magnetic and nonmagnetic species in the y direction was negligible. Whatever concentrations were present near the top surface of the capillary tube at a point x_1, y_1, z_1 were the same concentrations present at other points x_1, y_2, z_1 . For the flow-chip experiments considered here, there are two scattering species, and an increase in the concentration of the 435 nm particles in a region can enhance the fluorescence of the 910 nm particles in that region (and vice-versa). Furthermore, there are gradients in concentration in the y direction for both the magnetic and nonmagnetic species, so the fluorescence signals measured near the top surface of the channel are no longer representative of the concentration deeper into the channel.

As a first approximation, the concentration of each fluorescent species was treated as being linearly proportional to its fluorescence intensity. Because of this simplification, the experimental fluorescence-intensity profiles presented in this chapter only provide a qualitative description of the true concentration profiles.

5.3 Micro-chip experiments

A summary of the experimental results obtained using the micro-chips is given by Park [1]. Due to problems with clogging, all of the chips were eventually lost and only two experiments provided meaningful results. The most accurate of these experiments is summarized in Figure 5-10, with the mixture being injected into the channel at a velocity of $15\ \mu\text{m/s}$. In this figure, $t = 0\ \text{sec}$ is defined as the time when the leading edge of the mixture enters the region where the magnetic cores are present (active region). The three plots correspond to the profiles when the leading edge of the mixture reached halfway down the active region, when the edge made it all the way across the active region, and when 75% more volume was injected into the channel.

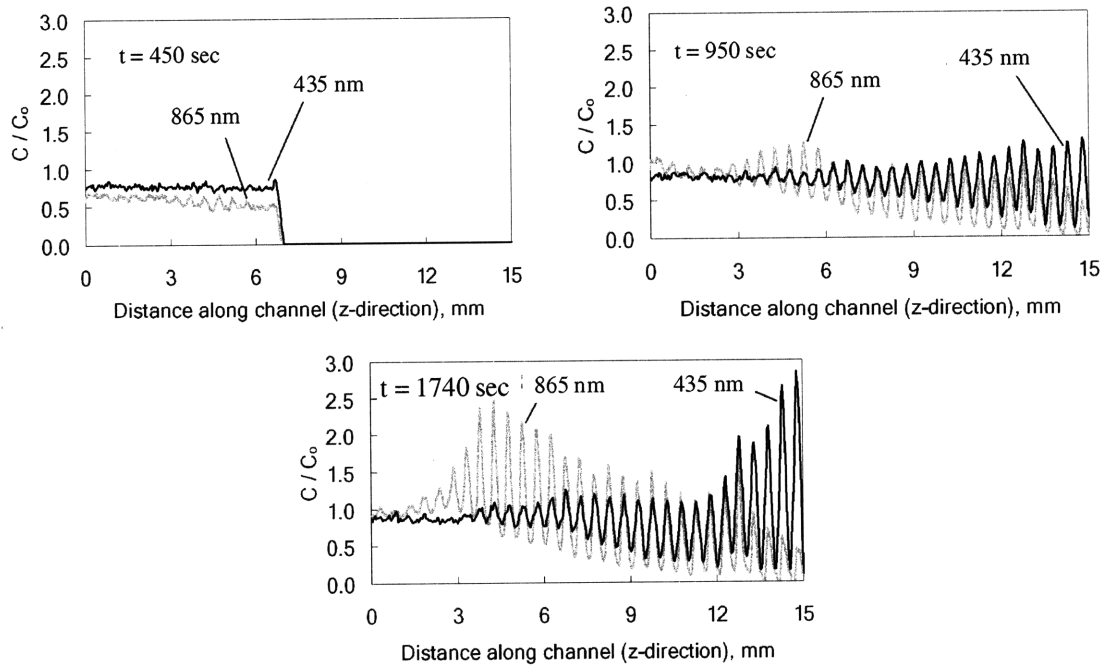


Figure 5-10: Experimental results for size-based trapping of latex beads.

As seen in the last plot, there is size-based trapping in the flow channel, with the larger particles being trapped further upstream. The sets of peaks are not completely separated from each other due to the continuous feeding of both species, resulting in an

overlap of the trapped 865 nm particles and the 435 nm particles being fed. Comparing the last two plots, we see that the 865 nm beads present near the end of the trapping region reached that location during the initial filling of the channel. Once the leading edge made it further downstream and the velocity reached an equilibrium profile, the 865 nm beads appear to be completely trapped before reaching $z = 12$ mm. The 435 nm particles, on the other hand, were never completely trapped.

If the force density in the y direction were negligible, the trapping force in the z direction would have to be an order of magnitude higher than the values given in Figure 5-4 to achieve trapping at a fluid velocity of $15 \mu\text{m/s}$. The reason we were able to achieve trapping in this experiment was because the x and y force densities forced the latex beads towards the top and bottom walls of the channel, as these are the regions where the magnetic field strength is the lowest (see Figure 5-5). Near the walls, the fluid velocity is much smaller than its mean value, and trapping can be achieved using smaller trapping force densities. Unfortunately, this transverse migration also led to more dispersion, as is apparent by the broad trapping regions observed in Figure 5-10.

5.4 Continuum and Brownian modeling

As attempt to model the microphysics taking place in the trapping experiments was initially made using the continuum models developed in Chapter 4. Due to sharp concentration gradients near the walls, which resulted in singularities near the regions where the latex beads accumulated, Brownian dynamics-type models were used instead to approximate the concentration profiles of the beads. These simulations were able to capture the experimental trends qualitatively, but could not predict them quantitatively due to the numerous simplifications made in the model and in converting the experimental fluorescence-intensity profiles into concentration profiles.

5.4.1 Governing continuum equations

For negligible changes in density, the governing equation for the concentration of the latex beads is given by

$$\frac{\partial C_p}{\partial t} + \underline{v} \cdot \nabla C_p = -\nabla \cdot \underline{J}_p. \quad (5.5)$$

The velocity of the fluid at equilibrium is the expression for steady-state flow in a rectangular channel,

$$\underline{v} = \bar{v} K \sum_{n=1,3,\dots}^{\infty} \frac{1}{n^3} (-1)^{\frac{n-1}{2}} \left[1 - \frac{\cosh\left(\frac{n\pi y}{L_x}\right)}{\cosh\left(\frac{n\pi L_y}{2L_x}\right)} \right] \cos\left(\frac{n\pi x}{L_x}\right) \hat{i}_z. \quad (5.6)$$

In the above expression, L_x and L_y are the width and height of the channel, respectively, \bar{v} is the mean velocity of the mixture, \hat{i}_z is a unit vector in the z direction, and the constant K is given by

$$K = \frac{48}{\pi^3 \left(1 - \frac{192L_x}{\pi^5 L_y} \sum_{m=1,3,\dots}^{\infty} \frac{\tanh(2m\pi)}{m^5} \right)}. \quad (5.7)$$

Eq. (5.6) is valid over the range $-\frac{L_x}{2} \leq x \leq \frac{L_x}{2}$ and $-\frac{L_y}{2} \leq y \leq \frac{L_y}{2}$.

A plot of this velocity profile is given in Figure 5-11, with the mean velocity being 15 $\mu\text{m/s}$ and L_x and L_y being 100 μm and 110 μm , respectively. In our model, both L_x and L_y were taken to be 100 μm , as accounting for the small differences in their actual values did not have noticeable effects on the results. As before, the diffusive flux is given by

$$\underline{J}_p = -\mathcal{D}_{pf} \nabla C_p \left[1 + 8(1 - \tilde{\beta}) v_p C_p \right] - \frac{\mathcal{D}_{pf} v_p}{RT} [C_p \mu_o M \nabla H], \quad (5.8)$$

with all the terms in the expression defined in the previous chapter. The magnetic nanoparticles obey the analogous equations,

$$\frac{\partial C_m}{\partial t} + \underline{v} \cdot \underline{\nabla} C_m = -\underline{\nabla} \cdot \underline{J}_m \quad (5.9)$$

and

$$\underline{J}_m = -\mathcal{D}_{mw} \underline{\nabla} C_m [1 + 8v_m C_m] + \frac{\mathcal{D}_{mw} v_m (1 - v_m C_m)^2}{RT} [C_m \mu_o M_m \underline{\nabla} H] . \quad (5.10)$$

The above set of equations is valid as long as the concentration of the species is not too large (the excess potential term is only valid up to first order in volume fraction) and the concentration gradients occur over length scales much larger than the species sizes (continuum assumption). For numerical purposes, the gradients in concentration must also take place over length scales not much smaller than the thickness of the channel.

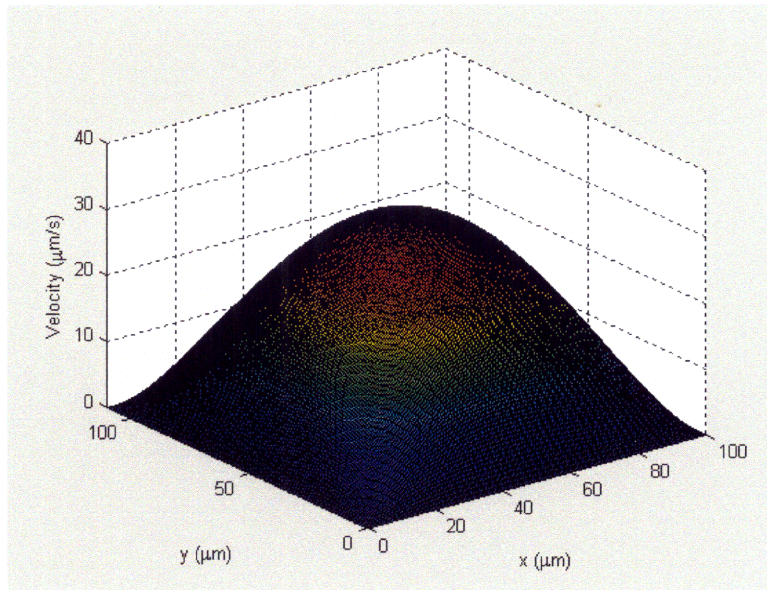


Figure 5-11: Velocity profile in a rectangular channel.

The boundary conditions require that there is no flux normal to any of the four channel walls. Since there is a non-zero force density in the y direction at the top and bottom walls, there must be a concentration gradient at the wall to balance this force. For the latex beads, this gradient is given by

$$\frac{\partial C_p}{\partial y} = - \frac{v_p C_p f_y}{\left[1 + 8(1 - \tilde{\beta}) v_p C_p\right] RT}, \quad (5.11)$$

where

$$f_y = \mu_o M \frac{\partial H}{\partial y}. \quad (5.12)$$

At short times, before the concentration becomes large near the walls, eq. (5.11) reduces to

$$\frac{\partial C_p}{\partial y} = - \frac{v_p C_p f_y}{RT}. \quad (5.13)$$

The characteristic length scale over which the latex bead concentration changes is thus given by

$$\ell_p \sim \frac{RT}{v_p f_y}. \quad (5.14)$$

For the magnetic nanoparticles, the force density of interest is in the x direction, pulling the magnetic nanoparticles towards the magnetic cores. Again, this force does not vanish at the walls, and a similar analysis yields

$$\ell_m \sim \frac{RTC_m}{f_x}, \quad (5.15)$$

where

$$f_x = \mu_o M \frac{\partial H}{\partial x}. \quad (5.16)$$

In order for the continuum approximation to be valid, we need to have $\ell_m \gg 1\mu\text{m}$ and $\ell_p \gg 1\mu\text{m}$, since the diameter of the latex beads is on the order of a micron. Since the half-width of the channel L_H is $50\mu\text{m}$, a different way to express this requirement is that both ℓ_m/L_H and ℓ_p/L_H must be $O(1)$ or greater everywhere in the channel.

The above requirements were tested using the peaks in the force densities given in Figure 5-6. The results are summarized in Figure 5-12, where the color-bar on the right

serves as a legend for the ratios ℓ_m/L_H or ℓ_p/L_H . As seen in the figure, the continuum assumption is valid for the 435 nm beads only over the first 12 cores (out of 30). For the 865 nm beads, the continuum assumption fails everywhere in the active region of the channel, meaning that the concentration gradients would occur over length scales comparable to or smaller than the size of the beads. In both cases, the sharp gradients in concentration at the top and bottom walls of the channel are too large for continuum models to be applicable. These sharp gradients indeed led to singularities and unphysical values in the concentration profiles when continuum simulations were attempted.

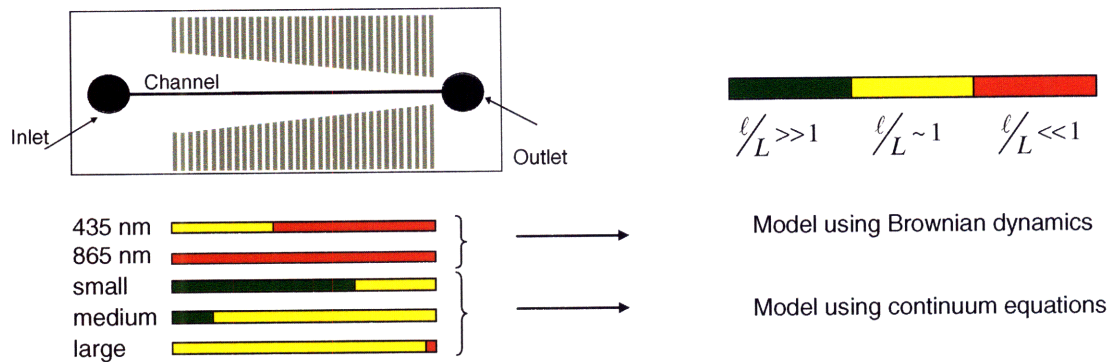


Figure 5-12: Test of the validity of continuum models for the flow-chip experiments as a function of the distance down the channel (z).

In Figure 5-12, the magnetic nanofluid was treated as a mixture of 3 different-sized magnetic species dispersed in water, as discussed in Chapter 2 and applied previously in Chapter 4. For the magnetic nanofluid, the analysis indicates that the continuum approximation should be valid everywhere except near the last core. Continuum simulations for the concentration profile of the magnetic nanoparticles were successful and no unphysical values were obtained, as expected from the results given in the figure.

Based on the analysis presented in Figure 5-12, the concentration profile for the magnetic nanofluid was obtained by solving the continuum eqs. (5.9) and (5.10). For the latex beads, the sharp concentration gradients near the top and bottom walls made the continuum model invalid, and their concentration profile was instead obtained using Brownian dynamics.

5.4.2 Brownian dynamics

The governing equation for Brownian dynamics comes from a force balance on the latex beads [3],

$$m_p \frac{d\mathbf{v}_p}{dt} = \underline{\mathbf{F}}_H + \underline{\mathbf{F}}_B + \underline{\mathbf{F}}_P , \quad (5.17)$$

where m_p is the mass of a bead, v_p its velocity, F_H is the hydrodynamic drag from the fluid continuum, F_B is the random Brownian force from fluid molecules, and F_P are all the surface and body forces resulting from external fields and interactions with other beads. For time scales much longer than the relaxation time for the beads to reach terminal velocities, the inertial term can be neglected. Eq. (5.17) thus becomes

$$6\pi\eta_f a_p \left(\frac{d\mathbf{r}}{dt} - \mathbf{v}_f \right) = \underline{\mathbf{F}}_B + \underline{\mathbf{F}}_P(\mathbf{r}, t) , \quad (5.18)$$

where \mathbf{r} is a position vector for the location of the bead and the velocity of the carrier fluid \mathbf{v}_f is approximately given by eq. (5.6). To leading order,

$$\underline{\mathbf{F}}_P(\mathbf{r} + \Delta\mathbf{r}, t + \Delta t) \approx \underline{\mathbf{F}}_P(\mathbf{r}, t) , \quad (5.19)$$

so the position of a bead is described by

$$\mathbf{r}(t + \Delta t) - \mathbf{r}(t) \approx \mathbf{v}_f \Delta t + \frac{\underline{\mathbf{F}}_P(\mathbf{r}(t))}{6\pi\eta_f a_p} \Delta t + \underline{\mathbf{X}} . \quad (5.20)$$

In the above expression, the vector quantity $\underline{\mathbf{X}}$ accounts for random displacements due to Brownian motion. It can be approximated by normally distributed random displacements, with a standard deviation of [3]

$$\langle \underline{X} \rangle = \left\langle \frac{\underline{E}_B}{6\pi\eta_f a_p} \right\rangle = \sqrt{\frac{kT\Delta t}{3\pi\eta_f a_p}}, \quad (5.21)$$

where Δt is the time step taken in the simulations.

5.4.2.1 Particle-particle interactions

The force expression \underline{E}_p includes both magnetic forces and interactions of the particle of interest with other particles. Starting from a configuration of randomly distributed nonmagnetic beads, simulations using FORTRAN codes, which accounted for excluded volume and electrostatic interactions of each bead with all the other beads present in the mixture, were performed. Unfortunately, these simulations were very time-consuming (lasting 3 days each) and could not be performed at the volume fractions used in the experiments (the volume fractions used were 30 times smaller than the experimental volume fractions due to computer memory constraints). Because of the small concentrations used, the results were no different than the results obtained using no interaction between the beads. As a first approximation, inter-particle interactions were neglected in the simulations presented in this work.

5.4.3 Magnetic force-density fitting

As seen in Figure 5-6, the magnetic force densities, particularly in the x and y directions, have significant amounts of numerical noise. In order to reduce the noise input into the models, empirical relationships were created to fit the data using analytical functions. Figure 5-13 shows empirical fits to the cross-section averaged forces using analytic functions. These fits (shown in red) appear to be accurate for the larger z values, but their accuracy cannot be determined for smaller z values due to numerical noise in the data. The fits used in the figure were

$$f_x = [-1000 - 1900 \exp(0.355z)] \{1 - \exp(0.01z) + \sin^2[2\pi(z - 0.25)]\}, \quad (5.22)$$

$$f_y = [1000 + 800 \exp(0.39z)] \{-1 + \exp(0.01z) + \sin^2 [2\pi(z - 0.25)]\} , \quad (5.23)$$

$$f_z = [1000 + 410 \exp(0.398z)] \sin(4\pi z) , \quad (5.24)$$

where the unit for z is mm and f_i are in N/m^3 .

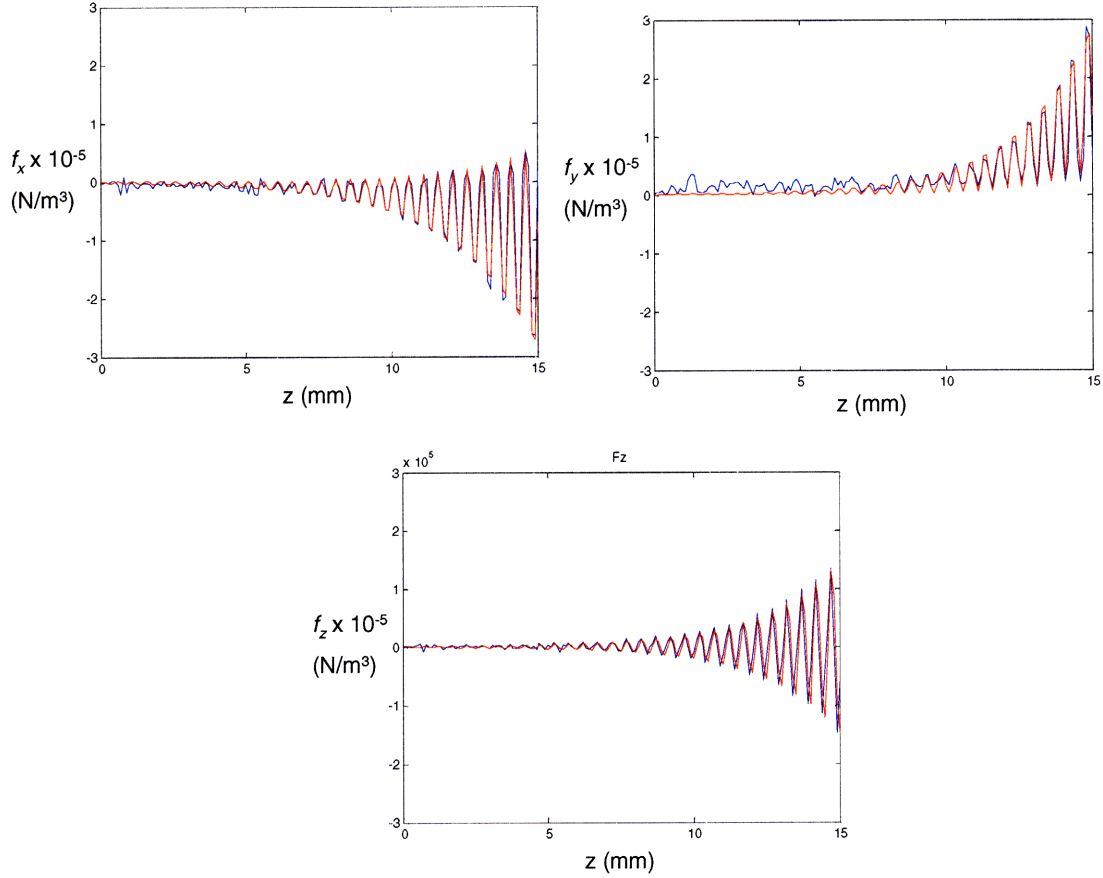


Figure 5-13: Empirical fits to the cross-sectional averaged magnetic force densities.

The force density in the z direction has a weak dependence on x and y , so the fit given by eq. (5.24) is applicable everywhere in the active region of the channel. However, as previously discussed in Section 5.1.3, the force densities in x and y directions vary considerable in all spatial directions. The force density in the x direction varies linearly with x , but has a more complex variation with y . Conversely, the force

density in the y direction varies linearly with y , but has a more complex variation with x . To improve the accuracy of the model, force densities of the form

$$f_x = [c_1 + c_2 \exp(c_3 z)] \{1 - \exp(0.01z) + \sin^2 [2\pi(z - 0.25)]\} \left[\frac{2x}{L_x} \right], \quad (5.25)$$

as suggested by the form of eq. (5.22) and the approximately linear dependence of the force density on x , were fitted at different y values. The values of these force densities at arbitrary y values were then obtained using linear interpolation. Similarly, force densities of the form

$$f_y = [c_1 + c_2 \exp(c_3 z)] \{-1 + \exp(0.01z) + \sin^2 [2\pi(z - 0.25)]\} \left[\frac{2y}{L_y} \right], \quad (5.26)$$

as suggested by the form of eq. (5.23) and the approximately linear dependence of the force density on y , were fitted at different x values. The value of each force density at arbitrary x values was then obtained using linear interpolation. In both of the above expressions, the origin ($x = 0, y = 0$) was taken to be at the center of the channel cross-section.

5.5 Model-predicted results

5.5.1 Magnetic nanoparticles

The concentration profiles for the different-sized magnetic nanoparticles were obtained using continuum simulations. The equations solved were eqs. (5.9) and (5.10), with the velocity profile given by eq. (5.6). After adding the individual concentrations and averaging the results over the cross section of the channel, we obtained the concentration profile given in Figure 5-14 at $t = 1740$ sec. As seen in the figure, there is negligible magnetic nanoparticle trapping over the first 10 mm of the channel, but the local concentration of magnetic nanoparticles more than doubles near the end of the active region. The magnetic force in this region is strong enough to trap (at least temporarily) some of the larger magnetic nanoparticles.

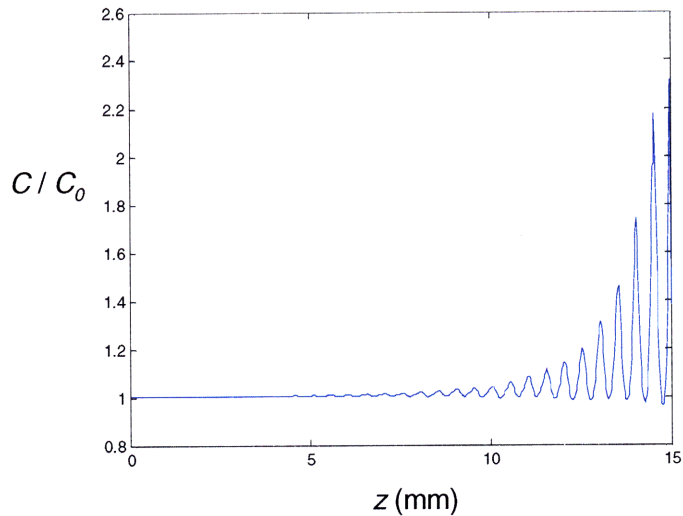


Figure 5-14: Normalized, cross-section averaged concentration of magnetic nanoparticles.

At first glance, it would appear that trapping of magnetic nanoparticles would increase the force density on the nonmagnetic beads near the end of the active region of the channel. Figure 5-15 shows cross section plots at $z = 14.5$ mm, near the end of the active trapping region, for the smallest and largest of the three magnetic nanoparticle sizes. In these plots, only a quarter of the channel cross-section is shown because of symmetry. The point $x = 0.05$ mm, $y = 0$ mm corresponds to the highest magnetic-field strength within the cross section, whereas the point $x = 0$ mm, $y = 0.05$ mm corresponds to the lowest magnetic-field strength within the same cross section. As seen in the figure, the magnetic nanoparticles, especially the larger ones, accumulated in regions where the local magnetic field was a maximum. Therefore, although the normalized concentration of magnetic nanoparticles increased over time over this cross-section, its value was less than unity in the region where the latex beads accumulated. Overall, trapping of magnetic nanoparticles within the active region of the channel reduced the effective trapping force-density on the latex beads.

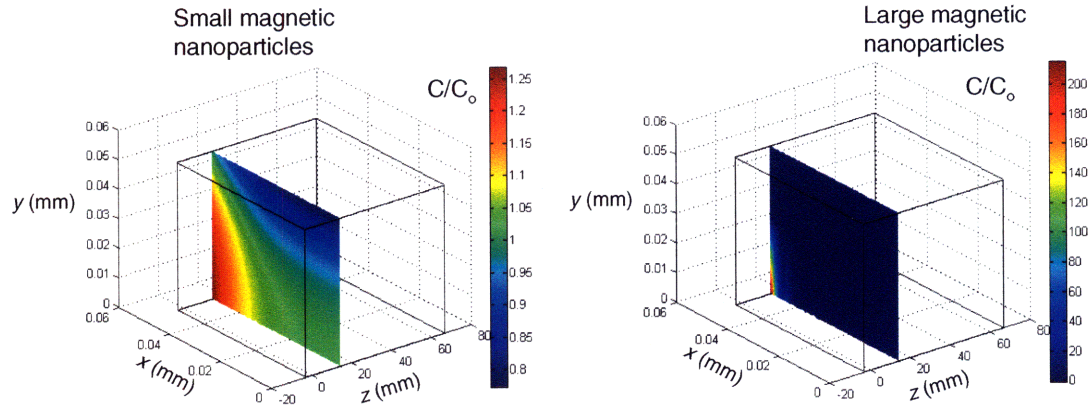


Figure 5-15: Normalized concentration of magnetic nanoparticles at the cross-section corresponding to $z = 14.5$ mm.

5.5.2 Latex beads

The concentration profiles obtained for the magnetic nanoparticles were recorded at discrete times and positions. This information was used to calculate the magnetic force on the latex beads as a function of time and space, as this force depends on the local concentration of the magnetic nanoparticles. Starting from a random orientation, the trajectories of individual 435 nm and 865 nm beads were calculated using the expression

$$\underline{r}(t + \Delta t) - \underline{r}(t) \approx \underline{v}_f \Delta t - \frac{2a_p^2 M \underline{\nabla} H}{9\eta_f} \Delta t + \underline{X}, \quad (5.27)$$

which was obtained from eq. (5.20) after neglecting particle-particle interactions. A new vector \underline{X} was generated at every time step for each latex bead using normally-distributed random-numbers, with a mean of zero and a standard deviation given by eq. (5.21). The force density was calculated from the expression

$$M \underline{\nabla} H = \frac{\phi_m(\underline{r}, t)}{\phi_{m,0}} (f_x \underline{i}_x + f_y \underline{i}_y + f_z \underline{i}_z). \quad (5.28)$$

The particles were confined to stay within the channel walls, but no attempt was made to keep them from overlapping. Volume exclusion effects would only be meaningful if the total number of particles used in the simulations were similar to the number of particles

used in the experiments. The time steps used were larger than the acceleration relaxation-times for the beads, but small enough such that $\langle X \rangle \ll L_x, L_y$.

The results of the simulation at $t = 1740$ sec. are compared to the experimental results in Figure 5-16. As seen in the figure, there is good qualitative agreement between the data and the simulations, both showing almost complete capture of the 865 nm beads, but incomplete capture of the smaller 435 nm beads. The height of the peaks is noticeably different, particularly for the 865 nm beads, but some of the difference may be due to the linear relationship between fluorescence and bead concentration used for the experimental results. Also, unlike the case for the pink 435 nm fluorescent beads, the purple 865 nm beads did exhibit some photobleaching during the experiments, and their fluorescence signal was weaker at the end of the experiments. This artifact was not known at the time the experiments were conducted.

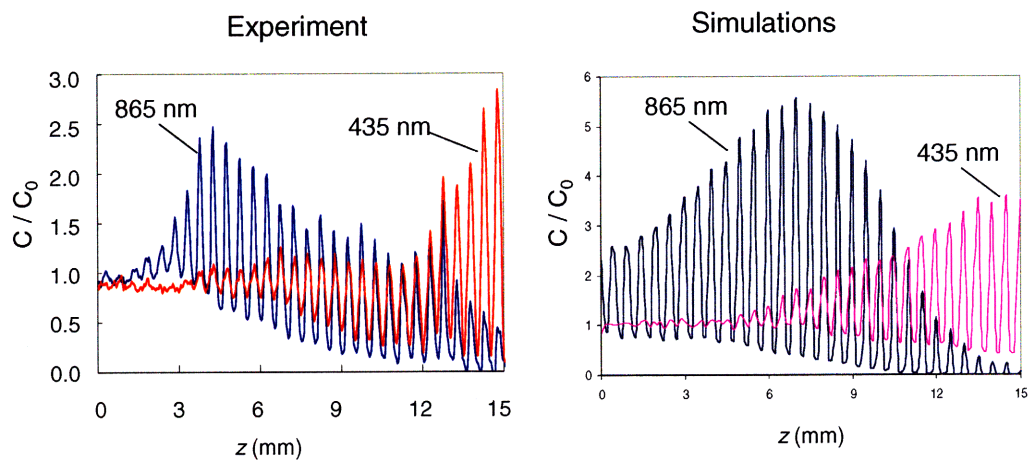


Figure 5-16: Comparison between experimental and model-predicted results for the size-based trapping of latex beads.

In the experiments, the parabolic-like velocity profile shown in Figure 5-11 was not fully developed near the leading front of the fluid as the channel was being filled. In this region of thickness $L_v \approx L_x$ for low Reynolds numbers [2], the velocity profile was three-dimensional and there was convective mixing of the latex beads. This may have resulted in some of the 865 nm beads being convected completely across the active

region of the channel, as seen in the second plot in Figure 5-10. There were also large fluctuations in velocity due to pressure buildups between the syringe and the channel. Neither of these artifacts was taken into account in the simulations.

The simulation results cannot be expected to be more quantitatively accurate due to the numerous simplifications made in the model. Numerical noise led to the use of empirical fitting functions to approximate the actual force densities. As discussed in Chapter 4, the magnetophoresis of latex beads in a magnetic nanofluid is highly sensitive to the resolution of the magnetic-field profile and the accuracy of the M - H relationship for the fluid, both of which were affected by the fitting process. Finally, the simulations neglect particle-particle interactions and hydrodynamic effects, both of which become important in the regions where the beads are trapped. Better quantitative agreement with the experimental data would require much more complexity in the model.

5.5.2.1 Effect of magnetic-field resolution

In Figure 5-13, empirical fits are presented for the force densities in all three directions, averaged across the channel cross-section. Figure 5-17 shows a comparison between the simulation presented in the previous section with a simulation performed using the cross-section averaged force densities. As seen in the figure, neglecting the variations in force density over the cross-section of the channel leads to more trapping of the 435 nm beads.

The reason for the large difference in the amount of 435 nm particle trapping between the two simulations is mainly due to the variation of f_y with x for larger values of z . Near $z = 0$ mm, when the opposing magnetic cores are further away from each other, f_y does not vary much with x . Near $z = 15$ mm, however, the opposing magnetic cores are much closer together, and the force density f_y is almost an order of magnitude higher near the side walls than near the center of the channel. Since the 435 nm beads are mostly near the center of the channel (i.e., near $x = 0$) at this point due to the force density f_x , the effective force density f_y pushing the beads towards the top and bottom walls is considerably smaller near $z = 15$ mm than the average value given in Figure 5-13. This is

not the case for the region where the 865 nm beads were trapped, so their trapping is not affected as much by using averaged force densities.

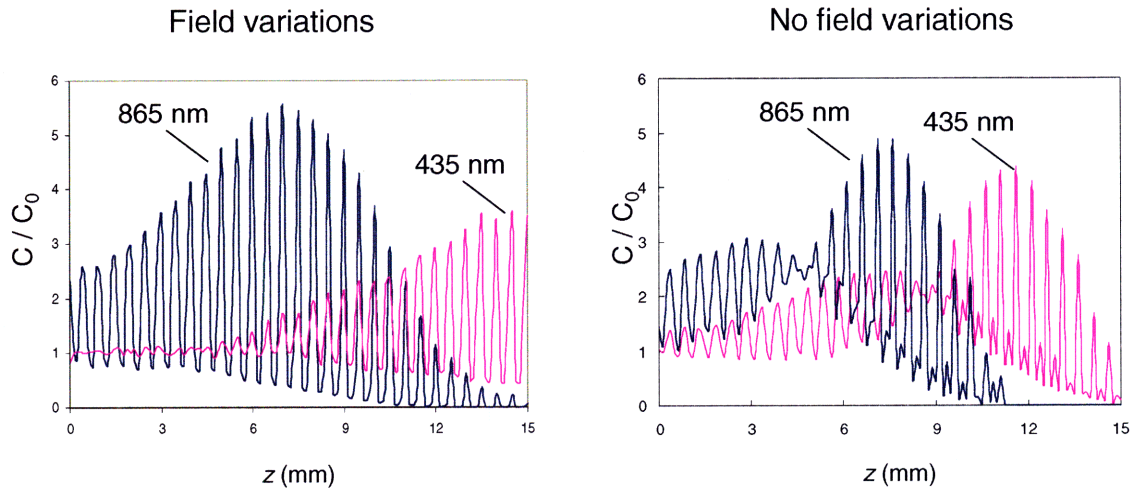


Figure 5-17: Effect of neglecting variations in the force densities over the channel cross-section.

5.5.3 Micro-chip simulation summary

As previously reported by Park [1], size-based trapping of a mixture of nonmagnetic particles was achieved using the concept illustrated in Figure 5-1. The larger 865 nm latex beads were trapped upstream and the smaller 435 nm beads were trapped further downstream within the active region of the flow channel. The amount of trapping was greatly enhanced by transverse migration of the latex beads towards the top and bottom surfaces of the channel, where the fluid velocity approaches zero.

Brownian dynamic simulations were used to model the experimental results. When variations in the force density are properly taken into account, the simulations were able to predict the experimental results semi-quantitatively. As expected, based on the sensitivity analysis performed in Chapter 4, the predicted results are highly sensitive to the magnetic force profiles used.

5.6 Plug-flow device

Although the micro-chip was successful in trapping nonmagnetic particles based on size, the resolution of the process was affected by the coupling between the 3-dimensional magnetic forces and the non-uniform velocity profile. In an attempt to eliminate such dispersion effects, a new setup was designed to allow for the flow channel to move at a constant velocity, as opposed to having the fluid flow within the channel. A schematic of this “plug flow” device is depicted in Figure 5-18. Instead of having pressure-driven flow through a capillary tube, a translation stage was used to move the capillary tube past a fixed magnetic-field profile. This resulted in a plug-flow profile for the velocity of the mixture with respect to the magnetic field.

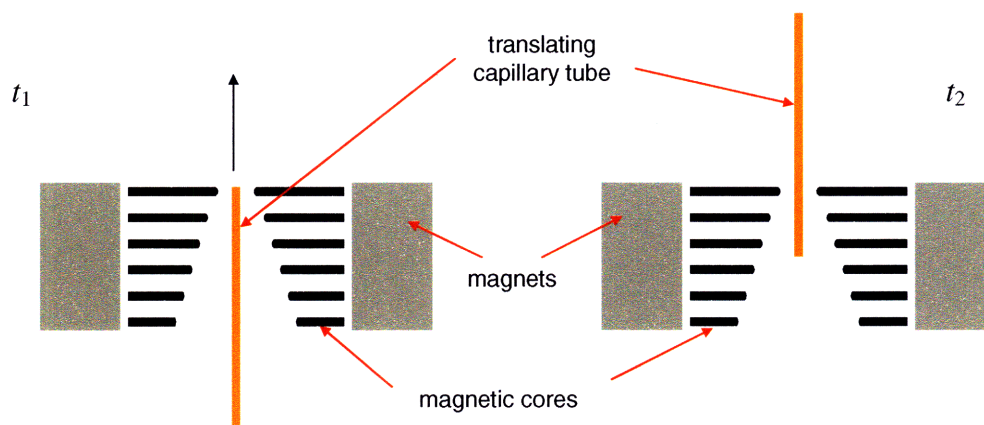


Figure 5-18: Schematic of “plug flow” device.

The magnetic fixture and capillary-tube holder used were fabricated in the MIT Central Machine Shop. Photographs of these components are shown in Figure 5-19. The main frame of the magnetic fixture was made out of iron, with a coating of black iron oxide to minimize the amount of reflected light. The closed loop (except for the small gap in the active trapping region) ensured that the magnetic flux was contained within the fixture. The same magnets previously used for the focusing experiments were used to generate the magnetic fields in this setup. A gap was needed between the magnets and

the iron core to yield the desired force-density profiles. A guiding channel grooved into an aluminum plate was used to keep the capillary tube as straight as possible (with respect to the magnetic fixture) as it travelled from left to right across the gap. The magnetic fixture was attached to an aluminum plate, which was used to mount the fixture onto an optical table.

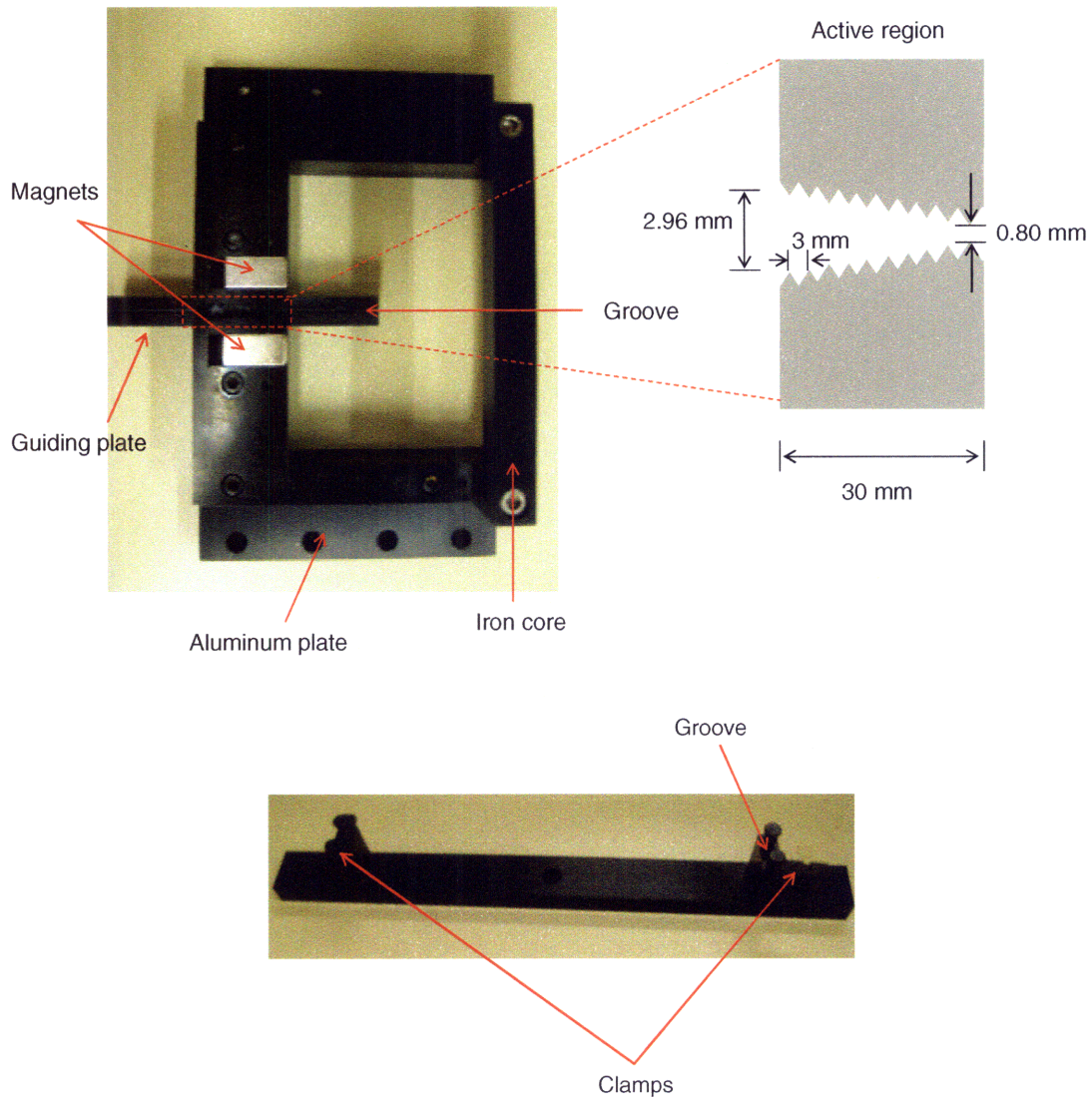


Figure 5-19: Magnetic fixture and tube holder used for the plug-flow experiments.

The tube holder shown at the bottom of Figure 5-19 was used to secure and guide the capillary tube through the gap in the magnetic fixture. The tube itself (Fiber Optic Center, New Bedford, MA) was 1 foot long and had a square cross-section, with an ID of 0.3 mm and an OD of 0.6 mm. The tube holder was attached to a translating stage (Parker Daedal MX80 miniature linear motor stage, Axis New England, Woburn, MA), which was externally controlled and was capable of travelling at velocities as low as 1 $\mu\text{m/s}$.

5.6.1 Magnetic and force fields

The magnetic field in the active region was calculated numerically using Maxwell 3D. The field intensity and resulting force density in the flow direction for a 0.3 vol % magnetic nanofluid, averaged across the capillary-tube cross-section, are shown in Figure 5-20. As before, the force density resembles the schematic profile depicted in Figure 5-1. The gap present between the magnets and the magnetic core prevented large spikes in magnetic-field gradients near the edge of the magnet and resulted in force-density peaks that grew monotonically with z .

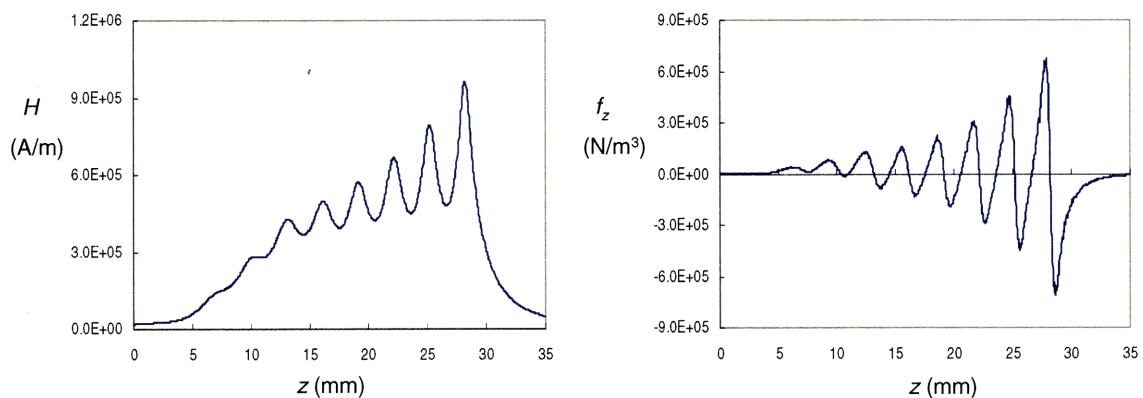


Figure 5-20: Magnetic field and force-density distributions for a 0.3 vol % magnetic nanofluid.

Since the fluid velocity was uniform everywhere, smaller force densities such as the ones generated by the micro-chip would no longer result in trapping of the smaller 435 nm latex beads. Also, the dimensions of the gap were limited by the thickness of the capillary tube used, which had an OD much larger than the width of the micro-chip flow-channel. In order to trap 435 nm beads in a fluid moving at 5 $\mu\text{m/s}$, a magnetic fluid three times as concentrated as the one used in the micro-chip experiments was required.

The use of thinner capillary tubes was not feasible due to alignment and image-registration issues. The plug-flow experiments required the capillary tube to travel distances of 45 mm in the z direction while keeping its axis on the plane $x = 0$. Any deviations in the x direction greater than 10% of the capillary-tube thickness would lead to time-dependent magnetic forces as well as errors in image registration and data processing. The 0.6 mm OD capillary tubes, with the use of the guiding groove photographed in Figure 5-19, proved to be the thinnest tubes that could remain near $x = 0$, $\pm 10\%$ of the tube thickness, while traveling a distance of 45 mm in the z direction.

5.6.2 Sample preparation

As before, the samples were prepared in 2 mL plastic vials, with the typical sample volume being 200 μL . Some common amounts for each of the components used are summarized in Table 5.2. For this set of experiments, only one fluorescent species was used at a time to avoid the overlap in fluorescence spectra.

Table 5.2: Common sample volumes and concentrations used in the plug-flow experiments

Component	Amount (μL)	Concentration in Mixture
2.3 wt % magnetic fluid	135	0.3 vol %
1 wt % latex beads	20	0.1 vol %
1.28 SG sugar solution	21	10.4 vol %
3.5 mM SDS	14.25	0.25 mM
0.2 M NaCl solution	4.75	4.75 mM
DI water	5	-
total	200	-

5.6.3 Data acquisition

Since only one fluorescent species was used in each experiment, the data-acquisition setup used was the same one depicted earlier in Figure 4-8. The only difference was that Computer 1 was also used to control the movement of the translation stage using a modified triggering code. The camera was stationary with respect to the magnetic fixture, so the mixture appeared to be flowing at a uniform velocity with respect to the camera.

5.6.4 Data processing

In each of the trapping experiments, a half-filled capillary tube traveled a distance of 45 mm through the active region of the magnetic core at a velocity of 5 $\mu\text{m/s}$. This distance is 1.5 times the length of the active region (30 mm) so that the amount of fluid passed by the active region was approximately the same as in the micro-chip experiments. A total of 31 images (including the one taken at $t = 0$ sec, corresponding to the time when the fluorescent beads first entered the active region) were taken at five-minute intervals.

Before the start of each experiment, a set of 31 background images was taken at the normal operating conditions using a capillary tube filled with a 0.3 vol % magnetic nanofluid. These images of the portion of the tube passing through the active region were taken at 1.5-second intervals while the capillary tube was traveling at 1 mm/s. The images corresponded to the location where the tube would be present in the actual experiments. The high velocity used during these background measurements did not allow for any magnetic fluid concentration gradients to develop. Taking 31 background images instead of one allowed for more accurate data processing, since the tube position in the x direction did vary slightly as the tube was traveling. The same procedure was repeated for a capillary tube filled with the full mixture in order to obtain the reference images. The rest of the data processing was performed as described previously in Section 4.2.

5.6.5 Experiments

5.6.5.1 Focusing

Due to the small dimensions of the gap in the magnetic fixture, no direct magnetic-field measurements could be made. To ensure that the magnetic-field profile agreed at least qualitatively with the numerical results presented in Figure 5-20, focusing experiments were performed with two different mixtures, one containing the larger 910 nm fluorescent beads and the other containing the smaller 435 nm beads. The samples were loaded into the capillary tubes by capillary action, and the ends of the tubes were sealed with glue. Since the predicted force-density profile had peaks which increased in magnitude with increasing values of z , the heights of the focusing peaks were expected to exhibit a similar behavior.

As seen in Figure 5-21, the height of the focusing peaks increased with increasing values of z in both experiments, implying that the force density shown in Figure 5-20 is at least qualitatively valid. In Figure 5-21, a 0.1 vol % magnetic nanofluid was used, and the images were taken at $t = 2$ (black), 4 (blue), 6 (green), and 8 seconds (red).

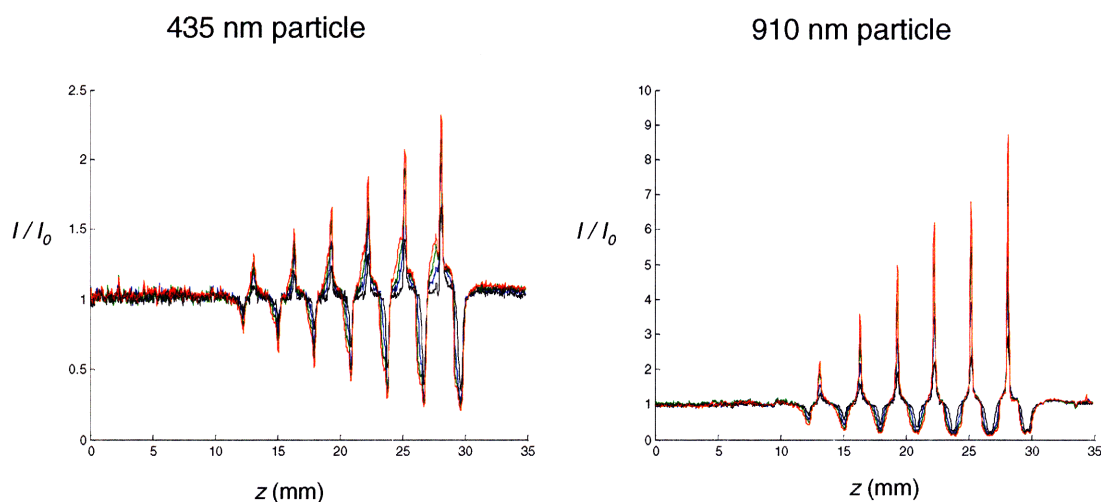


Figure 5-21: Fluorescence-intensity profiles for 435 nm (left) and 910 nm (right) fluorescent beads immersed in a 0.1 vol % magnetic nanofluid. The fluid velocity was zero in these experiments.

5.6.5.2 Size-based trapping

The initial set of trapping experiments attempted was analogous to the flow-chip experiments discussed in Chapter 4. The capillary tube was filled half-way with the mixture, with the ends of the tube sealed with glue, and placed on the tube holder with the edge of the mixture aligned with the point at $z = 0$. The capillary tube was then moved past the magnetic fixture at a velocity of $5 \mu\text{m/s}$ over a distance of 45 mm. Unfortunately, due to the larger magnetic forces and the much larger capillary-tube cross-section, the leading edge of the sample kept breaking apart and generating small air bubbles as the tube was moving past the fixture. These air bubbles acted as nonmagnetic bodies immersed in the ferrofluid and were trapped in the different trapping regions of the fixture. The bubbles affected the fluorescence signal enough that none of the trapping experiments yielded any meaningful results.

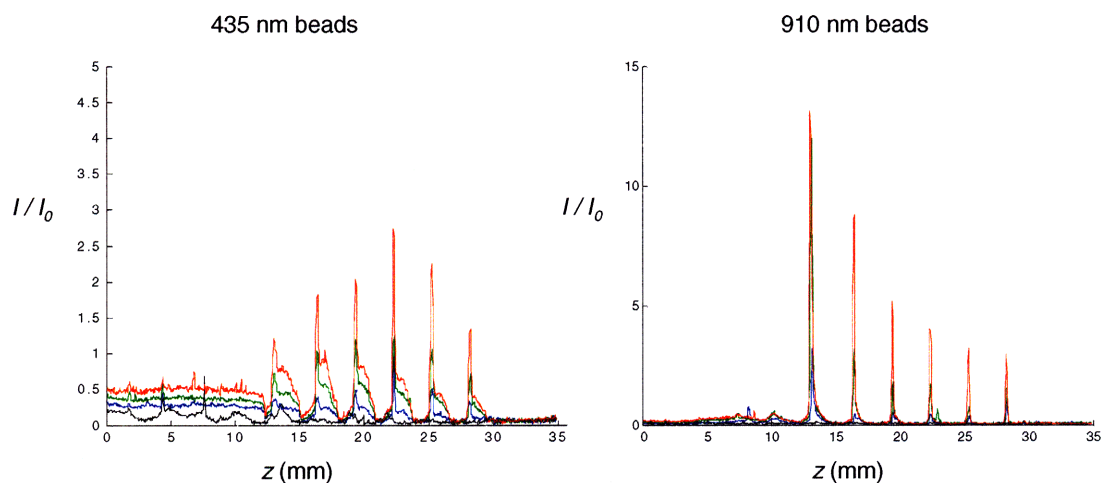


Figure 5-22: Fluorescence-intensity profiles for 435 nm (left) and 910 nm (right) fluorescent beads immersed in a 0.3 vol % magnetic nanofluid, with the capillary tube traveling at $5 \mu\text{m/s}$.

A new set of experiments was conducted by filling 3/4 of the capillary tube with DI water and the rest with the mixture of interest. Due to mixing during the loading

process and additional diffusion before the start of each experiment, some of the mixture was present as far as half way down the tube. At $t = 0$, the capillary tube was placed in the holder with the midpoint of the tube at $z = 0$. As before, the capillary tube was moved past the magnetic fixture at a velocity of $5 \mu\text{m/s}$ over a distance of 45 mm. The results obtained for both 435 nm and 910 nm beads are shown in Figure 5-22.

As seen in the plots, the normalized fluorescence-intensity (and the corresponding concentration) of the latex beads was less than unity at the entrance of the active trapping region ($z = 0$). This was due to the dilution with the water occupying the other 3/4 of the tube. We observe size-based trapping in the figure, with the 910 nm particles being trapped further upstream, but again there appears to be a significant amount of dispersion. Previously performed Brownian simulations predicted that most of the 435 nm particles should have been trapped at $z = 22$ mm and the 910 nm particles at $z = 14$ mm, with minimum amounts of overlap.

The reason for the dispersion is believed to be related to dilution effects. Since the first few latex beads passing through the active region were suspended in a more dilute magnetic nanofluid (due to mixing with water), they required larger magnetic-field gradients in order to be trapped. The magnetic nanofluid concentration increased as more of the mixture entered the active region, and trapping of the latex beads was attained with lower magnetic-field gradients. It is believed that the time-dependent force density artificially introduced into the experiments yielded most of the dispersion effects observed in Figure 5-22.

5.6.6 Discussion

The device discussed in this section was able to produce the required plug-flow profile designed to reduce the amount of dispersion present in the micro-chip experiments. However, the experiments performed with this device again yielded broad concentration-peak distributions, although this time apparently due to experimental artifacts. Perhaps the most effective way to minimize dispersion⁴ was to use a 0.3 vol % magnetic nanofluid to fill 3/4 of the tube instead of using water. This way, any mixing between the mixture and the filler fluid would not result in a decrease in the trapping-

force density. Due to time constraints, such experiments could not be completed and no definitive results are available.

5.7 Summary and conclusions

As previously reported by Park [1], the micro-chip experiments proved that size-based trapping can be achieved using a balance between magnetophoretic forces and flow-induced drag. The amount of trapping was greatly enhanced by transverse migration of the latex beads towards the top and bottom walls of the channel. This enhanced trapping came at the expense of reduced resolution due to flow-induced dispersion. Continuum simulations were used to model the concentration profile of the magnetic nanoparticles in the active region of the flow-chip channel. Due to the large concentration gradients present near the channel walls, continuum approaches could not be used for the latex beads. Instead, Brownian simulations, which neglected all particle-particle interactions, were able to provide semi-quantitative results for the concentration profiles of the latex beads.

The enhancement in trapping due to transverse migration of the beads was negated by a loss of resolution due to dispersion. In an attempt to improve on the resolution of the trapping results obtained using the micro-chip, a “plug flow” device was fabricated to reduce the amount of dispersion associated with nonuniform velocity profiles. Instead of flowing the mixture through a channel, the entire channel was moved with respect to a stationary magnetic field, resulting in a uniform velocity profile. Due to artifacts introduced during the experiments, the plug-flow device was not able to improve on the results obtained using the micro-chip.

5.8 Bibliography

1. Park, E.S. *Microfabricated Focusing Systems for the Separation of Submicrometer Particles*. M.S. thesis, Massachusetts Institute of Technology, 2004.

2. Deen, W.M. Analysis of Transport Phenomena. Oxford University Press, New York, 1998.
3. Van Gunsteren, W.F. and Berendsen, H.J.C. Algorithms for Brownian dynamics. *Molecular Physics*, 45(3): 637-647, 1982.

Chapter 6

6. Concluding Discussion

The goal of this thesis was to investigate the magnetophoretic focusing and trapping of submicron, nonmagnetic species immersed in magnetic nanofluids in the presence of nonuniform magnetic fields. Focusing was achieved using two pairs of permanent magnets, which forced fluorescently-tagged polystyrene beads to focus in the region between the two magnet pairs. Size-based trapping was achieved using a microchip and a “plug flow” device that produced spatially increasing magnetic field gradients that trapped flowing polystyrene beads at different locations, depending on their relative sizes. A potential application of this work is size based separation and focusing of species such as DNA, viruses, cell fragments, inclusion bodies, and other biological species in the submicron range. Since our techniques do not involve any binding of magnetic nanoparticles, they are equally applicable to the trapping and separation of synthetic species as well.

6.1 Principal contributions

The first contribution of this work is the development of the governing equations for multi-component diffusion in the presence of nonuniform magnetic fields. This set of equations reduces to the classic results given in the literature when electromagnetic fields are not present [1]. In the absence of nonidealities arising from the presence of the applied fields, this set of governing equations reduces to the classic results obtained by treating the magnetic field effects as externally applied body forces. The only work previously done in this area was that of Blums [2], valid for constant density systems.

Another contribution of this work is the fundamental understanding of the mechanisms involved in the focusing of nonmagnetic species in magnetic nanofluids. The continuum model developed was able to predict the experimental results quantitatively over the range of particle sizes, magnetic fluid concentrations, and

magnetic field profiles studied. So far, most of the work published in the literature involves the trapping of individual nonmagnetic species, with the only previous study on focusing being the work published by Fateen [3].

The last major contribution of this work is the understanding of the mechanisms involved in the size-based trapping of nonmagnetic species immersed in magnetic nanofluids. Our model was able to semi-quantitatively predict the experimental results previously published by Park [4]. The model served as a guide for the design of other devices intended to minimize the amount of flow-induced dispersion present in the micro-chip experiments published by Park.

6.2 Limitations

6.2.1 Multicomponent diffusion

The multicomponent equations derived in this work are of course not useful for processes where continuum descriptions are not valid. These equations were useful in studying the focusing of nonmagnetic species in the absence of flow, but could not be applied to the flow experiments. Another limitation is that, in the form presented in Chapter 3, the equations cannot account for anisotropies in the activity coefficients. Finally, the set of equations is only valid for the case where \underline{M} and \underline{H} are parallel and there are no electrical currents in the fluid. Free currents and non-equilibrium values of \underline{M} (i.e., \underline{M} and \underline{H} are not parallel) are both sources of entropy that are not accounted for in this work [5].

6.2.2 Focusing model

Besides the short-comings already described in Section 6.2.1, the focusing model developed in this work is only valid up to leading order in the volume fraction of the magnetic nanoparticles and nonmagnetic particles. At higher concentrations, the two-body approximations used to derive the excess chemical potentials are no longer valid.

The nonmagnetic particles must also be much larger than the magnetic nanoparticles for the pseudo-binary approximation used to be applicable. A large size ratio is also required for the force-density used on the nonmagnetic particles to be valid. Finally, since our model only uses the first three moments of the magnetic nanoparticle size distribution, the predictions are expected to be less accurate at long times, especially for highly polydisperse nanofluids.

6.2.3 Trapping devices

Although the micro-chip was able to achieve size-based trapping of nonmagnetic particles, the trapping regions for the two species overlapped to do dispersion effects. The plug-flow device presented in this work could potentially improve on the resolution of the trapping regions, but the low velocities needed (in the order of $5\ \mu\text{m/s}$) lead to very low throughputs. As such, the devices discussed in this work are limited to analytical applications, where smaller sample volumes are required.

6.3 Recommendations for future work

The trapping devices presented in this work require low fluid velocities, thus hindering their applicability for higher throughput processes. One way to overcome the velocity limitations is to have multi-stage processes, where instead of trapping species against flow one could simply divert their paths numerous times and achieve spatial or temporal separations at higher throughputs. Although the trapping devices presented here provide a better framework for studying negative magnetophoresis in the presence of flow, they are not adequate for higher throughput applications.

6.4 Bibliography

1. Bird, R.B. Five decades of transport phenomena. *AIChE Journal*, 50(2): 273-287, 2004.

2. Blums, E., Mikhailov, Yu. A., and Ozols, R. *Heat and Mass Transfer in MHD Flows*. World Scientific Publ. Co., Singapore, 1987.
3. Fateen, S. *Magnetophoretic Focusing of Submicron Particles Dispersed in a Polymer-Based Magnetic Fluid*. Ph.D. thesis, Massachusetts Institute of Technology, 2002.
4. Park, E.S. *Microfabricated Focusing Systems for the Separation of Submicrometer Particles*. M.S. thesis, Massachusetts Institute of Technology, 2004.
5. Rosensweig, R.E. Continuum equations for magnetic and dielectric fluids with internal rotations. *Journal of Chemical Physics*, 121(3): 1228-1242, 2004.